Durham E-Theses

Towards interferometry with bright solitary waves in a ring

YU, MANFRED,MAN,HOI

Towards interferometry with bright solitary waves in a ring

Manfred Man Hoi Yu

A thesis submitted in partial fulfilment
of the requirements for the degree of
Doctor of Philosophy

Durham University

Department of Physics
Durham University

February 3, 2016

Towards interferometry with bright solitary waves in a ring

Manfred Man Hoi Yu

Abstract

This thesis presents the work towards the realisation of an interferometer using bright solitary waves in a ring. The splitting of a bright solitary wave, which is created from a ^{85}Rb Bose-Einstein condensate in an optical waveguide, is realised through scattering from a narrow potential well formed from a tightly focussed red detuned laser beam. We observe reflection of up to 25% of the atoms, along with the trapping of atoms at the position of the potential. Such a reflected fraction is much larger than the theoretical predictions for a single, narrow Gaussian potential. A more detailed model, which accounts for the diffraction pattern of the laser beam, suggests that the presence of these small subsidiary intensity maxima is the cause of the enhancement in quantum reflection.

An upgrade of the apparatus sees a new set of magnetic coils, a compact coil mount, and a crossed optical dipole trap with independently controllable beams implemented. This enables the control of magnetic curvature and dipole trap position, and maximises the optical access to the science cell. To generate a ring trap for the interferometry scheme, a spatial light modulator (SLM) is incorporated into the experiment. Through underfilling the SLM panel with the laser beam, and the use of the analytical first phase guess prior to the error minimising Mixed Region Amplitude Freedom (MRAF) algorithm, we are able to generate speckle-free, high quality holograms of arbitrary shapes. Furthermore, we demonstrate atom trapping in a ring potential, which is formed at the intersection of the SLM beam and a red detuned horizontal light sheet.

Declaration

I confirm that no part of the material offered has previously been submitted by myself for a degree in this or any other University. Where material has been generated through joint work, the work of others has been indicated.

Manfred Man Hoi Yu
Durham, February 3, 2016

The experimental data presented in this thesis is available for download via: [dx.doi.org/10.15128/bn999672v](dx.doi.org/10.15128/bn999672v).

For mum, dad, and Herrick.

Acknowledgements

in the lab, or getting grumpy having been stuck in the office till late night writing my thesis, she never failed to keep me going and put a smile on my face. *Kokorokara kanshashiteorimasu.* Thank you for standing by my side. Thank you for all the heart-warming moments, and may it continues for many years to come.

Last, but not least, I would like to thank my mum, dad, and my twin brother Herrick, for all their loves and supports. I would not have gotten this far were it not for them. I thank my parents for always offering me the best caring and upbringing, even if receiving education in the United Kingdom at an early age would mean sacrificing precious times together in Hong Kong. Throughout my PhD, my family had given me a tremendous amount of helps and confidence that got me going. Mum, dad, and Herrick: I love you, and I am forever grateful for everything you have done for me.

Contents

List of Figures

List of Tables

Chapter 1

Introduction

1.1 Background

1.1.1 Bose-Einstein condensation

Bose-Einstein condensation (BEC) is a phenomenon predicted by Bose [1] and Einstein [2, 3] in 1924 for an ideal Bose gas where particles obey Bose-Einstein statistics. Unlike the half-spin fermionic particles that follow the Pauli exclusion principle, there is no statistical limit on populating quantum energy states with integer-spin bosons. At sufficiently low temperature, the bosonic particles macroscopically occupy the lowest energy state and the system 'condenses'. The quantum mechanical wavefunctions of individual bosons spatially overlap each other and merge into a single matter-wave. This is in fact a quantum phase transition as the condensation is manifested from the quantum statistics. BEC is closely connected to the rise of superfluidity in Helium and superconductivity involving Cooper pairs of electrons [4–6].

It was not until about 70 years after the prediction that the first atomic BEC was experimentally realised. In 1995, Wieman and Cornell demonstrated the condensation of ^{87}Rb [7], while the condensation of ^{23}Na was achieved by Ketterle [8]. The scientific significance of these experimental breakthroughs was recognised by the Nobel prize in Physics in 2001. Following these observations, we have since seen an escalating interest in BEC physics. To date, BECs of various dilute alkali gases have been created, such as ^{7}Li [9],

^{39}K [10], ^{41}K [11], ^{85}Rb [12, 13], and ^{133}Cs [14]. Adding to the family is a host of other bosonic isotopes of elements, which includes calcium [15], strontium [16–18], ytterbium [19], erbium [20] and chromium [21, 22]. All of these have opened up the gateways to a broad range of advanced experiments that demonstrate quantum mechanics on a macroscopic scale. For instance, particle-wave duality – a property that lies at the heart of the bizarre world of quantum mechanics, can be displayed through the interference between condensates [23, 24]. Through balancing the dispersive nature of the condensate and the strength of the attractive interatomic interaction, one creates a macroscopic excitation known as a *bright soliton* [25]. It is robust to collisions with other solitons, while multi-soliton interaction at a potential barrier is phase-dependent. These properties, which will be discussed shortly, are central to the motivation of this work, where we wish to utilise such a matter-wave to construct an interferometer for rotational sensing.

1.1.2 Soliton and bright solitary waves

Mathematically, solitons are localised particle-like solutions to 1-dimensional (1D) nonlinear differential equations [26]. They exhibit the following properties [27]:

- Their wave profile is maintained during propagation;

- They are localised, and decay or become constant at infinity;

- They are robust to collisions with other solitons.

It should be stressed that a true soliton only arises in 1D systems. In reality, we can only at best create a quasi-1D system in the 3D physical world. While the features of a true soliton are still observed with the additional dimensions (see examples below), these systems inevitably deviate from the description of a true soliton. Hence, to differentiate from a soliton, its 3D counterpart is referred to as a *solitary wave*. However, the term *soliton* and *solitary wave* are commonly used interchangeably in literature.

Solitons were first discovered by John Scott Russell in 1834 when he encountered the non-dispersive waves in the shallow water of the Union Canal [28].

Described as 'wave of translation' in his own words, the first experimental study of solitary waves was published in 1844 [28]. Extensive studies of solitons have since been carried out in a diverse range of fields and media, which include nonlinear optics and optical fibres [29–33], plasma physics [34], magnetism [35], and the human body [36].

In a degenerate Bose gas, the weak interatomic interaction gives rise to nonlinearity in the system. In the ultracold environment, the strength of such interactions is determined by the *s*-wave scattering length, a quantity that can be tuned by exploiting a Feshbach resonance [37]. Utilising such tunability, the first experiments of BECs with attractive interactions were performed with ^{7}Li [9] and later on with ^{85}Rb [12]. The stability of these condensates, however, is strongly dependent on the trap geometry. In particular, an increasing number of atoms in a 3-dimensional (3D) BEC leads to instability of the condensate. These systems tend to infinitely increase the density in order to reduce the interaction energy, which eventually results in a collapse of the degenerate gas [25]. Given the name 'Bosenova', this phenomenon has been experimentally observed [38–40], where a stable BEC implodes following a change from repulsive to attractive interatomic interaction in a 3D trap. Remarkably, the stability of the attractive condensate is enhanced if it is placed in a trap where the confinement along one direction is weak, or ideally, effectively removed [25]. In such a trap, precise tuning of the scattering length allows an exact cancellation between the attractive interactomic interaction and the dispersive wave-like nature of the condensate along this 'free' direction, resulting in the formation of bright solitary waves.

In 2002, single *bright solitary waves* from ^{7}Li were realised at ENS, Paris [41]. Here, the attractive condensates with $N \approx 2 \times 10^4$ atoms were observed to propagate over $1.1\,\text{mm}$ in the optical waveguide without dispersion. In the same year, soliton trains from ^{7}Li were observed in another experiment at Rice [42]. Later on in 2006, the formation of multiple solitons after the collapse of an attractive ^{85}Rb BEC in a 3D trap was demonstrated at JILA [43], while a single ^{85}Rb bright solitary wave was first realised here in Durham in 2012 [44].

Interestingly, bright solitons possess particle-wave duality on a macroscopic level: in a 3D geometry, the outcome of the interactions between two particle-like solitons depends on the relative *phase* between them [45, 46]. This has been experimentally observed: the solitons in the Rice and JILA experiments collided and repelled each other during the oscillation in the trap [42, 43]. This led to the conclusion that, while the origin is not satisfactorily explained, there exists a π phase difference between the neighbouring solitons [46]. Recently, in-phase and out-of-phase binary soliton collisions, along with various phase dependent collisional dynamics, have been extensively studied experimentally [47]. These observations, however, highlight again that much theoretical work is still required in order for us to understand the soliton dynamics fully. Indeed, the phase relation between the two solitons in ref. [47], which were created by dividing a single condensate using a repulsive barrier, was not controllable. Nevertheless, the study of phase-sensitive macroscopic collisional behaviour has sparked broad interests in constructing future interferometers using bright solitary waves [42, 48–52], as will be explained in the following section.

1.1.3   Matter-wave interferometry

Interferometers have long been established as an important tool in physics for precision measurements. In an optical interferometer, a light wave is first coherently split at a beam splitter. The two resulting partial waves subsequently recombine, forming an interference pattern which depends on the relative phase arising from the path difference before recombination. Matter-wave interferometers make use of the wave-like properties of a particle. With a non-zero mass, such an interferometer is highly sensitive to inertial effects such as rotation and acceleration. The first experimental realisation of the interference in atoms was achieved by Ramsey in the 1950s [53]. However, it was not until about two decades later that the inertial effect on matter-waves was first demonstrated, where a quantum mechanical phase shift of neutrons in a gravitational field was reported [54]. With advancing laser technology, the first experiments in matter-wave interferometry with atoms were eventually realised in the early 1990s [55, 56]. These experiments made use of two-photon stimulated Raman transitions, using a laser pulse to split the atomic matter-wave (originally in the hyperfine ground state) into a superposition of

partial waves with different momenta. Analogous to the optical interferometer, the phase of the two wavepackets evolves before recombining through the application of a second laser pulse, creating interference depending on the relative phase shift. Matter-wave interferometry has since seen a dramatic growth, demonstrating a broad range of applications, such as inertial sensing [57], and measurements of the gradient of the Earth's gravitational field [58, 59], the gravitational constant [60], and the rotation rate [61–63].

The ability to split and recombine bright solitary waves and their phase-dependent collisional behaviours have made them an intriguing candidate for interferometry. In particular, the interacting solitary wave is predicted to provide an interferometer that overcomes the standard quantum limit of accuracy [49]. Such improvement in sensitivity has attracted many proposed schemes of interferometers [49, 64, 65] and precision measurements such as surface probing [48]. Recently, the first soliton interferometer of the Mach-Zehnder type has been experimentally realised [66]. This interferometer is constructed by driving Bragg transitions through the use of an optical lattice aligned colinear with the optical waveguide. It is found that the solitonic matter-waves enhance the visibility of the interferometer fringes.

In this thesis, we present the work towards the realisation of rotational sensing with bright solitary waves – a scheme originally proposed in refs. [51, 52]. The key components are narrow potentials for splitting and recombining solitons, as well as a ring trap for soliton propagation. A ring geometry, where the axial trapping is absent, provides a system that describes a true soliton that arises from the integrable nonlinear Schrödinger equation. More interestingly, this interferometer does not rely on inspecting the interference structure of condensates, but rather interpreting the relative phase directly from the population transfer between the two split solitons after a scattering event. Hence, such a scheme presents an exciting and an alternative way to traditional matter-wave interferometers for precise inertial sensing.

1.2 Thesis context

This thesis presents work towards the realisation of rotational sensing using bright solitary waves formed from ^{85}Rb condensates. The first part of this work presents the observation of quantum reflection of such matter-waves from a narrow potential well. The experimental studies of soliton splitting highlight the dependence of soliton collisional behaviour on the soliton velocity, well depth, and the structure of the narrow potential. Gaining understanding of soliton interaction with attractive potentials also serves as a springboard towards one of the long term goals of the experiment – to precisely probe the potential of a dielectric surface with bright solitons [48].

In the second and main part of this work we focus on developing the experimental equipment and techniques that allow us to realise the bright solitary wave interferometer. An apparatus upgrade is carried out, which sees the implementation of new magnetic coils, a new optical dipole trap, along with redesigned coil mounts and homebuilt electronics. Furthermore, a ring trap, a key component of the interferometry scheme proposed in [51, 52], is generated through a device known as a spatial light modulator (SLM). Through phase imprinting, one can manipulate the light into desired intensity patterns. This presents a great scope for generating ring traps for solitary waves, as well as atom trapping in any arbitrary potentials. The transfer of ultracold atoms from the dipole trap into the ring trap will also be discussed.

Prior to the author's (MMHY) contribution to this work, the experiment was already well developed by the following researchers: Sylvi Händel (SH), Anna Marchant (AM), and Timothy Wiles (TW). SH was involved in the preliminary stage of the experiment which includes the construction of the optical setup for laser cooling, the vacuum system, and the magnetic transport. Both SH and AM carried out the optimisations and characterisations that led to the first observation of ^{87}Rb condensate in our laboratory. AM and TW developed and characterised the crossed dipole trap, and subsequently, AM demonstrated the creation of ^{85}Rb BEC through direct evaporative cooling. While a brief overview of the work up to the creation of ^{85}Rb BEC is presented in this thesis, the readers are advised to refer to the theses of SH [67] and AM [68] for in-depth discussions. Moreover, TW's work on the experi-

mental control system can be found in ref. [69].

Throughout this thesis we focus on the work undertaken by MMHY, which are as follows: the alignment and characterisation of the waveguide was achieved by TW and MMHY, which led to the realisation of the bright solitary matter-waves and the observation of classical reflection from a broad barrier performed by AM. MMHY designed and characterised the tightly focussed 852 nm light sheet, while the alignment and the initial experiments with the narrow potential well was performed by MMHY and TW. MMHY and AM proceeded to demonstrate quantum reflection of the bright solitary waves from the potential well. For the upgrade of the apparatus, MMHY, AM, and Ana Rakonjac (AR) were involved in the design, construction, and implementation of the new magnetic coils and dipole beams. AM and AR demonstrated the creation of ^{87}Rb BEC in our new system. Building on Jan Becher's (JB) initial work on the SLM, MMHY optimised the performance of the SLM which yielded smooth and speckle-free holograms. The SLM setup and the horizontal light sheet optical setup in the main experiment were designed and aligned by MMHY. The light sheet characterisation was performed by MMHY and AR, while that of the SLM beam was carried out by MMHY. Finally, MMHY, AM, and AR demonstrated the transfer of atoms from the crossed dipole trap into the ring trap, which is formed at the intersection of the SLM and the horizontal light sheet beams.

1.3   Thesis outline

The structure of this thesis is as follows:

- Chapter 2 provides a brief outline of the theoretical framework of bright solitary waves and their interaction with narrow potentials.

- Chapter 3 describes the experimental apparatus and various experimental techniques that are utilised for the measurements presented in this thesis.

- Chapter 4 describes the journey from creating ^{85}Rb condensates via direct evaporative cooling to the realisation of bright solitary waves [13, 44].

- Chapter 5 reports the results of quantum reflection of a bright solitary wave from a narrow potential well [70].

- Chapter 6 describes the upgrade of the experimental apparatus. It records the modelling, design, and implementation of our new magnetic coils, optical dipole trap, and electronics. This chapter then demonstrates the condensation of ^{87}Rb in the upgraded setup.

- Chapter 7 describes the generation of arbitrary intensity patterns using an SLM. A comprehensive optimisation of hologram quality is presented in this chapter.

- Chapter 8 contains details of the implementation of the SLM beam and a light sheet beam into the experiment. This chapter then reports the observation of atom trapping in the ring trap.

- Finally, Chapter 9 summarises the work presented in this thesis and presents the future goals and outlook of the experiment.

Chapter 2

Theoretical background

2.1 Introduction

In this chapter, we present a brief overview of the theoretical work behind the goal of this project – to construct a bright solitary matter-wave interferometer for precise rotational sensing. Starting with introducing the BEC and the Gross-Pitaevskii equation (GPE), we discuss the bright soliton solution to the 1D GPE, soliton interaction with narrow potentials, and the utilisation of the phase-dependent soliton recombination at a potential barrier in construction of interferometers.

A soliton, a self-focussing non-dispersive wave packet, can be formed from a degenerate Bose gas by balancing the attractive interatomic interactions and the dispersion of the condensate, as discussed in Section 1.1.2. Maintaining its shape while it propagates, this mesoscopic matter-wave exhibits robust particle-like bahaviour, enabling the study of quantum mechanics on a much larger scale. The dynamics of binary solitary wave collisions have been theoretically visited within the framework of mean field GPE [45, 46]. The creation of multiple solitons can be achieved through the splitting of solitary wave at narrow potentials. This process has been extensively studied theoretically with both repulsive potential barriers [64, 65, 71–73] and attractive potential wells [74, 75]. For splitting to occur, the incoming soliton must carry a kinetic energy larger than the difference between its ground state energy and the total ground state energy of the resulting solitons [72, 73, 76].

In the regime where such an event is energetically allowed, the probabilities of transmission and reflection depend strongly, but not exclusively, on the kinetic energy of the incoming solitary wave compared to the potential energy of the barrier/well. This creation of coherent localised condensates is analogous to a beam splitter that coherently splits a light beam. The two resulting solitary waves after splitting can subsequently be recombined by scattering at a second potential barrier [77]. The outcome of the recombination depends strongly on the relative phase between the two solitary waves [45, 46]. As such, soliton splitting and recombination have been suggested as a fundamental component in the construction of matter-wave interferometers [49, 52, 77, 78]. In particular, much to our interest, an interferometer for rotational sensing can be formed by splitting and recombining the solitary waves that are confined in a ring geometry [51, 52]. On the other hand, in a regime where splitting is energetically disallowed, one can generate a quantum superposition state of solitary waves, or the so-called Schrödinger cat state [50, 76, 79, 80].

2.2 Bright solitary matter-waves from a BEC

2.2.1 Bose-Einstein condensation

In a system of non-interacting, indistinguishable bosonic particles, the thermal de Broglie wavelength of each particle is conventionally defined as

$$\lambda_{\mathrm{dB}} = \sqrt{\frac{2\pi\hbar^2}{mk_{\mathrm{B}}T}}, \tag{2.1}$$

where m is the mass of the particle, T is the temperature of the ideal Bose gas, $\hbar$ is the reduced Planck constant, and k_{B} is the Boltzmann constant. Following Bose-Einstein statistics, such a system undergoes a quantum phase transition when it is cooled to a low temperature where the de Broglie wavelengths of the individual bosons start to overlap [6, 81]. This phenomenon of condensation occurs at a critical temperature T_c when the phase space density (PSD)
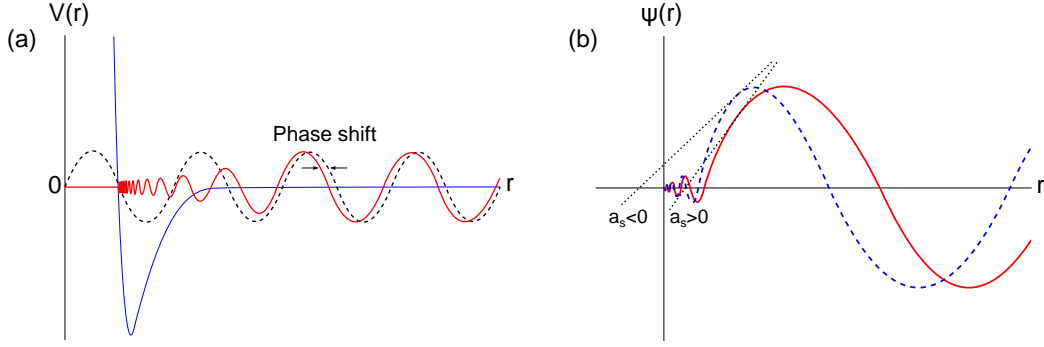
Figure 2.1: Low energy scattering between atoms and the origin of the *s*-wave scattering length a_s. (a) Effect of low energy scattering from a molecular potential $V(r)$ (blue). The potential is a combination of the electrostatic repulsion and van der Waals attraction. At long range, regardless of the potential, the overall effect from scattering is a phase shift in the wavefunction (red solid) compared to the wave scattered from a point-like particle at $r = 0$ (black dashed). Figure adapted from ref. [86]. (b) At low energy the phase shift is proportional to the scattering length a_s. This quantity can be geometrically interpreted as the intersection of the tangent (black dotted lines) to the unperturbed wavefunction at the vanishing point of the interatomic potential with the r-axis [87]. Here, the red, solid (blue, dashed) curve illustrates the positive (negative) scattering length.

$$\text{PSD} = n\lambda_{\text{dB}}^3 = \zeta\left(\frac{3}{2}\right) = 2.612, \tag{2.2}$$

where n is the particle density [6, 81]. $\zeta(\alpha) = \sum_{j=1}^{\infty} j^{-\alpha}$ is known as the Riemann Zeta function. The critical temperature for an N-atom bosonic system is

$$T_c = \frac{E_\alpha}{k_{\text{B}}}\left(\frac{N}{\zeta(\alpha)}\right)^{1/\alpha}, \tag{2.3}$$

where the parameter α depends on the trap geometry [82]. For a harmonic trap with trap frequencies $(\omega_x, \omega_y, \omega_z)$, $\alpha = 3$ and $E_\alpha = \hbar(\omega_x\omega_y\omega_z)^{1/3}$. For a uniform trap and a toroidal (ring) trap, $\alpha = 3/2$ and $\alpha = 5/2$ respectively. Their respective expressions for E_α can be found in literatures such as [83] (uniform) and [84, 85] (ring).

2.2.2 The Gross-Pitaevskii mean-field model

In contrast to the ideal Bose gas, alkali atoms confined in an optical or magnetic trap do in fact interact with each other [6]. The Gross-Pitaevskii

mean-field model is a well established description of the dilute[1], weakly-interacting Bose gas system. This system contains N interacting identical bosons with mass m in the condensate which are trapped in an external global potential $U(\mathbf{r})$. This mean-field model only holds if the BEC ground state is macroscopically populated, i.e. $N \gg 1$ and $T \ll T_c$. The N-body Hamiltonian of the mean-field model is given by the second quantisation form [88]

$$
\begin{aligned}
\hat{H} = \int \mathrm{d}\mathbf{r}\, \hat{\Psi}^\dagger(\mathbf{r}, t) \left(-\frac{\hbar^2}{2m}\nabla^2 + U(\mathbf{r}) \right) \hat{\Psi}(\mathbf{r}, t) \\
+ \frac{1}{2} \int \mathrm{d}\mathbf{r}\,\mathrm{d}\mathbf{r}'\, \hat{\Psi}^\dagger(\mathbf{r}, t)\hat{\Psi}^\dagger(\mathbf{r}', t)V(\mathbf{r} - \mathbf{r}')\hat{\Psi}(\mathbf{r}', t)\hat{\Psi}(\mathbf{r}, t)
\end{aligned}
\tag{2.4}
$$

where $\hat{\Psi}(\mathbf{r}, t)$ and $\hat{\Psi}^\dagger(\mathbf{r}, t)$ represent the annihilation and creation field operators of bosons respectively. The interactions must be dominated by two-body collisions at low energy where it is sufficient to consider only the s-wave partial waves, characterised by the s-wave scattering length a_s. We refer to Fig. 2.1 for a pictorial explanation of the origin of a_s. In this limit it is shown that, regardless of the interatomic potential, the overall effect on the scattered wave at long range is a phase shift [86] (see Fig. 2.1(a)). Thus one can simplify such interactions by replacing the molecular potential (shown in blue in Fig. 2.1(a)) by an effective potential $V(\mathbf{r} - \mathbf{r}') = g\delta(\mathbf{r} - \mathbf{r}')$ where the nonlinearity g is given by $g = 4\pi\hbar^2 a_s/m$ [82, 88, 89]. Employing this effective potential, and normalising the wavefunction to atom number $N = \int \mathrm{d}\mathbf{r}\,|\Psi(\mathbf{r}, t)|^2 = \int \mathrm{d}\mathbf{r}\, n(\mathbf{r}, t)$ (where $n(\mathbf{r}, t)$ is the particle density), the Heisenberg representation of Eq. 2.4 takes the form

$$
i\hbar\frac{\partial}{\partial t}\Psi(\mathbf{r}, t) = \left[-\frac{\hbar^2}{2m}\nabla^2 + U(\mathbf{r}) + gN|\Psi(\mathbf{r}, t)|^2 \right] \Psi(\mathbf{r}, t),
\tag{2.5}
$$

which is the mean-field Gross-Pitaevskii equation (GPE). The nonlinearity coefficient can take either positive or negative values depending on the sign of a_s, where $a_s > 0$ ($a_s < 0$) corresponds to repulsive (attractive) interatomic interactions. In some systems, the strength of this interaction can be controlled via a Feshbach resonance. This will be detailed in Chapter 4. The

---

[1]This commonly refers to Bose gases with density below $10^{15}\,\mathrm{cm}^{-3}$ [82].

external potential $U(\mathbf{r})$ in the GPE can take many forms. Experimentally, BECs have been confined in both magnetic potentials [90, 91] and pure optical dipole potentials [92–95]. The generation of these trapping potentials in our experiment will be presented in Chapter 3. These commonly used 'traditional' traps are well approximated by a 3D harmonic trap

$$U(\mathbf{r}) = \frac{1}{2}m(\omega_x^2 x^2 + \omega_y^2 y^2 + \omega_z^2 z^2), \tag{2.6}$$

where $\omega_x, \omega_y, \omega_z$ are the trap frequencies in their respective directions.

Non-interacting solution

The ground state energy of the condensate is characterised by the chemical potential, μ, which is the energy required to remove a particle from the system. By substituting $\Psi(\mathbf{r}, t) = \phi(\mathbf{r}) \exp(-i\mu t/\hbar)$ into Eq. 2.5, one obtains the time-independent GPE in the form of

$$\mu\phi(\mathbf{r}) = \left[-\frac{\hbar^2}{2m}\nabla^2 + U(\mathbf{r}) + gN|\phi(\mathbf{r})|^2 \right] \phi(\mathbf{r}). \tag{2.7}$$

In the non-interacting regime, where $g = 0$, Eq. 2.7 is reduced to the Schrödinger equation for a single particle. Assuming the non-interacting condensate is trapped in a 3D harmonic confinement described by Eq. 2.6, the ground state solution is given by

$$\phi(\mathbf{r}) = \left(\frac{m\bar{\omega}}{\pi\hbar} \right)^{3/4} \exp\left[-\frac{m}{2\hbar} \left(\omega_x^2 x^2 + \omega_y^2 y^2 + \omega_z^2 z^2 \right) \right], \tag{2.8}$$

where $\bar{\omega} = (\omega_x\omega_y\omega_z)^{1/3}$.

Thomas-Fermi solution

In the limit of $Na_s/\bar{l} \gg 1$, where $\bar{l} = \sqrt{\hbar/m\bar{\omega}}$ is the mean harmonic oscillator length, the strong repulsive interactions push the atoms further out in the trap. This leads to a condensate density profile broader than that of the non-interacting ground state solution. The kinetic energy term in Eq. 2.7 becomes small when compared to the dominant interaction and potential terms, and hence can be neglected. This is known as the Thomas-Fermi approximation, where the density profile of the trapped condensate is given

by

$$n(\mathbf{r}) = \begin{cases} (\mu - U(\mathbf{r}))/gN & \text{for } \mu > U(\mathbf{r}), \\ 0 & \text{elsewhere.} \end{cases} \tag{2.9}$$

It is clear from Eq. 2.9 that the density of the condensate drops to zero at $U(\mathbf{r}) = \mu$. This defines the Thomas-Fermi radius. For a spherically-symmetric harmonic trap where $\bar{\omega} = \omega_{x,y,z}$, the Thomas-Fermi radius of the condensate is

$$R_{\text{TF}} = \sqrt{\frac{2\mu}{m\bar{\omega}^2}}, \tag{2.10}$$

where the chemical potential in the Thomas-Fermi limit takes the form

$$\mu = \frac{\hbar\bar{\omega}}{2} \left(\frac{15Na_s}{\bar{l}} \right)^{2/5}. \tag{2.11}$$

2.2.3   Reduction to 1D GPE

By constructing a strongly anisotropic trap, one can engineer the effective dimensionality of the system. Consider a cylindrical trap by setting $\omega_r = \omega_y = \omega_z$ with $\omega_r \gg \omega_x$. If the transverse harmonic oscillator length $a_r = \sqrt{\hbar/m\omega_r} < \xi$, where

$$\xi = \frac{1}{\sqrt{8\pi n a_s}} \tag{2.12}$$

is the healing length of the BEC[2], the elongated BEC can be considered to be effectively 1D [25]. In this limit, one can factorise the classical field function $\Psi(\mathbf{r}, t)$ into

$$\Psi(\mathbf{r}, t) = \psi(x, t)\chi(y)\chi(z) \equiv \psi(x, t)\sqrt{\frac{m\omega_r}{\pi\hbar}} \exp\left(-\frac{m\omega_r(y^2 + z^2)}{2\hbar} \right). \tag{2.13}$$

If we substitute Eq. 2.13 into the 3D GPE (Eq. 2.5) and integrate over the transverse degrees of freedom, we arrive at

---

[2]The distance over which the BEC density grows from 0 to n.

$$i\hbar\frac{\partial}{\partial t}\psi(x,t) = \left[-\frac{\hbar^2}{2m}\frac{\partial^2}{\partial x^2} + \frac{m\omega_x^2 x^2}{2} + g_{1D}N|\psi(x,t)|^2\right]\psi(x,t), \qquad (2.14)$$

where $g_{1D} = 2\hbar\omega_r a_s$ [96, 97] (a factor of a constant energy shift $\hbar\omega_r$ is omitted as it can be absorbed into the 1D chemical potential [98]). Eq. 2.14 is known as the 1D GPE.

2.2.4   Soliton solution

In the homogeneous regime ($\omega_x \to 0$), Eq. 2.14 becomes a standard integrable nonlinear Schrödinger equation (NLSE) which takes a common form of

$$i\frac{\partial u}{\partial t} + \frac{1}{2}\frac{\partial^2 u}{\partial x^2} + u|u|^2 = 0. \qquad (2.15)$$

Zakharov and Shabat showed that the NLSE can in fact be exactly solved by a method known as inverse scattering transform [99] which leads to soliton solutions. For a repulsive nonlinearity ($g > 0$), the solution describes a dark soliton, which is characterised by a notch in the condensate density with a sharp phase gradient of the wavefunction at the position of the local density minimum [100]. Dark solitons in a BEC have been realised via various methods, such as the manipulation of the BEC phase through phase imprinting [101, 102], the manipulation of the BEC density where the local reductions in density evolve into dark solitons [103, 104], and a combination of the previous two methods [105]. On the other hand, for an attractive nonlinearity ($g < 0$), the solution in fact describes a bright soliton. In the case of the 1D GPE (Eq. 2.14), *in the absence of axial confinement*, the exact solution is given by

$$\psi(x,t) = \frac{a_r}{\sqrt{2|a_s|l_s}}\text{sech}\left(\frac{x - vt}{l_s}\right)\exp\left[i\frac{mv}{\hbar}x + i\left(\frac{\hbar l_s}{2m} - \frac{mv^2}{2\hbar}\right)t\right], \quad (2.16)$$

where

$$l_s = \frac{a_r^2}{|a_s|N} \qquad (2.17)$$

is the spatial extent of the soliton and v is the soliton velocity [25]. It is clear that solutions of this form possess the unique properties of solitons. For instance, they do not decay over time due to the absence of real exponents in

Eq. 2.16. In collision with another soliton, while they are subject to a shift in position and phase, the soliton profiles are maintained asymptotically [106].

2.3   Stability and collapse

In reality, BECs created in the laboratory are intrinsically 3D objects in a 3D trap. The introduction of the additional dimensions and the non-vanishing inhomogeneous trap potential ($\omega_x > 0$) removes the integrability of the NLSE. The new ground state thus deviates from the true soliton solution described in Eq. 2.16. However, such a system still supports solutions that exhibit the non-dispersive soliton-like nature, which are formally known as bright solitary waves, as discussed in Section 1.1.2. The stability of the 3D attractive condensate can be understood by variational analysis [107, 108]. We begin by expressing the energy functional of the time-independent *dimensionless* 1D GPE[3] as

$$\tilde{E}_{1D}[\psi] = \int \mathrm{d}\tilde{x} \left[\frac{1}{2} \left| \frac{\partial}{\partial \tilde{x}} \psi(\tilde{x}) \right|^2 + \frac{\alpha^2 \tilde{x}^2}{2} |\psi(\tilde{x})|^2 - \frac{1}{2} |\psi(\tilde{x})|^4 \right], \qquad (2.18)$$

where $\alpha = \hbar \omega_x / 4m\omega_r^2 |a_s|^2 N^2$. As the soliton units will be used throughout the rest of this section and the earlier parts of Section 2.4, the tilde, which denotes the dimensionless variables, will be omitted for brevity. In the homogeneous limit ($\omega_x \to 0$), one retrieves the integrable NLSE with an exact soliton solution of a sech profile. In contrast, in the limit of infinite axial confinement ($\omega_x \to \infty$) the solution $\psi(x)$ tends towards a Gaussian function. One can readily visualise that the ground state of the true soliton solution transforms from a sech profile to a Gaussian profile by reducing the anisotropicity of the external potential $U(\mathbf{r})$ [97]. As such, it is appropriate to choose a Gaussian *ansatz* as the wavefunction in a 3D cylindrical trap geometry, given by

$$\Psi(\mathbf{r}) = \left(\frac{1}{\pi^{3/2} a_x a_r^2 b_x b_r^2} \right)^{\frac{1}{2}} \exp \left[-\frac{1}{2} \left(\frac{x^2}{a_x^2 b_x^2} + \frac{r^2}{a_r^2 b_r^2} \right) \right], \qquad (2.19)$$

---

[3]The soliton rescaling is commonly used due to the mathematical convenience [97]. Denoting dimensionless variables with tildes, the conversions from physical units to soliton units are as follows: length $x = \tilde{x}\hbar^2 / mg_{1D}N$, time $t = \tilde{t}\hbar^3 / mg_{1D}^2 N^2$, energy $E = \tilde{E}mg_{1D}^2 N^2 / \hbar^2$ [109].
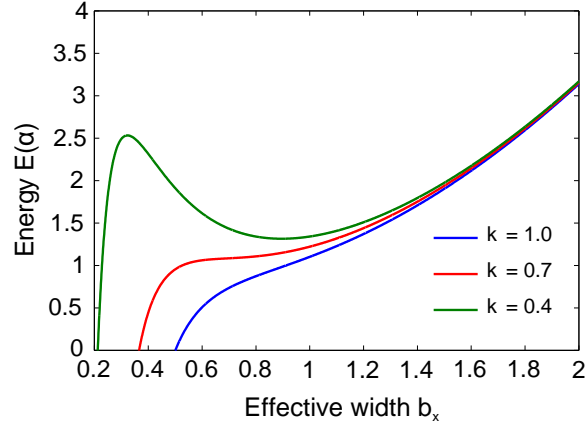
Figure 2.2: The metastable state and the collapse of an attractive 3D BEC. The plot shows the energy per particle in an isotropic harmonic trap (in units of α as defined in the text) as a function of the variational Gaussian width b_x for different values of $k = N|a_s|/a_r$.

where $a_x = \sqrt{\hbar/m\omega_x}$ is the axial harmonic oscillator length, b_r and b_x are the dimensionless radial and axial lengths that characterises the Gaussian *ansatz*. Substituting Eq. 2.19 into the 3D equivalent of Eq. 2.18,

$$
E_{3D}[\Psi] = \int d\mathbf{r} \left[\frac{1}{2}\nabla\Psi(\mathbf{r}) \cdot \nabla\Psi^*(\mathbf{r}) \right.
$$
$$
\left. + \frac{\alpha^2}{2}\left(x^2 + \frac{\omega_r^2 r^2}{\omega_x^2}\right)|\Psi(\mathbf{r})|^2 - 4\pi\left(\frac{|a|N}{a_r}\right)^2|\Psi(\mathbf{r})|^4 \right], \tag{2.20}
$$

one obtains the energy functional of the BEC trapped in a 3D cylindrical potential

$$
E_{3D}(b_x, b_r) = \frac{\alpha}{4}\left[\left(b_x^2 + \frac{2\omega_r}{\omega_x}b_r^2\right)\right.
$$
$$
\left. + \left(\frac{1}{b_x^2} + \frac{2\omega_r}{\omega_x}\frac{1}{b_x^2}\right) - \sqrt{\frac{8\omega_r}{\pi\omega_x}}\frac{N|a_x|}{a_r}\frac{1}{b_x b_r^2}\right]. \tag{2.21}
$$

The three terms in Eq. 2.21 represent the kinetic energy, trap potential, and the interaction energy. This variational analysis shows that the interaction is dependent on the trap geometry. Here, we define the dimensionless interaction parameter

$$
k = \frac{N|a_s|}{a_r}. \tag{2.22}
$$

To demonstrate how the strength of this interaction term relates to the condensate stability, let us consider a spherically symmetric trap, where we set $\omega_x = \omega_r$ and $b_x = b_r$. The energy functional of a condensate in this isotropic geometry, in units of α, is plotted for different values of k as shown in Fig. 2.2. A local energy minimum, hence the condensate metastability, only exists for some values of k. Beyond this critical value k_c, which is commonly referred to as the collapse parameter, the condensate is unstable and undergoes collapse. For an isotropic condensate, $k_c = 0.671$ [88, 96, 110]. Consequently, one can define the critical number of the system as

$$N_c = \frac{k_c a_r}{|a_s|}. \tag{2.23}$$

An attractive condensate in a 3D trap with $N > N_c$ is regarded as unstable and collapse follows. This phenomenon has been observed experimentally in ^{7}Li [38] and ^{85}Rb [39, 40, 68]. Interestingly, formation of multiple solitons has been observed following the collapse of an attractive 3D BEC [42, 43]. In summary, it is vital to balance N, a_r, and a_s in order to realise bright solitary waves experimentally [41, 42, 44, 47].

2.4 Soliton scattering from narrow potentials

As mesoscopic, self-focussing structures, bright solitary waves present a rich testing ground for the realisation of quantum mechanical effects on a macroscopic scale. One of the major long-term aims of this experiment is to probe atom-surface interactions with the dielectric surface of a prism. At short range, the interaction is dominated by the attractive van der Waals and Casimir-Polder potentials [111, 112]. Scattering from such a potential, significant quantum reflection is predicted if the kinetic energy of the soliton is sufficiently low. More specifically, it is when the local wave vector k changes by more than k over a distance of $1/k$ [48, 113]. That is, one requires a slow soliton and a rapidly changing potential. In the case of a repulsive potential, quantum tunnelling is predicted when the system approaches similar conditions [114]. Indeed, theoretical studies have shown that there exists a wide range of behaviours for solitons interacting with narrow potential barriers/ wells depending on the energy regime [51, 72, 73, 75–77]. In essence, the

kinetic energy E_k, dependent on the soliton's velocity, is transferred into the interaction energy through the soliton's collision with the potential [109]. Soliton splitting, including 50:50 splitting, can only occur if

$$E_k > E_s = [E_G(N - n) + E_G(n)] - E_G(N), \qquad (2.24)$$

where the splitting energy E_s is the difference between the ground state energies E_G of the two resulting solitons (one with n and one with $N - n$ atoms) and the original, incoming soliton with N atoms. This is defined as the *high energy regime.* In contrast, some splitting events become energetically forbidden when $E_k \lesssim E_s$, and hence entering the *low energy regime.* The boundaries of these regimes will be discussed in this section. Although we will not discuss it further in this thesis, one should be aware that collisions with narrow potentials also yield a time-decaying radiation, in addition to the outgoing solitons [72]. Other interesting outcomes, such as the formation of the soliton molecules [115], have also been reported. In the following discussion, we closely follow the works by Helm [51, 52, 77, 109] and Gertjerenken [76].

2.4.1 High energy regime

Let us consider first the splitting of the bright solitary wave at a narrow repulsive barrier. By comparing the splitting on Gaussian barriers to splitting on delta-function barriers, it can be seen that the reflection or transmission coefficients are strongly dependent on the width of the barrier [65, 77, 109]. These studies have been carried out in a 1D GPE framework with a homogeneous configuration. The physical system can be expressed by adding an additional barrier potential to the dimensionless 1D GPE in Eq. 2.18

$$E[\psi] = \int dx \left[\frac{1}{2} \left| \frac{\partial}{\partial x} \psi(x) \right|^2 + \left(V_b(x) + \frac{\alpha^2 x^2}{2} \right) |\psi(x)|^2 - \frac{1}{2} |\psi(x)|^4 \right], \quad (2.25)$$

where $V_b(x)$ is the dimensionless expression of the additional narrow barrier. Here, we set $\omega_x = 0$ to remove the harmonic confinement. Two types of barrier potentials are explored, namely

$$V_b(x) = \begin{cases} q\delta(x) & \text{for delta-function potential,} \\ \frac{2q}{w_x\sqrt{2\pi}}\exp\left(-\frac{2x^2}{w_x^2}\right) & \text{for Gaussian barrier with } 1/e^2 \text{ radius } w_x, \end{cases}$$
$$(2.26)$$

where $q = \int_{-\infty}^{\infty} V_b(x)\,\mathrm{d}x$ defines the strength of the barrier. A key result from ref. [72] shows that after the collision with the barrier at a velocity v,[4] the amplitudes of the transmitted (A_T) and reflected (A_R) solitons are given by

$$A_\mathrm{T} = \max(0, 2|t(v)| - 1) \quad \text{and} \quad A_\mathrm{R} = \max(0, 2|r(v)| - 1), \qquad (2.27)$$

where $t(v)$ and $r(v)$ are the magnitudes of the transmitted and reflected components for plane waves in linear quantum mechanics. The transmission and reflection coefficients from the delta function barrier are

$$T(v) = |t(v)|^2 = \frac{v^2}{v^2 + q^2} \quad \text{and} \quad R(v) = |r(v)|^2 = \frac{q^2}{v^2 + q^2}. \qquad (2.28)$$

In events where $A_\mathrm{T} = 0$ or $A_\mathrm{R} = 0$, the outgoing wave does not contain a soliton, but instead only radiation will be observed [77].

This result is compared with the case of a Gaussian barrier. It is shown that the discrepancy of the transmission coefficients between the Gaussian barrier and the delta function increases with the ratio q/v [77]. For a fixed, finite barrier width, the higher the potential height is, compared to the kinetic energy E_k, the lower the transmission as the wave function decays. In contrast, for $E_k > V_b(0)$ where the soliton has sufficient energy to 'go over the barrier', one enters the classical transmission regime which sees a greatly enhanced transmission. As such, to ensure soliton splitting at a narrow barrier in the high energy regime without classical transmission, the soliton velocity v *in soliton units* must satisfy

$$\frac{v^2}{2} \ll \frac{2q}{w_x\sqrt{2\pi}}, \qquad (2.29)$$

or equivalently in *dimensional, S.I. units*, it is simply

---

[4]The soliton unit for velocity is $|g_{1\mathrm{D}}|N/\hbar = 2\omega_r|a_s|N$.

$$v \ll \sqrt{\frac{2V_0}{m}}, \tag{2.30}$$

where V_0 is the height of the barrier[5]. For the rest of this thesis, we will resume the use of the physical, dimensional units. Eq. 2.30 is plotted in Fig. 2.3(a), which indicates the boundary between the classical transmission and the high energy regimes. Although it is not shown in Fig. 2.3(a), as mentioned previously, the system enters the low energy regime when $E_k \lesssim E_s$. The transition into such a regime will be discussed in Section 2.4.2.

In scattering the soliton from a narrow potential *well*, studies on the Rosen-Morse potential [74] and the rectangular well [75] suggest that narrow potentials, with width smaller or comparable to the spatial extent of the soliton, are needed for observable quantum reflection. For significant quantum reflection from the potential, one again requires low velocity (see Section 5.2). In particular, adding to reflection and transmission as an outcome of the scattering event, nonlinear trapping at the potential well occurs for slow solitons. This is due to the resonant interaction between the soliton and the bound states in the potential well, as well as the loss of centre of mass kinetic energy of the soliton via radiation loss [75]. Such soliton dynamics can be potentially utilised to experimentally probe the bound states of the localised potential well.

2.4.2   Low energy regime

For a slow soliton incident on a narrow potential where $E_k \lesssim E_s$, the kinetic energy of the soliton becomes insufficient to split the soliton into two spatially well separated parts. This describes the low energy regime where splitting events become inaccessible and thereby a mesoscopic quantum superposition is created. Such transition from the high to low energy regime is somewhat analogous to a quantum mechanical transition from a product state wavefunction to an entangled system where the soliton can only be observed to be fully transmitted or reflected from the potential [51, 76].

---

[5]While it is not explicitly written in the expression, the width w_x of the barrier should be at least comparable with, or less than, the spatial extent of the soliton [77].
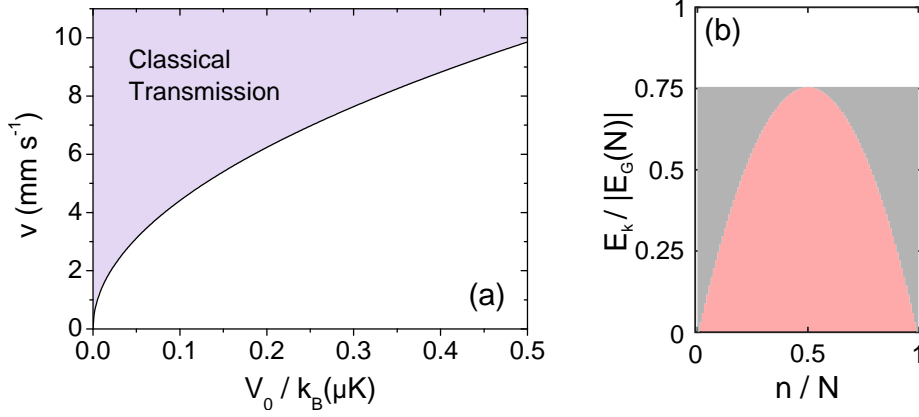
Figure 2.3: (a) The purple region indicates the regime where only classical transmission can occur, as defined in Eq. 2.30. The system undergoes transition into the high energy regime when the velocity drops below the boundary. (b) Energetically allowed and disallowed splitting in the low energy regime. Parameters are as defined in the text. For $E_k/|E_G(N)| \geq 0.75$, all states are energetically allowed (white). For $E_k/|E_G(N)| < 0.75$, splitting events, starting from 50:50 splitting, become energetically disallowed (red). Grey shows the splittings that remain energetically allowed. Figure taken from ref. [76].

The following analysis of soliton splitting is based on a classical comparison between the soliton ground state energies before and after a splitting event, *regardless* of the type and strength of the perturbation potential. Consider the system without axial trapping (by setting $\alpha = 0$ in the 1D homogeneous energy functional Eq. 2.18). As previously defined, let N and n be the total atom number in the condensate and the number of atoms in one of the resulting solitons respectively. The *dimensional* ground state energy of an N-particle soliton is [76]

$$E_G(N) = -\frac{1}{24}\frac{mg_{1D}^2}{\hbar^2}N(N^2 - 1).$$
(2.31)

For splitting to occur, one must satisfy the condition stated in Eq. 2.24. Hence, by substituting Eq. 2.31 into Eq. 2.24, and subsequently dividing it by $|E_G(N)|$, we arrive at[6]

$$\frac{E_k}{|E_G(N)|} \geq 3\frac{n}{N}\left(1 - \frac{n}{N}\right).$$
(2.32)

With the centre of mass kinetic energy defined as $E_k = N\hbar^2k^2/2m =$

---

[6]Here, we take the mean field limit, where $N \to \infty$ and $g_{1D} \to 0$ with $Ng_{1D} =$ constant [76].

$Nmv^2/2$, we find that the required velocity for which all splitting events are energetically allowed is

$$v \geq \sqrt{\frac{6}{m} \frac{n}{N^2} \left(1 - \frac{n}{N}\right) |E_G(N)|}. \qquad (2.33)$$

$\frac{n}{N}\left(1 - \frac{n}{N}\right)$ within Eq. 2.32 maximises when $n/N = 0.5$, or 50:50 splitting. This sets the boundary between the high and low energy regimes. In order for a continuum of splitting events including 50:50 splitting to occur, one must satisfy the condition $E_k/|E_G(N)| \geq 0.75$, or $v \geq \sqrt{3|E_G(N)|/2mN}$, which is indicated by the white region of Fig. 2.3(b). Using the experimental parameters presented in Chapter 5, where $N = 6000, a_s = -7\,a_0, \omega_r = 2\pi \times 18.2\,\text{Hz}$, this is equivalent to $v \geq 0.13\,\text{mm s}^{-1}$. Below this velocity, some splitting events (starting with 50:50 splitting) are energetically disallowed (red) and thereby describe a quantum superposition. This region can be referred to as the Schrödinger kitten state as there exists a spread of possible states which can be expressed as [76]

$$|\psi\rangle_n = \frac{1}{\sqrt{2}} \left(|N - n, n\rangle + e^{i\alpha}|n, N - n\rangle\right), \quad n \lesssim \frac{N}{4} \qquad (2.34)$$

in Fock-state notation. At small $E_k/|E_G(N)|$ (the exact boundary depends on N), one retrieves the Schrödinger cat state, expressed as

$$|\psi\rangle_0 = \frac{1}{\sqrt{2}} \left(|N, 0\rangle + e^{i\alpha}|0, N\rangle\right), \qquad (2.35)$$

where all the particles are observed to be either transmitted or reflected on an individual measurement. These macroscopic quantum superpositions of solitary waves offer interesting physics, such as the generation of mesoscopically entangled Bell states from distinguishable solitons [116], and applications for atom interferometry experiments [50, 80].

2.4.3   Soliton recombination

Solitons in 1D

In a true 1D environment, the soliton-soliton interaction is completely elastic. After collision, while there are asymptotic shifts to the position and phase,

the amplitude of the solitons remains unaffected [106]. Thus a potential
barrier is required to facilitate the soliton recombination. This is achieved
by arranging the barrier at the position where the two solitons collide. The
outcome of such collision depends strongly on the relative phase difference
$\Delta\phi$ between the two incoming solitary waves. For two identical solitary waves
in the high energy regime colliding at a delta-function barrier (one travelling
at a velocity $+v$ and its counterpart at $-v$), the absence of axial trapping
yields an exact analytical expression of the transmission coefficient from the
barrier. For well separated outgoing solitary waves,

$$T_{\pm} = \frac{1}{2}[1 \pm \sin(\Delta\phi)], \qquad (2.36)$$

where T_+ and T_- represent the fraction of the total atom number that end
up in their respective sides of the barrier [51]. Numerical calculation in the
same literature shows, however, that such relation is skewed as a result of
the interactions between the solitary waves as they approach the potential
barrier.

Solitons in higher dimensions

A non-vanishing axial trap frequency introduces additional dimensions to
the system, which can lead to inelastic soliton collisions [46, 117, 118]. The
outcome of these collisions is strongly dependent on the phase difference $\Delta\phi$
between the two solitons. At $\Delta\phi = 0$, as the two solitons fully overlap each
other, it is possible that the number of atoms in the condensate exceeds
the critical number N_c [46]. Within the framework of GPE, such a system
will undergo collapse. On the other hand, at $\Delta\phi = \pi$, the two solitons
effectively 'repel' each other which suppresses the collapse [46]. This stability
was in fact observed over a range of phase difference $\pi/2 \leq \Delta\phi \leq 3\pi/2$
by Carr *et al.* [117]. For intermediate phases $0 < \Delta\phi < \pi$, population
transfer between the two solitons at the collision can occur [46]. The phase
dependence of the bright soliton collision has been recently experimentally
demonstrated [47]. In addition, the relative velocity of the solitons plays a
key role in the outcome, where one can restore the elasticity if the velocity
is sufficiently high [46].
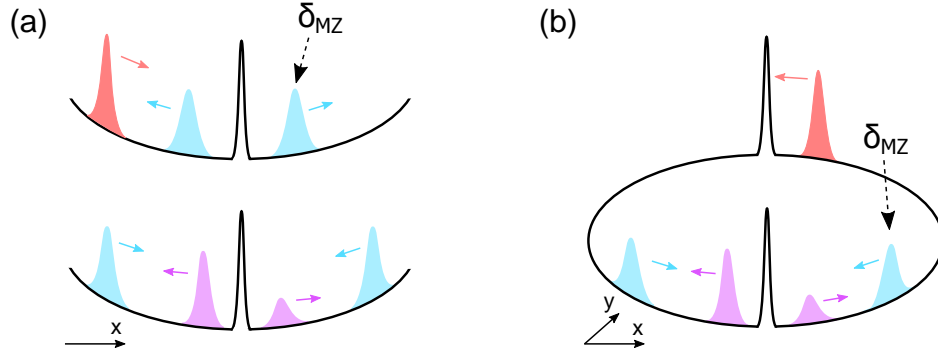
Figure 2.4: Schematic of the Mach-Zehnder interferometer with bright solitary waves in (a) a harmonic potential, and (b) a toroidal/ring potential. A single solitary wave (red) is split into two solitons (blue) from a narrow potential barrier. In propagation to their point of collision at a barrier the system accumulates a phase δ_{MZ}. Experimentally, δ_{MZ} can be gained by imprinting a phase on one of the solitons. The solitons then recombine at the barrier, with the outcome (purple) used do deduce δ_{MZ}. Adapted from ref. [109].

2.5   Interferometry with bright solitary waves

Bright solitary waves offer an intriguing resource for performing interferometry [42, 48–52, 64, 65, 77, 80, 119]. Indeed, the ability to coherently split and recombine bright solitary waves at a narrow potential is analogous to splitting a light beam at a beam splitter in an optical interferometer [72, 73]. In this section, we will discuss the construction of two interferometers, namely the Mach-Zehnder interferometer and the Sagnac interferometer, using the bright solitary waves.

2.5.1   Mach-Zehnder interferometry

In optics, a Mach-Zehnder interferometer is a device that can determine the relative phase between two incoming coherent light beams [120]. Constructing this system with bright solitary waves, one requires the following three steps:

1. Coherent splitting of the solitary wave at a narrow potential barrier, which requires the single solitary wave to be in the high energy regime.

2. Evolution of the two matter-waves within the system, while the relative phase difference increases by the amount δ_{MZ} (in practice, one can imprint a phase shift to one of the solitons to actively control δ_{MZ}).

3. Recombination at a narrow barrier located at the point of final soliton collision.

The outcome is dependent on the total phase difference $\Delta\phi$ which is determined by examining the population transfer of atoms after step 3. In the case of a delta-function barrier, upon splitting the system picks up a $\pi/2$ relative phase difference, itself a good estimate for splitting at a narrow Gaussian barrier [77]. An in-depth discussion on the phase accumulation at a splitting event from a barrier with a finite width can be found in ref. [78]. The total phase shift in Eq. 2.36 is hence $\Delta\phi = \pi/2 + \delta_{\mathrm{MZ}} + \epsilon$, where ϵ is the parameter that quantifies the velocity dependent skewness [51].

The interferometer has been considered in two different trap geometries [51], namely a weakly harmonically trapped system and a toroidal/ring trap geometry shown in Fig. 2.4(a) and (b) respectively. While the former is experimentally straightforward to create, the presence of axial trapping removes the integrability of the system. Given a high anisotropy, as discussed in Section 2.2, solitary waves in such a geometry still possesses features of a true soliton and thus are applicable to interferometry. A ring trap, on the other hand, gives a periodic geometry where the axial trapping is absent. In such a geometry, the matter-waves are exact soliton solutions in the mathematical context, where the recombination process at the narrow barrier is well described analytically, as discussed in Section 2.4.3. Generation of a ring trap will be discussed in Chapter 7.

Both configurations of a Mach-Zehnder interferometer show similar features, where behaviours are closely linked to the energy regime of the solitons. For the high energy regime, the interference follows Eq. 2.36 with $\epsilon \approx 0$. In the transition to the low energy regime ($v \sim 0.13\,\mathrm{mm\,s^{-1}}$ with the parameters in Chapter 5), ϵ increases and the interference curve is skewed. In the low energy regime, the interferometer becomes impracticable, which is caused by the disallowed splitting events where dynamics are complicated by the sensitivity to quantum fluctuations in the position and momentum of the solitons [51].
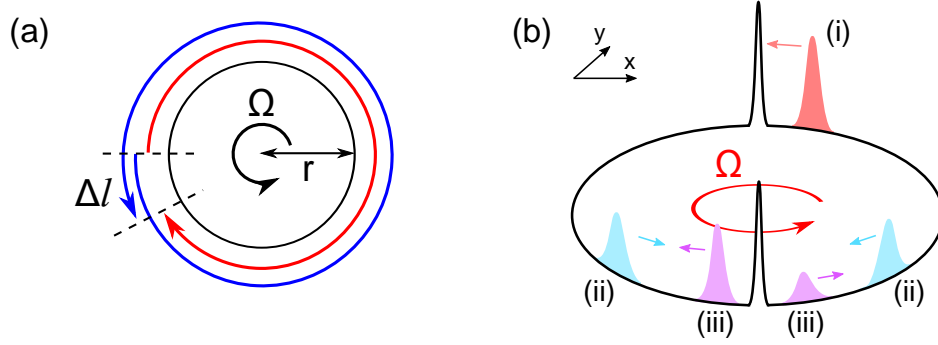
Figure 2.5: Construction of a Sagnac interferometer with bright solitary waves. (a) The Sagnac effect. Path lengths of the two counterpropagating waves in a rotating frame of radius r at angular frequency Ω have a total difference of $2\Delta l$. (b) Sagnac interferometry with bright solitary waves. The solitons propagate along the ring potential in a rotating frame. The interferometer consists of three steps: (i) The initial soliton (red) splits at the first barrier. (ii) The two resulting solitons (blue) propagate along the ring where the Sagnac phase accumulates. (iii) The two solitons recombine at the second barrier at half the distance of the circumference from the first barrier, where the outcome (purple) depends on the phase difference.

2.5.2   Sagnac interferometry

The ring geometry is intrinsically interesting because there are interesting dynamical phase effects associated with the multiply connected regions. One of which is the Sagnac interferometer, first experimentally demonstrated with light in a rotational frame by Sagnac [121, 122]. This concept is illustrated in Fig. 2.5(a). Over time Δt, a wave moving at a constant velocity v propagates over a distance $\Delta L = v\Delta t$ and picks up a phase shift $\Delta\phi = 2\pi\Delta L/\lambda$. Sagnac interferometry considers two waves counterpropagating at velocity v in a rest frame in a ring geometry with radius r. If the ring rotates at an angular velocity Ω,[7] the wave travelling in the same direction as the rotation covers a longer distance than its counterpart at the point of interference. This leads to a phase difference $\delta_{\mathrm{S}} = 4\pi\Delta l/\lambda$ between the two waves just before the collision. In a generalised Sagnac picture of any closed path, the phase difference is given by

$$\delta_{\mathrm{S}} = \frac{4\pi}{v\lambda}\boldsymbol{\Omega}\cdot\mathbf{A}, \tag{2.37}$$

where $\mathbf{A}$ is the area enclosed by the paths of the two waves [61, 123]. The Sagnac interferometer has been extended from light to matter-waves, where

---

[7]We only consider low rotation velocity, where $v \gg r\Omega$.

rotational phase shifts have been observed in neutron [124], electron [125], and atom [56] interferometers. A thorough discussion in [52] suggests that the Sagnac interferometer can be realised in the framework of splitting and recombination of solitary waves in a ring geometry. Rather than observing a shift in the Ramsay fringes in the atom interferometer [56], one looks for the population transfer between the solitons after recombining at a narrow barrier. Illustrated in Fig. 2.5(b), the setup is identical to the Mach-Zehnder interferometer in a ring geometry except that the phase difference is manifested by the rotation of the laboratory frame[8] at rate Ω. While a full analysis of the phase evolution can be found in ref. [52], one arrives at the same expression of δ_S by replacing λ in Eq. 2.37 with the de Broglie wavelength $\lambda = 2\pi\hbar/mv$ of an atom with mass m [61]. The Sagnac phase shift is thus

$$\delta_S = \frac{2m}{\hbar}\boldsymbol{\Omega} \cdot \mathbf{A} = \frac{2m}{\hbar}\Omega\pi r^2. \tag{2.38}$$

Analogous to the Mach-Zehnder interferometer, the transmission coefficient after the recombination at the second barrier is

$$T_\pm = \frac{1}{2}\left[1 \pm \sin\left(\delta_S + \frac{\pi}{2} + \epsilon\right)\right] = \frac{1}{2}[1 \pm \cos(\delta_S + \epsilon)]. \tag{2.39}$$

Velocity once again plays an important role in the transmission at the recombination stage, with the spectrum suffering skewness towards the low energy regime. Sharp transmission responses are expected for sufficiently fast solitons with numbers of atoms $N \gtrsim 1000$, where one can confidently deduce the Sagnac phase δ_S [52].

2.5.3   Quantum enhancement in measurement precision

The quantum superposition of the mesoscopic bright solitary waves in the low energy regime can be exploited as quantum enhancement of the measurement precision [126]. Creating superpositions of ultracold atoms counterpropagating around a ring trap, it is shown that such entanglement is capable of

---

[8]Helm *et al.* [52] also considers a single barrier system, which will not be discussed in this context.

carrying out Heisenberg limited precision measurements [127]. That is, the ultimate quantum limit allowed by quantum mechanics with the precision scales as $1/N$, where N being the number of non-interacting particles in the system. This Heisenberg limit, however, can be surpassed in a nonlinear Hamiltonian where all possible k-body interactions are included. Here, the optimal sensitivity for an entangled initial state is scaled as $1/N^k$ [128]. In contrast, it is scaled as $1/N^{k-1/2}$ for an initial product state. Thus for a bright solitary wave manifested from a dilute Bose gas ($k = 2$), one can theoretically construct an interferometer with a precision beyond the quantum limit.

2.6 Summary

We have discussed the theoretical background relating to the creation of bright solitary wave from a BEC. We have focussed on the interaction of solitons with a narrow potential, where we have shown that a broad spectrum of outcomes are expected depending on the energy regimes of the system. Solitons can be split, and subsequently recombined at a narrow potential barrier positioned at the point of soliton collisions, with the outcome depending strongly on the relative phase between the incoming solitons. This sparks the theoretical and experimental interests in realising interferometers using bright solitary waves.

Chapter 3

Experimental overview

In this chapter, we provide a brief overview on the experimental apparatus and various techniques used for obtaining the data presented in this thesis. For more comprehensive details and the in-depth optimisations of the apparatus, we refer to the following previous theses: refs. [67–69]. The x, y-axes are as defined in Fig. 3.1, while z-axis represents the vertical direction.

3.1 Apparatus

In our experiment, atoms are first laser cooled in the magneto-optical trap (MOT) chamber before being delivered to the science cell via magnetic transport [67]. In this section, we outline the key components of the experimental apparatus that are involved in this process, which include the vacuum chamber, the laser systems, and the magnetic transport using magnetic coils mounted on a motorised translation stage.

3.1.1 Vacuum chamber

We refer to Fig. 3.1 for the experimental setup of the vacuum table. The vacuum system is comprised of the MOT chamber and the science cell. These two sections are connected through a differential pumping stage, which enables fast loading of the MOT with relatively high background pressure whilst ensuring an UHV environment for maintaining long lifetimes of atoms in the science cell. The atoms are transported from the MOT to the science cell
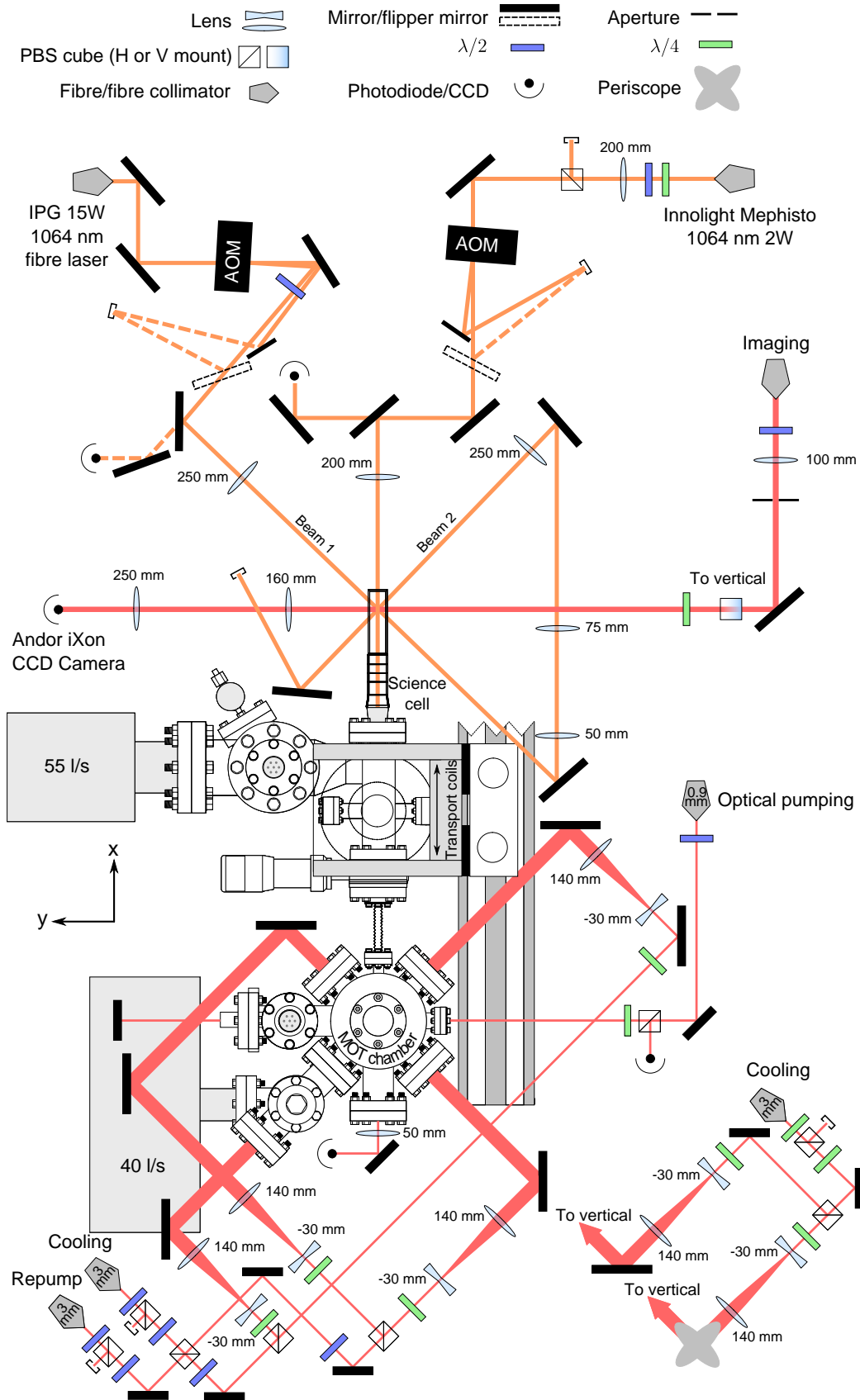
Figure 3.1: The experimental apparatus of the vacuum table. Figure adapted from ref. [69].

using the coils mounted on a motorised translation stage. An obstacle (a right angled prism) is located midway between the two chambers. There are two main reasons for implementing an obstacle along the transport axis: firstly, it blocks the line of sight path for any stray hot atoms heading towards the science cell, and secondly, it prevents the damage of the MOT camera from high power beams that enter from the back of the science cell by diverting the beams out of the system. Inside the glass science cell is a super-polished Dove prism, which is designed for the purpose of probing atom-surface interactions using bright solitary waves [48]. Previously, we have already observed evaporation of a thermal cloud via such interaction by utilising the prism [129]. Around the glass cell is a pair of magnetic coil mounts, which accommodate copper coil pairs that generate the quadrupole field, the bias field, and the shim fields. The dimensions of the magnetic coils are detailed in ref. [67]. It should be highlighted that the vacuum system is located on a separate optical table from the main laser system. This is to isolate possible vibrations caused by the motorised translation stage, which could reduce the quality of the laser frequency stabilisation.

3.1.2 Laser system

The laser table houses two Toptica DL100 (150 mW) extended cavity diode lasers to produce light for cooling, repumping, spectroscopy, optical pumping, and imaging. An additional Toptica BoosTA tapered amplifier is employed to increase the power of the MOT beams, which enables us to use a larger MOT beam size ($1/e^2$ diameter ~ 30 mm) and hence a larger capture volume.

In order to stabilise the DL100 lasers at the desired transition frequencies, two different locking methods are used. For the cooling laser, modulation transfer spectroscopy [130] is used to lock at -230 MHz from the ^{85}Rb D_2 ($5^2S_{1/2} \rightarrow 5^2P_{3/2}$) $F = 3 \rightarrow F' = 4$ transition. The repump laser, on the other hand, is locked -230 MHz from the ^{85}Rb D_2 $F = 2 \rightarrow F' = 3$ via frequency modulation spectroscopy [131]. In Chapters 6 – 8 ^{87}Rb is used, with the lasers locked with the same offsets from the D_2 $F = 2 \rightarrow F' = 3$ (cooling) and $F = 1 \rightarrow F' = 2$ (repump) transitions.

The frequency detuning and the intensity of the beams described above are all controlled via the acousto-optic modulators (AOMs), which allow precise control and fast switching times. The light is subsequently delivered to the vacuum optical table by optical fibres.

3.1.3 Magnetic transport

The transport coils are a pair of anti-Helmholtz magnetic coils mounted on a motorised translation stage (Parker 404XR). In loading the trap, the quadrupole gradient is switched on to $45\,\mathrm{G\,cm^{-1}}$ and subsequently ramped to the transportation gradient of $180\,\mathrm{G\,cm^{-1}}$ in 500 ms. After the loading of atoms from the MOT chamber, the transport coils are accelerated at $1\,\mathrm{m\,s^{-2}}$ until the velocity reaches $0.26\,\mathrm{m\,s^{-1}}$. The velocity is maintained before it decelerates at $1\,\mathrm{m\,s^{-2}}$ to rest at the location of the static quadrupole trap around the science cell[1]. The overall transportation time and distance are $\sim 2\,\mathrm{s}$ and $51\,\mathrm{cm}$ respectively.

To avoid the obstacle, a Helmholtz coil pair is used, which generates a bias magnetic field of 216 G in order to shift the atoms in the transport quadrupole trap upwards by 1.2 cm at the position of the obstacle. It should be pointed out that the acceleration of such a shift ($\sim 4\,\mathrm{m\,s^{-2}}$) and the initial acceleration of the transport sequence are both very low compared to the acceleration due to the quadrupole trap gradient $\sim 40\,\mathrm{m\,s^{-2}}$. Thus any heating effects during the transport are minimal [67].

3.1.4 Lasers for optical dipole trapping

Optical crossed dipole trap

A crossed dipole trap in the science cell is formed from a single Gaussian beam, derived from the 1064 nm IPG YLR LP-SF 15 W fibre laser, in a bow-tie configuration [68]. As shown in Fig. 3.1, the dipole beam first enters the science cell at 45° to the glass surface (beam 1), which is then intersected by itself at 90° (beam 2). The beam radii of beam 1 and beam 2 at the intersection are $136\,\mu\mathrm{m}$ and $125\,\mu\mathrm{m}$ respectively. The trap centre is

---

[1]The magnetic coil configurations around the science cell are detailed in [67] which will not be discussed here.

located at $\sim 6\,\mathrm{mm}$ from the prism surface and $160\,\mu\mathrm{m}$ below the magnetic zero of the quadrupole field (this offset z_{offset} is to prevent Majorana loss, see Section 3.3.1). The intensity of the beam is controlled by a single AOM operating in a servo loop.

Optical waveguide

The light for the optical waveguide is derived from a $1064\,\mathrm{nm}$ Innolight Mephisto $2\,\mathrm{W}$ laser. The beam enters the science cell through the back of the Dove prism, intersecting at $\sim 45°$ relative to either of the dipole beams. The beam is focussed to $117\,\mu\mathrm{m}$ and the intensity is again controlled by an AOM.

3.2 Laser cooling in the MOT chamber

The first stage of the cooling sequence is performed in the MOT chamber (details of the operation of a MOT are documented in textbooks [86, 87] and thus will not be discussed). This involves three stages:

1. The MOT: it is in the usual configuration with three pairs of counter-propagating beams, as illustrated in Fig. 3.1. Typically $\sim 1\times 10^{9}$ atoms are loaded into the MOT in $\sim 30\,\mathrm{s}$.

2. The compressed-MOT (CMOT): once the MOT stage is complete, a $20\,\mathrm{ms}$ CMOT stage follows. This step involves relaxing the quadrupole trap gradient from $10\,\mathrm{G\,cm^{-1}}$ to $5\,\mathrm{G\,cm^{-1}}$, reducing the repump light intensity and increasing the detuning of the cooling light (from $-15\,\mathrm{MHz}$ to $-35\,\mathrm{MHz}$) simultaneously. This allows the atoms to fall into the $F = 2$ state. Atoms are cooled due to a reduction in the atom-photon scattering rate, and thus a denser sample can be achieved.

3. Optical molasses: the main difference between the optical molasses and the MOT is that the magnetic field is absent for the former. The polarisation gradient of the beams experienced by the atoms leads to further cooling of the sample [132]. For a during of $15\,\mathrm{ms}$, the detuning of the cooling light is further increased to $-90\,\mathrm{MHz}$ in the absence of the quadrupole field.

After the molasses cooling stage, the ^{85}Rb atoms are optically pumped with a 2 ms pulse to the low field seeking $F = 2, m_F = -2$ state. The cooled atomic sample is subsequently transferred to the magnetic quadrupole trap generated by the transport coils.

3.3 Experimental techniques

In this section, we summarise various basic experimental techniques that are used throughout this document, which includes magnetic trapping, optical dipole trapping, levitation against gravity, different trap configurations, evaporative cooling, and absorption imaging.

3.3.1 Magnetic trapping

Magnetic trapping is achieved using the quadrupole trap generated by the quadrupole coils which are in anti-Helmholtz format. The coils are aligned along the z direction where x and y represent the radial directions. In a changing magnetic field ΔB, an atom with a magnetic dipole moment μ experiences a change in energy

$$\Delta E = \mu \Delta B = m_F g_F \mu_\mathrm{B} \Delta B, \tag{3.1}$$

where m_F, g_F, and μ_B are the atom's magnetic sub-level, the hyperfine Landè g-factor, and the Bohr magneton respectively. As atoms align themselves along the magnetic field lines, the magnetic potential $U(\mathbf{r})$ is hence proportional to the magnitude of the magnetic field such that

$$U(\mathbf{r}) = \mu |B(\mathbf{r})|. \tag{3.2}$$

The quadrupole magnetic field has the form $|B(\rho, z)| \approx (\partial B/\partial \rho)\sqrt{\rho^2 + 4z^2}$, where $\rho^2 = x^2 + y^2$ [87]. The magnetic field varies linearly along the coil axis at a quadrupole gradient of $B_z' = \partial B/\partial z = 2\partial B/\partial \rho$, which is used for providing levitation of atoms against gravity (see Section 3.3.2). Away from the field zero at $z = 0$, the atoms would feel the trapping potential as long as they remain in the low field seeking trappable state. Atom trapping in
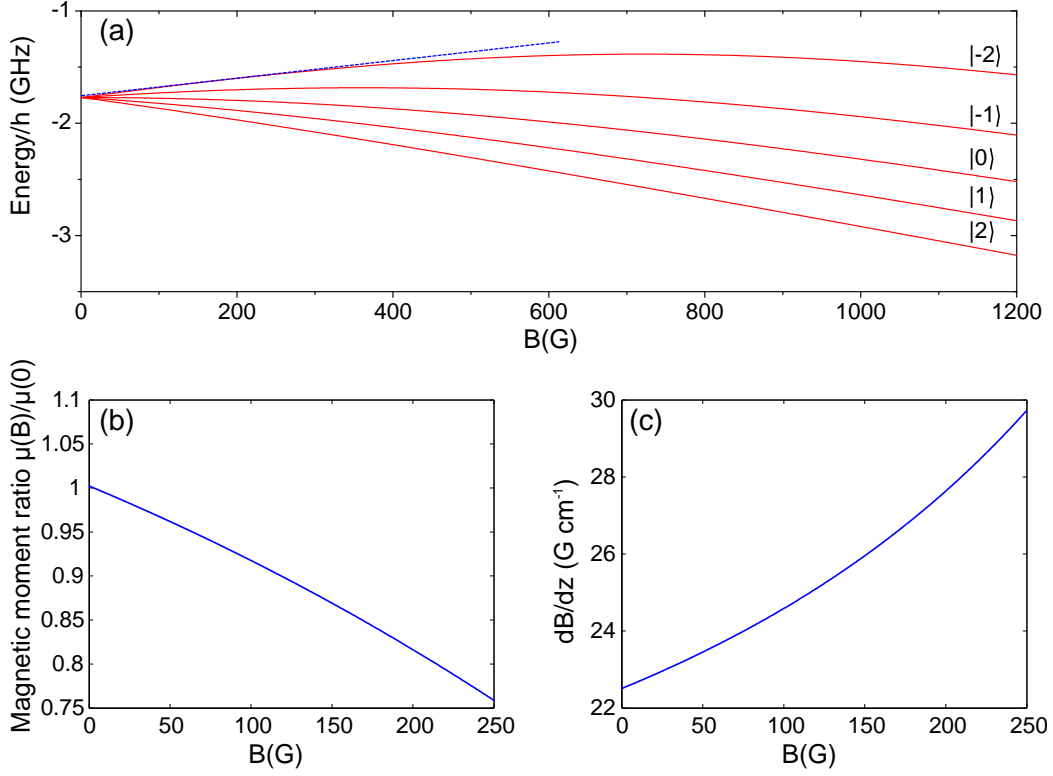
Figure 3.2: The levitation gradient for ^{85}Rb atoms in the $F = 2$, $m_F = -2$ state at an external magnetic field. (a) The Breit-Rabi diagram for ^{85}Rb atoms in the $F = 2$ hyperfine ground state. The magnetic moment μ at a magnetic field B_0 is the gradient of the energy as a function of the field. The dashed line indicates the magnetic moment μ of the $F = 2$, $m_F = -2$ state at $200\,\mathrm{G}$. (b) The normalised change in magnetic moment μ at a given magnetic field B. (c) The quadrupole gradient required for exact levitation.

the quadrupole trap is only effective if the change of the field vector is slow compared to the Larmor frequency

$$\omega_{\mathrm{Larmor}} = m_F g_F \mu_{\mathrm{B}} B / \hbar, \tag{3.3}$$

which decreases when an atom approaches the field zero. A spin flip into an untrappable state might then occur. This phenomenon is known as the Majorana spin flip [133], which leads to atom loss from the trap [134].

3.3.2 Levitation

The system is said to be exactly levitated when the quadrupole gradient exactly cancels out the gravitational gradient. Via Eq. 3.2, this condition is

$$\mu B'_z = mg, \tag{3.4}$$

where m is the atomic mass and g is the acceleration due to gravity. In the absence of additional magnetic fields, the levitation gradient for ^{85}Rb in the $F = 2, m_F = -2$ state (^{87}Rb in the $F = 1, m_F = -1$ state) is $22.4\,\mathrm{G\,cm^{-1}}$ ($30.5\,\mathrm{G\,cm^{-1}}$).

Throughout the work with ^{85}Rb, a bias field B is employed for tuning the interatomic interaction via a Feshbach resonance (see Section 4.1.1). Such a magnetic field leads to Zeeman splittings of the hyperfine states as a result of the coupling between the orbital and spin angular momenta of the atoms. This is represented by the Breit-Rabi diagram, as shown in Fig. 3.2(a). The magnetic moment μ, defined as the rate of change of Zeeman energy at a given field B (blue dashed line of Fig. 3.2(a)), thus becomes a function of the bias field B. As shown in Fig. 3.2(b), in the weak field regime of Zeeman splitting, the magnetic moment $\mu(B)$ of ^{85}Rb ^{2}S$_{1/2}$ $F = 2$, $m_F = -2$ hyperfine spin state decreases with an increasing magnetic field. Using Eq. 3.4, the exact levitation gradient at a given bias field can be calculated, as shown in Fig. 3.2(c).

3.3.3 Optical trapping

While a detailed description of optical dipole trapping is given elsewhere [94], we will briefly outline the key equations that are used throughout this work. The underlying principle of an optical dipole trap comes from the interaction between the far detuned light field and the induced dipole moment. At large detunings, the dipole force, which dominates over the radiation force from photon scattering, is proportional to the intensity gradient of the light field. In a limit of large detuning[2] and negligible saturation, the dipole trap potential depth from the dipole force of a Gaussian beam is expressed as

$$U_0 = \alpha I_0, \tag{3.5}$$

---

[2]Such that the detuning is much larger than the fine electronic transition structure of an atom.
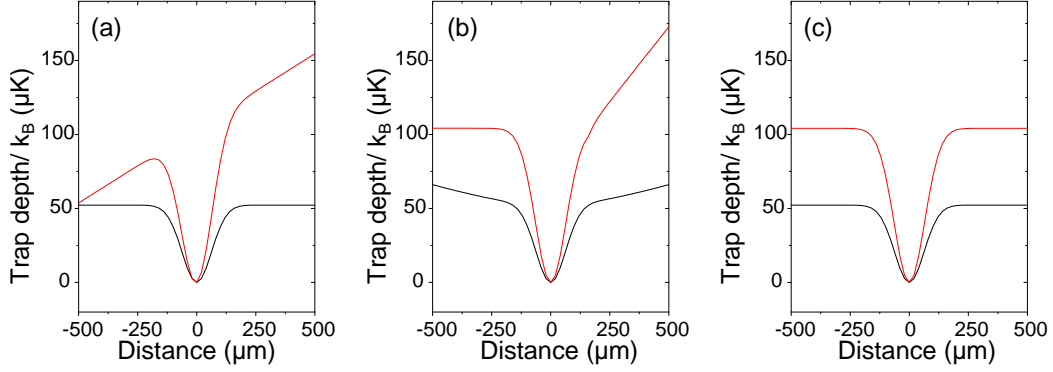
Figure 3.3: Examples of different trap configurations. The optical trap shown is the crossed dipole trap described in Section 3.1.4 operating at 10 W. The black (red) curves show the combined potential along the dipole beam propagation (vertical) direction. (a) The pure trap. (b) The hybrid trap, operating at a levitation gradient but no bias field. (c) The levitated trap.

where

$$I_0 = \frac{2P}{\pi w_x w_y}, \tag{3.6}$$

which is the peak intensity of the beam with $1/e^2$ radii w_x and w_y at a power P. α is the polarisability of the atoms [135], which is given by

$$\alpha = -\frac{\pi c^2}{2} \sum_i \frac{D_i \Gamma_i}{\omega_i^3} \left(\frac{1}{\omega_i - \omega_{\mathrm{L}}} + \frac{1}{\omega_i + \omega_{\mathrm{L}}} \right). \tag{3.7}$$

Here, i denotes the transitions included in the sum. In particular, we sum over all D_1 and D_2 transitions of Rb, with $D_1 = 1$ and $D_2 = 2$ for D_1 and D_2 transitions respectively. Γ_i denotes the natural linewidths of the corresponding transition, ω_i is the transition frequency and ω_{L} is the laser frequency. Note that the sign of the optical detuning $\Delta \equiv \omega_{\mathrm{L}} - \omega_i$ has a direct influence on the dipole potential: a red detuned (blue detuned) beam, $\Delta < 0$ ($\Delta > 0$), would result a potential well (barrier) where atoms are attracted (repelled) by regions of high intensity.

3.3.4 Pure, hybrid, and levitated traps

Throughout this work, different combinations of the optical dipole trap, the quadrupole trap, and the magnetic bias field are used. The three configurations, namely the pure trap, the hybrid trap, and the levitated trap, are

described below:

Pure trap

Only the optical trapping is involved. In the absence of a levitation gradient, the gravitational potential gradient reduces the trap depth of the optical trap along the vertical direction, as shown in Fig. 3.3(a). The vertical trap depth can be higher or lower than the horizontal counterpart, depending on the beam power P.

Hybrid trap

The quadrupole trap is present in addition to the optical trap. Its gradient dominates the trap frequencies along the dipole beams, as well as providing levitation against gravity for atoms in the trap, as shown in Fig. 3.3(b). In a crossed dipole trap configuration, the presence of quadrupole gradient maximises the trap depth through levitation and provides confinement along the arms of the laser beams. Thus a hybrid trap offers a larger trap volume than an all optical trap (see Section 3.3.5). The strength of the confinement depends on the displacement between the dipole trap and the magnetic zero. Such displacement, z_{dis}, can be shifted by the magnetic bias field B via $z_{\mathrm{dis}} = z_{\mathrm{offset}} + B/B'_z$ ($z_{\mathrm{offset}} = 160\,\mu\mathrm{m}$ is the offset between the quadrupole trap and crossed dipole trap in the absence of bias magnetic field, see Section 3.1.4). The resulting trap frequency at the $z = 0$ plane, thus the axial trap frequency along a single dipole beam, is given by [134]

$$\omega_{\mathrm{axial}} = \frac{1}{2}\sqrt{\frac{\mu B'_z}{m z_{\mathrm{dis}}}}. \tag{3.8}$$

Levitated trap

From Eq. 3.8 one sees that an application of a magnetic bias field can effectively remove the magnetic confinement in the hybrid trap. In the experiments with ${}^{85}\mathrm{Rb}$, where $B \sim 165\,\mathrm{G}$ and $B'_z \sim 26\,\mathrm{G\,cm^{-1}}$ are commonly used, the shift is $z_{\mathrm{dis}} \sim 6\,\mathrm{cm}$. Here, the axial trap frequency along the dipole beams ω_{axial} is calculated to be $\sim 1\,\mathrm{Hz}$. This is illustrated in Fig. 3.3(c).

3.3.5   Evaporative cooling

Evaporative cooling selectively removes the most energetic atoms from the trap, and allows the remaining atoms to rethermalise to a lower temperature through elastic scattering. Two types of evaporative cooling are used throughout this work, namely the radio frequency (RF) evaporation and evaporation in an optical dipole trap.

RF evaporation
RF evaporation is employed at the beginning of the cooling sequence in the science cell. After the atoms are transported from the MOT chamber, they are transferred to the static quadrupole trap. More energetic atoms occupy a larger volume of the magnetic trap, and hence experience a higher magnetic field. By applying an RF field with frequency ω_{RF} that is in resonance with such atoms, spin flips occur when

$$\hbar\omega_{\mathrm{RF}} = \Delta m_F g_F \mu_B B, \tag{3.9}$$

where $\Delta m_F = 1$. These energetic atoms eventually end up in untrappable states and are subsequently lost from the magnetic trap. The remaining atoms in the trap then rethermalise to a new Maxwell-Boltzmann distribution with a lower mean energy.

Evaporation in an optical dipole trap
Direct evaporation is a process that describes the removal of the hotter atoms in the trapped atomic sample by lowering the trap depth. This is achieved by either ramping the beam power of an optical dipole trap down to a lower value, or by a gradually reducing the levitation and thereby 'tilting the trap' [136].

As mentioned previously, the resulting cloud rethermalises to a lower temperature. The cooling depends strongly on the elastic scattering rate. In order to reach degeneracy, an *efficient* evaporation is desirable. The evaporation efficiency is defined as

$$\gamma = -\frac{\log(\mathrm{PSD_f}/\mathrm{PSD_i})}{\log(N_\mathrm{f}/N_\mathrm{i})}, \tag{3.10}$$

where i and f denote the initial and final values of an evaporation ramp respectively [137]. By optimising γ, one achieves the highest increase in PSD with the lowest atom lost. The evaporation trajectory of ^{85}Rb will be discussed in Chapter 4.

Evaporative cooling is carried out in all three trap configurations described in Section 3.3.4. A detailed comparison between cooling atoms in these traps in our experiment can be found in previous theses [68, 69]. In brief, one defines an evaporation parameter, η, which quantifies how far into the kinetic energy distribution atoms are removed from a particular trap. This can be thought of as the fraction of the trap depth $U_0 = \eta k_\mathrm{B}T$ that the mean kinetic energy $k_\mathrm{B}T$ of the trapped atoms equilibrate to. While $\eta \sim 10$ for an optical trap [138], this quantity varies slightly with different trap geometries. For our hybrid trap, $\eta = 12.6(5)$, which is the highest among the trap types described in the previous section [68, 69]. In contrast, $\eta = 9.8(5)$ for our levitated trap. Interestingly, for the pure trap in our experiment, $\eta = 8.7(5)$ at higher powers and $\eta = 11.0(5)$ at lower powers. This transition is linked to the effect of gravity on the trap depth, where evaporation preferably occurs along the vertical direction at low beam power.

3.3.6 Absorption imaging

We use destructive absorption imaging to extract information about the cloud. The full calculation and derivation of various parameters, such as the number of atoms N and the temperature of the sample T, are detailed elsewhere [67–69, 139] and thus they will not be reproduced here. We will quote some of the key equations that are related to the measurements presented in this work.

Absorption imaging relies on the absorption of the resonant light by the atoms, from which the scattering of light leaves a shadow of the atomic sample when the remaining imaging probe beam is imaged. The amount of the light that remains after propagating through the atomic sample is

characterised by the optical depth (OD) via

$$I(x, z) = I_0 \exp(-\mathrm{OD}(x, z)), \tag{3.11}$$

where I_0 is the peak intensity of the imaging probe beam. OD is calculated by processing 3 separate images taken by the CCD camera:

- I_{atoms}: with presence of the atoms and the probe light;

- I_{probe}: probe light without the atoms;

- I_{bg}: the background noise without the probe light.

Using Eq. 3.11, the optical depth can hence be obtained through

$$\mathrm{OD}(x, z) = \ln \left(\frac{I_{\mathrm{probe}} - I_{\mathrm{bg}}}{I_{\mathrm{atoms}} - I_{\mathrm{bg}}} \right). \tag{3.12}$$

The optical setup for the horizontal imaging is shown in Fig. 3.1, which consists of two lenses between the atoms and the camera: lens 1 with a focal length of $f_1 = 160\,\mathrm{mm}$ is placed at $160\,\mathrm{mm}$ from the atoms, while lens 2 with a focal length of $f_2 = 250\,\mathrm{mm}$ is placed at $250\,\mathrm{mm}$ from the CCD sensor. For a correctly focussed system, the theoretical magnification factor is $f_2/f_1 = 1.56$. The magnification factor, and thus the pixel size on the camera, can be calibrated by mapping out the centre of mass of the atomic cloud in free fall due to gravity.

Number of atoms
Assuming the atomic cloud has a Gaussian shape with widths ($1/e^2$ radii) σ_x and σ_z in their respective directions, the number of atoms in the cloud can be calculated using

$$N = \frac{2\pi}{\sigma_0} \mathrm{OD}_{\mathrm{peak}} \sigma_x \sigma_z, \tag{3.13}$$

where $\sigma_0 = 3\lambda^2/2\pi$ for a two level atom [139].

Temperature of the atoms
The temperature of the atomic cloud is required for calculating various quan-

tities such as the peak density and the phase space density. The atomic sample undergoes ballistic expansion after being released from a harmonic trap. By measuring the cloud widths after various expansion times τ, also known as the time of flight (TOF), the temperature of the cloud in both horizontal (x) and vertical (z) directions can be extracted by fitting the straight line

$$\sigma_{x,z}^2(\tau) = \sigma_{x,z}^2(0) + \left(\frac{k_{\mathrm{B}}T}{m}\right)\tau^2, \tag{3.14}$$

where $\sigma(0)$ is the width of the atomic cloud in the trap [68, 139]. For long TOFs where $\sigma_{x,z}(\tau) \gg \sigma_{x,z}(0)$, an approximation can be made by neglecting the initial cloud width, which allows us to calculate the cloud temperature with a single absorption image. In our experiment, an expansion time of $\tau \gtrsim 18\,\mathrm{ms}$ is found to be sufficient to provide a good estimation of the temperature of a thermal cloud [68].

For atomic clouds that are close to degeneracy, one requires a relatively long expansion time ($\tau \sim 100\,\mathrm{ms}$) to observe the thermal expansion. In order to avoid the atomic cloud dropping 'off the screen', a levitated TOF is often employed instead, where the atomic cloud is levitated during the expansion after the release from the trap.

Part I

Experiments with a tunable
^{85}Rb BEC

Chapter 4

Formation of ^{85}Rb bright solitary matter-waves

^{85}Rb BEC was first realised in a weak Ioffe-Pritchard magnetic trap [12], and later on through sympathetic cooling with ^{87}Rb [140, 141]. In this chapter we demonstrate the creation of a condensate via direct evaporative cooling in an optical crossed dipole trap. The evaporation trajectory is carefully tailored in order to achieve a high evaporation efficiency. The BEC is subsequently transferred into an optical waveguide. Through precise tuning of the scattering length using a Feshbach resonance, we successfully realise the bright solitary wave which is robust against collision with a broad repulsive barrier. This chapter comprises results from refs. [13, 44].

4.1 Direct evaporation to ^{85}Rb Bose-Einstein condensation

4.1.1 The 155 G Feshbach resonance of ^{85}Rb

The interaction strength, determined by the nonlinearity g in the GPE (Eq. 2.5), can be controlled by a scattering resonance feature known as a Feshbach resonance. While a more in-depth discussion of the theoretical origin of the resonance can be found elsewhere [37], we explain the basic features of the resonance by using the two-channel model shown in Fig. 4.1(a). In scattering theory, an open channel refers to collisions between free parti-
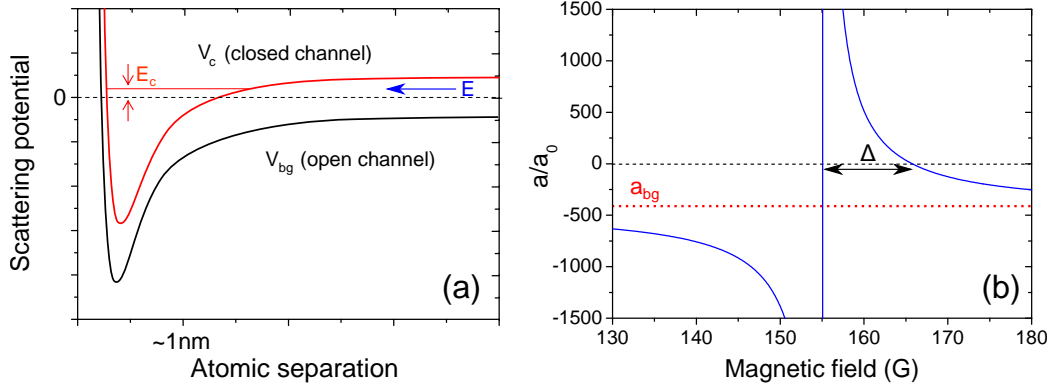
Figure 4.1: (a) The origin of Feshbach resonances: a schematic sketch of the two channel model. Resonance occurs when an interatomic collisional energy E is resonantly coupled to a bound state E_c of the closed channel. (b) The 155 G Feshbach resonance of ^{85}Rb atoms in the $F = 2, m_F = -2$ state. The background scattering length is $a_{bg} = -443(3) \, a_0$ (red dotted line), while the width of the broad resonance feature is $\Delta = 10.71(2) \, \text{G}$.

cles, while a closed channel supports a bound molecular state with energy E_c. These two channels are characterised by the molecular potential curves V_{bg} and V_c respectively as functions of the atomic separation, as sketched in Fig. 4.1(a). For large atomic separation, the two free atoms in the ultracold gas are connected asymptotically by V_{bg}. As the two free atoms approach, the potential is represented by the open channel. In the ultracold domain, the collisional energy E is typically low ($E \to 0$) [37]. A Feshbach resonance occurs when the bound molecular state E_c in the closed channel is energetically close to the collisional energy E. As such, even weak coupling can result in a strong mixing between the two channels. Providing that the magnetic moments differ for the two channels, such resonant coupling can be conveniently achieved by applying an external magnetic field, which effectively alters the energy difference between E_c and E. The ability in tuning atomic scattering properties has made the magnetically tuned Feshbach resonance a widely used tool for experiments such as the realisation of bright solitary matter-waves [41–44], the study of the BEC-BCS crossover [142, 143] and ultracold molecules [144, 145].

A magnetically tuned Feshbach resonance is described by a simple expression. By applying an external magnetic field B close to the Feshbach resonance magnetic field B_{res}, the variation of the s-wave scattering length takes the form

$$a_s(B) = a_{\text{bg}} \left(1 - \frac{\Delta}{B - B_{\text{res}}} \right), \tag{4.1}$$

where a_{bg} represents the background scattering length and Δ is the width of the resonance feature [146, 147]. The reason for using ^{85}Rb in our experiment is closely related to this equation. While essentially all isotopes of alkali-metal atoms exhibit Feshbach resonances, features with large widths Δ suitable for tuning the scattering properties are usually less accessible. Let us consider ^{87}Rb as an example: the broadest resonance, which appears at 1007 G, only has a width of $\Delta = 0.2$ G [148]. In contrast, for ^{85}Rb atoms in the $F = 2$, $m_F = -2$ state, the resonance at $B_{\text{res}} = 155.041(18)$ G is $\Delta = 10.71(2)$ G wide [149], which is shown in Fig. 4.1(b). At the zero crossing of the scattering length at 165.85(5) G [149], the variation of the scattering length (obtained by differentiating Eq. 4.1 and approximating $B \approx B_{\text{res}} + \Delta$ at around $a_s = 0$) is

$$\left. \frac{\mathrm{d}a_s}{\mathrm{d}B} \right|_{a_s=0} = a_{\text{bg}} \left. \frac{\Delta}{(B - B_{\text{res}})^2} \right|_{a_s=0} \approx \frac{a_{\text{bg}}}{\Delta} = -40 \, a_0 \, \text{G}^{-1}. \tag{4.2}$$

This broad Feshbach resonance of ^{85}Rb at an easily achievable magnetic field hence allows precise tuning of the scattering length in the vicinity of $a_s = 0$, which has already been broadly used for controlling interatomic interactions in a condensate [12, 39, 40, 43, 150, 151]. The tunability of the scattering length thus makes ^{85}Rb an attractive candidate for realising solitary waves experimentally.

4.1.2 Elastic and inelastic scattering

The first step in creating bright solitary waves requires a tunable ^{85}Rb condensate. However, unlike the commonly used ^{87}Rb, evaporative cooling of ^{85}Rb atoms is more difficult [12, 147, 153]. This is caused by two main factors: low elastic and high inelastic collision rates.

Elastic scattering
Efficient evaporation relies on a high 'good-to-bad' collision ratio. 'Good' collisions refer to the elastic scattering between atoms, while 'bad' collisions
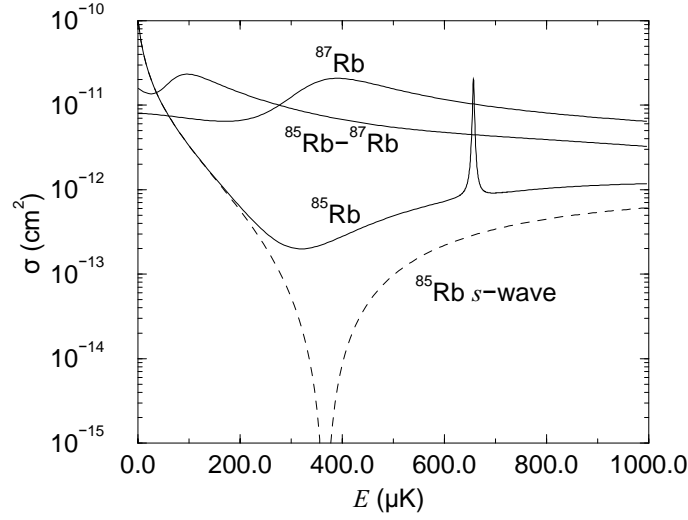
Figure 4.2: The elastic scattering cross-section for ^{87}Rb – ^{87}Rb, ^{85}Rb – ^{87}Rb, and ^{85}Rb – ^{85}Rb collisions at different collision energies. Figure taken from [152].

refer to the inelastic scattering. Elastic collisions are responsible for the rethermalisation of the atomic cloud that remains in the trap after the removal of more energetic atoms. Such a collision rate is given by [154]

$$\Gamma_{\mathrm{el}} = \langle n \rangle \sigma \langle v_{\mathrm{rel}} \rangle, \tag{4.3}$$

where $\langle n \rangle$ is the mean density of the atomic cloud and $\langle v_{\mathrm{rel}} \rangle$ is the mean relative velocity where $\langle v_{\mathrm{rel}} \rangle = \sqrt{16 k_B T / m \pi}$ for atoms in a harmonic trap [155]. σ is the elastic scattering cross-section. For a low temperature collision[1] between indistinguishable bosons, it takes the form

$$\sigma = \frac{8 \pi a_s^2}{1 + k^2 a_s^2}, \tag{4.4}$$

where k is the wavevector [156]. Due to the energy dependence of σ, the collision rate (Eq. 4.3) is often expressed as $\Gamma_{\mathrm{el}} = \langle n \rangle \langle \sigma v_{\mathrm{rel}} \rangle$. Furthermore, rather different from $\langle n \rangle$ and $\langle v_{\mathrm{rel}} \rangle$, σ is a scattering property that is strongly dependent on the isotope. It can be seen in Fig. 4.2 that for the collisional energy, defined as $\langle E \rangle = m \langle v_{\mathrm{rel}} \rangle^2 / 2$, the elastic scattering cross-section of ^{85}Rb – ^{85}Rb collision is less than that of ^{87}Rb – ^{87}Rb and ^{85}Rb – ^{87}Rb collisions for $\langle E \rangle \gtrsim 100\,\mu\mathrm{K}$ [152]. The variation of σ of ^{85}Rb – ^{85}Rb collision cross-section

---

[1]Such that the de Broglie wavelength of the atom is much larger than the geometric mean of the scattering length and the effective range of the interaction [156].

features a Ramsauer-Townsend type minimum at $\sim 375\,\mu$K [152], which is almost two orders of magnitude lower than that of ^{87}Rb – ^{87}Rb collisions. The low elastic cross-section of ^{85}Rb – ^{85}Rb collisions means that the evaporation is less efficient than the cases where ^{87}Rb is involved. Consequently, long evaporation times are required owing to the slow rethermalisation.

Inelastic scattering

In addition to the elastic scattering, atoms suffer from inelastic collisions which ultimately lead to atom loss from the trap. There are three main loss mechanisms: background loss, two-body inelastic collisions, and three-body inelastic collisions.

Background loss is caused by collisions of trapped atoms with high energy background particles in the vacuum at room temperature. Subject to the quality of the vacuum, this is generally the least dominant among the three loss mechanisms. Two-body losses originate from dipole relaxation when two particles collide. This can cause spin flips to an untrappable states. The loss rate goes as $\Gamma_{2-\text{body}} = -K_2\langle n \rangle$, where K_2 is the two-body decay constant [139]. In contrast, three-body inelastic collisions leads to three-body recombination. This describes the process where two atoms form a molecule and a third unbound atom carries away the excess energy and momentum from the collision. The molecular binding energy ϵ released is often very large compared to a typical trap depth and so both the molecule (carrying $\epsilon/3$) and the single atom (carrying $2\epsilon/3$) are too energetic to remain in the trap [157]. Alternatively, if the highly energetic atom or molecule remains in the trap, it is possible for further collisions with other atoms in which the excess kinetic energy causes heating. The loss rate of such process is characterised by $\Gamma_{3-\text{body}} = -K_3\langle n^2 \rangle$, where K_3, scales with a_s^4 [158–160], is the three-body decay constant. It is worth mentioning that both loss rates become more prominent for higher atomic densities. Previous works have experimentally determined the decay constants for ^{85}Rb far from the broad Feshbach resonance (a magnetic field of $250\,$G was used), which are [139, 153]

$$K_2 \approx 2 \times 10^{-14}\,\text{cm}^3\,\text{s}^{-1} \quad \text{and} \quad K_3 \approx 4 \times 10^{-25}\,\text{cm}^6\,\text{s}^{-1}. \tag{4.5}$$
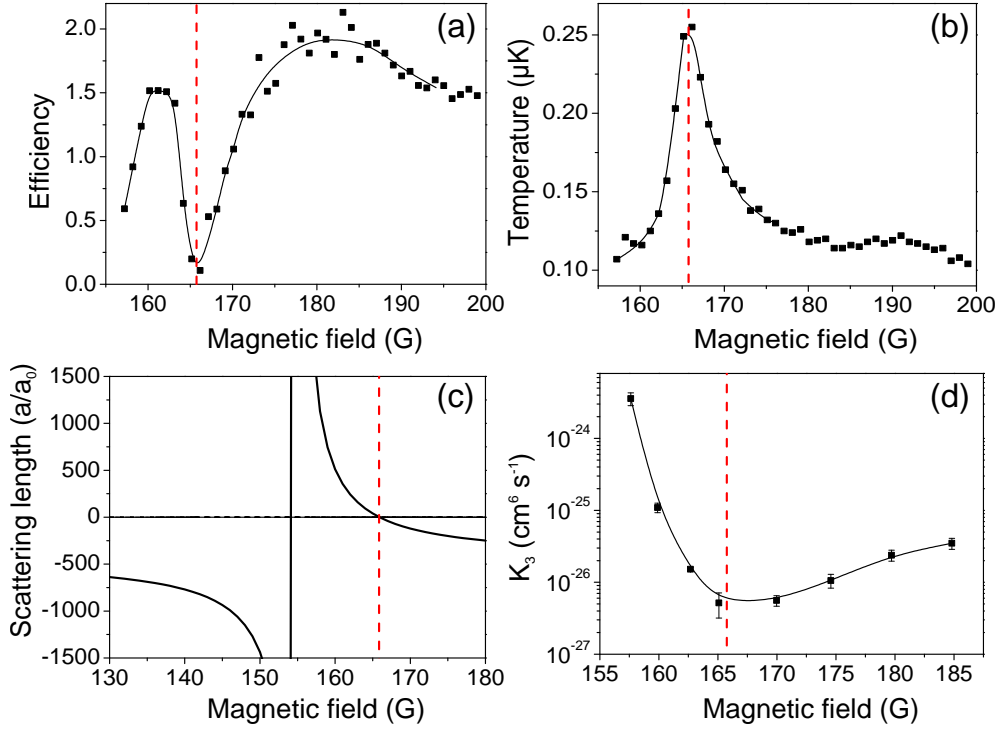
Figure 4.3: (a) Efficiency γ of a fixed evaporation trajectory at different magnetic fields. (b) The corresponding temperature of the thermal cloud. (c) The wide Feshbach resonance of the $F = 2$, $m_F = -2$ state of ^{85}Rb. (d) Three-body recombination rate K_3 shows strong magnetic field dependence. The red dashed line indicates zero crossing of a_s. Solid black lines in (a), (b), and (d) are guides to the eye only. Figure taken from [13].

In constrast, for ^{87}Rb [139, 161],

$$K_2 \approx 3 \times 10^{-18}\,\mathrm{cm^3\,s^{-1}} \quad \text{and} \quad K_3 \approx 4 \times 10^{-29}\,\mathrm{cm^6\,s^{-1}}, \qquad (4.6)$$

which are both approximately four orders of magnitude lower than those of ^{85}Rb. As a result, direct evaporative cooling of ^{85}Rb to degeneracy is extremely challenging as the efficiency is undermined by the high loss rate. Fortunately, since both K_2 and K_3 are dependent on the scattering length [162, 163], the evaporation efficiency of ^{85}Rb can be improved by making use of the Feshbach resonances. It has been demonstrated in various atomic isotopes of alkali-metals that both quantities can be tuned over several orders of magnitude and the atom loss thereby suppressed [139, 141, 150].

4.1.3   Efficient evaporative cooling

We achieve efficient evaporation through understanding the interplay between the elastic and inelastic scattering close to the Feshbach resonance. The atomic cloud for such a measurement is prepared as follows: after the transfer into the science cell quadrupole trap, the atomic cloud typically contains $\sim 5 \times 10^8$ atoms at a temperature of $\sim 380\,\mu$K. Due to the low elastic scattering rate at this temperature, forced RF evaporation (consists of several ramps and holds) is carried out for a total duration of 26 s. This results in a cloud of 3×10^7 atoms at $42\,\mu$K with PSD $= 5 \times 10^{-5}$. To proceed, atoms are loaded into the crossed dipole trap (which is switched on at a constant power of 10.1 W throughout the RF evaporation) by relaxing the quadrupole gradient from $180\,\mathrm{G\,cm^{-1}}$ to $\sim 21.5\,\mathrm{G\,cm^{-1}}$ in 500 ms, which is just below the exact levitation gradient at $22.4\,\mathrm{G\,cm^{-1}}$ (see Section 3.3.2). Despite only 20% of the magnetically trapped atoms being transferred into the optical trap, there is a gain of a factor of 30 in the PSD as a result of an increase in trap frequencies and the atoms equilibrating to a lower temperature ($\sim 10\,\mu$K) in the new trap. As the crossed dipole trap is located $\sim 160\,\mu$m from the quadrupole field zero (see Section 3.1.4), the atoms experience a small magnetic bias field of ~ 0.3 G which maintains the alignment of the quantisation axis. Evaporation in the hybrid trap follows by ramping the beam power down to 2.7 W in 5 s. Due to the magnetic confinement along the wings of the dipole beam, the trap depth is set by the vertical direction. At this stage, we wish to apply a bias field of ~ 155 G in order to access the Feshbach resonance to control the scattering properties such that efficient evaporation can be achieved. As such, the magnetic confinement of the trap is effectively removed and atoms now only remain in the crossed region of the trap.

To tailor an optimised evaporation trajectory, our aim is to examine at what magnetic field yields the most efficient cooling. We explore this by indirectly probing the efficiency γ (Eq. 3.10) through a fixed evaporation routine for different magnetic fields. The efficiency for a 50 G window spanning the zero crossing of the Feshbach resonance is shown in Fig. 4.3(a). Despite a clear peak at 161 G, the broader $a_s < 0$ peak at $175 - 185$ G gives a marginally better performance. As the magnetic field approaches the zero crossing of the

scattering length at $\sim 166\,\mathrm{G}$, the elastic scattering rate decreases according to Eq. 4.3 and Eq. 4.4. This leads to poor rethermalisation, and as a result, one observes a peak in the atomic temperature shown in Fig. 4.3(b).

We wish to extract the magnetic field dependence of the three-body loss coefficient. To achieve this, an atomic cloud at $T \sim 0.15\,\mu\mathrm{K}$ is first prepared at $175\,\mathrm{G}$. The magnetic field is then ramped to a new value in $10\,\mathrm{ms}$, while the trap is subsequently deepened from $1.4\,\mu\mathrm{K} \times k_\mathrm{B}$ to $27.5\,\mu\mathrm{K} \times k_\mathrm{B}$. In doing so, the loss of atoms from evaporation due to a relative difference between the cloud temperature in the new field and the trap depth is suppressed. The lifetime of such a trap allows us to measure the atom loss and the heating of the cloud caused by three-body collisions. The K_3 coefficient can be determined by fitting the data with the solutions to the coupled differential rate equations

$$\frac{\mathrm{d}N}{\mathrm{d}t} = -\frac{N}{\tau_\mathrm{bg}} - \beta\frac{N^3}{T^3} \quad \text{and} \quad \frac{\mathrm{d}T}{\mathrm{d}t} = \beta\frac{N^2}{T^3}\frac{T + T_h}{3}, \qquad (4.7)$$

where τ_bg is the decay time from background collisions, T_h is the recombination heating energy per lost atom, and $\beta = K_3(m\bar{\omega}^2/2\pi k_\mathrm{B})^3/\sqrt{27}$ ($\bar{\omega}$ is the geometric mean of the trap frequencies as defined in Section 2.2.2) [157]. While it is likely that both two and three-body collisions contribute to the atom loss from the trap, it is generally difficult to differentiate between the two loss mechanisms [147]. Therefore, due to the high atomic density in the compressed trap, combined with a stronger density dependence of the three-body loss rate over the two-body loss rate (see Section 4.1.2), we choose to neglect the two-body effect in fitting the data.

As shown in Fig. 4.3(d), the minimum inelastic rate appears near the zero crossing of the Feshbach resonance. This, however, coincides with the region with low elastic collision and hence poor evaporation efficiency. Away from $a_s \sim 0$, the inelastic losses for $a_s < 0$ are marginally lower compared to $a_s > 0$ and hence a better evaporation performance for the region at $175 - 185\,\mathrm{G}$. Thus, to proceed in the cooling, we operate at a bias field within the range of $175 - 185\,\mathrm{G}$ in order to achieve efficient evaporation.
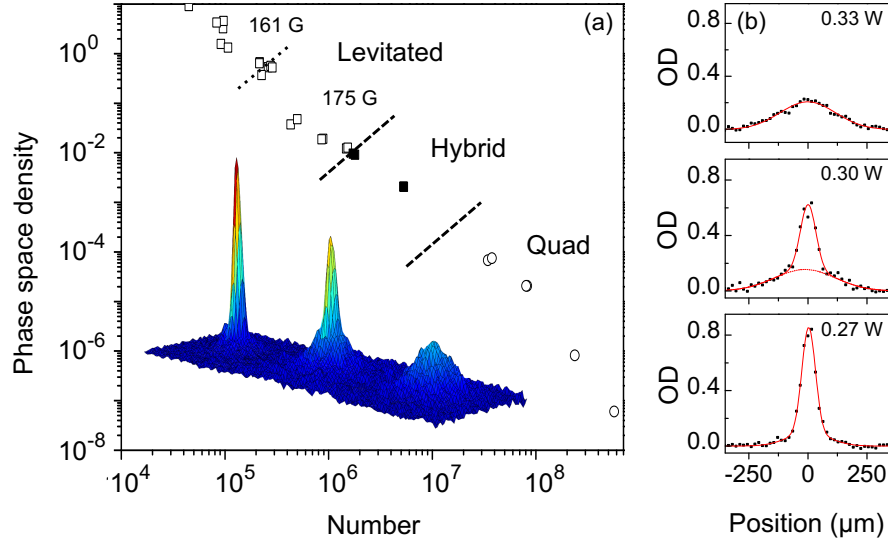
Figure 4.4: Creation of ^{85}Rb via direct evaporative cooling. (a) Evaporation trajectory to reach BEC. RF evaporation in the quadrupole trap (circles) and evaporation in hybrid trap (black squares) are performed at ~ 0 G. Initial evaporation in the levitated trap is performed at 175 G, which is decreased to 161.3 G during the latter stage of cooling (for PSD > 0.5), shown in hollowed squares. Inset: from right to left shows the density profiles for a thermal, bimodal and condensed atomic cloud. (b) Horizontal cross-sections of the condensate column density for a thermal (top), bimodal (centre) and condensed (bottom) sample as the dipole beam power is reduced. Figure taken from [13].

4.1.4 Bose-Einstein condensation

Following the hybrid trap evaporation, to create a levitated trap, the bias field is ramped rapidly (~ 10 ms) to 175 G. After a brief hold for 500 ms, two more evaporation ramps were carried out resulting in an atomic sample of 2.5×10^5 atoms at 150 nK with PSD = 0.5. The bias field is then ramped to 161.3 G ($a_s \sim 315 a_0$) because a stable condensate cannot be formed at the negative scattering length at 175 G ($a_s \sim -205 a_0$) [164]. Further evaporation is carried out, and at a power of 0.3 W, condensation of ^{85}Rb is observed. The final trapping geometry is almost spherical, with trap frequencies of $\omega_{x,y,z} = 2\pi \times (31, 27, 25)$ Hz . The overall evaporation time in the dipole trap spans for 14.5 s, and the optimised complete evaporation trajectory is shown in Fig. 4.4(a). Through varying the final beam power, we record the transition from the thermal cloud to condensate as shown in Fig. 4.4(b). At a trap depth of ~ 360 nK, we are able to produce a pure ^{85}Rb BEC containing $\sim 4 \times 10^4$ atoms.
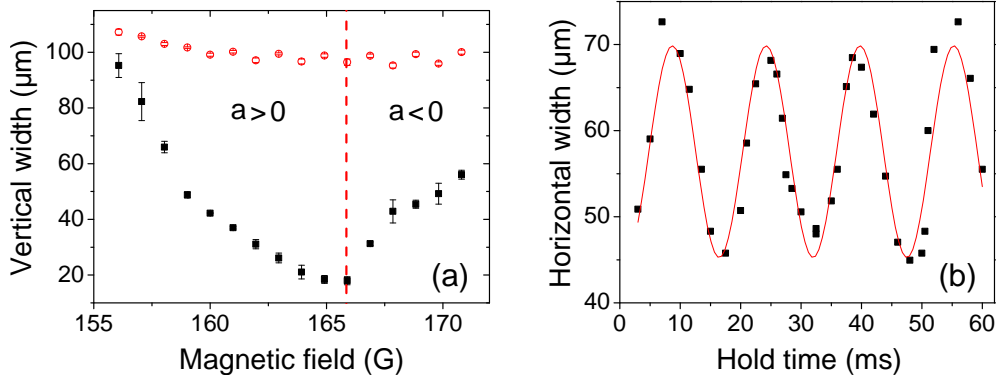
Figure 4.5: Demonstration of the tunable interactions of ^{85}Rb BEC. (a) Cloud width along the vertical direction after a fixed expansion time at different scattering lengths. The measurement is carried out for both a condensate (black squares, 55 ms TOF) and a thermal cloud (red circles, 25 ms TOF). (b) Breathing mode oscillation of the cloud width when the scattering length is jumped from $\sim 315\,a_0$ to $\sim 50\,a_0$ and held in the trap at the final scattering length. Figure taken from [13].

To demonstrate the tunability of the atomic interactions of a condensate, two simple experiments are carried out. In the first measurement the magnetic field is jumped to a new value within the range of $155-175\,$G at the point of release from the dipole trap. The size of the cloud is measured after a 55 ms expansion time. As shown in Fig. 4.5(a), a change in the scattering-length-dependent interaction strength manifests a change in the cloud size (black squares). At large and positive a_s, the cloud expands rapidly. The expansion decreases as a_s approaches the zero crossing at 165.75 G. By further reducing the magnetic bias field, a_s becomes large and negative, where the condensate becomes unstable and subsequently undergoes collapse [40]. This leads to an increase in the measured cloud size. The same experiment for a thermal cloud shows a distinct contrast, where the comparatively low density leaves the atomic sample insensitive to the atomic interactions. As a result, there is no observable change in the cloud size at different magnetic fields.

In the second measurement, the magnetic field applied to the trapped BEC is jumped to a new value where the corresponding scattering length changes from $\sim 315a_0$ to $\sim 50a_0$. The instantaneous change of scattering length (to small but positive a_s in a near spherical trap) puts the system well in the Thomas-Fermi regime. Such a sudden change of the Thomas-Fermi radius
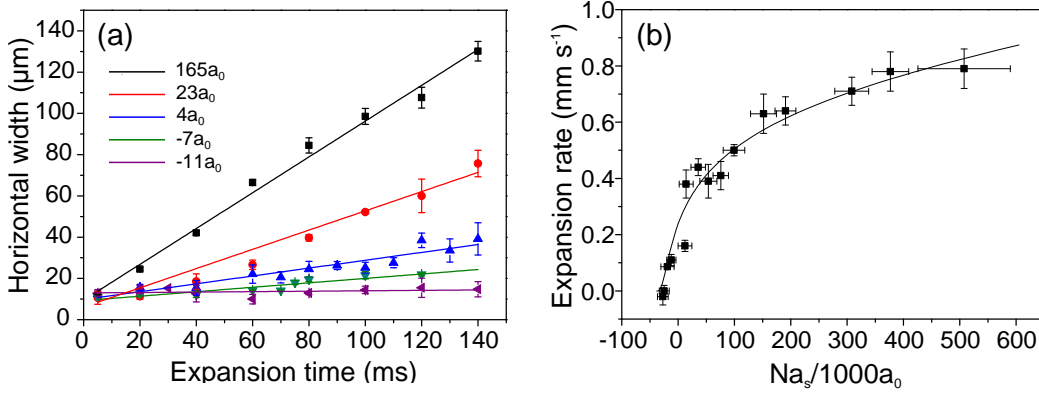
Figure 4.6: BEC expansion over propagation time at different scattering lengths a_s. (a) Condensate expansion in the waveguide at different values of scattering lengths. The horizontal width is the root mean square radius of the condensate, and the solid lines are linear fits to the experimental data. (b) The change of condensate expansion rate as a function of N and a_s. The solid curve is the theoretically calculated expansion rate using a cylindrically symmetric 3D GPE [44]. Figures taken from ref. [44].

($R_{\text{TF}} = 11\,\mu m \rightarrow 8\,\mu m$ using Eq. 2.10) would induce a breathing mode oscillation of the condensate width at a frequency of $\sqrt{5}\bar{\omega}$ [88]. This oscillatory feature is observed, as shown in Fig. 4.5(b), at a frequency in good agreement with the expected value [13].

4.2 Realisation of bright solitary matter-wave

We remind ourselves that bright solitary waves are well localised wavepackets with attractive interatomic interactions in a quasi-1D geometry where their amplitude and width are maintained over time. In proceeding to the realisation of such matter-waves, we first need to place the condensate in a geometry that mimics the 1D condition. This is achieved by transferring the condensate from the 3D crossed dipole trap into the single optical waveguide described in Section 3.1.4. For details of the alignment and the characterisation of the waveguide see refs. [68, 69].

In order to transfer the condensate into the waveguide, we first ramp the magnetic field close to $a_s = 0$ in 50 ms. This reduces the equilibrium width of the condensate and thereby places the condensate approximately in the harmonic oscillator ground state of the dipole trap. After a 10 ms hold to allow the bias field to stabilise, the waveguide is switched on at 0.17 W and
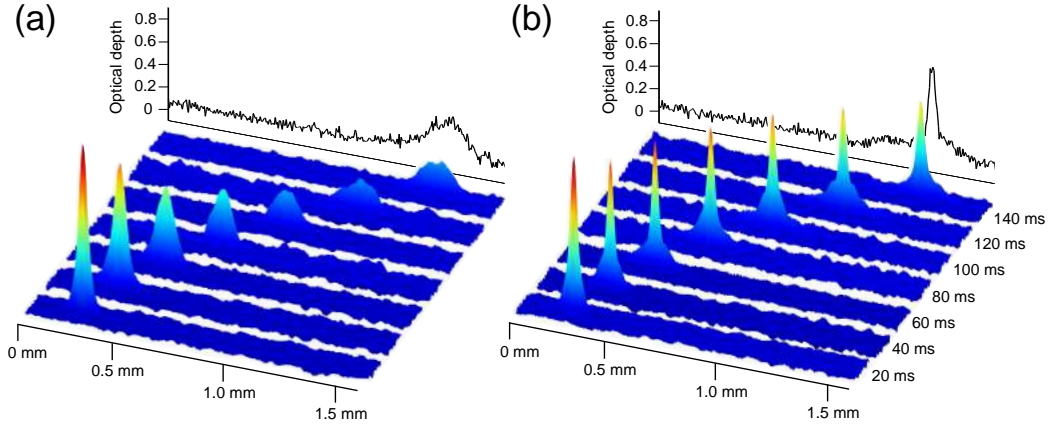
Figure 4.7: Density profiles of (a) a repulsive BEC ($a_s = 58\,a_0, N = 3.5 \times 10^3$) and (b) a bright solitary wave ($a_s = -11\,a_0, N = 2.0 \times 10^3$) as they propagate along the waveguide. The crosscuts of the OD are the horizontal profiles of the condensates after 140 ms propagation. Figures from ref. [44].

the dipole beam is switched off simultaneously. The waveguide beam power is chosen such that the radial trap frequency $\omega_{y,z}$ approximately matches that of the crossed dipole trap at the final stage of evaporation. To maximise the trap depth of the waveguide, the quadrupole trap gradient is jumped to the exact levitation gradient of $\sim 26\,\mathrm{G\,cm^{-1}}$ (see Fig. 3.2(b)) at the same step. Together with a bias field of $\sim 165\,\mathrm{G}$, the magnetic trap frequency along the waveguide, calculated using Eq. 3.8, is $\sim 1\,\mathrm{Hz}$ which dominates over the optical trap frequency ($\sim 0.1\,\mathrm{Hz}$). The trap frequencies of this waveguide potential are $\omega_{x,y,z} = 2\pi \times (1, 27, 27)\,\mathrm{Hz}$.

The minimum of the weak magnetic harmonic potential is located at $\sim 2.6\,\mathrm{mm}$ from the crossed dipole trap further away from the prism, thus the condensate is set in motion towards the trap minimum as soon as the transfer is complete. The realisation of a bright solitary wave requires the spatial extent of the BEC to remain unchanged during its propagation along the waveguide. To search for the scattering length $a_s < 0$ where the resulting attractive interatomic interaction exactly balances out the dispersion of the matter-wave, we measure the rate of expansion of the condensate at various scattering lengths. In order to do so, we simply switch the magnetic field to a new value after the crossed dipole trap is removed. The effect of the final scattering length on the size of the BEC during its propagation along the waveguide is shown in Fig. 4.6(a). As the scattering length decreases, the expansion ceases. Shown in Fig. 4.6(b), the expansion rate of the con-

densate with $N = 2 \times 10^3$ atoms drops to essentially zero at $a_s = -11a_0$. The lack of dispersion of the attractive condensate thus indicates the formation of bright solitary wave. In Fig. 4.7, we compare the propagation of a repulsive BEC ($a_s = 58a_0, N = 3.5 \times 10^3$) with the bright solitary wave ($a_s = -11a_0, N = 2 \times 10^3$). The dispersion of the repulsive BEC along the axial direction of the waveguide reduces the OD during the propagation, where such significant drop is absent for the bright solitary wave.

4.3   Reflection from a broad repulsive barrier

We examine the robustness of the particle-like bright solitary wave by using a wide ($1/e^2$ radius of $130\,\mu$m) and a repulsive ($532\,$nm) Gaussian barrier. This beam intersects the waveguide at $\sim 45°$, where the point of intersection is displaced from the crossed dipole trap by $455\,\mu$m further away from the prism. As the barrier is much wider than the size of the soliton, only classical outcomes are expected. Hence, much like 'rolling a ball up a hill', only a full reflection or transmission is expected depending on the kinetic energy of the system compared to the barrier height. Let us simplify our system by neglecting the loss of kinetic energy as the solitary wave approaches the broad barrier potential. This gives an upper bound to the kinetic energy of the solitary wave at the position of the barrier, which is $\sim 440\,$nK$\times k_{\rm B}$ (or $\sim 9\,$mm$\,$s^{-1}). By using a barrier with its potential height greater than the kinetic energy, and in the case shown in Fig. 4.8(a) and (b) where a potential of $760\,$nK $\times k_{\rm B}$ is used, clean reflection is observed. Lowering the barrier height will eventually see the solitary wave carrying sufficient kinetic energy to 'roll all the way up the hill' and over to the other side of the barrier. The position of the solitary wave at $150\,$ms after release against different barrier heights are shown in Fig. 4.8(c). In addition, Fig. 4.8(d) shows the comparison of the condensate widths between a soliton with barrier, repulsive BEC with barrier, and a freely propagating repulsive BEC. While the bright solitary wave maintains its shape without dispersion throughout the propagation time, the width of the repulsive BEC with the presence of the barrier shows an oscillatory behaviour. This is in contrast with the unobstructed case where the repulsive BEC expands linearly. We attribute this as a consequence of the large spatial extent of the dispersive BEC, which causes a
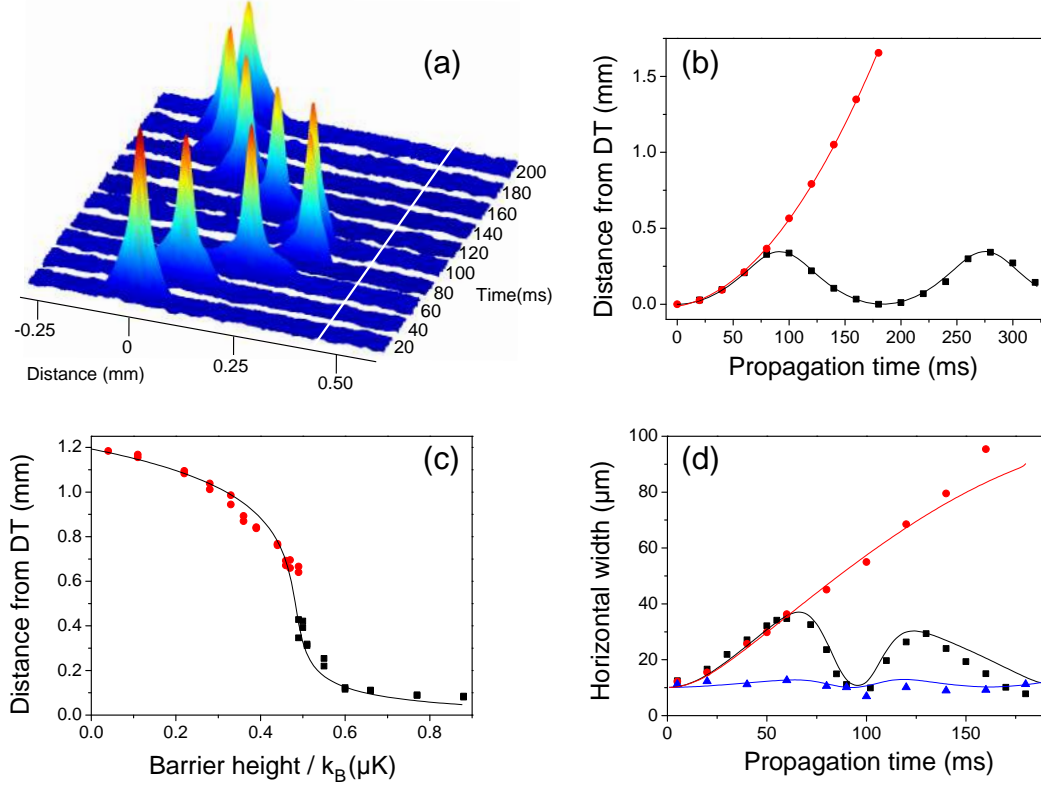
Figure 4.8: Classical reflection from broad potential barrier. (a) Density profiles of a bright solitary wave reflected from a broad repulsive barrier with its position marked by the solid white line. (b) The centre of mass position of the solitary wave after it is released into the waveguide, in presence (black square) and absence (red circle) of the barrier. (c) The centre of mass position of the solitary wave 150 ms after it is released into the waveguide, as a function of the barrier height. Red circle (black square) indicates full transmission (reflection). (d) The root mean square width of the condensate as it propagates in the waveguide. Red circles: a repulsive BEC ($a_s = 58\,a_0$, $N = 3.5 \times 10^3$) in absence of the barrier. Black square: a repulsive BEC in presence of the barrier. Blue triangles: a bright solitary wave ($a_s = -11\,a_0$, $N = 2.0 \times 10^3$). The solid lines in (b), (c), and (d) are theoretical curves described in ref. [44]. Figures taken from ref. [44].

strong compression as it goes against the barrier.

4.4   Summary

We have demonstrated that efficient evaporation of ^{85}Rb can be achieved by tuning the scattering properties in the vicinity of a Feshbach resonance. Through this, a tunable ^{85}Rb BEC with $N = 4 \times 10^4$ atoms is formed from direct evaporative cooling in an optical crossed dipole trap. After the transfer into the waveguide, the expansion of the propagating condensate ceases as the scattering length decreases. At $a_s = -11\,a_0$ and $N = 2 \times 10^3$, the matter-wave propagates over 1 mm without dispersion and the bright solitary wave is formed. The particle-like behaviour of the bright soliton is shown through a classical collision with a broad repulsive barrier. This is an important stepping stone towards the probing of macroscopic quantum mechanical behaviour through scattering the bright solitons from narrow potentials.

Chapter 5

Quantum reflection from a narrow attractive potential

5.1 Introduction

Previously, we demonstrated the creation of bright solitary waves by tuning the interatomic interaction of the ^{85}Rb BEC in an optical waveguide using a Feshbach resonance. The matter-wave, observed to remain undispersed after propagation for over $1\,\text{mm}$, showed robust classical reflection from a broad repulsive barrier. The next objective is to probe quantum effects with the mesoscopic wave packets. While one of the main goals of the experiment is to explore atom-surface interactions using bright solitary waves incident on the Dove prism, it is extremely challenging to achieve with the experimental setup. Currently, the solitary wave is released from the dipole trap $\sim 6\,\text{mm}$ from the prism surface. This is beyond the maximum observed propagation distance ($\sim 1.5\,\text{mm}$) from which the atomic cloud remains soliton-like. An upgrade to the apparatus is hence required to realise such experiments, which will be discussed in detail in Chapter 6.

In the present chapter, we focus on the realisation of quantum reflection of bright solitary waves from a narrow optical potential *well*. Contrasting to a repulsive barrier where both classical and quantum reflection and transmission are possible [44, 69], reflection from a static potential well is a distinctive quantum behaviour. Depending on the probed parameter regime, theoretical
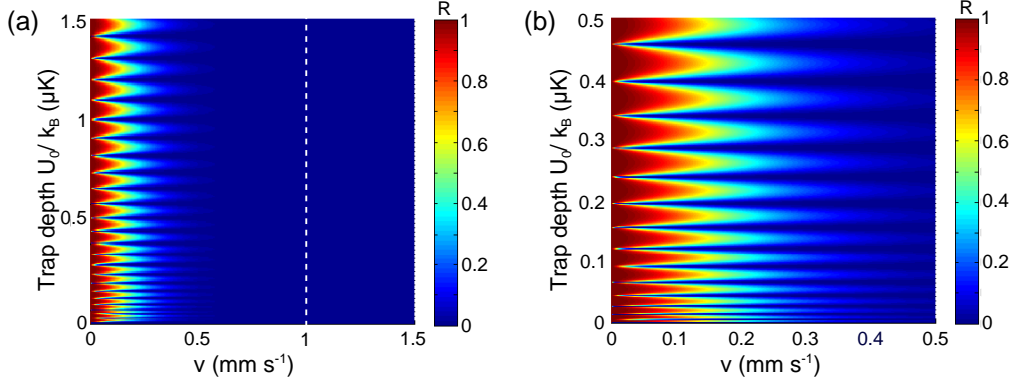
Figure 5.1: Theoretical prediction of quantum reflection from the narrow potential well. (a) Plot of the reflection coefficient R of a single particle from the Rosen-Morse potential, defined in Eq. 5.3. Here, $d = (1.9/1.66)\,\mu\text{m} = 1.14\,\mu\text{m}$. The dashed line indicates the velocity of the solitary wave in our measurements. (b) Zoomed-in version of (a).

studies have demonstrated that such a system exhibits significant quantum reflection for low energy solitons [74]. Significant resonant trapping is also predicted when the attractive potential is capable of supporting a number of bound states [75]. In the following, we will discuss the generation of the narrow attractive potential, followed by the measurements and the analysis of the results obtained from our system.

5.2 Narrow attractive Gaussian potential

We refer to the detailed theoretical analysis and calculation by Wiles [69] on the requirement of the apparatus in order to observe quantum reflection of the bright solitary wave from a potential well. In brief, let us consider a simplified picture where we approximate the solitary wave with a single particle. After release, this particle propagates along the x-direction towards a potential well with a Gaussian form

$$V_{\text{G}}(x) = -U_0 \exp\left[-\frac{2x^2}{w_x^2}\right], \tag{5.1}$$

where $U_0 > 0$ denotes the trap depth and w_x is the tightly focussed waist. It is calculated that, for observable quantum reflection, one requires $w_x \lesssim 2\,\mu\text{m}$ and a *low* solitary wave velocity [69]. This velocity requirement can be evaluated by first considering an incoming plane wave incident on a potential

$$V(x) = -U_0 \text{sech}^2 \left(\frac{x}{d} \right), \tag{5.2}$$

which is known as the Rosen-Morse potential. This potential $V(x)$ approximates $V_G(x)$ when setting $d = w_x/1.66$, and it has an exact expression for the reflection coefficient of a single atom with mass m and kinetic energy E_k [165]

$$R = \frac{\cos^2 \left(\frac{\pi}{2} \sqrt{1 + 8mU_0 d^2/\hbar^2} \right)}{\sinh^2(\pi k d) + \cos^2 \left(\frac{\pi}{2} \sqrt{1 + 8mU_0 d^2/\hbar^2} \right)}, \tag{5.3}$$

where

$$k = \sqrt{\frac{2mE_k}{\hbar^2}} = \frac{mv}{\hbar}. \tag{5.4}$$

This approximation, plotted in Fig. 5.1(a) (with a close-up in Fig. 5.1(b)), shows that for $w_x = 1.9 \ \mu$m, a small incoming velocity ($\lesssim 0.5 \, \text{mm s}^{-1}$) is needed to observe any reflection from an incoming plane wave, regardless of the trap depth. In particular, one requires $v \lesssim 0.4 \, \text{mm s}^{-1}$ for $> 10\%$ reflection, while $v \lesssim 0.2 \, \text{mm s}^{-1}$ is required for $> 50\%$ reflection to be observed. An additional optical system for the narrow potential, as well as a mechanism for velocity control, are thus necessary.

5.2.1 Optical setup

To generate a narrow potential, we design an optical system such that the resulting beam profile is a form of light sheet. Such an optical system is tailored to produce a desired focus of $\lesssim 2 \, \mu$m. That is, one requires the diffraction limit of the system, defined by the airy radius r_{Airy}, to satisfy

$$r_{\text{Airy}} = 1.22 \frac{\lambda f}{D} \lesssim 2 \, \mu\text{m}, \tag{5.5}$$

where D is the diameter of the optical aperture [166]. While it is clear that one desires a short f with a large lens diameter, the spatial limitation of the experimental apparatus restricts the choice of the optics. With atoms positioned 12 mm from the glass surface, the lower limit of the focal length
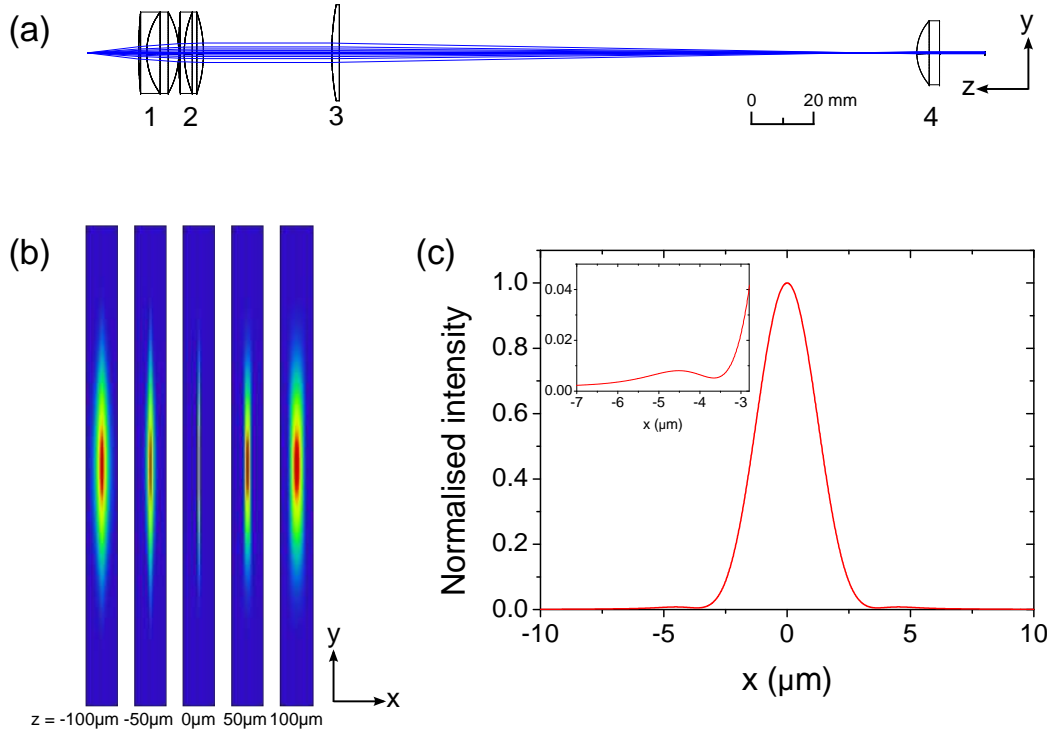
Figure 5.2: Narrow Gaussian potential beam modelling using *Zemax*. (a) Geometric ray tracing shows how the beam propagates to form the elongated direction of the potential. The diagram is to scale. The details of the lenses are listed in Table 5.1. (b) Simulation of the beam propagation via Physical Optics Propagation (POP) on *Zemax*. $z = 0 \, \mu$m indicates the position of the tightly focussed waist. The beam radii in x-direction $w_x(z)$ are (from left to right): $14 \, \mu$m, $7.4 \, \mu$m, $1.9 \, \mu$m, $7.4 \, \mu$m, and $14 \, \mu$m. The dimensions of the images are: height $= 1.26$ mm, width $= 0.06$ mm. (c) Cross-sectional cut of the tightly focussed beam waist. Inset shows a close-up of the first subsidiary intensity maxima of the diffraction pattern.

Number	Lens	Maker	f (mm)	Glass type(s)
1	AC254-040-B	Thorlabs	40	N-SH6HT, N-BAF10
2	AC254-060-B	Thorlabs	60	N-SF6HT, N-LAK22
3	160-YD-25	Comar	160	N-BK7
4	AL2018-B	Thorlabs	18	S-LAH64

Table 5.1: Lenses in the attractive potential system, which are ordered and numbered according to Figure 5.2(a). Note that lens 3 is a cylindrical lens.

f of the last optic is fixed. With the limits set by Eq. 5.5, one requires the numerical aperture (NA), defined as $NA = \eta \sin(\arctan(2f/D))$,[1] to satisfy $NA > 0.25$. While high NA is commonly achieved using microscope objectives or complex multi-element lenses in atomic experiments [167–169], they are ruled out due to their short focal lengths and spatial requirements. To produce a beam with the required waist size, we use a series of spatially separated lenses, which are carefully chosen and modelled using the optical design program *Zemax*.

The optical system comprises of 4 optics is shown in the ray diagram in Fig. 5.2(a) with the optics listed in Table 5.1. Here, we use the light derived from a homebuilt $\lambda = 852\,\text{nm}$ diode laser. It is delivered to the main experimental setup using a single mode optical fibre, while an AOM is employed for power control. As illustrated in Fig. 5.2(a), the fast diverging beam from the fibre output is collimated by a pair of achromatic doublets with focal lengths $f = 40\,\text{mm}$ (lens 1) and $f = 60\,\text{mm}$ (lens 2) to a $1/e^2$ radius of $\sim 2.3\,\text{mm}$. It then passes through a cylindrical lens with $f = 160\,\text{mm}$ (lens 3), which focusses the beam along the y-axis while keeping the x radius constant. The now elongated beam is focussed by a high NA aspheric lens ($NA = 0.488$) with $f = 18\,\text{mm}$ (lens 4) to form a light sheet. In the *Zemax* simulation, the distance between the last surface of lens 3 and first surface of lens 4 is set to 180 mm. This is chosen such that the beam appears to be collimated in the y-direction after the last lens. Using the rearranged equation of the Gaussian beam propagation, $w_x(z) = w_x(0)\sqrt{1 + (z/z_R)^2}$, with the assumption that the Rayleigh range $z_R \gg f$, we estimate that the expected waist size along the x-direction is

---

[1] η is the refractive index of the medium. Here, we assume the propagation of the light field is in air, thus we set $\eta = 1$.

$$w_x(0) \approx \frac{\lambda f}{\pi w_x(f)} = 2.1 \, \mu\text{m}, \tag{5.6}$$

where $w_x(z)$ denotes the x beam radius at a position along z, with the focus at $z = 0$. The calculated diffraction limit using Equation 5.5 is $0.94 \, \mu\text{m}$ which satisfies the requirement of $r_{\text{Airy}} \lesssim 2 \, \mu\text{m}$.[2] Since we will only refer to the beam size at $z = 0$ for the rest of the chapter, we will use the simplified notation of $w_x \equiv w_x(0)$ and $w_y \equiv w_y(0)$.

A direct measurement has been attempted to measure the beam dimensions of the complete optical setup using existing measurement apparatus, which includes a knife-edge mounted on a translation stage driven by a differential actuator with a smallest graduation of $0.5 \, \mu\text{m}$ (Thorlabs DM22). This has proved to be problematic due to the large aspect ratio of the beam radii of the two axes, as even a slight tilt of the light sheet relative to the knife-edge would lead to an invalid beam size measurement. A full characterisation of the narrow potential is accomplished by the use of the trapped atoms at the potential which will be discussed in Section 5.2.3. Nevertheless, calculating using Zemax's Physical Optics Propagation (POP) function[3], one can visualise the beam propagation as shown in Fig. 5.2(b). The calculation shows that the optical system yields an elongated potential with beam radii $(w_x, w_y) = (1.9 \, \mu\text{m}, 280 \, \mu\text{m})$, which is within the desired range of $\lesssim 2 \, \mu\text{m}$ along the x-direction. A cross-sectional cut of the beam profile w_x is shown in Fig. 5.2(c). Notice that there exist weak diffraction patterns on both sides of the tight focus. Despite a peak intensity of 0.8% of that of the central peak, these subsidiary maxima play a significant role in the reflection probability from the potential well. This will be discussed in depth in Section 5.6.

5.2.2 Alignment

The narrow potential beam formed by the optical system described in Section 5.2.1 enters the science cell vertically from above, as illustrated in Fig. 5.3(a). With a tight focus of $w_x = 1.9 \, \mu\text{m}$, which translates to Rayleigh

---

[2]The diameter of lens 4 is $20 \, \text{mm}$.

[3]In contrast to geometric ray tracing, POP considers a coherent light with diffractions from all surfaces along its propagation path taken into account.
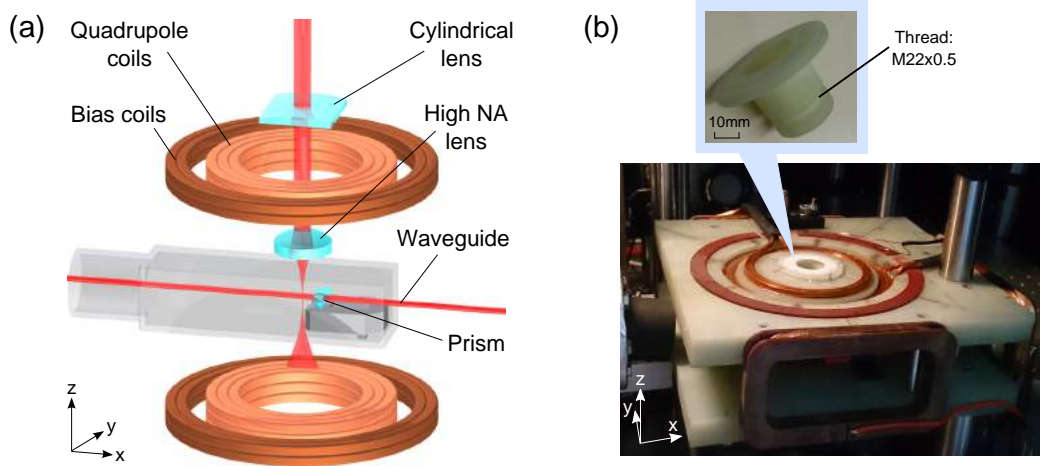
Figure 5.3: Optical setup of the narrow attractive potential. (a) The experimental setup. Atoms are cooled in the crossed dipole trap (not shown), and then transferred into the optical waveguide. Additional axial confinement is provided by the magnetic quadrupole and bias fields. The beam of the narrow attractive potential enters the science cell from above, with the tightly focussed waist w_x intersecting with the waveguide. While not shown in the diagram, a steering mirror is located between the cylindrical lens and the second collimation lens for transverse beam alignment. (b) The adjustable mount for the high NA aspheric lens. The inset shows the lens mount made from TUFNOL epoxy glass fabric laminates grade G10. With the lens glued on to the bottom of the mount, the M22 × 0.5 (in mm) thread (equivalent to $1.4\,\mu\mathrm{m\,deg^{-1}}$) allows us to accurately adjust the z position of the tightly focussed waist. The mount, which has a clear aperture of (diameter) 18 mm, is mounted in the aperture of the coil mount above the science cell.

range $z_\mathrm{R} = \pi w_x^2 / \lambda = 13\,\mu\mathrm{m}$, the beam diverges rapidly away from the waist, as shown from the simulation in Fig. 5.2(b). Hence one requires a mechanism to adjust the z position of the waist precisely for vertical beam alignment. This is achieved by mounting lens 4 on a threaded lens mount with a pitch of $1.4\,\mu\mathrm{m}\,\mathrm{deg}^{-1}$ which is shown in Fig. 5.3(b). By turning the mount, the waist position is displaced vertically while the waist size remains constant as the beam is collimated along the x-direction before lens 4.

The alignment of the narrow attractive potential involves three stages: the initial alignment, horizontal alignment, and vertical alignment.

Initial alignment:

We follow the procedure outlined in [69] (Section 7.4.2). In brief, one first centres the probe beam for vertical imaging[4] on the atoms at the crossed dipole trap. The probe beam then functions as a reference for the narrow potential beam to overlap. This guarantees the beam is located closed to the crossed dipole trap.

Horizontal alignment:

After the initial alignment, one aligns the x position of the beam using trapped atoms in the waveguide. At the intersection of the narrow attractive potential and the waveguide, the resulting trap depth is the sum of the two potentials, i.e. atoms will see a sudden dip in the potential. Thus the alignment is carried out by looking for a disruption of atom density along an elongated atomic cloud. Such a cloud is created by magnetically confining the thermal atoms along the waveguide with a combination of magnetic quadrupole field B_z' and the magnetic bias field. Such a magnetic harmonic potential dominates the weak optical axial trapping ($< 0.1\,\mathrm{Hz}$) and has a trap frequency defined by Eq. 3.8. Whilst the exact levitation gradient is used during the alignment, different bias fields have been employed for different desired spatial extent of the elongated cloud. During the atom expansion in the waveguide, the potential well remains constant at maximum beam

---

[4]Despite having a focussed vertical imaging system as outlined in ref. [69], the images are disrupted by harsh fringes possibly due to the extra sensitivity of vibrations when using a high NA imaging lens. The vertical imaging system hence is not used for measurements beyond the alignment stage.
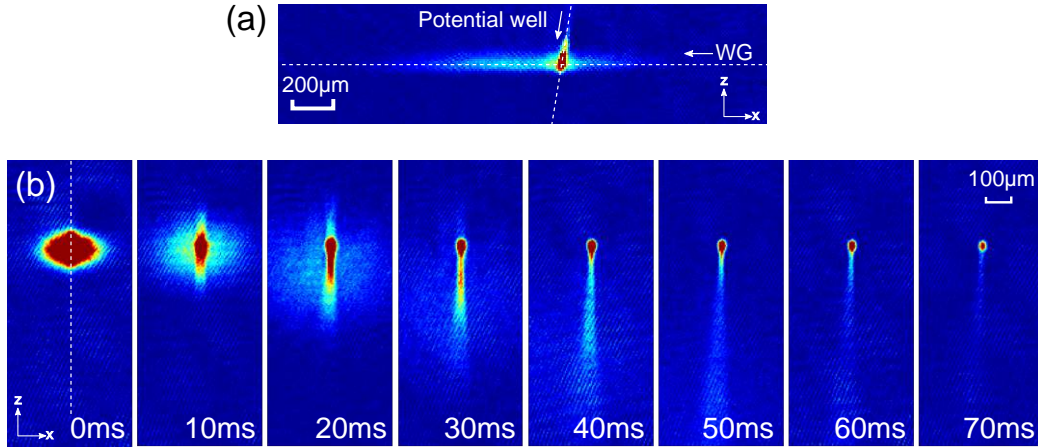
Figure 5.4: The alignment of the narrow potential. The beam is in a form of a light
sheet, with its larger waist along the direction of the imaging probe beam.
(a) Alignment of the horizontal position. The presence of the potential well
causes a disruption in a cigar-shaped atomic cloud in the waveguide, confined
axially with the magnetic harmonic potential. Note in this snapshot that
the beam of the potential well is tilted. (b) Atom trapping in the narrow
potential at different time instances after the crossed dipole trap is switched
off. The position of the trapped atoms in the final image indicates the
position of the waist.

power. Fig. 5.4(a) shows an example where the narrow potential is located.
By adjusting the steering mirror between lens 2 and lens 3, one can thus
optimise the horizontal position of the potential with the trapped atoms.

Vertical alignment:

Precise vertical alignment requires trapping atoms in the narrow potential
well only. Given that the expected tightly focussed waist is $w_x = 1.9\,\mu$m
(and $w_y \sim 280\,\mu$m), the calculated trap depth and trap frequency along the
z-direction *with levitation* are $2.1\,\mu$K and $2\pi \times 170$ Hz respectively at a beam
power of 3.87 mW. Hence the potential well should suffice to trap and hold
atoms with a temperature of $\lesssim 200$ nK [138]. The atom loading is carried
out by first overlapping the x position of the potential well with the crossed
dipole trap. The magnetic quadrupole gradient is set to just under levitation
at 20.8 G cm^{-1}. After evaporatively cooling the atoms in the pure crossed
dipole trap to $T \sim 100$ nK, the potential well is switched on at 3.87 mW. At
the end of the evaporation, atoms are held in the 3-beam trap for 100 ms
before the dipole beams are switched off. Fig. 5.4(b) shows a sequence of
images of different time instances after the switching off of the crossed dipole
trap. While the hottest atoms in the single beam trap escape from the waist
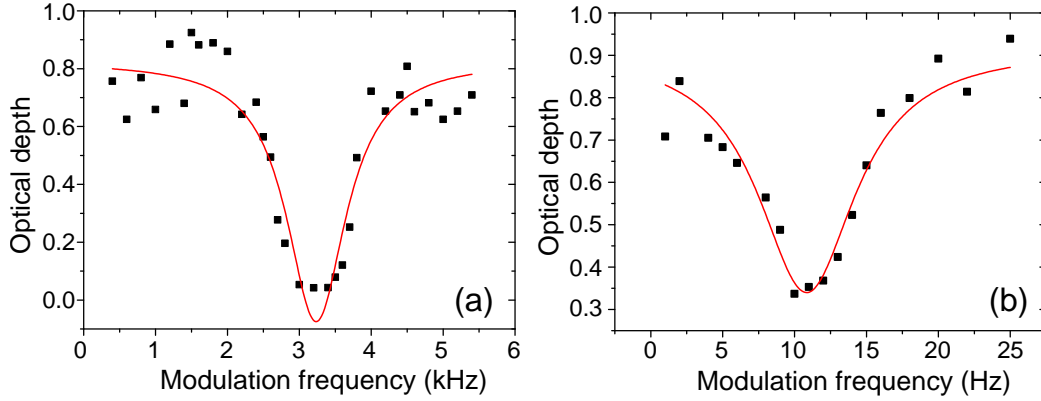
Figure 5.5: Trap characterisation using parametric heating. Measurements are carried out at a beam power of 3.87 mW. A Lorentzian line shape is fitted to the first harmonic resonance feature corresponding to (a) w_x and (b) w_y.

under gravity, the atoms soon equilibrate with the single beam trap where atoms can be held in such trap for over 1 s. One can thus use the trapped atoms to align the vertical position of the waist by adjusting the lens mount.

The potential well is aligned such that the waist w_x intersects the waveguide at 160 μm from the crossed dipole trap.

5.2.3   Trap characterisation

Using the atoms trapped in the narrow potential well, one can extract information about the trap such as the trap frequency and the trap depth. There are two methods used in this thesis to measure the former: 1. by displacing the atomic sample from the centre of the harmonic potential and record the oscillatory motion of the centre of mass of the cloud after it is released, and 2. via parametric heating [94]. Here the trap frequencies are measured by the second method. Adding modulation to the laser beam power can result a driven oscillator where energy is efficiently injected into the trapped atoms. This increases the temperature of the atoms and eventually leads to atom loss from a trap with a finite trap depth. This resonance feature is most noticeable at the first harmonic (twice the trap frequency) and it can be used to verify the beam waist.

The oscillation frequencies of the potential well ω_x and ω_y are related to the optical trap depth U_0 and the $1/e^2$ beam radii (w_x and w_y) by

$$\omega_x = \left(\frac{4U_0}{mw_x^2}\right)^{1/2} \quad \text{and} \quad \omega_y = \left(\frac{4U_0}{mw_y^2}\right)^{1/2} \tag{5.7}$$

using the harmonic approximation [94]. By substituting the expressions for the peak intensity (Eq. 3.6) and the trap depth (Eq. 3.5) of a Gaussian beam into Eq. 5.7, we obtain

$$w_x = \left(\frac{\omega_y}{\omega_x^3}\gamma P\right)^{1/4} \quad \text{and} \quad w_y = \left(\frac{\omega_x}{\omega_y^3}\gamma P\right)^{1/4}, \tag{5.8}$$

where $\gamma = \frac{8\alpha}{\pi m} = 1.02 \times 10^{-10}\,\mathrm{m^4\,J^{-4}\,s^{-4}}$ for ^{85}Rb atoms at $\lambda = 852\,\mathrm{nm}$. Using this relation, we can compute the beam radii from the trap frequencies in both radial directions of the Gaussian beam at a particular beam power.

To perform parametric heating, we use an identical experimental sequence used for z alignment of the potential well described in Section 5.2.2. Holding the atoms at the tightly focussed waist at $3.87\,\mathrm{mW}$ for $1\,\mathrm{s}$ after the switching off of the dipole trap, a sine-wave modulation is then applied to the beam power for $1\,\mathrm{s}$. The results are shown in Fig. 5.5, where the trap frequencies are measured to be $\omega_x = 2\pi \times 1.62(13)\,\mathrm{kHz}$ and $\omega_y = 2\pi \times 5.4(5)\,\mathrm{Hz}$. Using Eq. 5.8, the beam radii at $z = 0$ are calculated to be $w_x = 1.9(2)\,\mu\mathrm{m}$ and $w_y = 570(40)\,\mu\mathrm{m}$. Note while w_x is in excellent agreement with the simulated value in *Zemax*, w_y appears to be about twice of the estimated value. One plausible explanation is that the distance between lens 3 and lens 4 is different from the simulation after the z alignment of the potential well. In contrast to the x-direction, the beam size increases in the y-direction further along the beam path away from the focus of lens 3. Nevertheless, with a waist $w_x = 1.9(2)\,\mu\mathrm{m}$, we are in a good position to proceed to realising quantum reflection of a bright solitary wave.

5.3 Velocity control

The scattering of a bright solitary wave from a repulsive [51, 77] or attractive potential [75] is predicted to vary with the energy relationship between the solitary wave and the potential barrier/ well. In the case of a narrow
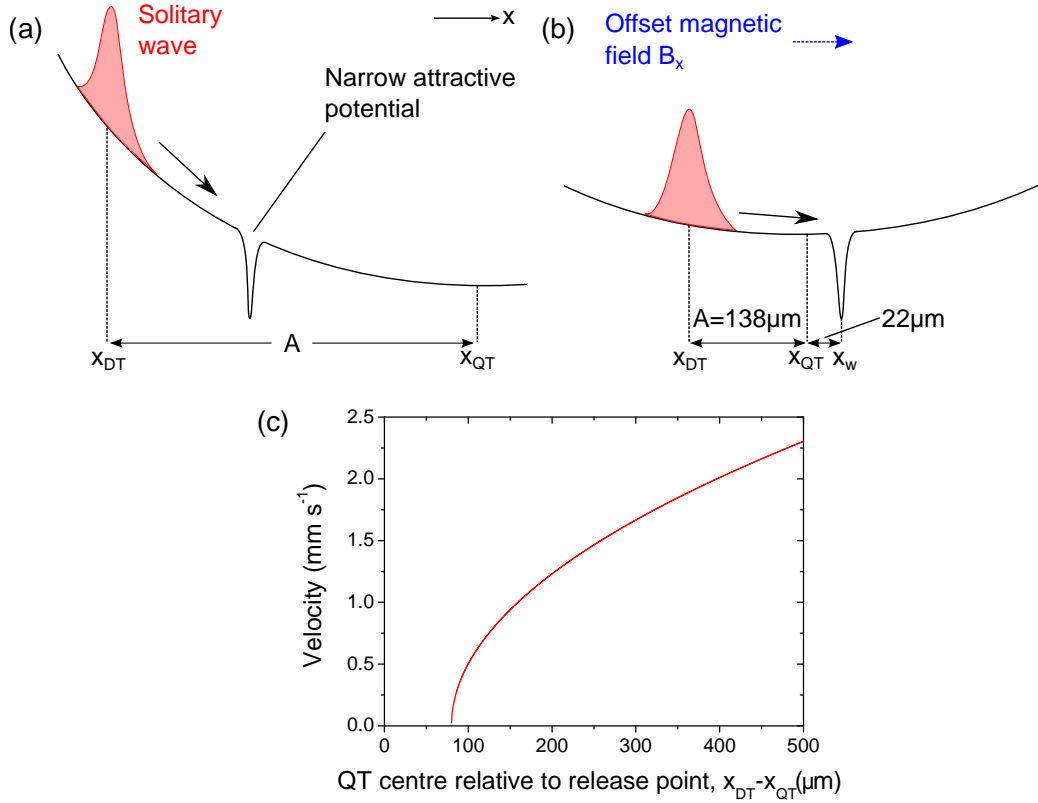
Figure 5.6: Velocity control of solitary wave. Here the distance between the solitary wave and the narrow potential well is fixed. A shows the oscillation amplitude of the solitary wave. (a) No offset magnetic field. (b) With offset magnetic field B_x. It shifts the quadrupole trap centre x_{QT} towards the starting position of the solitary wave x_{DT}. The position of the narrow attractive potential is marked as x_w. (c) The velocity of the solitary wave at the position of the potential well x_w as a function of the distance between the quadrupole trap (QT) centre x_{QT} and the release point x_{DT}. The distance $x_w - x_{DT}$ is fixed at $160\,\mu$m.

attractive potential, the probability of observing quantum reflection is enhanced if the incoming solitary wave is sufficiently *slow* [74]. In particular, it is calculated in Section 5.2 that observable quantum reflection ($\gtrsim 10\%$) in the current setup only arises for velocity $\lesssim 0.4\,\mathrm{mm\,s^{-1}}$. It is thus essential to have control over the velocity of the solitary wave, in addition to the well depth, which is controlled by changing the laser power with the AOM.

The propagation of the solitary wave along the waveguide is due to a weak harmonic potential produced by the combination of the magnetic quadrupole field gradient B'_z and the magnetic bias field B, as seen in Eq. 3.8. As illustrated in Fig. 5.6(a), upon release, the solitary wave undergoes harmonic oscillation, and the maximum velocity v_{max} (at the bottom of the magnetic potential) is related to the oscillation amplitude A by $v_{\mathrm{max}} = A\omega_{\mathrm{axial}}$. Assuming no energy loss in the system, the amplitude A is the distance between the release point x_{DT} and the centre of the quadrupole trap x_{QT}. By denoting x_{w} as the position of the narrow potential well, the velocity of the solitary wave at the position of the narrow potential is [68]

$$v = -\omega_{\mathrm{axial}}(x_{\mathrm{DT}} - x_{\mathrm{QT}})\sqrt{1 - \left(\frac{x_{\mathrm{w}} - x_{\mathrm{QT}}}{x_{\mathrm{DT}} - x_{\mathrm{QT}}}\right)^2}. \tag{5.9}$$

Hence, the velocity v can be controlled by shifting the position of the magnetic potential centre. For low velocity, one needs to shift the magnetic potential centre from the original position ($\sim 2.6\,\mathrm{mm}$ away from the dipole trap where the solitary wave is released) to a position close to the dipole trap, as illustrated in Fig. 5.6(b). Such a shift can be achieved by applying an offset magnetic bias field B_x along the x-direction, where the displacement of the trap centre is given by ref. [129]

$$\Delta x = \frac{2B_x}{B'_z}. \tag{5.10}$$

In the following experiment, we position the narrow potential well at $x_{\mathrm{w}} - x_{\mathrm{DT}} = 160\,\mu\mathrm{m}$ from the crossed dipole trap where the solitary wave is released. As illustrated in Fig. 5.6(b), the axial waveguide potential is at $138\,\mu\mathrm{m}$ from the crossed dipole trap and $22\,\mu\mathrm{m}$ from the narrow attractive potential, resulting in an incident velocity at the potential well of $\sim 1\,\mathrm{mm\,s^{-1}}$.
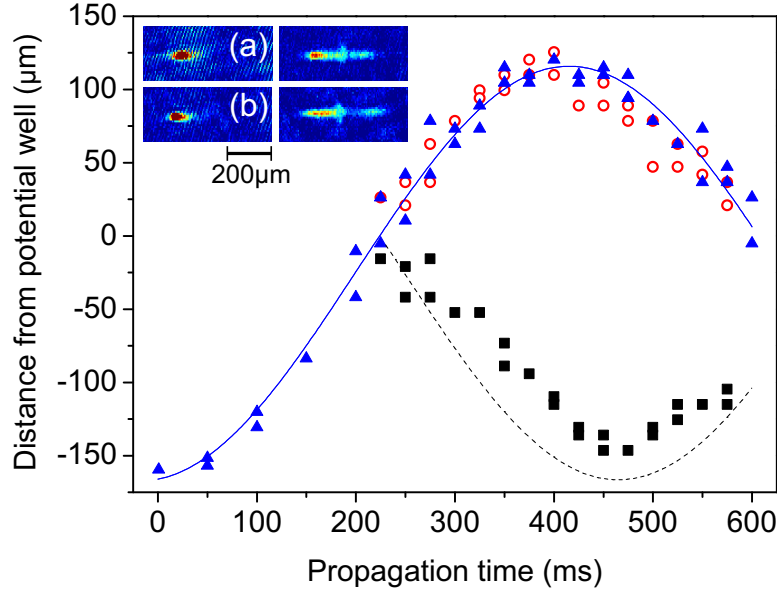
Figure 5.7: Quantum reflection of the bright solitary wave from the narrow Gaussian potential. The position of the solitary wave, relative to the potential well, is plotted as a function of propagation time. In the absence of the well (blue triangles) the atoms undergo harmonic motion in the waveguide (theoretical trajectory indicated by solid line). In the presence of the well the solitary wave splits, with atoms being both transmitted (red circles) and reflected (black squares) from the attractive potential. The black dashed curve shows the theoretical trajectory of an elastic collision. Inset: False colour images taken at (a) 375 ms and (b) 475 ms with the narrow attractive potential present (right) and absent (left).

Note that it is larger than the desired velocity of $\lesssim 0.4\,\mathrm{mm\,s^{-1}}$. Whilst this method of velocity control is capable of reducing the velocity $v < 1\,\mathrm{mm\,s^{-1}}$, as shown in Fig. 5.6(c), the velocity dependence on oscillation amplitude means that the motion of the solitary wave is difficult to resolve with our horizontal imaging, which has a pixel size of $5.2\,\mu\mathrm{m}$.

5.4   Quantum reflection of the matter-wave

In the preparation of the bright solitary wave, we proceed with a similar method described in Chapter 4. In order to load the ^{85}Rb BEC with $N \sim 6 \times 10^3$ from the crossed dipole trap into the optical waveguide, we first ramp the scattering length to a small and positive value, $\sim 5a_0$ in 50 ms. This is followed by simultaneously ramping the crossed dipole beams off and the waveguide beam on in 250 ms. At the same time, the magnetic quadrupole

field gradient is ramped up to exactly levitate the atoms, while the magnetic bias field is ramped to give an s-wave scattering length of $a_s = -7\,a_0$. This value of a_s is chosen such that the condensate dispersion is balanced by the attractive interatomic interactions, thereby creating bright solitary waves. The offset magnetic field is also switched on at this stage to displace the magnetic trap centre along the x-direction. The resulting background potential has trap frequencies of $\omega_{x,y,z} = 2\pi \times [1.15(5), 18.2(5), 18.2(5)]\,\mathrm{Hz}$.

With the measured beam sizes obtained from parametric heating described in Section 5.2.3, one can calculate the exact trap depth of the narrow attractive potential. In our initial experiment, the potential well depth is set to $1\,\mu\mathrm{K} \times k_\mathrm{B}$, which is switched on at the beginning of the waveguide loading procedure described above. After the release of the solitary wave into the waveguide, its position is tracked by imaging multiple instances of the same experimental sequence at different times. Once the solitary wave reaches the well at $\sim 200\,\mathrm{ms}$, we observe a splitting of the wavepacket and identify three distinct resulting fragments: atoms transmitted, reflected, and confined at the potential well. The centre of mass positions of both the transmitted and reflected atomic clouds are tracked and plotted in Fig. 5.7. The majority of atoms in the solitary wave are transmitted (red circles), following the same trajectory as in the freely propagating case (blue triangles), undergoing harmonic motion in the waveguide (solid line). Around 25% of the atoms are reflected from the narrow attractive potential and propagate in the opposite direction to the transmitted component (the method of obtaining the number in each cloud will be explained in Section 5.5). It is observed that the turning point of the reflected atoms occurs $\sim 50\,\mathrm{ms}$ later than for the transmitted atoms. This is due to the $22\,\mu\mathrm{m}$ displacement of the well position from the centre of the oscillation. By comparing the measured trajectory of the reflected fragment with that of an elastic collision (black dashed curve on Fig. 5.7), we note that the turning point is $\sim 20\,\mu\mathrm{m}$ short of the release position. This suggests that some energy is dissipated during the splitting process. The remaining atoms, which account for $\lesssim 10\%$ of the total atom number, are confined close to the attractive potential.

5.5 Well depth dependence of the quantum reflection probability

To explore the effect of the potential well depth relative to the energy of the incoming solitary wave, we vary the beam power of the potential well whilst keeping all other parameters constant. The solitary wave is split and the resulting fragments are allowed to spatially separate before imaging. This corresponds to 475 ms of propagation time from the point of release. To calculate the reflection probability, three fixed regions of the absorption images are defined: transmitted (T), confined (C), and reflected (R) as shown in the inset of Fig. 5.8 (a). The number of atoms associated to T, C, or R is measured by taking the sum of the pixel values in each of these regions. Using these values, we define the reflection probability as $R/(R + C + T) \times 100\%$, while the values for the transmitted and confined parts are calculated in the same way.

We find there is no observable reflection from the narrow potential well for trap depths $< 100\,\mathrm{nK} \times k_{\mathrm{B}}$. Above this threshold, we see that the probability of reflection increases sharply (Fig. 5.8 (a)), and correspondingly the number of atoms transmitted drops (Fig. 5.8 (b)). For a trap depth of $1\,\mu\mathrm{K} \times k_{\mathrm{B}}$, we observe a reflection of $\sim 25\%$. We also note that the number of atoms confined at the position of the well increases with increasing well depth, as shown in Fig. 5.8 (c).

In these splitting experiments we observe the width of the transmitted and the reflected clouds to be larger than the original solitary wave. This result is, at least qualitatively, in agreement with the theoretical description of a solitary wave in a quasi-1D geometry [25]. For the original solitary wave with the parameters presented in Section 5.4, the spatial extent of the soliton, defined by Eq. 2.17, is calculated to be $l_s \approx 3\,\mu\mathrm{m}$. Hence, theoretically, the reflected fragment from the potential well with depth $1\,\mu\mathrm{K} \times k_B$, which accounts for $\sim 0.25N$ atoms, should acquire 4 times the size of the original solitary wave. However, limited by the resolution of our imaging system and the distance by which the resulting clouds can be spatially separated, we are unable to reliably fit a Gaussian line shape to the images and thus we are
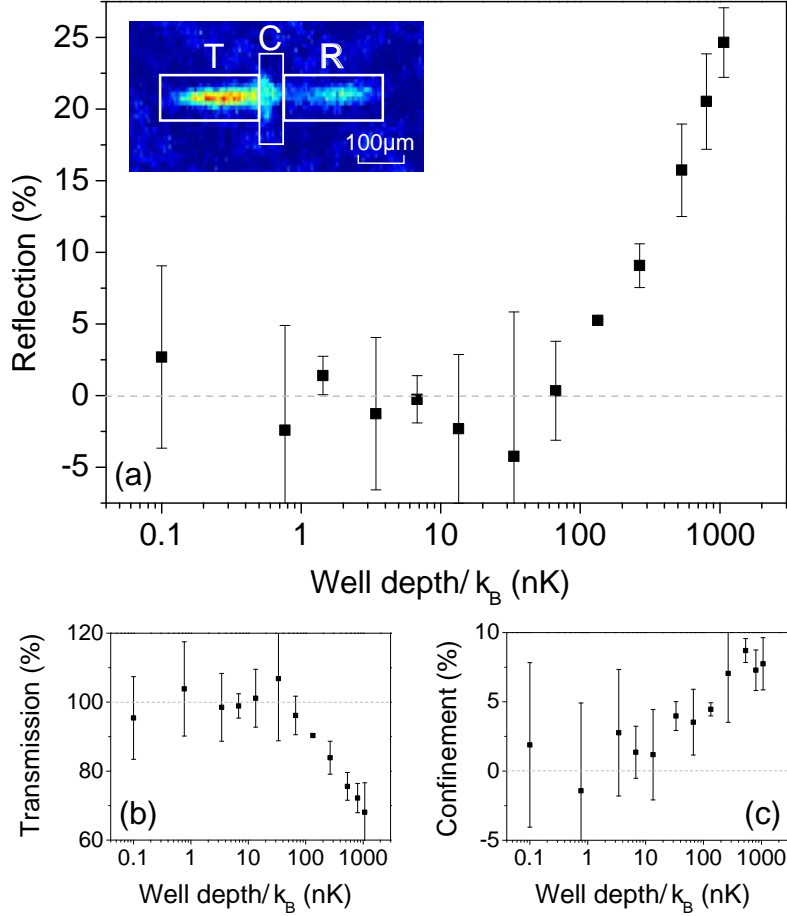
Figure 5.8: Energy dependence of the quantum reflection probability. (a) Percentage of incoming atoms reflected as a function of well depth. Atoms reach the well with a velocity of $1\,\mathrm{mm\,s^{-1}}$. Below a well depth of $\sim 100\,\mathrm{nK} \times k_B$ no appreciable reflection is observed. Inset: Reflection percentage is expressed as the number of atoms in the region labelled 'R' as a percentage of the total atom number calculated for the three boxed regions shown. These regions correspond to atoms being classified as transmitted (T), confined (C) or reflected (R) from the well. The percentage of atoms (b) transmitted and (c) confined is calculated in a similar way. The negative data points in (a) and (c) are manifested from the subtraction of the background noise from the absorption image.
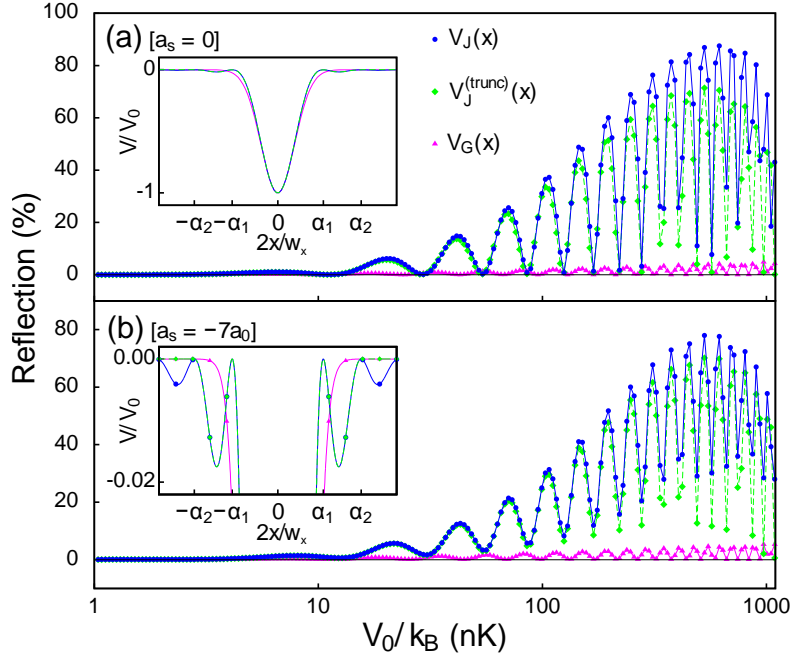
Figure 5.9: Reflection coefficients as a function of potential well depth for (a) non-interacting wavepackets and (b) bright solitary waves in a simplified 1D model of the experiment. Results are shown for an ideal Gaussian potential well possessing a single potential minimum [$V_G(x)$], and for diffraction pattern [$V_J(x)$] and truncated diffraction pattern [$V_J^{(\mathrm{trunc})}(x)$] potentials which possess subsidiary minima. Insets show the form of the potentials; see text for details.

unable to report a quantitative figure for the increase in width.

5.6   Discussion

We recall that the velocity of the solitary wave is higher than the desired value of $v \lesssim 0.4\,\mathrm{mm\,s^{-1}}$. With a higher momentum, the measured reflection fraction of $\sim 25\%$ somewhat contradicts the theoretical prediction. We address this discrepancy by examining the effect of the structure of the potential well on the quantum reflection probability.

We first confirm the lack of substantial reflection from the narrow Gaussian potential $V_G(x)$ (Eq. 5.1) by numerical simulations of the 1D GPE (see the lower curves in Fig. 5.9). In these simulations,[5] we use a simplified model

---

[5]The numerical simulations of the 1D GPE are courtesy of the theory group of the Joint Quantum Centre (JQC), Durham-Newcastle.
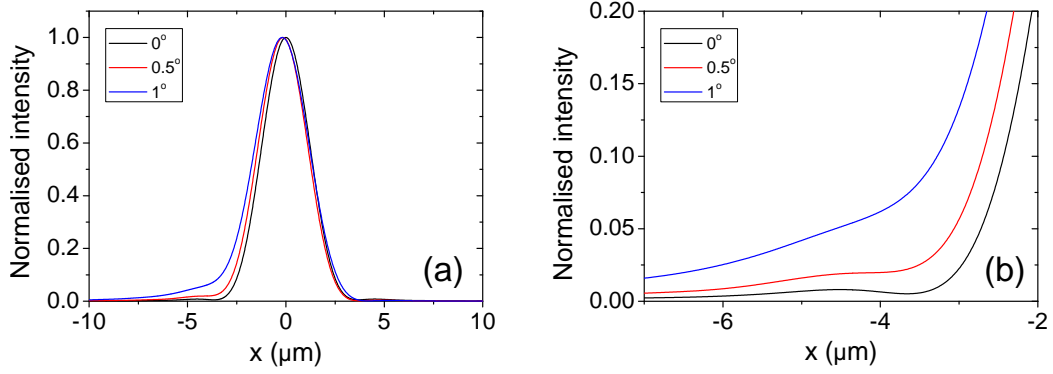
Figure 5.10: Effect of the tilt of the beam on the structure of the potential well. (a) *Zemax* simulation of the beam profile at the tightly focussed waist with small deviation angles of the beam from the normal of lens 4. (b) Zoomed-in version of (a).

of the experiment as follows, which consists of a quasi-1D GPE similar to Eq. 2.14

$$i\hbar\frac{\partial\psi(x,t)}{\partial t} = \left[-\frac{\hbar^2}{2m}\frac{\partial^2}{\partial x^2} + V(x) + U(x,t) + g_{1D}N|\psi(x,t)|^2\right]\psi(x,t), \quad (5.11)$$

where $U(x,t)$ represents the time-dependent background potential. We model the latter as

$$U(x,t) = \frac{1}{2}m\left[\omega_{x_{DT}}(t)^2(x - x_{DT})^2 + \omega_{x_{QT}}(t)^2(x - x_{QT})^2\right], \quad (5.12)$$

where $x_{DT} = -160$ μm ($x_{QT} = -22$ μm) represents the position of the minimum of the dipole trap (quadrupole trap) potential along the waveguide, or the x-direction. The trap frequencies for these potentials are ramped linearly over the first $\tau = 250$ ms: $\omega_{x_{DT}}(t) = \max\{\omega_{DT}(\tau - t)/\tau, 0\}$ and $\omega_{x_{QT}}(t) = \min\{\omega_{QT}t/\tau, \omega_{QT}\}$, for $\omega_{DT} = 2\pi \times 30$ Hz and $\omega_{QT} = 2\pi \times 1.15$ Hz. The static narrow potential well $V(x)$ is centred at $x = 0$, and the atoms move towards positive x. $N = 6000$ atoms are used in the simulation. For the nonlinearity term $g_{1D} = 2\hbar\omega_r a_s$, $\omega_r = 2\pi \times 18.2$ Hz which is the radial trapping frequency of the waveguide. We work with $\psi(x,t)$ normalised to unity, and initialise the simulation with $\psi(x,t)$ in the ground state of the system for potential $U(x,t = 0)$.

As shown in Fig. 5.9, wavepackets in the model described above only exhibit very weak reflection ($\lesssim 4\%$) from the Gaussian potential $V_G(x)$, both for the non-interacting case $a_s = 0$ (Fig. 5.9(a)), and the case of bright solitary waves with $a_s = -7a_0$ (Fig. 5.9(b)).

In order to explain the enhanced quantum reflection in the experiment, we look more closely at Eq. 5.3. One possible explanation is a mismatch of the energy relation. However, the movement of the solitary wave (by mapping out the centre of mass motion at different time after release) rules out the possibility that the velocity is less than half of $1\,\mathrm{mm\,s^{-1}}$. On the other hand, a potential width $< 1.9\,\mu\mathrm{m}$ would also enhance the probability of reflection. This motivates us to consider the effects of subsidiary diffraction maxima of the red-detuned light field used to create $V(x)$, which is predicted by the *Zemax* simulation shown in Fig. 5.2(c). For a light field that passes through a lens with a solid circular aperture, one expects the intensity (one dimensional) $I(x)$ to have a Fraunhofer diffraction pattern in a form of

$$I(x) = I_0 \left(\frac{2\lambda f J_1 \left(\frac{\pi D x}{\lambda f} \right)}{\pi D x} \right)^2 , \tag{5.13}$$

where I_0 is the peak laser intensity, D is the aperture diameter, and J_1 represents a Bessel function of the first kind with $n = 1$ [170–172]. In general, the less intense subsidiary maxima have a narrower width than the central maximum. For instance, in our system, using Eq. 5.13, the theoretical value of the width between the central maximum and the first minimum (i.e. the Airy disk) is $0.94\,\mu\mathrm{m}$, while the width between the first minimum and the second maximum is $0.32\,\mu\mathrm{m}$. Eq. 5.3 suggests that, at least when taken in isolation, the subsidiary maxima may be liable to produce significant reflection, albeit very low trap depth. In addition, the presence of multiple potential wells can itself enhance reflection — as seen, for example, in Bragg reflection of BECs from a multiple-well lattice with slowly-varying well depths [173] — although in our case the rapid variation in the well depths precludes a similar quantitative analysis.

The exact dimensions of the diffraction pattern at the tightly focussed waist,

however, are not precisely known. The alignment of the narrow attractive potential requires both mirror steering and rotating the lens mount, as discussed in Section. 5.2.2. Thus it is likely that the incident angle of the beam on the high NA aspheric lens (lens 4) deviates from 90°. Such deviation causes the diffraction pattern to skew to one side. As illustrated in Fig. 5.10, the resulting intensity profile, and hence the structure of the subsidiary maxima, is very sensitive to the incident angle. Nevertheless, as a generic model, and using Eq. 5.13, we consider a potential associated with the intensity pattern of Fraunhofer diffraction from an aperture as

$$V_J(x) = -V_0 \left[\frac{w_x}{x} J_1 \left(\frac{2x}{w_x} \right) \right]^2 , \qquad (5.14)$$

and the same potential truncated after the first subsidiary maximum (second subsidiary intensity minimum);

$$V_J^{(\text{trunc})}(x) = \begin{cases} V_J(x) & |2x/w_x| < \alpha_2, \\ 0 & |2x/w_x| \geq \alpha_2, \end{cases} \qquad (5.15)$$

where α_2 is the second positive zero of $J_1(x)$. As shown in Fig. 5.9 (inset), these potentials have a similar central minimum to $V_G(x)$, but with an addition of one ($V_J^{(\text{trunc})}(x)$) or a decaying series ($V_J(x)$) of subsidiary minima. The results of simulations for both noninteracting wavepackets, Fig. 5.9(a), $a_s = 0$ and for bright solitary waves, Fig. 5.9(b), $a_s = -7a_0$, show that the reflection is greatly enhanced for both of these potentials compared to $V_G(x)$, for the range of well depths used in the experiment. The presence of subsidiary diffraction maxima in the beam producing the potential well thus provides a plausible explanation for the enhanced reflection probabilities observed in the experiment. The similarity of the results for $V_J(x)$ and $V_J^{(\text{trunc})}(x)$ indicates that the oscillatory structure of the reflection coefficient is primarily a transmission resonance effect, attributable to the three-well potential composed of the main beam maximum and the largest two subsidiary diffraction maxima.

There are a few differences evident when the experimental results are compared to the simplified model. Firstly, in the generic model, one expects negligible confinement ($< 1\%$) at the potential well. Secondly, the experi-

mental curve of reflection exhibits no resolved oscillations and has a lower overall magnitude. We have excluded small shot-to-shot changes in the incoming soliton velocity due to small ($\sim \pm 5\ \mu$m) shifts in the alignment of the experimental potentials as a cause of this, since changing the initial displacement of the soliton by up to $\pm 5\ \mu$m in the model leads to a negligible change in reflection coefficient. We therefore suspect that these differences arise from effects not captured by our simple model, which may include the exact structure of the potential well (possibly including time-dependent fluctuations), three-dimensional effects, and finite-temperature effects.

5.7 Summary

In summary, we have observed quantum reflection of a bright solitary matter-wave from a narrow, attractive potential. Such a potential, formed by a tightly focussed laser beam, is produced through a carefully tailored optical system designed using *Zemax*, where the waist is measured to be $1.9(2)\ \mu$m along the propagation direction of the solitary wave. With controls on both the well depth and the velocity of the solitary wave, reflection probabilities of up to 25% are observed, with the remaining atoms either transmitted or becoming trapped at the position of the potential well. Modelling of the system suggests that the exact spatial characteristic of the potential well is crucial in determining the amount of reflection observed, with the presence of multiple diffraction intensity maxima, rather than a single Gaussian maximum, playing an essential role. The realisation of quantum reflection and the splitting of the solitary waves is an important stepping stone towards the construction of an interferometer with bright solitary waves. In the next stage of the experiment, we proceed to construct an interferometer in a ring geometry where the splitting and recombination of the solitary wave is facilitated by a repulsive barrier. Detailed in Chapter 2, such a system preserves the integrability owing to the absence of axial trapping. This allows us to study the interferometry using true solitons from NLSE in the mathematical sense. In long term, the measurements of soliton splitting at the attractive potential also taught us how to study quantum reflection due to the surface Casmir-Polder potential, where the robust nature of the bright solitary waves makes them the ideal candidates for such experiments [48].

Part II

Towards rotational sensing with bright solitary waves

Chapter 6

Experimental upgrade

Previously, with the use of the apparatus described in Chapter 3, we demonstrated the creation of bright solitary waves in Chapter 4. This is achieved by transferring the ^{85}Rb BEC from a crossed dipole trap into an optical waveguide. By scattering the bright solitary waves from a tightly focussed potential well, we demonstrated the quantum reflection of such matter-waves from a narrow attractive Gaussian potential in Chapter 5. However, in proceeding to advanced experiments with the solitary waves such as probing the atom-surface interaction and interferometry, an upgrade of the apparatus is required. In this chapter, we first lay out the limitations of the existing setup, which are then tackled by an implementation of a new setup of the magnetic coils and the optical dipole trap. We conclude the chapter by the demonstration of the creation of ^{87}Rb condensates with the use of the upgraded experimental apparatus.

6.1   Limitations of the existing setup

- **Magnetic fields and background harmonic potential:** The motion of the solitary wave has relied on the $1\,\mathrm{Hz}$ background harmonic potential resulting from the combination of the quadrupole gradient and bias magnetic field, a result given by Eq. 3.8. We have discussed in Section 5.3 that the velocity of the solitary wave is directly related to the oscillation amplitude of the motion, that is, the distance between the centre of the crossed dipole trap and the weak harmonic potential

83

along the waveguide. This method poses a shortfall if one wishes to study the solitary waves at a low velocity as the centre of mass would appear to be almost at rest if the oscillation amplitude is close to, or below, the resolution of the imaging system. In particular, with the parameters presented in Chapter 5, $v \lesssim 0.13\,\mathrm{mm\,s^{-1}}$ is needed if one wishes to observe quantum superpositions with bright solitary waves (see Section 2.4.2). This requires an oscillation amplitude of the solitary wave to be $\lesssim 21\,\mu\mathrm{m}$ using Eq. 5.9 (here we assume the potential barrier locates at the minimum of the quadrupole trap potential). With a pixel size of $5.2\,\mu\mathrm{m}$ in our imaging system, it is extremely difficult to resolve such scattering events. Furthermore, the presence of the unremovable background harmonic potential also sets a limit to the anisotropy of trap frequency that the atoms would experience.

- **Inflexibility of the dipole trap:** To compensate for the insufficient beam power of the single mode $15\,\mathrm{W}$ $1064\,\mathrm{nm}$ IPG laser, it was opted to form a crossed dipole trap in a bow-tie configuration to give the desired trap depth of $\sim 100\,\mu\mathrm{K} \times k_\mathrm{B}$. Crossing at $6\,\mathrm{mm}$ away from the prism surface to avoid the beam being clipped by the prism, the current setup is not suitable for the atom-surface interaction experiment with solitary waves [48] as it requires the transport of a degenerate gas over a distance greater than we have been able to demonstrate.

- **Restricted optical access:** The current coil mount covers an unnecessarily large area, which makes it difficult to place any optics at $\lesssim 120\,\mathrm{mm}$ from the centre of the science cell. Optical access is very limited as space is taken up by the optics for dipole beams in a bow-tie configuration, the waveguide, the imaging probe beam, and the supporting posts for the top coil mount. This makes it extremely difficult to install extra optical systems, such as a tightly focussed light sheet, which is necessary for providing the vertical confinement of the ring traps, which will be discussed in Chapter 8.

- **Vertical optical setup:** One of the main aims of this project is to develop a ring potential, a vital component in the interferometry scheme proposed in [52]. In order the measure the Earth's rotation, the generation of such a potential (which will be discussed in Chapter 7) requires the implementation of a laser beam that enters the science cell

vertically. Thus, in addition to the optics for generating the narrow potential and vertical imaging, more optics are required to be mounted above the coil mount. It is hence essential to develop a rigid hardware which allows the optics to be secured above the coils.

To address the limitations, the following upgrades have been implemented:

- Additional magnetic coils, namely curvature and cancellation coils, have been developed to control the curvature of the magnetic field;

- A compact coil mount has been designed to increase the optical access;

- A vertical breadboard has been designed to accommodate the optics of the vertical optical systems;

- A new optical dipole trap has been developed, where each dipole beam can be independently controlled;

- With the use of an acousto optical deflector, and a home built voltage multiplier circuit, one of the dipole beams can be displaced transversely. This enables us to translate the crossed dipole trap towards the prism.

The design, implementation, and optimisation of these upgrades will be discussed in detail in the following sections. As tuning the scattering length through a Feshbach resonance is not required for the system optimisation, ^{87}Rb atoms are used for the rest of this thesis owing to their relatively low inelastic losses compared to ^{85}Rb [150, 159, 161].

6.2   Magnetic trap upgrade

In this section, we concentrate on the removal of the magnetic curvature, as well as a compact design of the magnetic coils and mount to maximise the optical access.

6.2.1   Curvature and cancellation coils

An integral part of the new magnetic coil design is to introduce an additional pair of coils for curvature control. Named the *curvature coils*, an ideal design
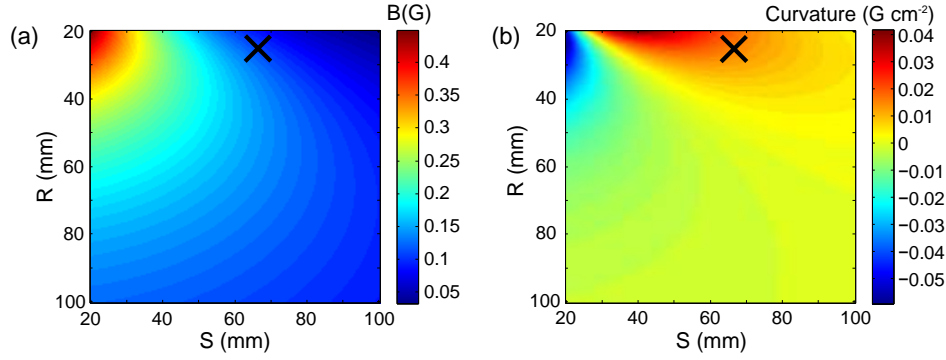
Figure 6.1: (a) Magnetic field and (b) curvature calculations of a pair of coils, each with 1 turn and 1 A in a R and S parameter space. The mark (x) indicates the chosen dimensions of the curvature coils.

should have a maximised curvature that cancels the 1 Hz background trap frequency, but also has a minimised effect to the overall bias magnetic field near the field centre. Both quantities, namely the bias magnetic field and the field curvature, depend strongly on the coil radius R and the coil separation S (as defined in Appendix A). Calculated using Eq. A.3, the axial magnetic field at the mid point of the coil pair is presented in Fig. 6.1(a). It shows that in order to minimise the resulting magnetic bias field, a small R and $S \gg R$ is desirable. This, however, does not coincide with the region that satisfies the first requirement. As shown in Fig. 6.1(b), the maximum magnitude of the curvature is achieved where R is small and $S \simeq 2.5R$. Thus upon the introduction of the curvature coils, it is inevitable that the resulting magnetic field contributes to the overall bias field.

This led to the design of a pair of magnetic coils that cancels the bias field produced by the curvature coils at the centre of the coils. The *cancellation coils* are connected to the curvature coils in series such that they produce an equal but opposite magnetic field to the curvature with the same current I. Denoting Cv and Cl for curvature and cancellation coils respectively, and using Eq. A.3 evaluated at the mid point of the coil pair, the required condition is

$$\frac{n_{\mathrm{Cv}} R_{\mathrm{Cv}}^2}{\left[(\frac{S_{\mathrm{Cv}}}{2})^2 + R_{\mathrm{Cv}}^2\right]^{3/2}} = \frac{n_{\mathrm{Cl}} R_{\mathrm{Cl}}^2}{\left[(\frac{S_{\mathrm{Cl}}}{2})^2 + R_{\mathrm{Cl}}^2\right]^{3/2}}. \tag{6.1}$$

Furthermore, we choose the Helmholtz configuration for the cancellation

coils, namely $R_{\mathrm{Cl}} = S_{\mathrm{Cl}}$, such that the contribution of the curvature by such a coil pair is minimal. Hence the relation between these two set of coils is simplified to

$$\frac{n_{\mathrm{Cv}} R_{\mathrm{Cv}}^2}{\left(\frac{4}{5}\left(\left(\frac{S_{\mathrm{Cv}}}{2}\right)^2 + R_{\mathrm{Cv}}^2\right)\right)^{3/2}} R_{\mathrm{Cl}} = n_{\mathrm{Cl}}, \tag{6.2}$$

which allows us to design the most appropriate cancellation coils. To finalise the coil design, spatial restrictions such as an aperture reserved for vertical imaging, and the space occupied by the water-cooled quadrupole coils, are taken into account. By fixing the radii of the $n_{\mathrm{Cv}} = 33$ turns curvature coils to be $R_{\mathrm{Cv}} = 24\,\mathrm{mm}$, the smallest separation without taking up the space reserved for the quadrupole coils (See Fig. 6.4) is $S_{\mathrm{Cv}} = 66\,\mathrm{mm}$. Note that it is larger than $S_{\mathrm{Cv}} = 47\,\mathrm{mm}$ where the curvature for $R_{\mathrm{Cv}} = 24\,\mathrm{mm}$ is maximum. In keeping the coils and the coil mount compact, the Helmholtz cancellation coils have the radii R_{Cl} and separation S_{Cl} both at $51.4\,\mathrm{mm}$. Using Eq. 6.2, one calculates the required number of turns for the cancellation coils is $n_{\mathrm{Cl}} = 20$. The measured dimensions and magnetic fields of the two additional coils pairs are presented in Appendix A, along with the quadrupole and bias coils which are identical to the original design.

To demonstrate the use of the curvature and cancellation coils, the radial and axial magnetic fields at $5\,\mathrm{A}$ are presented in Fig. 6.2(a) and (b), where the red curves are the fits using Eq. A.3 and Eq. A.4. Fig. 6.2(c) shows that the additional coils are capable in both increasing the trap frequency and producing anti-trapping, depending on the direction of the current in the coils. While the magnetic field at the mid point of the coils is too small for the Hall probe used to provide a reliable measurement, it can be deduced from the fits in Fig. 6.2(a) and (b). As suggested in Fig. 6.2(d), the magnetic field is not perfectly cancelled. When operating, the coils introduce an additional field of $40\,\mathrm{mG\,A^{-1}}$ which contributes directly to the overall magnetic bias field. At the zero crossing of the scattering length of $^{85}\mathrm{Rb}$ atoms in the $F = 2, m_F = -2$ state at $166\,\mathrm{G}$, the additional field causes a change in scattering length by $|\Delta a_s| = 1.6\,a_0\,\mathrm{A^{-1}}$ (using Eq. 4.2). As a result, the current applied to the bias coils will require adjustment when operating the additional coils in order to obtain a desired combined magnetic bias field.
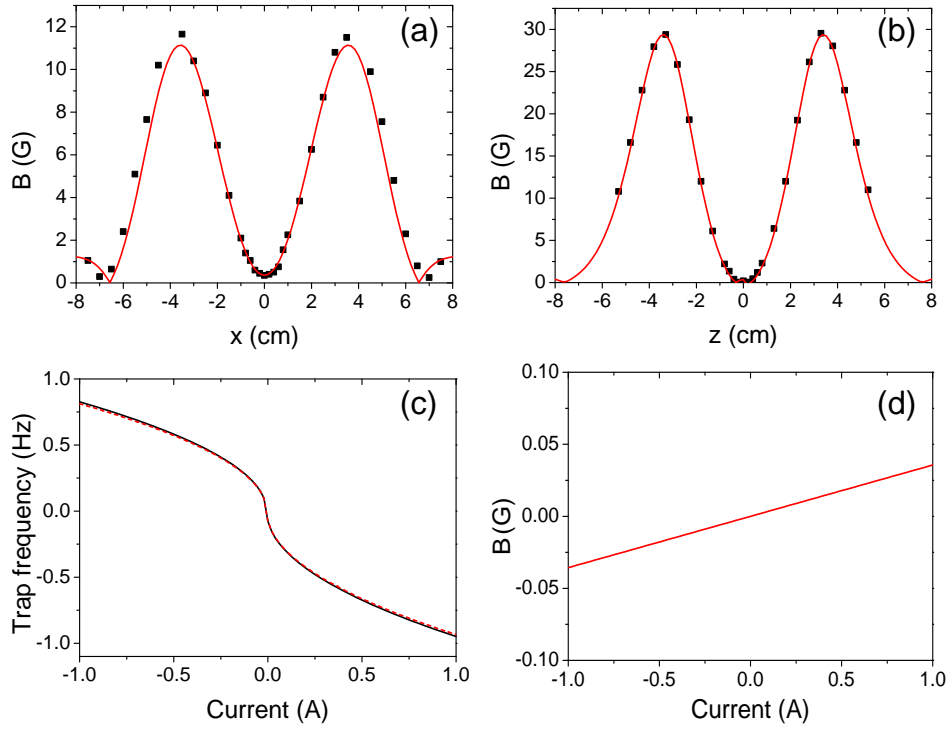
Figure 6.2: Magnetic field and curvature generated by the combined curvature coils and cancellation coils system with a current of 5 A. Here, the discrete data points and the curves are experimental measurements and theoretical calculation respectively. (a) Total magnetic field along the radial direction. (b) Total magnetic field along the axial direction. (c) Comparison of the trap frequency between curvature coils only (black, solid) and curvature coils cooperating with the cancellation coils (red, dashed). (d) Total magnetic bias field at the centre when both curvature and cancellation coils are used, which varies at $40\,\mathrm{mG\,A^{-1}}$.
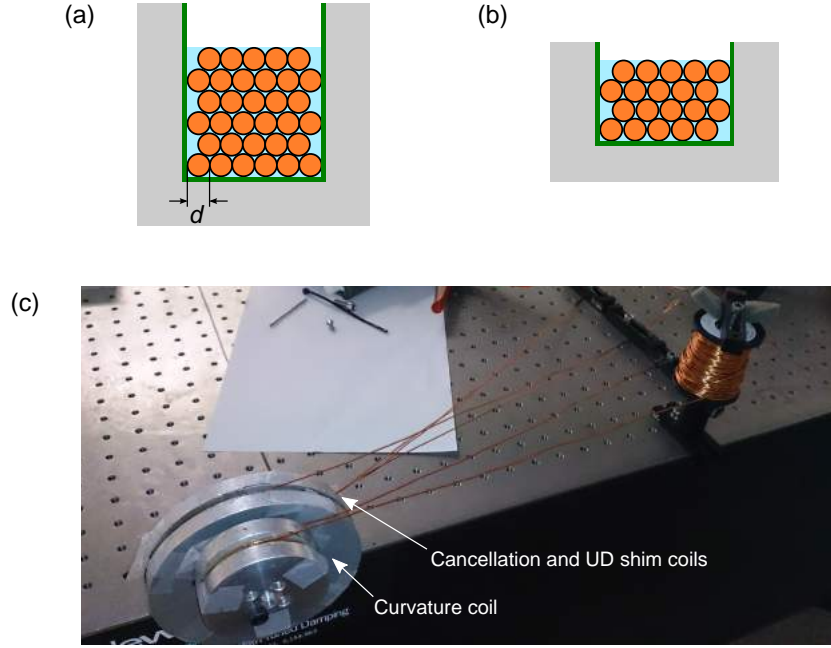
Figure 6.3: Illustration of the method of winding the small coils. The copper wire (orange), glued using epoxy adhesives (blue), is arranged in the aluminium coil former (grey) protected by a thin layer of mylar (green). (a) The arrangement of the curvature coils, with a spacing of $6d$ between the walls. (b) The arrangement, with a different number of layers, of the cancellation coils and the shim coils. The spacing between the walls is $5.5d$. (c) Simultaneous winding of the curvature coils (smaller radius), the cancellation and the UD shim coils (larger radius).

6.2.2 Winding small coils

In addition to the introduction of the curvature and cancellation coils, the shim coils, which are responsible for shifting the quadrupole centre and field nulling, were redesigned in the new setup in order to generate larger magnetic fields. Wound using a diameter $d = 0.8\,\mathrm{mm}$ copper wire, the 3 sets of shim coils, namely the North-South (NS), East-West (EW), and Up-Down (UD), shift the field zero along the x, y, and z direction respectively. These coils are designed to be compact in order to be placed closed to the science cell to generate higher magnetic fields with fewer turns and lower currents. As illustrated in Fig. 6.3, the coils are wound in aluminium coil formers where the spacing between the walls is carefully chosen. All the walls are protected by a thin layer of mylar as epoxy adhesive glue is applied to each layer of wires. By applying force at both ends of the wire during the winding process, the tension firmly forces the wire into the structure where each layer is $d/2$ offset from the layer below. This minimises the spacing between the wires

and hence maximises the rigidity of the coil. Once the glue is set, the coil can be completely separated from the coil formers where the mylar can be removed. These compact coils can then be simply inserted to the coil mount with a predetermined separation distance.

6.2.3   Coil mount and coil arrangement

The magnetic coils are secured in a coil mount (made from G10), which consists of a top and a bottom component separated by 36 mm. As shown in Fig. 6.4(a), pairs of quadrupole coils (quad), bias coils (bias), the curvature coils, cancellation coils, and the UD shim, sit in the grooves with depths that provide the desired coil separation. In addition, the RF coil, necessary for RF evaporation in the early phase of atom cooling in the science cell, is positioned on top of the bottom coil mount. The 2 turn circular RF coil with diameter 37 mm is wound from $d = 1.0$ mm a copper wire. In order to match the impedance of the RF amplifier, a high power (3 W) 50 Ω resistor (Multicomp MCKNP02UJ0500B00) is connected to the RF coil in series. The axis of the magnetic coils, marked by the dotted-dashed line, is located at ~ 3 mm from the surface of the Dove prism. This distance is chosen to avoid atom loss from getting too close from the prism [67]. The top mount has its area greatly reduced by 65% from the previous design, allowing optics to be placed and mounted on the M6 threaded holes shown in Fig. 6.4(b) closer to the science cell. There is a M36×1 threaded aperture at the centre of both coil mounts, which enable us to securely mount and adjust high NA lenses if high imaging resolution is required. Moreover, the compact design of the EW and NS shim coils, as seen in Fig. 6.4(c), maximises the optical access to the science cell.

6.2.4   Installation of the magnetic coils

The connections of the magnetic coils to the power supply and the cooling water from the barrier cooler are identical to the previous generation described in [67]. The current through all the coils are controlled by a home-built LabVIEW programme 'DExTer' as detailed in [69].

The alignment of the coils, in essence, is to locate the atomic cloud trapped
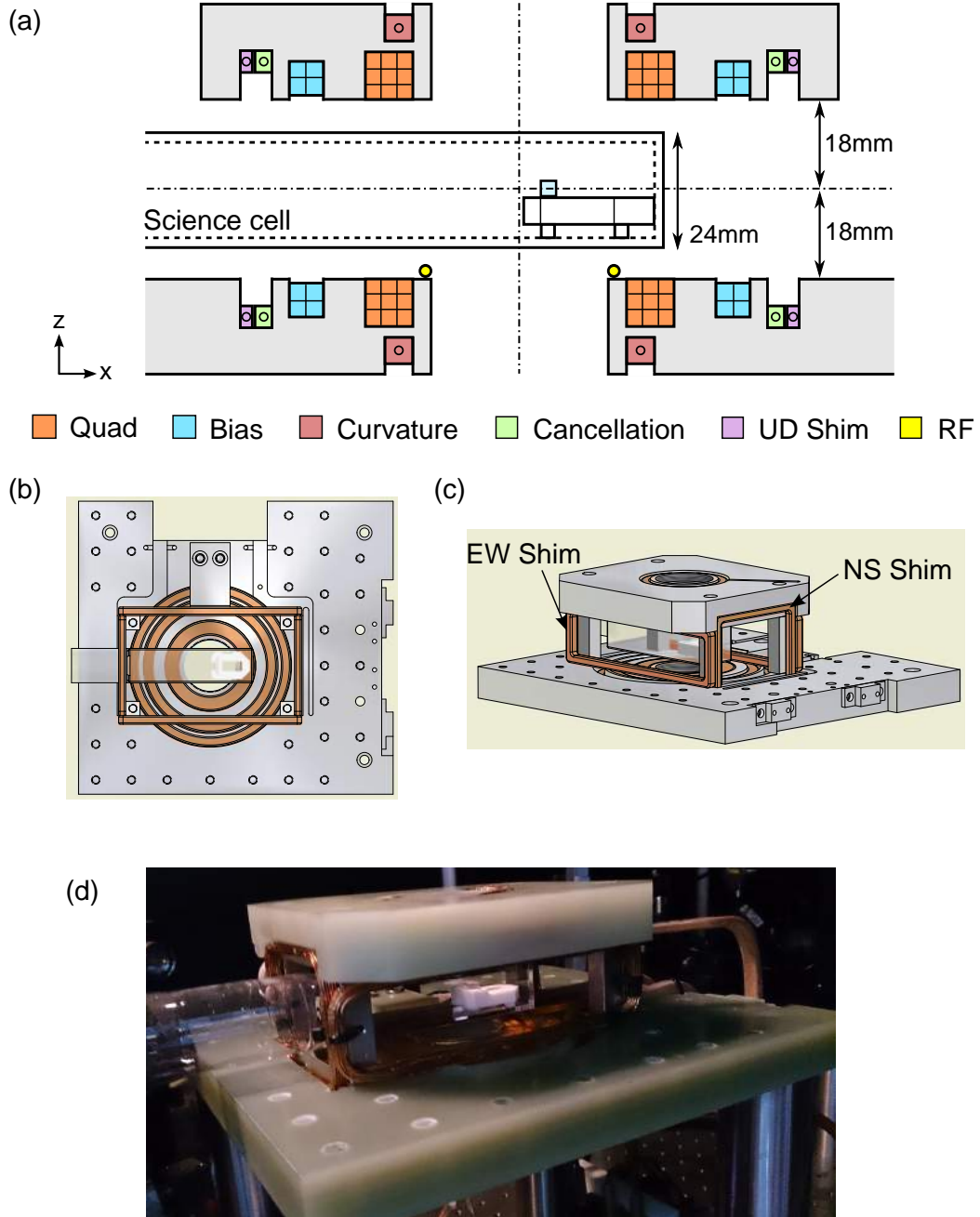
Figure 6.4: Coil mount upgrade. (a) A cross-sectional cut of the coil assembly around the science cell. The squares and circles in the coils denote water-cooled 3.5 mm×3.5 mm and $d = 0.8$ mm copper wires respectively. This is with an exception of the curvature coils and the RF coil which are wound from $d = 1.0$ mm wires. (b) Bird's eye view of the coil arrangement. (c) The location of the rectangular NS and EW shim coils. (d) Coil assembly showing the enhancement of optical access to the science cell, due to the former-free coils.
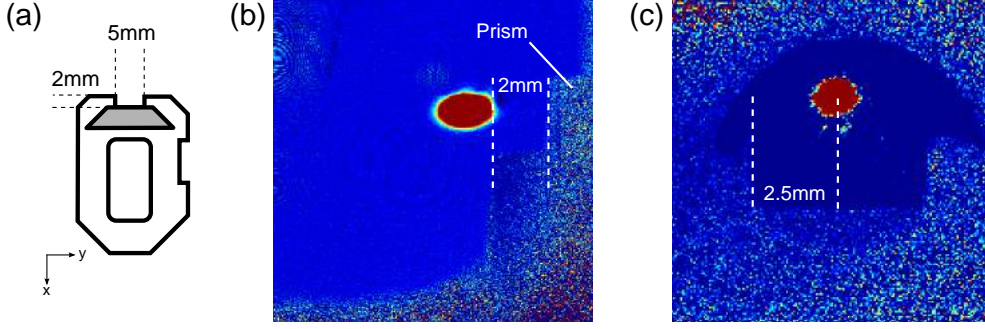
Figure 6.5: Magnetic coil alignment. (a) The dimensions of the prism (grey) and prism mount (white) used for coil alignment (bird's eye view). Images of the atomic clouds trapped in the quadrupole trap using (b) horizontal imaging and (c) vertical imaging systems.

in the quadrupole magnetic potential close to the prism without atom loss due to the surface. The coil mount is first carefully positioned such that the science cell locates in between the top and bottom mounts and through one of the NS shim coils, as illustrated in Fig. 6.4(d). The number of atoms transferred from the transport magnetic trap into the science cell quadrupole trap is shown to remain approximately constant over $\sim 5\,\mathrm{cm}$ displacement between the two coil axes [67]. Thus by using the existing transfer routine detailed in Section 3.1.3, one obtains a trapped atomic sample for precise alignment, albeit with unoptimised transfer. Making use of the dimensions of the prism and prism mount (see Fig. 6.5(a)), we use both temporary setups of horizontal and vertical absorption imaging to position the quadrupole trap centre at $\sim 3\,\mathrm{mm}$ from the front surface of the prism. As shown in Fig. 6.5(b) and (c), where the trapped atoms are imaged after $2\,\mathrm{ms}$ TOF, the position of the coil mount is finalised such that the trapped atoms are located normal to the mid point of the prism.

6.3 Vertical optical systems

In the vertical direction, a vertical breadboard (made from G10) is designed to accommodate the optics for vertical imaging and additional systems such as the creation of arbitrary trap potentials (see Chapters 7 and 8). As shown in Fig. 6.6, the $300\,\mathrm{mm} \times 230\,\mathrm{mm}$ breadboard overhanging above the science cell has a total of 90 M6 threaded through holes which enable us to populate the board for future use. This vertical breadboard is mounted on
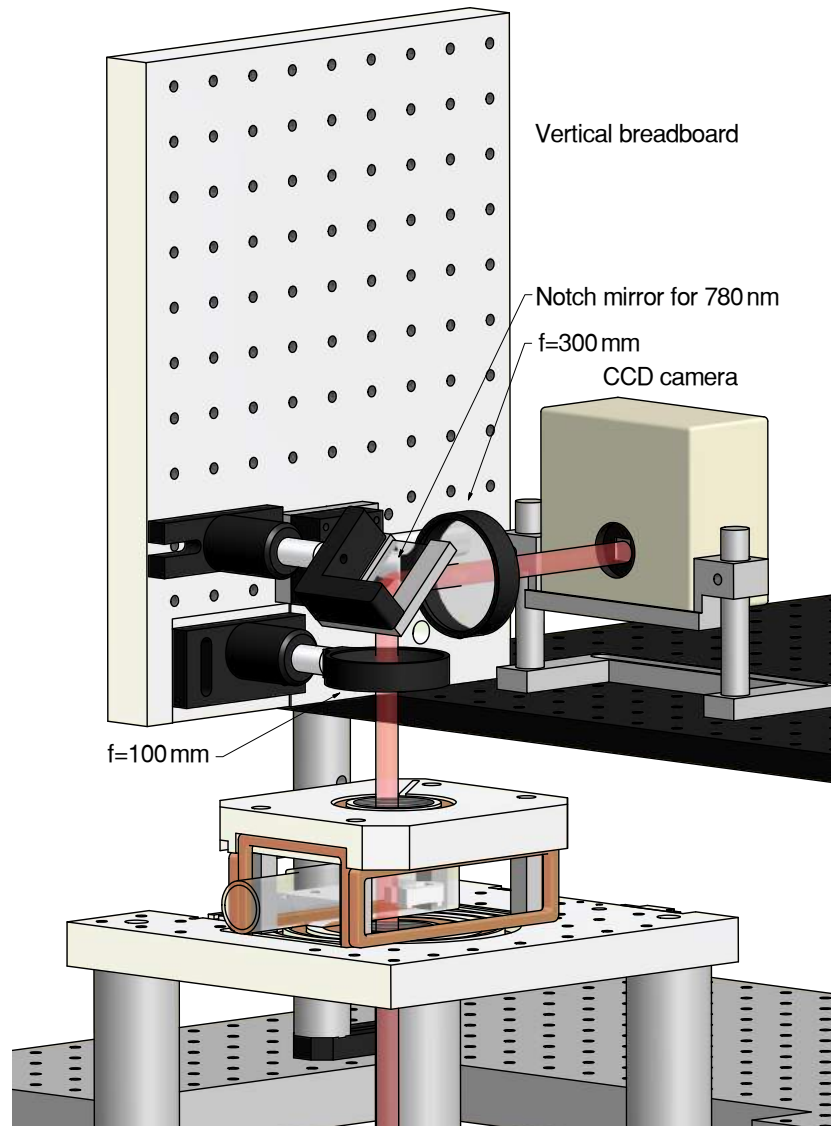
Figure 6.6: Vertical breadboard provides versatility in mounting optics to send laser beams from above, as well as being used for vertical imaging. The probe beam, coloured in red, enters the science cell from below and is incident on the CCD after passing through the imaging lenses. For illustration purpose, the rest of the vacuum chamber beyond the science cell is not drawn here.

an aluminium breadboard (black). It should be noted that this aluminium breadboard is not directly on top of either the coil mount or the transport coils to prevent magnetic field distortion from induced eddy currents.

For the vertical imaging, an $f = 100$ mm achromatic lens (Thorlabs AC508-100-B) and an $f = 300$ mm achromatic lens (Thorlabs AC508-300-B) are used, resulting a $3\times$ magnification. This gives a pixel size of $2.6\,\mu$m, which is nearly half of that of the horizontal imaging ($5.1\,\mu$m). To enable accurate focussing, the $f = 100$ mm lens and $f = 300$ mm lens are placed on a slidable slot and a translation stage respectively. In between the lenses, there is a notch dichroic beamsplitter (Semrock NFD01-785-25$\times$36) which reflects light with $\lambda = 750 - 840$ nm. The focussing procedure of the vertical imaging system typically involves two simple steps (assuming the probe beam is centred on the atoms):

1. Focus the probe beam to a spot by the second lens. The positions of the second lens and the camera are adjusted such that the waist appears at the CCD sensor.

2. Install the first lens. With a small target of an atomic cloud (typically from a crossed dipole trap, which will be discussed shortly), adjust the position of the lens such that the measured cloud width is minimised as defocusing causes image distortion. See [67, 69] for more detailed examples.

6.4   Optical dipole trap upgrade

6.4.1   Optical setup

In the new dipole trap setup, we replaced the 15W IPG laser with a 50W multimode IPG laser (YLR-50-LP-AC-Y12) with wavelength $\lambda = 1070$ nm. With over three-fold increase in the laser power, a crossed dipole trap with trap depth $> 100\,\mu$K $\times k_{\mathrm{B}}$ can be comfortably formed from two independent beams split from the single laser source. In contrast to the original setup, the new optical setup sees one beam passes through the Dove prism perpendicularly along the x-direction, while its counterpart enters the science cell along
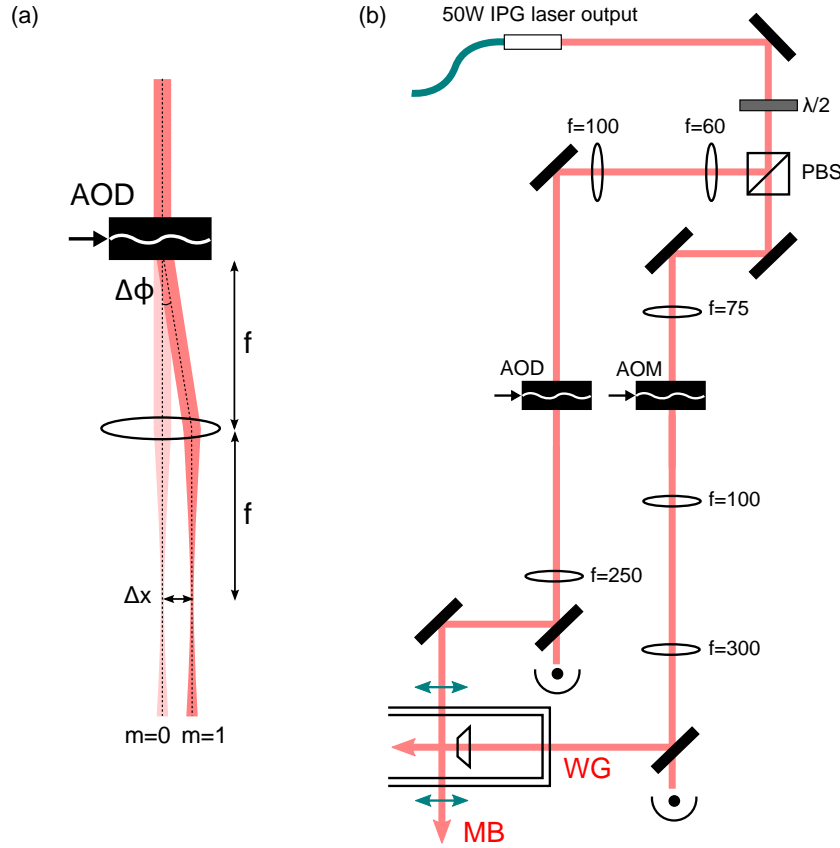
Figure 6.7: The new dipole trap setup. (a) Beam diffraction into first order ($m = 1$) by the acousto opitcal deflecter (AOD). The lens is placed at one focal length f from the AOD such that the transmitted beam paths are parallel to the zeroth order ($m = 0$) beam regardless of the diffraction angle ϕ. (b) Optical setup. The laser output is split into the waveguide (WG) and the moving beam (MB) which intersect in the science cell. The position of the crossed diople trap can be displaced along the WG by varying the drive frequency applied to the AOD, which is indicated by the green arrows on the MB.

the y-direction. With independent control in beam power, this configuration allows smooth transfer of the BEC from the crossed dipole trap into a single beam by simply ramping the second beam off after degeneracy is reached. For this reason, we name the first beam the waveguide (WG) as it resembles the waveguide of our original setup.

For optimal loading of atoms from the magnetic quadrupole trap (QT) into the optical dipole trap (DT), the DT centre needs to be located close to the QT centre. At $\sim 3\,\mathrm{mm}$ from the prism surface, the DT position is too far away from the prism surface for future experiments of atom-surface interaction. Thus, a mechanism is needed for adjusting the position of the second beam, here named the moving beam (MB), for translating the DT from close to the QT towards the surface of the prism. This is achieved by the implementation of an acousto optical deflecter (AOD, Isomet D1135-T110L-TC)[1]. The working principle of an AOD is identical to an AOM except that the device is optimised for beam deflection, which is well documented in the literature [174, 175]. In brief, by applying an acoustic frequency to the crystal medium TeO_2, the input optical beam is diffracted into different orders $m = 0, 1, 2, \ldots$ under Bragg diffraction when it passes through the crystal. Adjusting the beam alignment into the AOD can maximise the diffraction efficiency at $m = 1$. The diffraction angle ϕ is given by

$$\phi = \frac{\lambda \nu}{v_s},\tag{6.3}$$

with v_s and λ denoting the speed of sound in the crystal medium and the wavelength of light respectively [176]. The applied acoustic frequency, ν, is controlled by a tunable RF driver RFA3110-4, which varies linearly ($85 - 145\,\mathrm{MHz}$) with an input voltage ($0 - 10\,\mathrm{V}$). With a maximum scan angle of $\phi = 13\,\mathrm{mrad}$, the beam displacement is achieved by focussing the deflected beam from the AOD using a converging lens with focal length f. This lens is placed at a distance f from the output of the AOD such that the beam paths after the lens are always parallel, as shown in Fig. 6.7(a). The waist of the MB is located $2f$ from the AOD where it intersects with the WG. Providing the Rayleigh range z_R of the WG is sufficiently large, one expects minimal change in the DT geometry over the MB displacement of

---

[1]The centre frequency and the RF bandwidth are $110\,\mathrm{MHz}$ and $50\,\mathrm{MHz}$ respectively.

$$\Delta x = f \Delta \phi = \frac{f \lambda \Delta \nu}{v_s}. \tag{6.4}$$

The optical layout of the new DT system is presented in Fig. 6.7(b). With an output beamsize of $788(4)\,\mu$m, the laser beam is split into two by a polarisation beam splitter. The WG, with its power controlled using an AOM (Isomet M1080-T80L-NIR), enters the science cell through the back of the prism and intersects the MB. For the purpose of beam alignment, the last lenses in both beam paths, namely $f = 300\,$mm (Thorlabs AC254-300-C) for the WG and $f = 250\,$mm (Thorlabs AC254-250-C) for the MB, are mounted on translation stages. Using Eq. 6.4, one calculates that the expected range of the MB displacement is $3.25\,$mm. Note that the MB after the last mirror shares the same path with the probe beam for horizontal absorption imaging. Thus to avoid obstructions to the probe beam, the mirror (reflection at $\lambda = 1070\,$nm and transmission at $\lambda = 780\,$nm) with a dimension of $25\,$mm$\times36\,$mm is fixed on a plate mounted directly on the coil mount. Given the ability to form a dithered time averaged trap, which will be discussed in Section 6.4.2, a smaller MB waist is chosen compared to the WG. The waists of the MB and WG are measured to be $65(1)\,\mu$m and $102(1)\,\mu$m respectively[2]. Note that as a precaution, the WG power is restricted to $\lesssim 6\,$W to limit the laser power dissipation inside the vacuum system.

6.4.2 Time averaged optical potential

By taking the response time of the electronics into account, the output beam of the AOD can be scanned at a frequency ν_{scan} in excess of $\sim 5\,$kHz. This is comfortably higher than the radial trapping frequency $\nu_{\text{MB}} = 420\,$Hz at a trap depth of $100\,\mu$K $\times k_{\text{B}}$. In the scenario where $\nu_{\text{scan}} \gg \nu_{\text{MB}}$, atoms in such trap cannot respond kinematically (for instance, 'following' the beam movement) but rather see a time averaged optical potential. Scanning at a much higher frequency also prevents parametric heating of atoms that occurs if $\nu_{\text{scan}} \approx 2\nu_{\text{MB}}/n, n = 1, 2, \ldots$ [94, 177]. These potentials are smooth with the resolution limited by the beam waist. Depending on the RF power profile,

---

[2]These are measured by a home built Gaussian beam profiler which consists of a high resolution Thorlabs CMOS camera DDC1545M and a MATLAB Gaussian fitting programme. Measurements are carried out at low power - at 10% of the maximum laser output.
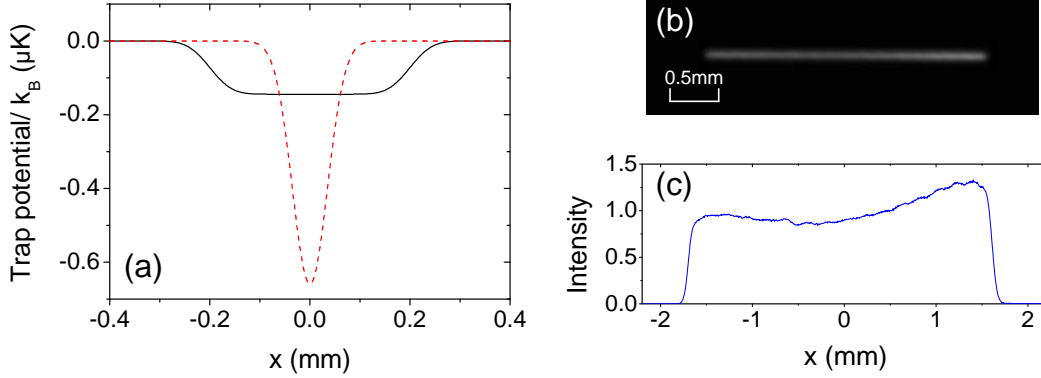
Figure 6.8: Time averaged optical potential. (a) Simulation of trap depths of the stationary MB (red) and MB with dithering amplitude of $200\,\mu$m (black) in a triangular waveform, both at $40\,$mW. (b) Measured intensity of the MB dithered at maximum range with amplitude of $\sim 1.5\,$mm. (c) Normalised intensity of the cross-section of (b).

different intensity patterns in 1D can be generated with one AOD, which can be extended into 2D with an extra AOD or a dual-axis AOD [178]. This, along with other methods of arbitrary potential generation, will be discussed in Chapter 7.

Fig. 6.8(a) illustrates an example of the time averaged potential when the MB is dithered in a triangular waveform at an amplitude of $200\,\mu$m ($\Delta\nu \sim 3\,$MHz). As the beam power remains constant in the simulation, the larger area that the dithered potential covers leads to a lower trap depth than the stationary beam. The dithering yields an elongated, flat-bottomed trap potential. Fig. 6.8 (b) and (c) show the measured time averaged intensity with the maximum scanning range of $3.25\,$mm ($\Delta\nu \sim 50\,$MHz) in a triangular waveform. While the intensity can be approximated to be constant in short scanning range, the intensity profile is skewed at maximum scanning range. We attribute this as a result of a varying diffraction efficiency of the AOD across the RF bandwidth. Nevertheless, as we will demonstrate shortly in Section 6.7, applications of the time averaged potential, such as the creation of an elongated BEC, typically only requires a short scanning range ($\sim 100\,\mu$m) and hence the effect of the skewness is minimal.
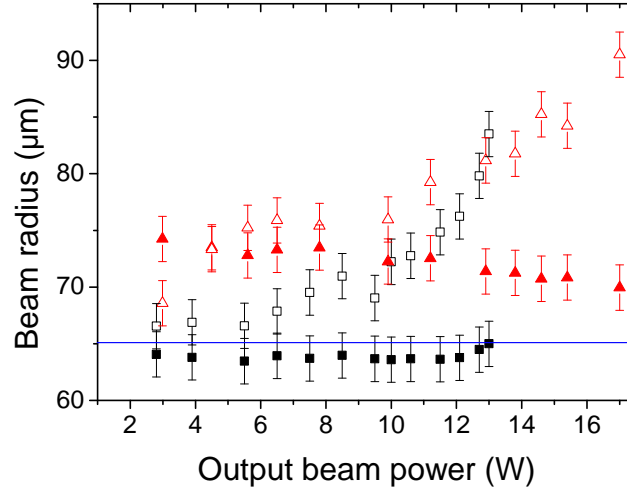
Figure 6.9: Thermal lensing effect in AOD. The MB radii are measured at a fixed point (waist position after the $f = 250\,\text{mm}$ lens at low laser power and RF power) along the horizontal (solid) and vertical (hollow) directions against different output beam power of the AOD. The measurement is repeated for two laser output set points: 50% (black squares) and 77% (red triangles). This is equivalent to $13.2\,\text{W}$ and $20.3\,\text{W}$ incident on the AOD respectively. The blue line indicates the beam size measured at a very low power.

6.4.3 Thermal lensing in AOD crystal

In forming a time averaged potential, higher power is required for a larger dithering amplitude in order to maintain the overall trap depth. For this reason, $\sim 20\,\text{W}$ is reserved for the MB, which is four times the maximum power of WG. However, by applying a high power of $20.3\,\text{W}$ (equivalent to laser set point of 77%) on the AOD, we noticed that the output beam size deviates from the value measured at low power. As shown in Fig. 6.9, while the output beam power increases by applying higher RF power, the vertical (horizontal) waist size increases (decreases). This is the thermal lensing effect in the TeO_2 crystal, which is mainly caused by the existence of impurities [179, 180]. These sites absorb both optical and acoustic energies, resulting a non-uniform temperature distribution in the crystal which affects the performance of the AOD. Hence, this effect is more prominent when a higher optical and/or acoustic energy is used. Indeed, as shown in Fig. 6.9, the ellipticity of the beam waist increases with RF drive power. At low RF drive power, the average waist size is $> 70\,\mu\text{m}$ in the case of $20.3\,\text{W}$ (red triangles) incident on the AOD, while the beam converges to a smaller waist of $65\,\mu\text{m}$ at a lower optical power of $13.2\,\text{W}$ (black squares), where the laser output is set to 50%. Moreover, for all RF drive power tested, the beam radii
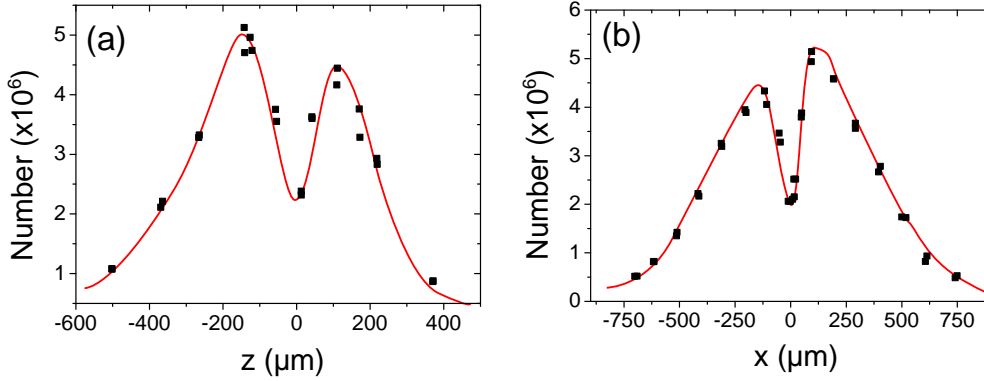
Figure 6.10: Alignment of the moving beam. The number of atoms trapped in the MB beam varies with the (a) vertical and (b) horizontal beam position relative to zero of the magnetic quadrupole field at $(x, z) = (0, 0)$. The red curves are a guide to the eye only.

are measured to be larger at a higher beam power of $20.3\,\mathrm{W}$. This leads to a lower trap depth at the same output power when a higher incident optical power is used. Hence, in order to avoid deformation of the beam shape, both low incident optical and RF powers are favourable. We thus only operate the AOD when the laser power incident on the device is $\lesssim 5\,\mathrm{W}$, while also keeping a low RF power at a diffraction efficiency below 50%.

6.4.4   Alignment and trap characterisation

The alignment of the dipole beams is carried out by first optimising the position of the MB and subsequently aligning the WG to form the crossed dipole trap. To do this, we examine the number of atoms loaded into the hybrid single beam dipole trap at different positions relative to the quadrupole trap zero. The horizontal and vertical positions of the beam are scanned through steering the second to last mirror in the MB path. The experimental routine is inherited from before the rebuild: after the transportation, the MB is switched onto $10.4\,\mathrm{W}$ during the RF evaporation in the quadrupole trap at $180\,\mathrm{G\,cm^{-1}}$. The tight quadrupole trap is then relaxed from $180\,\mathrm{G\,cm^{-1}}$ to just under levitation at $30\,\mathrm{G\,cm^{-1}}$ in $250\,\mathrm{ms}$. After the ramp, the atoms are held in the single beam trap with weak magnetic confinement for $500\,\mathrm{ms}$ before an $8\,\mathrm{ms}$ TOF for horizontal absorption imaging. From Fig. 6.10 where we plot the number variation against scan, we can roughly estimate the position of the field zero as Majorana spin flips causing a dip in the measured atom number. This measurement allows us to locate the MB at $\sim 150\,\mu\mathrm{m}$
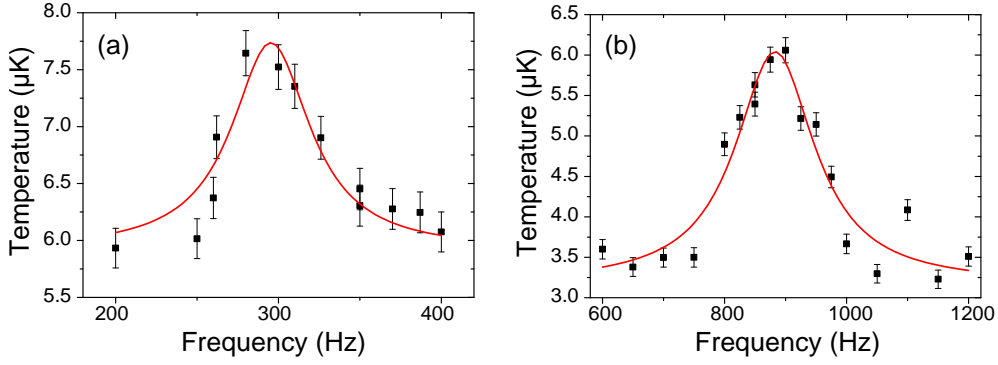
Figure 6.11: Parametric heating measurement in the new dipole beams.   Here a Lorentzian curve is fitted to the first harmonic of the resonance feature to find the centre. (a) WG at 3.75 W. (b) MB at 5.08 W.

below the plane of the field zero [134].

Once the MB is aligned, it serves as a target for the alignment of the WG. By loading atoms into the WG with a weak magnetic confinement, the cigar shaped atomic cloud after 2 ms TOF indicates the position of the beam. By steering the last mirror of the WG path, the vertical and horizontal positions of the WG can be optimised (such that it crosses the MB) via horizontal and vertical imaging respectively. The crossed dipole trap is formed at the intersection of the two beams, which is at a default position of 2.96 mm from the Dove prism.

The trap frequencies of both beams are determined by parametric heating measurements (see Section 5.2.3). Assuming the beams are perfectly circular, the expression relating the beam waist w and the radial trapping frequency ω_r is

$$w = \left(\frac{8\alpha P}{\pi m \omega_r^2} \right)^{1/4},\tag{6.5}$$

which is a simplified version of Eq. 5.8, where P is the beam power and α is the the polarisability for Rb at $\lambda = 1070$ nm. The measurements are carried out for each single beam trap individually. For the WG (MB), initial evapo-ration is carried out until the beam power reaches 1.25 W (1.91 W). The beam power is then ramped back up to 3.75 W (5.08 W) in 25 ms (50 ms) to sup-press the evaporation. Power modulation is then applied for 500 ms (250 ms)
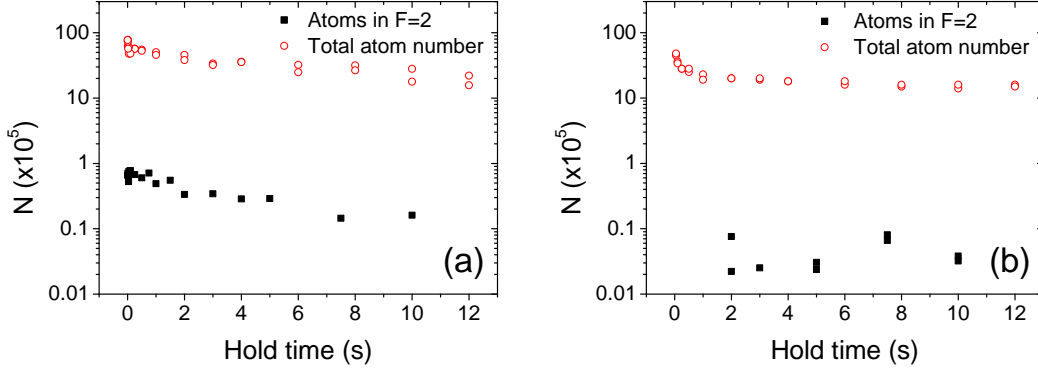
Figure 6.12: Pumping to $F = 2$ state by the multimode laser with two different MB powers, namely (a) 20.3 W and (b) 5.1 W. Atoms are imaged without the use of repump light to determine the number of atoms in $F = 2$. The measurements are then repeated with the use of repump light, where the total atom number is measured.

before the atomic cloud is imaged. The results are shown in Fig. 6.11, where the trap frequencies for MB (at 5.08 W) and WG (at 3.75 W) are measured to be $2\pi \times 441(2)$ Hz and $2\pi \times 148(2)$ Hz respectively. This translates to $w_{\mathrm{MB}} = 70(1)\,\mu$m and $w_{\mathrm{WG}} = 110(1)\,\mu$m. Both waists are in good agreement with the measurements obtained using the beam profiler, as presented in Section 6.4.1.

6.4.5 Atoms pumped into $F = 2$ state by multimode laser

In Chapter 4, we discussed the minimisation of two and three body losses during evaporative cooling in the creation of ^{85}Rb BEC. While three body inelastic collisions are not as severe between the ^{87}Rb atoms (see Section 4.1.2), the use of a multimode laser introduces an extra channel for atom loss. With its broad multi-frequency spectrum, typically in hundreds of GHz, a range of longitudinal modes are distributed with a separation of ~ 15 MHz [181]. The linewidths of the D1 and D2 atomic transitions are 6 MHz, while the hyperfine splitting of the ground state, namely the $F = 1$ and $F = 2$ states, is 6.834 GHz. As explained in [181, 182], it is likely that there exists 2 longitudinal modes separated by this frequency. As a result, optical pumping from the normally populated $F = 1$ state to $F = 2$ by the laser via a 2 photon Raman transition is possible. Driven by collisions, transitions back to $F = 1$ might follow, from which the internal energy is converted into kinetic energy

of the colliding atoms. As the kinetic energy is much higher than the trap depth, such a process leads to an overall loss in atom number from the trap.

To examine this, we carry out the same measurement as suggested in [181]. Normal absorption imaging requires atoms to be repumped to the $F = 2$ state as the probe beam drives the closed transition $F = 2 \rightarrow F' = 3$. Hence imaging the atomic sample *without* the repump beam allows us to identify the number of atoms that are excited to the upper hyperfine ground state by the 1070 nm laser. Imaging the atoms after a variable hold time in the dipole trap, the measurement is repeated for two different MB powers as shown in Fig. 6.12. Consistent with the literature, a higher laser power pumps more atoms into the $F = 2$ state initially. It is then followed by a decay with increasing hold time, which corresponds to the decay of the total atom number in the trap [181]. However, rather different from the published observations [181], the $F = 2$ population is only a very small fraction of the overall atom number. In our case, 20.3 W in the MB has an intensity of $264\,\mathrm{kW\,cm^{-2}}$ which pumps 1.6% of atoms into the upper hyperfine ground state. It contrasts with 21% reported in [181] when a beam with an intensity of $309\,\mathrm{kW\,cm^{-2}}$ is used. Since the majority of our experimental sequences are run at low power to avoid beam deformation by the AOD, we conclude that this pumping effect should only have a minimal contribution to the atom loss.

6.5   Voltage multiplier circuit

In Section 6.4.1, it is mentioned that the diffraction angle of the AOD for the MB is controlled by a single voltage input to the driver. Thus to control the initial loading position, the trap width when dithered, and the movement of the crossed trap along the WG generally requires a carefully tailored voltage signal. One possible solution is through implementing a programmable function generator to supply the suitable voltage to the AOD. However, simple functions such as ramping up the modulation amplitude is a non-trivial operation for such function generators. Instead, we have devised a straightforward way to change and modulate the supply voltage at any point during an experimental routine by using the voltage multiplier circuit shown in Fig. 6.13.
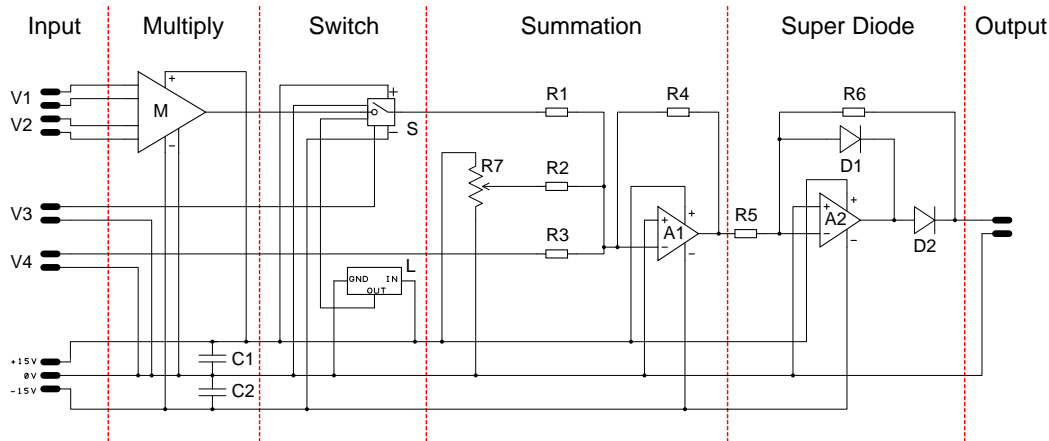
Figure 6.13: The voltage multiplier circuit, runs on $\pm 15\,\mathrm{V}$, has a final output voltage as a multiplication and summation of different voltage inputs. The components are listed in Table 6.1.

Item	Type	Component details
V1		Voltage Input 1
V2	BNC input	Voltage Input 2
V3		Switch trigger
V4		LabVIEW voltage offset
M	Voltage multiplier chip	AD633
S	Analog switch	DG418
L	Linear voltage regulator	7805
A1,A2	Op Amp	TL082
R1		$51\,\mathrm{k\Omega}$
R2	Resistor	$62\,\mathrm{k\Omega}$
R3,R4,R5,R6		$10\,\mathrm{k\Omega}$
R7	Trimmer	$10\,\mathrm{k\Omega}$
D1,D2	Diode	BAT46
C1,C2	Capacitor	$100\,\mathrm{nF}$

Table 6.1: Components of the voltage multiplier circuit.
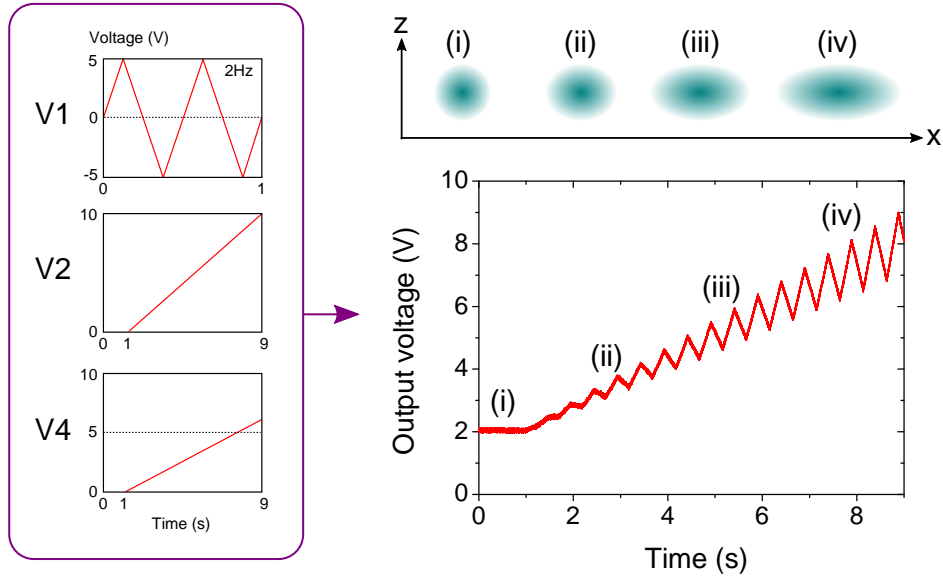
Figure 6.14: Demonstration of the output of the voltage multiplier. The inputs are as follow: V1 is a 2 Hz triangular wave with an amplitude of 5 V, V2 varies linearly from 0 – 10 V in 8 s, V4 varies linearly from 0 – 6 V in 8 s, and a default offset at 2 V. The green circles/ovals (i) – (iv) illustrate the shapes and the positions of the time averaged potential at their corresponding points in the plot of the output voltage.

At the heart of this circuit, the multiplier chip (marked M) outputs a voltage which is a multiplication of the two inputs, namely V1 and V2, with a scaling factor. Interchangeable with each other, one is connected to a function generator that generates a desired waveform usually at a frequency $\sim 5\,\text{kHz}$, while one is connected to the analog LabVIEW output with control voltage $0 - 10\,\text{V}$. The latter acts as a scaling factor of the oscillation amplitude and thus allows to control the width of the dithered trap when the circuit is employed as an input for the AOD.

Once the multiplier is switched on at V3, the modulation will be added on top of two offset voltages: one is a direct offset at input V4 that takes the analog voltage output from LabVIEW, while one is a built-in default offset via the trimmer R7. All of the voltage inputs and initial values are added at the summation stage, which forms the final output voltage. An example of the circuit in operation is illustrated in Fig. 6.14. At (i), there is no dithering (V2 = 0 V) and movement (V4 = 0 V), hence the output voltage is simply the default offset at R7. The trap potential is non-dithered and at default position. From time = 1 s onwards, the oscillation amplitude
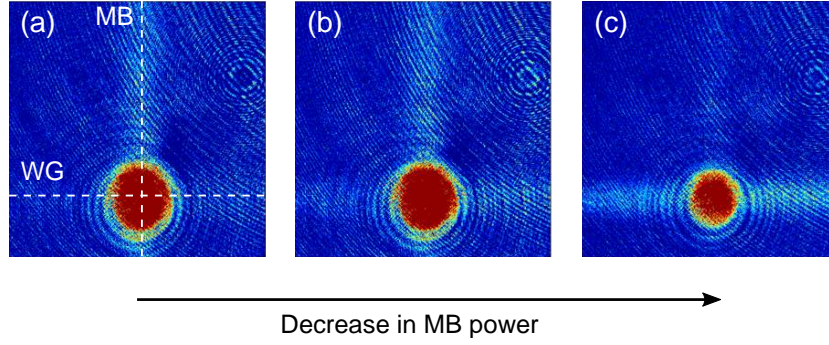
Figure 6.15: Balancing power in both dipole trap beams. Atoms are evaporated along different paths depending of the relation between the trap depth of MB (U_{MB}) and WG (U_{WG}). (a) $U_{\text{MB}} > U_{\text{WG}}$. (b) $U_{\text{MB}} \sim U_{\text{WG}}$. (c) $U_{\text{MB}} < U_{\text{WG}}$.

increases linearly with the application of V2, while the offset voltage increases linearly by ramping V4 up. As a result, one expects both the dithering amplitude and the positional offset to increase with time. The final output voltage of the circuit is given by

$$\text{Output} = [\text{Default offset at R7}] + \text{V4} + 0.02 \times \text{V1} \times \text{V2}. \qquad (6.6)$$

Note from Fig. 6.13 that the output is lower bounded at $0\,\text{V}$ through the super diode. This limit is for the purpose of protecting the RF driver from a negative voltage.

6.6 Evaporative cooling to quantum degeneracy

With the new magnetic coils and optical dipole beams installed and optimised, we are in a good position to perform evaporative cooling in the crossed dipole trap to reach degeneracy. After the initial cooling in the MOT, $N = 1.7 \times 10^8$ ^{87}Rb atoms at a temperature $T = 130\,\mu\text{K}$ are transferred to the quadrupole trap at the science cell. This is followed by 3 RF ramps for RF evaporation in the quadrople trap with a gradient of $180\,\text{G}\,\text{cm}^{-1}$, yielding $N = 2.4 \times 10^7$ atoms with $\text{PSD} = 4 \times 10^{-5}$ and $T = 42\,\mu\text{K}$. The dipole beams are also switched on, with the dipole laser output set to 77% ($38.5\,\text{W}$). While the WG power is servoed to $5.6\,\text{W}$, the MB is *not* servoed at this stage. Here,
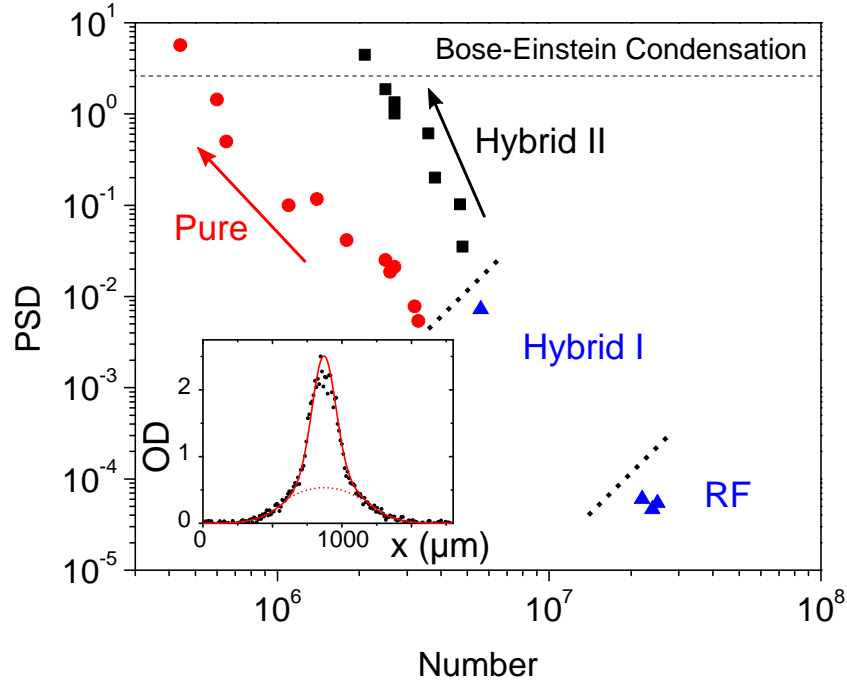
Figure 6.16: Evaporation trajectory to ^{87}Rb BEC in a pure optical dipole trap. The dashed line denotes the BEC transition point at PSD = 2.61. The dotted lines partition the evaporation into three stages, namely RF evaporative cooling in the magnetic trap (RF), evaporative cooling via MB ramp in a hybrid trap (Hybrid I), and direct evaporative cooling in a pure/hybrid trap via simultaneous MB and WG ramps (Pure/Hybrid II). Inset: Horizontal cross-section of the condensate column density of a bimodal cloud. The solid red curve is a double Gaussian fit where the dotted red curve shows the thermal fraction of the condensate.

the RF power applied to the MB AOD is kept at 50% diffraction efficiency, which gives an output power of 7.0 W.[3] In doing so, the thermal lensing effect in the AOD crystal at high RF power is reduced. The loading of atoms into the crossed dipole trap is completed by relaxing the quadrupole gradient to $30\,\mathrm{G\,cm^{-1}}$.

At this point, the trap depth of the MB is significantly larger than the WG, which causes the atoms to preferentially evaporate along the MB as shown in Fig. 6.15(a). In contrast, Fig. 6.15(c) shows that atoms will preferentially escape from the crossed dipole trap via the WG if the trap depth relation is reversed. Thus, the first stage of evaporative cooling performed in the hybrid trap is aimed at balancing the trap depths such that evaporation occurs along

---

[3]A pure crossed trap with the stated beam powers has a combined trap depth (along the beam) of $179\,\mu\mathrm{K}\times k_\mathrm{B}$.

both beams, as shown in Fig. 6.15(b). Knowing the beam waists allows us to calculate the power relation between the beams for a balanced trap: equating the equations for the trap depth for both beams (using Eq. 3.5 and Eq. 3.6) yields a simple relation between the beam powers P and waists w

$$P_{\mathrm{WG}} = \frac{w_{\mathrm{WG}}^2}{w_{\mathrm{MB}}^2} P_{\mathrm{MB}} = 2.47 P_{\mathrm{MB}}. \tag{6.7}$$

Using this equation, it is calculated that $2.3\,\mathrm{W}$ in the MB gives an equal trap depth as $5.6\,\mathrm{W}$ does in the WG. This power is reached by first ramping the laser output power from 77% to 35% in $1\,\mathrm{s}$ and keeping the AOD RF power constant at 50%. It is then followed by a $200\,\mathrm{ms}$ MB ramp in RF power whilst the laser power is kept constant. This method has an advantage of enhanced resolution for servoing the MB at power below $4.3\,\mathrm{W}$. At this point, $\mathrm{N} = 3.2 \times 10^6$ atoms with $\mathrm{T} = 8\,\mu\mathrm{K}$ and $\mathrm{PSD} = 7.8 \times 10^{-3}$ remain in the trap, which is shown in the 'Hybrid I' region marked in blue in the evaporation trajectory in Fig. 6.16. To proceed to condensation, we compare the differences of experimental sequences and evaporation trajectories between evaporation in a pure trap and a hybrid trap.

Pure trap

After $2\,\mathrm{s}$ of rethermalisation hold, the quadrupole gradient is slowly ramped off in $200\,\mathrm{ms}$ resulting a pure optical dipole trap. During this stage a small bias field ($\sim 1\,\mathrm{G}$) is ramped on to define the quantisation axis in the trap, which prevents atom loss from the optical trap due to spin flips to other states. This is followed by $3.25\,\mathrm{s}$ of linear ramps of MB and WG power and rethermalisation holds where the trap depths of both beams are kept the same. In the absence of levitation against gravity, vertical evaporation eventually dominates in the later stage of the cooling trajectory as the gravitational force becomes comparable to the dipole forces applied to the atoms. The evaporation trajectory is shown in red circles (marked 'Pure') in Fig. 6.16. Degeneracy is reached with pure condensates of $N = 5 \times 10^5$, which is comparable to the results obtained using the old crossed dipole trap ($N = 6 \times 10^5$) [68]. The final trap depth in the absence of levitation is $1.4\,\mu\mathrm{K} \times k_{\mathrm{B}}$ and the final trap frequencies are $2\pi \times (66, 103, 98)\,\mathrm{Hz}$.
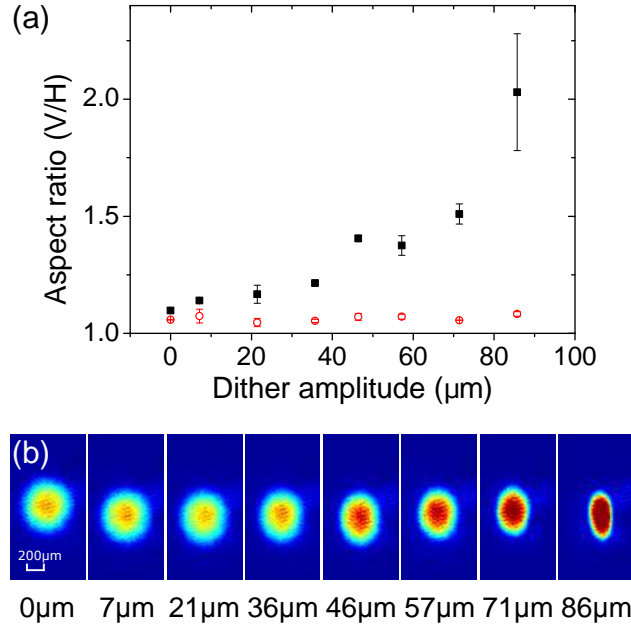
Figure 6.17: (a) The aspect ratio (vertical/horizontal) of the BEC (black square) and the thermal cloud (red circle) at 110 ms after release from the time averaged potential, as a function of the dither amplitude of the MB. (b) The absorption images of the BEC data in (a) at various dither amplitude.

Hybrid trap

In contrast to the pure trap experimental sequence, the quadrupole gradient is kept at $\sim 30\,\mathrm{G\,cm^{-1}}$ throughout the evaporation. Evaporation along the vertical direction thus dominates at all stages due to the magnetic confinement along the dipole beams. Over 16 s, 5 linear ramps of MB and WG power and rethermalisation holds are carried out, where the optimised evaporation trajectory is presented in black squares (marked 'Hybrid II' in black) in Fig. 6.16. One can immediately see that fewer atoms are removed for the gain in PSD in the process compared to the pure trap case, in which degeneracy is reached with $N = 1.1 \times 10^6$ atoms – about twice the number of atoms in the pure trap BEC. The final calculated trap depth is $\sim 820\,\mathrm{nK} \times k_\mathrm{B}$ and the trap frequencies are $2\pi \times (25, 39, 47)\,\mathrm{Hz}$.

6.7 Creation of an oblate BEC

In this section, we demonstrate the creation of an oblate BEC in an elongated trap. This is achieved by dithering the MB at the end of the evaporative cooling in the hybrid trap described in Section 6.6. In doing so, the shape of the

crossed trap is changed from near-spherical to elongated. By releasing a condensate from such an elongated trap, the cloud expands anisotropically, in which faster expansion is expected along the direction where the trap confinement is stronger. In the case of a non-interacting BEC, this effect is a consequence of the Heisenberg uncertainty principle, $\Delta x \Delta p > \hbar$, where Δx and Δp represent the spread in position and momentum respectively. Here, the tighter axis has a smaller spread in position Δx, and thus a bigger momentum spread Δp which results in a faster expansion of the condensate along that direction [183]. In the case of ^{87}Rb BECs where interatomic interactions are repulsive (^{87}Rb has a positive background scattering length of $a_s \sim 100\, a_0$ [184]), this effect is amplified as the repulsive interaction pushes the atoms further apart in the direction where the atoms are initially tightly confined [183].

The measurement is carried out by adding a dither ramp after degeneracy is reached with the use of the voltage multiplier described in Section 6.5. With the application of a 5 kHz oscillatory voltage input in a triangular waveform at V1, the dithering amplitude of the MB is ramped up by a straightforward linear voltage ramp at V2 to a target value in 100 ms. The atoms are then held in the time averaged potential for a further 100 ms. Throughout the dithering, the MB and WG beam powers remain constant. By switching both beams off, the atoms are released where the aspect ratio (vertical/horizontal) of the cloud is recorded after 110 ms TOF. As shown in Fig. 6.17(a) (and the absorption images in Fig. 6.17(b)), the aspect ratio increases with the dither amplitude, which confirms that the atomic samples remain condensed after the transfer into the elongated trap. In contrast, such feature of anisotropic expansion is absence for a thermal cloud[4], as shown in Fig. 6.17(a).

6.8 Summary

In this chapter, we have discussed the experimental upgrade of the magnetic coils and a new dipole trap. The introduction of the curvature and cancellation coils enables us to control the curvature of the magnetic field without adding a large magnetic bias field. To accommodate these coils alongside

---

[4]$N \sim 2 \times 10^6$ and PSD ~ 1.

with the quadrupole, bias, and shim coils, a compact coil mount is designed which enhances the optical access. The crossed dipole trap in a bow-tie configuration is replaced by two independent beams, namely the waveguide (WG) and the moving beam (MB), derived from a $50\,\text{W}$ $\lambda = 1070\,\text{nm}$ fibre laser. While the WG enters the science cell through the Dove prism perpendicularly, the MB, with the ability to displace the intersection along the WG driven by the AOD, enters the science cell along the horizontal imaging probe beam path. The homebuilt voltage multiplier circuit, which controls the RF frequency of the AOD, enables us to easily displace the dipole trap towards the Dove prism, as well as creating a time averaged potential. In order to avoid the deformation of the MB due to the thermal effect in the AOD crystal, we have shown that it is favourable to use both low input laser and RF powers whenever it is possible. We finish the chapter by demonstrating ^{87}Rb BEC creation in the newly implemented magnetic and optical setup.

Chapter 7

Generation of arbitrary optical potentials

7.1 Introduction

So far, we have realised the splitting of bright solitary waves at a narrow Gaussian potential. The second generation of the experiment allows the adjustment in dipole trap position and magnetic field curvature. One last bolt missing in the mechanism for realising the rotational interferometry experiment with bright solitary waves described in Chapter 2 is the ring shaped atomic trap.

Ultracold atomic gas experiments in a potential with a ring geometry have been of great interest in studies, including superfluidity [185], persistent current [186–188], and atomic superconducting quantum interference device (SQUID) [189, 190]. Many methods have been developed to generate such potentials, such as magnetic trap manipulation [191, 192], RF dressing [193], and optical trapping using a Laguerre-Gaussian beam [186] or the conical refraction property of biaxial optical crystals [194]. These robust ring geometries have yielded exciting experimental results.

As the level of complexity in the experiments advances, extending from ring potentials to more arbitrary optical potentials has become possible. We recall the implementation of dipole trapping via time-averaged potentials in

our new system. An additional AOM with a scanning axis orthogonal to its first counterpart would create a 2D drawing canvas. Already atom trapping in potentials generated through this method have been realised for condensate interference [195], atomic SQUID [189], and matter-wave circuits [196]. In addition, arbitrary shaped potentials can be created by applying an intensity mask with blue detuned optical potentials [197, 198].

In this chapter, we will focus on developing techniques of phase imprinting on a red-detuned Gaussian beam using a spatial light modulator (SLM). Part of the family of diffractive optical elements, such devices have been incorporated into cold atom experiments to generate arrays of dipole traps [199–203], arbitrary trap potentials [185, 204, 205], and atom guiding potentials [206]. As we will see shortly, the ability to generate desired trap geometries creates a whole new playground for experiments, which includes bright solitary waves in ring traps and degenerate gases in a 2D finite square well.

7.2 Spatial light modulator (SLM)

7.2.1 Phase modulation of light

From everyday life to laser optics, we are familiar with light focussing by an optical lens and light refraction by a prism. When a light field of wavelength λ is transmitted through such optical elements with reflective index η, it experiences a phase shift

$$\Delta\phi = 2\pi\frac{(\eta-1)l}{\lambda},\tag{7.1}$$

where l is the thickness of the optics. One can intuitively understand this by considering a light field with a source infinitely far away, incident perpendicularly on a classical converging lens. The plane wavefront experiences a continuous phase change in the radial direction of the lens, which results in a conversion to a spherical wavefront that converges to a focal point.

As the phase shift of wavefront has a periodicity of 2π, one can in fact design elements with $|l\eta/\lambda| < 1$ that reproduce the properties of classical
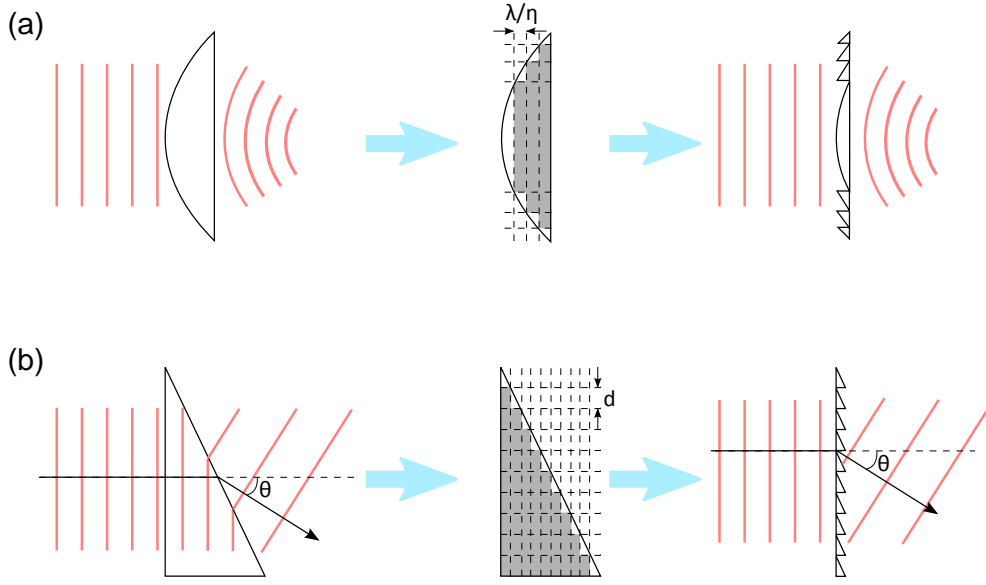
Figure 7.1: Generation of diffractive optics. (a) From a classical plano-convex lens (left) to a Fresnel lens (right). (b) From a refractive prism (left) to a blazed grating (right). The red lines represent the wavefronts of a monochromatic light while the black arrows perpendicular to the wavefronts show the propagation direction of the light. The material in the grey region is removed as it does not affect the final phase shift of the light.

optics. These optical components, such as the Fresnel lens, are known as the diffractive optical elements (DOEs) [207]. The transformation from a classical plano-convex lens to its Fresnel counterpart requires removal of blocks of material of thickness λ/η as shown in Fig. 7.1(a). Each block contributes to a phase shift of 2π and thus has no overall contribution to the phase. The resulting DOE, a Fresnel lens which modulates the phase of the incoming wavefront *smoothly* from 0 to 2π, is known as the *kinoform*. DOEs manipulate light patterns with high diffraction efficiency [208], thus there has been a great interest for optical engineers to design and fabricate DOEs that modify wavefronts into desired patterns.

Consider a right angle refraction prism as shown in Fig. 7.1(b). With the same principle, truncating the gradient in a periodicity of d resembles the blazed grating. The relation between the grating period d and the diffraction angle θ_m of light incident on a reflective grating at an angle θ_i is given by

$$m\lambda = d(\sin\theta_i + \sin\theta_m), \tag{7.2}$$
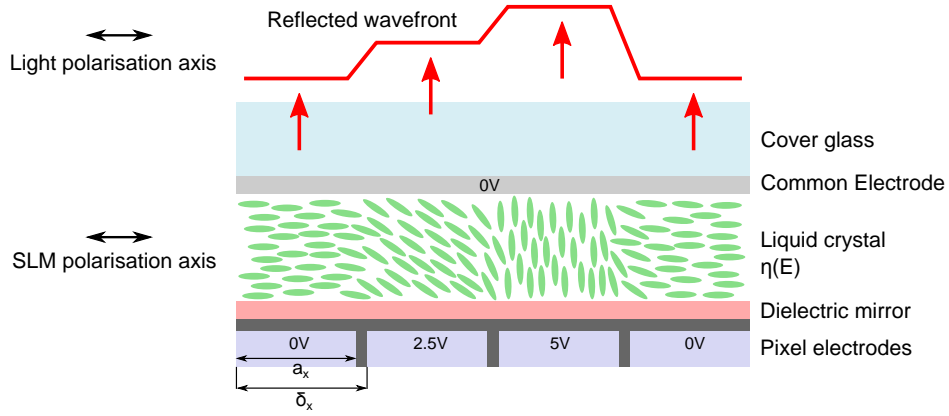
Figure 7.2: Cross-section of the SLM panel. The orientation of the liquid crystal, hence the refractive index η, depends on the electric field E applied by the pixel electrodes. The light field, reflected from the dielectric mirror, double-passes the crystal layer and picks up a phase modulation depending on the voltage applied at each individual pixel. Note that the example voltages are only for illustrative purpose.

where m is the diffraction order. These traditional DOEs are tailored for specific applications, and therefore lack flexibility as a new specimen is required even for a minor change of use. In the next section, we will see that the more advanced, reconfigurable SLM overcomes this problem of inflexibility.

7.2.2   Working principle

The SLM modulates the phase of the incident light field via a reconfigurable phase imprinting array. A typical configuration is illustrated in Fig. 7.2. In the absence of an applied voltage at the electrodes, the elongated liquid crystal molecules are aligned such that their long axes are parallel to the *SLM polarisation axis* and perpendicular to the optical axis. An application of voltage at each electrode, which is independently controllable, produces an electric field E that rotates the long axis towards the optical axis. A light field with its polarisation axis aligned parallel to the SLM polarisation axis would hence experience an electric field dependent refractive index $\eta(E)$ as it passes through the liquid crystal. This allows the phase to be spatially modulated and hence a spatially dependent phase information can be imprinted on to the reflected light.

The pixelated SLM plane is illustrated in Fig. 7.3. Across the area of $L_x \times L_y$, the panel comprises $N_x \times N_y$ pixels. Each pixel has an aperture with an area

Manufacturer	Boulder Nonlinear Systems (BNS)
Model	PDM512-1064-DVI (Standard XY series)
N_x, N_y	512, 512
L_x, L_y	7.68 mm, 7.68 mm
δ_x, δ_y	15 μm, 15 μm
β	100%
Damage threshold	10 W cm^{-2}

Table 7.1: Technical specifications of the SLM in our laboratory.

of $\delta_x \delta_y$, within which $a_x a_y$ is the effective pixel area. As phase imprinting only applies to the light field incident on the effective region, the ratio, known as the 'fill factor' $\beta = a_x a_y / \delta_x \delta_y$, defines the theoretical diffraction efficiency of the system. The closer β is to unity, the less light ends up in the zeroth order unmodulated fraction. The technical specifications of the SLM in our experiment are listed in Table 7.1. In practice, we measure $\sim 65\%$ in first order diffraction $m = 1$, $\sim 10\%$ in zeroth order $m = 0$, and the rest at other diffraction orders $m < 0$ and $m \geq 2$. This proportion is independent of the phase pattern. The 25% of light shared between these higher orders appear as ghost copies of the original image. They can be separated from the $m = 1$ image via a diffraction grating, which will be discussed in Section 7.3.

The SLM is operated with a NVIDIA graphics card, which supports a voltage scale of $2^{16} = 65536$, and is controlled using BNS's control software that translates a 24-bit 512×512 pixels kinoform in `.bmp` format into the corresponding voltages in the liquid crystal array[1]. Due to the nonlinear response of the liquid crystal, the voltage calibration supplied by the manufacturer, known as the look-up table (LUT), is required for the SLM to function properly. The kinoforms are generated using homebuilt MATLAB codes.

To see how a phase modulated light field can be reconstructed to form a desired intensity pattern, let us first consider the time independent complex amplitude

---

[1]The 24-bit image comprises of 8-bits of colour blue, 8-bits of green, and 8-bits of red. The hardware ignores the blue bits, thus operation of the SLM requires a 16-bit graphics card.

$$U(\mathbf{r}) \equiv a(\mathbf{r}) \exp\left(-i\phi(\mathbf{r})\right), \tag{7.3}$$

which satisfies the Helmholtz equation

$$(\nabla^2 + k^2)U(\mathbf{r}) = 0, \tag{7.4}$$

where $k = 2\pi/\lambda$ is the wavevector. A plane wave propagating along the z-direction incident on the x-y-plane at $z = 0$ can be expressed as a Fourier transform of a field comprised of an infinite number of infinitesimal plane waves as

$$U_0(x, y) = \int_{-\infty}^{\infty} \int_{-\infty}^{\infty} \chi_0(u, v) \exp\left(i2\pi(ux + vy)\right) \, du \, dv, \tag{7.5}$$

where $\chi_0(u, v) \, du \, dv$ represents the amplitude of such waves. In practice, the light field incident on the liquid crystals on the SLM often overfills the SLM pixelated panel. By defining $U_r(x, y)$ as the complex amplitude of the *reflected* light by the illuminated SLM pixels, we write

$$U_r(x, y) = U_0(x, y)t_A(x, y), \tag{7.6}$$

where $t_A(x, y)$ is known as the amplitude transmittance and a full expression can be found in [209]. Assuming that the propagation distance $z \gg \lambda$ and the diffraction is small compared to the path length, i.e. $(x^2 + y^2)^{1/2} < z$, the paraxial and Fresnel approximations are valid [210, 211]. The complex amplitude can then be simplified to

$$U_z(x, y) = U_r(x, y) * h(x, y), \tag{7.7}$$

where the convolution kernel $h(x, y)$ is defined as

$$h(x, y) = \frac{e^{ikz}}{i\lambda z} \exp\left[i\frac{\pi}{\lambda z}\left(x^2 + y^2\right)\right]. \tag{7.8}$$

This diffraction integral of a light field through free space can be readily extended to the Fourier transform properties of a lens. Imagine a positive lens with a large aperture and minimal aberration, the pupil effect of such

optics can be neglected [210]. Placing the lens at a distance Δ from the plane of transmittance (SLM plane) as shown in Fig. 7.3, the resulting light field U_f at the focal plane f from the lens is related to U_r by

$$U_f(u,v) = \frac{1}{i\lambda f} \exp\left[i\frac{k}{2f}\left(1 - \frac{\Delta}{f}\right)(u^2 + v^2)\right] \mathcal{F}\left[U_r(x,y)\right]\left(\frac{u}{\lambda f}, \frac{v}{\lambda f}\right),$$

(7.9)

where $\mathcal{F}[\,\cdot\,](u/\lambda f, v/\lambda f)$ represents the forward Fourier transform evaluated at spatial frequencies $(u/\lambda f, v/\lambda f)$ [210, 211]. Note that in the case of $\Delta = f$, the additional quadratic phase in Eq. 7.9 vanishes, which leaves us an exact Fourier transformation between the SLM plane and the focal (Fourier) plane. While the Fourier transform relation is not exact for $\Delta \neq f$ due to the presence of the quadratic phase, such an additional phase factor has no consequence in the intensity distribution at the Fourier plane $I_f(u,v)$ as it only involves $I_f(u,v) = |U_f(u,v)|^2$. This relation allows us to reshape the light field at the Fourier plane by applying a phase modulation such that the Fourier transformation of the resulting U_r is the desired intensity pattern. However, in practice, an analytical solution of U_r with the correct phase information only exists for a small class of patterns, which will be discussed in Section 7.4. Fortunately, there are powerful algorithms developed in which U_r can be numerically calculated such that the resulted U_f is very close to the desired pattern. This will be discussed in Section 7.3.

7.2.3 Optical setup

The testing and optimisation of kinoform computations are carried out using the optical setup shown in Fig 7.3. We use a fibre coupled 1064 nm laser beam (Roithner LaserTechnik RLT1060-150G), which is collimated to a desired beam radius. For initial measurements, the beam is collimated to a $1/e^2$ radius of $\sim 5\,\mathrm{mm}$ in order to cover the entire SLM array. At this beam size, the intensity at each pixel is roughly comparable, thus the wavefronts incident on the SLM can be estimated as plane waves. The polarisation axis of the light beam is aligned parallel to the SLM polarisation via the $\lambda/2$ waveplate and the PBS. When the axes are parallel (perpendicular), we measure $< 10\%$ $(> 75\%)$ of the incoming light resulted in the zeroth order
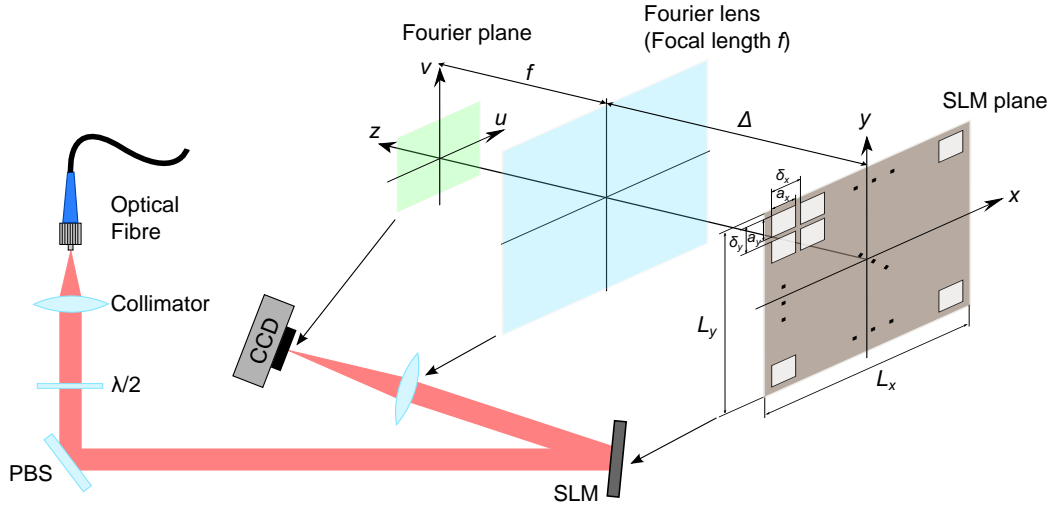
Figure 7.3: Typical optical setup for SLM testing. On the right hand side it shows the propagation of the modulated beam from the pixelated SLM plane (brown) at $z = 0$, through the Fourier lens of focal length f (blue) at $z = \Delta$ to the focal plane, or Fourier plane (green), at $z = \Delta + f$. Both the light and SLM polarisation axes are into the page.

beam. To maintain a high performance in phase modulation, the beam is incident on the SLM at a shallow angle (typically $\sim 10°$) from the normal. The reflected beam is collected and focussed by an achromatic lens with focal length $f = 150\,\text{mm}$ placed at a distance $\Delta = f$ from the SLM.[2] This is the Fourier lens described in Section 7.2.2, which creates an intensity pattern at the Fourier plane at $z = 2f$. A CCD camera (Andor LUCA, pixel size $= 8\,\mu\text{m}$) is placed in the Fourier plane for imaging the resulting intensity pattern.

7.2.4 Region of optimal performance

Before looking into the generation of the phase patterns and the intensity patterns at the Fourier plane, it is necessary to understand the limits of the optical setup. What is the smallest object in the Fourier plane? It is equivalent to the maximum *resolution* in the plane. For any optical system, it is defined by the diffraction limit, which is the distance between the first zeroes in the diffraction pattern.

---

[2]It should be reminded that, from the discussion in Section 7.2.2, the choice of Δ does not affect the intensity pattern at the Fourier plane.
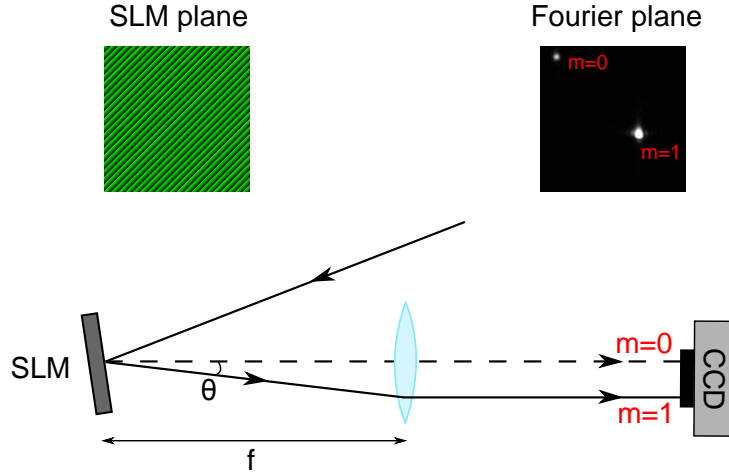
Figure 7.4: Experimental setup to measure the maximum diffraction angle. The SLM plane shows the kinoform of a grating with $a = 20$ and $b = 20$, where a and b are as defined in the main text. The Fourier plane shows the image of the displacement of the diffraction limited spot.

As our SLM has a fill factor of $\beta = 100\%$, we can simplify the problem by considering the whole SLM plane as a single square aperture as opposed to an array of disconnected pixels. Thus the amplitude transmittance in Eq. 7.6 takes a simplified form of

$$t_A(x, y) = \text{rect}\left(\frac{x}{L_x}\right) \text{rect}\left(\frac{y}{L_y}\right), \tag{7.10}$$

where the rectangular function is defined as

$$\text{rect}\left(\frac{x}{l}\right) = \begin{cases} 1 & |x| < l/2 \\ 0 & \text{otherwise.} \end{cases} \tag{7.11}$$

Substitute this to Eq. 7.9 and note that the intensity of a light field $I_f(u, v) = |U_f(u, v)|^2$, we retrieve the Fraunhofer intensity pattern from an rectangular aperture[3]

$$I_f(u, v) = \left(\frac{L_x L_y}{\lambda f}\right)^2 \text{sinc}^2\left(L_x \frac{u}{\lambda f}\right) \text{sinc}^2\left(L_y \frac{v}{\lambda f}\right). \tag{7.12}$$

By taking the cross-section of $I_f(u, v)$ along u (or v due to symmetry), it is straightforward to find the diffraction limit of the system,

---

[3]Here we assume the light field illuminating the aperture is a monochromatic plane wave with a unit-amplitude for simplicity.
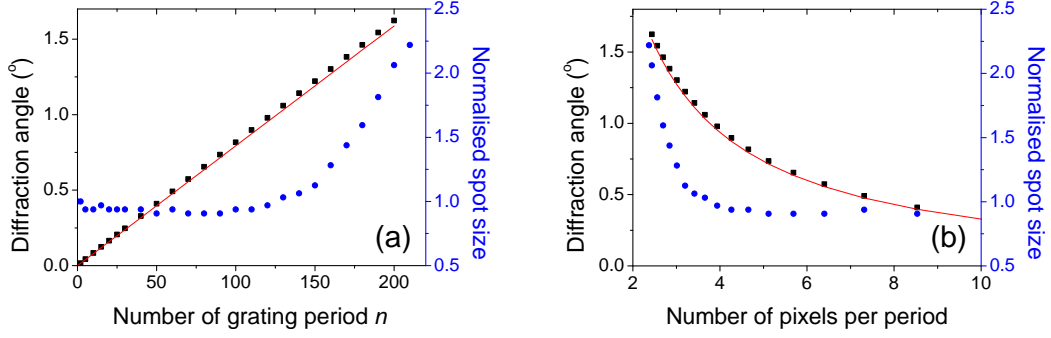
Figure 7.5: The change of diffraction angle (black) and normalised spot size (blue) with respect to (a) number of grating periods and (b) number of SLM pixels per grating period d. The red curves are expected values. Note that (b) only plots the data points for the number of grating period > 50, or $< 10\,\mathrm{px}$ per period.

$$a_{u,v} = \frac{\lambda f}{L_{x,y}}, \tag{7.13}$$

from which we define $a_{u,v}$ as the pixel size on the Fourier plane. For the optical setup described in Section 7.2.3, such a limit is calculated to be $a_{u,v} = 20.78\,\mu\mathrm{m}$. In addition, as we will see in Chapter 8, the Fourier plane can be rescaled and projected with the use of a telescope after the Fourier lens. In the case where the telescope consists of two lenses with focal lengths f_1 and f_2, the pixel size on the *new* Fourier plane is simply $a_{u,v}f_2/f_1$.

Now, is there an upper limit to the size of the image reconstructed at the Fourier plane? If there is, what is the limiting factor? To answer these questions, we remind ourselves that the SLM is a reconfigurable DOE that modulates the complex phase of a light field. A straightforward, simple method of determining the upper limit is to replicate the effect of a classical DOE and observe deviation from the expected effect, if any.

We recreate the diffraction grating discussed in Section 7.2.1 [208]. The phase of such a DOE is

$$\phi_{\mathrm{grating}}(x, y) = \left(\frac{2\pi a}{L_x} x + \frac{2\pi b}{L_y} y \right) \bmod 2\pi, \tag{7.14}$$

where a and b are the number of grating periods across the SLM in the x-direction and y-direction respectively. The total number of grating period

across the SLM is hence $n = a + b$, while each grating period has size

$$d = \frac{L_y}{b} \sin\left(\arctan \frac{L_x b}{L_y a}\right). \tag{7.15}$$

By placing the Fourier lens at $z = f$ as illustrated in Fig. 7.4, all the output beams after the lens will be parallel to the zeroth order axis marked $m = 0$ regardless of the diffraction angle. Hence the displacement x_d of the first order ($m = 1$) diffraction limited spot is simply given by

$$x_d = f \sin \theta_1 = \frac{f\lambda}{d}. \tag{7.16}$$

Fig. 7.5(a) shows that the diffraction angle θ_1, evaluated from x_d measured using the CCD camera, is in excellent agreement with the predicted curve (red) calculated from Eq. 7.16. Since the diffraction angle is less than $1.5°$, the small angle approximation is valid and hence the linear relationship between θ_1 and d. More interestingly, the spot size (blue) only remains constant for the number of grating periods up to $n \sim 130$. That is, as shown in Fig. 7.5(b), when the number of SLM pixels per grating period drops below 4. This is because one requires at least 4 discrete levels per grating period for the binary optic approximation[4] to the grating to hold [210]. With less than 4 pixels per period, the overall phase imprinted by the SLM no longer describes the diffraction grating which leads to an image distortion (here we see a smeared spot) at the Fourier plane. Hence, we conclude from Eq. 7.16 that the image at the Fourier plane should be kept within the radius

$$R_{\mathrm{max}} = \frac{f\lambda}{4a_{x,y}} \tag{7.17}$$

from the zeroth order spot. In our setup where an $f = 150\,\mathrm{mm}$ Fourier lens is used, the lower limit $a_{u,v}$ (the size of one pixel on the calculated Fourier plane, from Eq. 7.13) and upper limit R_{max} are calculated to be $21\,\mu\mathrm{m}$ and $2.7\,\mathrm{mm}$ respectively.

---

[4]Binary optical elements are discretised, step-like approximations to ideal continuous DOEs. They are often used in micromachining, with step size commonly on the order of a few microns.
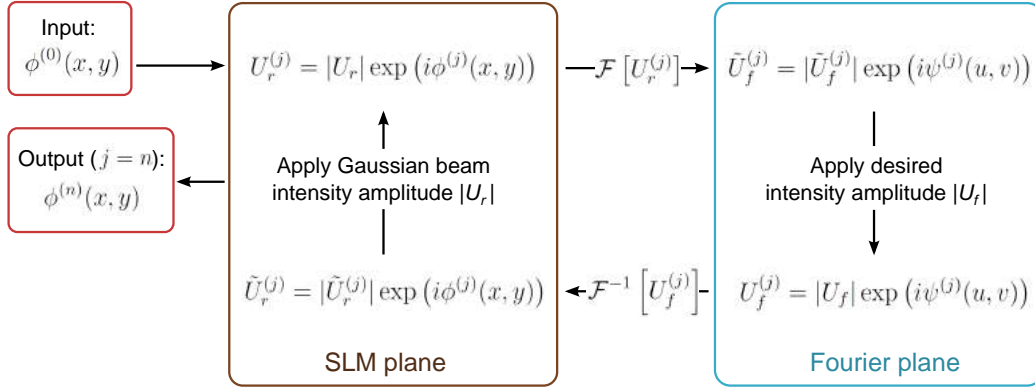
Figure 7.6: Illustration of the traditional Gerchberg-Saxtom algorithm. Starting off with a first phase guess $\phi^{(0)}(x,y)$ and an intensity profile $|U_r|$ on the SLM plane, the light field propagates back and forth between the SLM and Fourier planes. Subject to constraints in amplitude and free-varying phases, a final phase is retrieved after $j = n$ iterations.

7.3   Iterative Fourier Transform Algorithm

To achieve the goal of generating arbitrary optical traps, one must generate the kinoform that forms the desired intensity at the Fourier plane with its complexity beyond the likes of traditional DOEs. However, unlike the previous example of a diffraction grating where the kinoform is constructed analytically, such a method is not applicable to most intensity profiles. This *phase retrieval* problem is often approached by acquiring a numerical solution from which its Fourier counterpart is a close approximation to the desired intensity pattern. While different methods for phase retrieval have been developed such as the direct minimisation of a cost function [212] and the direct binary search [213, 214], the main method is typically the computationally efficient Iterative Fourier Transform Algorithm (IFTA) where the kinoform is constructed by propagating the light field to and from the SLM plane and the Fourier plane iteratively.

7.3.1   Gerchberg-Saxton algorithm

The most basic form of the IFTA is known as the Gerchberg-Saxtom algorithm [215–217]. Illustrated by the block diagram in Fig. 7.6, the convergence of the phase at the SLM plane is achieved by applying constraints to the amplitude of the complex amplitudes and allowing the phase in both SLM and Fourier domains to vary. We will discuss the algorithm briefly.

We first express the light fields U_r and U_f (the light fields at the SLM plane and the Fourier plane respectively), as a combination of a real amplitude and a complex phase. The first step of the algorithm is to choose an educated first phase guess $\phi^{(0)}(x, y)$ (the importance of a 'good' $\phi^{(0)}$ will be discussed in Section 7.3.4). $\phi^{(0)}$, together with the real amplitude $|U_r|$ which represents the beam profile of the input Gaussian beam apodised by the physical boundaries of the SLM panel, are the two domains of the input complex amplitude $U_r^{(1)}$. In the second step, we apply a Fast Fourier Transform (FFT) to $U_r^{(1)}$ to obtain $\tilde{U}_f^{(1)}$ with a phase $\psi^{(1)}(u, v) = \arg\left(\tilde{U}_f^{(1)}\right)$. In physical terms, this step is equivalent to the Fourier transform of the light field by the lens.

At this point the resulting amplitude $|\tilde{U}_f^{(1)}|$ is replaced by the target amplitude, related to the target intensity profile $I_f(u, v)$ by $|U_f| = (I_f(u, v))^{1/2}$. The new complex amplitude $U_f^{(1)}$ is subsequently reprojected to the SLM plane via an inverse Fourier transform. By applying the amplitude constraint, i.e. replacing the arbitrary amplitude $|\tilde{U}_r^{(1)}|$ with the original $|U_r|$, we have completed one iteration and obtained an evolved phase $\phi^{(1)}(x, y) = \arg\left(\tilde{U}_r^{(1)}\right)$. Repeating the algorithm will see the evolved intensity profile $|\tilde{U}_f^{(j)}|^2$ converge towards the target intensity I_f [215] as the error between these two intensity profiles minimises. At $j = n$th iteration, the iteration is terminated manually and outputs the final phase $\phi^{(n)}(x, y)$ as the kinoform. The choice of n will be discussed in Section 7.4.3.

7.3.2 Mixed-Region Amplitude Freedom (MRAF) algorithm

The straightforward Gerchberg-Saxton algorithm has a main shortcoming that the modulus constraints imposed on the SLM and the Fourier planes are non-convex[5] [218, 219]. The convergence is hence poor as there exist many local minima during the projection. The Mixed-Region Amplitude Freedom (MRAF) algorithm is a modified version of the Gerchberg-Saxton algorithm which improves the quality of the outcome image vastly by intro-

---

[5]Optimisation problems are non-convex when there exist many different local minima. In contrast, for a convex optimisation, local minima are themselves the global minimum.
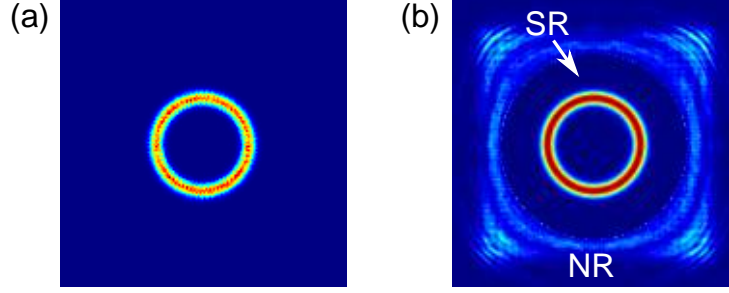
Figure 7.7: Comparison between calculated intensity profiles generated using (a) Gerchberg-Saxton algorithm and (b) MRAF with $r_{\rm SR} = 1\,{\rm mm}$ and $m = 0.6$. The target intensity is a ring with radius $r = 0.5\,{\rm mm}$, width $\sigma = 100\,\mu{\rm m}$, and the Fourier lens has focal length $f = 150\,{\rm mm}$.

ducing an additional degree of freedom [220].

Central to the enhancement of the image convergence of the MRAF algorithm is the introduction of an amplitude freedom in addition to the phase freedom of its predecessor. As the target image often only occupies a small fraction of the Fourier plane, suppressing the target intensity of the rest of the plane outside the region of interest to zero imposes unnecessary restriction to the convergence. MRAF modifies the algorithm by partitioning the Fourier plane into a signal region and the noise region. While the signal region, often just slightly larger than the target image, only allows the phase freedom, both the amplitude and phase domains are free parameters in the noise region. The relative distribution of the optical power in the two regions is quantified by the mixing parameter m, $0 \leq m \leq 1$ and the third step in the block diagram Fig. 7.6 is modified to

$$
U_f^{(j)} = \left[\sqrt{ m|U_f|^2 \big|_{\rm SR} \frac{\sum\limits_{u,v} |\tilde{U}_f^{(j)}|^2}{\sum\limits_{u,v \in {\rm SR}} |U_f|^2} } \right.
$$

$$
\left. + \sqrt{ (1-m)|\tilde{U}_f^{(j)}|^2 \big|_{\rm NR} \frac{\sum\limits_{u,v} |\tilde{U}_f^{(j)}|^2}{\sum\limits_{u,v \in {\rm NR}} |\tilde{U}_f^{(j)}|^2} } \right] \exp\left(i\psi^{(j)}(u,v) \right),
$$

(7.18)

where SR and NR denote the signal region and the noise region respectively.

In particular, throughout the rest of the chapter, we define SR as the region within the signal radius r_{SR} from the centre of the image. Fig. 7.7(b) shows the generation of a ring using the MRAF algorithm where a portion of the optical power is expected to be scattered in the noise region. This is compared with the same target intensity generated using the Gerchberg-Saxton algorithm as shown in Fig. 7.7(a). In practice, the mixing parameter m is determined empirically and usually requires executing the MRAF algorithm multiple times with different combinations of parameters such as r_{SR} and first phase guess $\phi^{(0)}$.

The MRAF algorithm is implemented to generate the phase patterns for the rest of this chapter. The output phase of the algorithm is added linearly to ϕ_{grating} to form the final kinoform. In particular, $a = b = 70$ (as defined in Eq. 7.14)[6] is chosen for the diffraction grating in order to shift the centre of the intensity pattern away from the zeroth order spot by 2.06 mm. This also eliminates the interference between the desired intensity pattern with its higher order ghost images [221]. Fig. 7.8(a) and (b) are examples of the final kinoform and the calculated intensity pattern (MRAF, $m = 0.3$, iteration $n = 50$) of a ring with $r = 1$ mm and width $\sigma = 100 \, \mu$m.

In principle, the quality of the convergence of the MRAF algorithm would yield a smooth and accurate intensity pattern on the Fourier plane. However, as shown in the camera image in Fig. 7.8(c), the Gaussian ring suffers from random, disjointed speckles which leads to a large discrepancy between the calculated and the measured image. It is not suitable to implement a trapping potential with such rapid intensity fluctuation. To create a speckle-free image, and thus a smooth potential, we first need to understand the origin of the speckles.

7.3.3   Random phase and speckles

The MRAF algorithm builds on the free varying phase domains on both planes. With no constraints imposed on the phase on the Fourier plane, it is likely that the phase $\psi^{(n)}(u, v)$ (which we have had no interest in thus

---

[6]This translates to $d = 78 \, \mu$m.
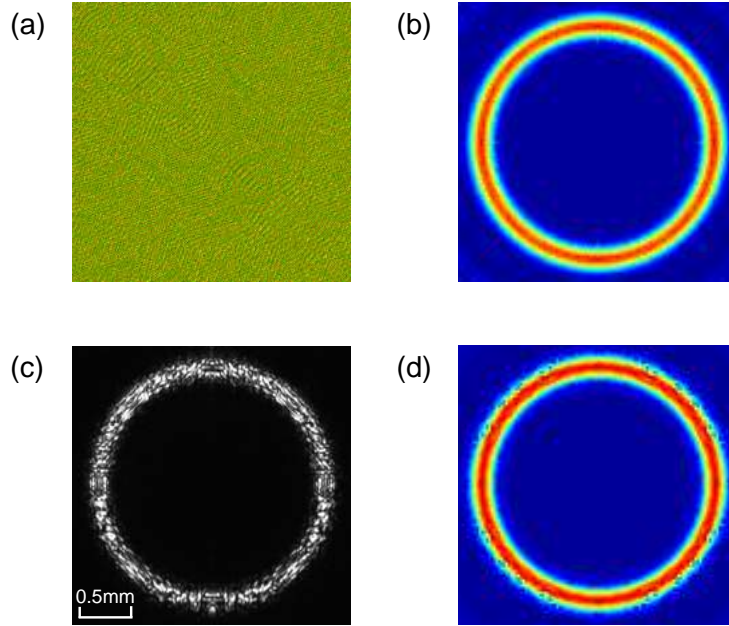
Figure 7.8: Generation of ring of $r = 1\,\text{mm}$ and $\sigma = 100\,\mu\text{m}$. (a) The kinoform at the SLM plane. (b) Calculated target image. (c) Measured intensity pattern at the Fourier plane. The ring is heavily distorted by speckles. (d) A calculated target image with a different first phase guess $\phi^{(0)}$. The ring contains multiple optical vortices which appear as intensity dips.

far) evolves to a random pattern with erratic spatial variation. Any adjacent pixels on the Fourier plane can thus be exactly, or close to, π out of phase. Since the light field from a laser source is *coherent*, we can deduce that the origin of the speckle in the images is a local reduction in intensity due to the destructive interference between the pixels.

The speckle problem is an intrinsic property of imaging with coherent light [210]. Different methods for speckle suppression in holograms have been developed, such as implementation of a partially coherent light source [222–225] or by means of time averaged intensity patterns of fast changing or superimposing multiple kinoforms [226–230]. These techniques often require a special or multiple laser source(s), a continuous change in polarisation, or continuously refreshing the kinoform (from which the maximum refresh rate of our SLM is only 60 Hz) and hence they are not applicable to ultracold atomic experiments.

7.3.4   Optical vortices and first phase guess

A second contributor to the intensity dips is the introduction of optical vortices. These are a result of phase singularities at which 0 to 2π phase windings occur, analogous to the fundamental mode of a Laguerre-Gaussian beam. If one wishes to remove such topological features, phase unwinding is required which disrupts the error-reduction MRAF algorithm. As a result, once the optical vortices form in the Fourier plane, they are very difficult to eliminate and therefore they remain throughout the later iterations [204]. To improve the control of the phase evolution, a technique of padding the input field based on the Shannon Sampling Theorem [204, 210, 231] has been widely implemented. Although there is a trade off in the efficiency of the diffracted light, one sees a sufficient drop in vortex numbers. Furthermore, it has been shown that a slowed convergence, such that in each iteration the new estimate phase $\psi^{(j)}$ only replaces part of the previously calculated value $\psi^{(j-1)}$, avoids the emergence of phase singularities [232].

These singularities are easily seen if one is careless with the first phase guess $\phi^{(0)}$. As an example, Fig. 7.8(d) shows a calculated image with multiple optical vortices on the outside edge of the ring. The only difference between Fig. 7.8(b) and (d) is that while the former uses a phase that resembles a ring as $\phi^{(0)}$, a phase of a defocussed Gaussian spot (also employed in [204]) is used for the input to generate the latter.

Indeed, as stressed by the original proposal of MRAF [220], the first phase guess $\phi^{(0)}$ as a controlled input to the algorithm, has a strong effect on the quality of the phase retrieval. As it is shown that a different choice of $\phi^{(0)}$ could result in a different phase $\psi^{(n)}$ (to generate rings with, and without, optical vortices), we will show in the next section that utilising this input freedom can lead to a more slowly varying output phase.

7.4   Analytical first phase guess

In order to create a smooth trapping potential, the phase $\psi^{(n)}$ should be continuous across the Fourier plane and absent of singularities. In identifying
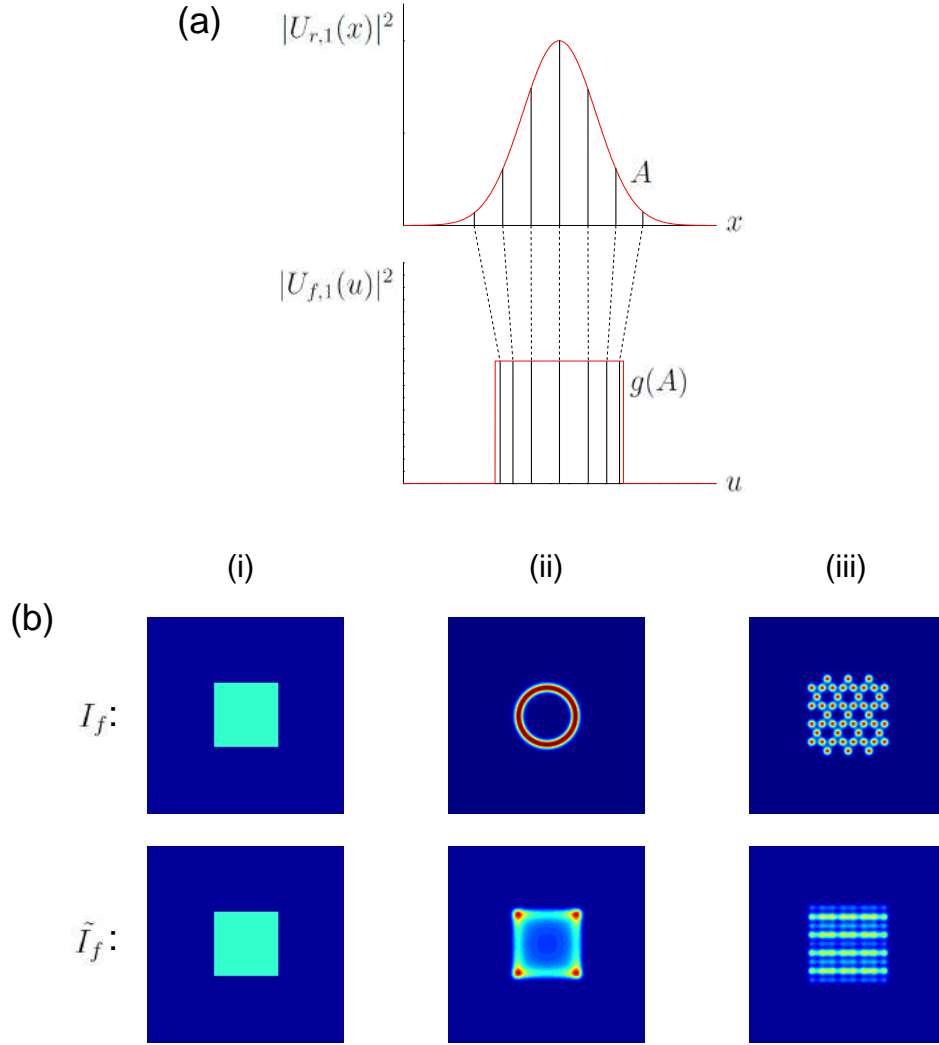
Figure 7.9: Geometrical beam shaping. (a) An analytically determined coordinate transformation g maps the Gaussian beam profile A into a rectangular profile $g(A)$, which is a separable intensity function. The illustration is adapted from [221, 233]. (b) Calculation of the input intensity $\tilde{I}_f$ for first phase guess of target intensities I_f of shapes (i) $1\,\text{mm}\times1\,\text{mm}$ square, (ii) Gaussian ring with $r = 0.5\,\text{mm}$, $\sigma = 100\,\mu\text{m}$, and (iii) Kagome lattice with each lattice site a Gaussian profile with $1/e^2$ radius $= 40\,\mu\text{m}$. $\tilde{I}_f$ as a close approximation of the target I_f, which is now separable in cartesian coordinates.

a 'good' first phase guess $\phi^{(0)}$, such that it yields a good approximation after the first Fourier transform with a smooth phase $\psi^{(0)}$, the following iterations would see a restricted evolution of $\psi^{(j)}$. This is due to a quick convergence as the algorithm starts at a point close to a local minimum where the phase is slowly varying.

7.4.1 Geometrical beam shaping

Let us take a step back to remind ourselves of the motivation for using the MRAF algorithm. The iterative algorithm is used to generate an image which stands as a good approximation to the target intensity pattern because the exact phase solution to most 2D Fourier transforms is often extremely difficult to obtain. There are, however, a small class of shapes where it is possible to find the exact analytical expression, one of which is where the target intensity pattern I_f is separable in the coordinates of the Fourier plane. This direct mapping from the SLM plane to the Fourier plane is known as *geometrical beam shaping*.

We follow closely the treatment in [221, 233]. Consider a function $g : \mathbb{R}^2 \to \mathbb{R}^2$ which defines a coordinate transform $g(x, y) \to (u, v)$, i.e. mapping the cartesian coordinates from the SLM plane to the Fourier plane. The phase retrieval consists of two steps: 1. to identify the function g that transforms a Gaussian beam shape to a particular intensity pattern, and 2. to express the phase ϕ in terms of g.

In an ideal case where no beam power is lost, we can express the geometrical beam shaping from an area A on the SLM plane as

$$\int_A |U_r(x, y)|^2 \, \mathrm{d}x \, \mathrm{d}y = \int_{g(A)} |U_f(u, v)|^2 \, \mathrm{d}u \, \mathrm{d}v, \tag{7.19}$$

where we simply equate the total intensity of the Gaussian beam $I_r(x, y)$ (LHS) to the target intensity $I_f(u, v)$ (RHS)[7]. Hence we can write

$$g(A) = I_f^{-1} \left[I_r(A) \right], \tag{7.20}$$

---

[7]We remind ourselves that the intensity and complex amplitude are related by $I = |U|^2$.

if both of the intensity functions can be found *and* are invertible. This applies to the special case we are considering, namely the intensity profiles are separable such that we can write

$$I_r(x,y) = \int_{-\infty}^{x} |U_{r,1}(x')|^2 \, \mathrm{d}x' \int_{-\infty}^{y} |U_{r,2}(y')|^2 \, \mathrm{d}y' = I_{r,1}(x)I_{r,2}(y) \qquad (7.21)$$

for the input, and similarly

$$I_f(u,v) = \int_{-\infty}^{u} |U_{f,1}(u')|^2 \, \mathrm{d}u' \int_{-\infty}^{v} |U_{f,2}(v')|^2 \, \mathrm{d}v' = I_{f,1}(u)I_{f,2}(v) \qquad (7.22)$$

for the output intensity. The mapping now becomes separable, Eq. 7.20 takes the form $g(x,y) = (g_1(x), g_2(y))$ where

$$g_1(x) = I_{f,1}^{-1}\left[I_{r,1}(x)\right] \quad \text{and} \quad g_2(y) = I_{f,2}^{-1}\left[I_{r,2}(y)\right]. \qquad (7.23)$$

According to the analysis in [234], one can realise the above coordinate transformation in a Fourier transform picture where the phase is expressed in terms of $g_1(x)$ and $g_2(y)$, and explicitly,

$$\phi_{\text{analytical}}(x,y) = \frac{2\pi}{\lambda f}\left(\int_{-\infty}^{x} g_1(x') \, \mathrm{d}x' + \int_{-\infty}^{y} g_2(y') \, \mathrm{d}y'\right). \qquad (7.24)$$

The factor at the front is a result of the specific transformation with a perfect lens f, where the output phase of the coordinates (u,v) at the Fourier plane is related to the input phase at the SLM plane at a spatial frequency $(u/\lambda f, v/\lambda f)$ as discussed in Section 7.2.2. It should be noted that the geometrical beam shaping maps the adjacent points on the SLM plane to adjacent points to the Fourier plane. Therefore, in principle the phase ψ at the Fourier plane is smooth providing $\phi_{\text{analytical}}(x,y)$ is smooth and continuous. As an example, Fig. 7.9(a) illustrates the beam shaping from a Gaussian profile to a rectangular function through coordinate transform g.

7.4.2   Analytically approximated first phase guess

Our goal is to find a good mechanism to calculate a good first phase guess which yields a good starting point for MRAF from which $\psi^{(n)}(u,v)$ remains smooth after error minimisation. However, so far the analytical phase can only be exactly solved if I_f is separable in the assigned orthogonal coordinates. Fortunately, while an exact solution does not exist for more complicated shapes, a close approximation to I_f, which in itself is separable, proves to remain a very good initial input that yields a smooth $\psi^{(j)}(u,v)$ [221]. The approximation $\tilde{I}_f$ can be obtained by forced separation of coordinates via

$$\tilde{I}_f(u,v) = \int_{-\infty}^{u} |U_f(u',v)|^2 \, \mathrm{d}u' \int_{-\infty}^{v} |U_f(u,v')|^2 \, \mathrm{d}v'. \qquad (7.25)$$

In practice, the target intensity pattern I_f (in $N_x \times N_y$ pixels) is first integrated along its two orthogonal axes, forming two vectors with lengths $N_x \times 1$ and $1 \times N_y$, which represent the intensity sums along the axes. A new intensity pattern $\tilde{I}_f$ is constructed from a tensor product between these two vectors. This new intensity profile is now separable and thus a phase $\phi_{\mathrm{analytical}}(x,y)$ can be obtained following the same procedure described in Section 7.4.1. $\tilde{I}_f$ of a square (here $\tilde{I}_f = I_f$ as the square is separable in cartesian coordinates), a ring, and a Kagome lattice are shown in Fig. 7.9(b).

In addition, the calculated phase $\phi_{\mathrm{analytical}}(x,y)$ can be multiplied by a prefactor of choice before being input into the MRAF algorithm as the first phase guess $\phi^{(0)}(x,y)$. This allows us to adjust the size of the intensity pattern $|\tilde{U}_f^{(1)}|^2$ after the first Fourier transform. The effect of this degree of freedom on the convergence of the MRAF algorithm will be investigated in Section 7.4.3.

7.4.3   Exploring the parameter space

From calculating the input phase $\phi^{(0)}$ to obtaining the output phase $\phi^{(n)}$ from the MRAF algorithm, there are four parameters that affect the outcome, namely: the size of $|\tilde{U}_f^{(1)}|^2$, the size of the signal region, the mixing parameter m, and the number of iterations n. In this section, we explore this parameter space and investigate the effect of each parameter on the quality
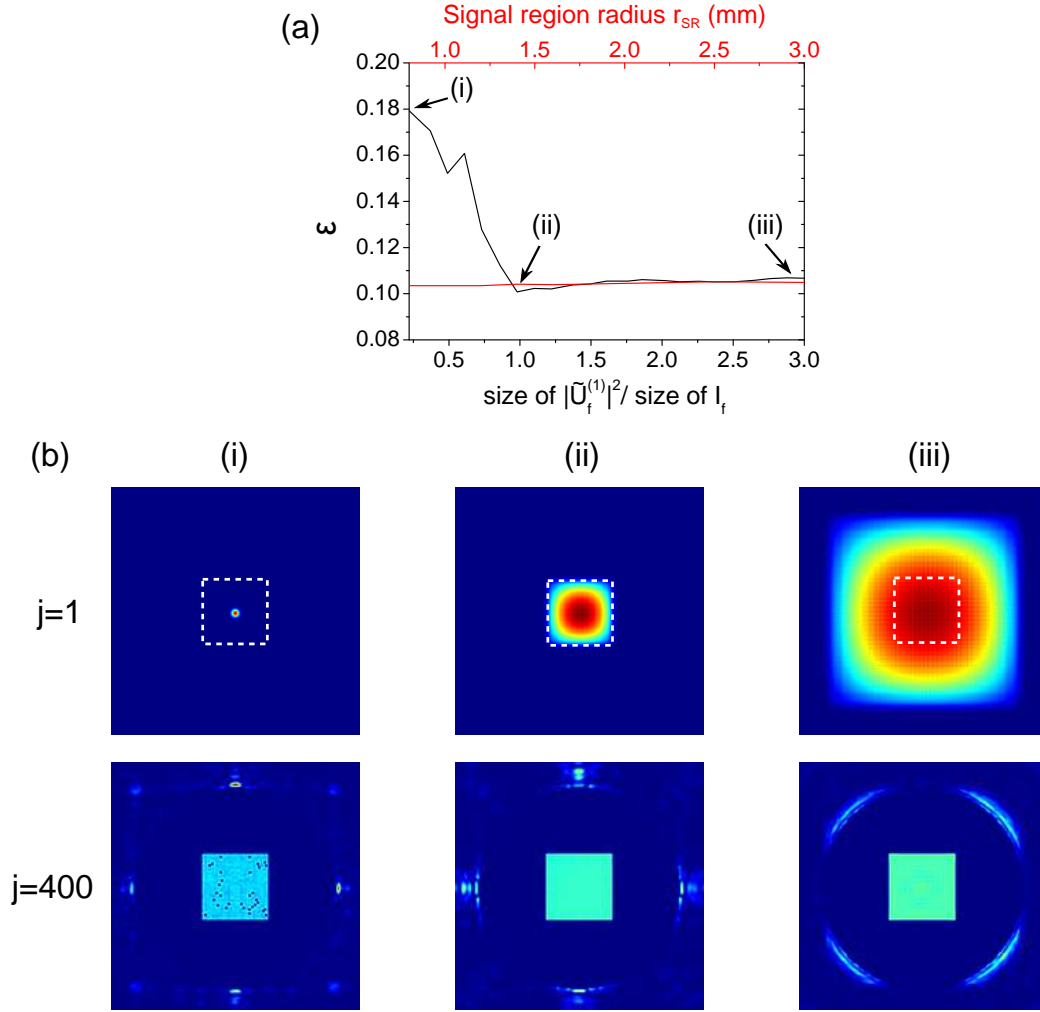
Figure 7.10: Error analysis on varying the sizes of the signal region and the target image of the first phase guess. (a) Error as a function of the signal region radius (red) and the ratio of the square sizes $|\tilde{U}_f^{(1)}|^2/I_f$ (black). (b) $|\tilde{U}_f^{(j)}|^2$, $j = 1$ and $j = 400$ iterations with different square sizes $|\tilde{U}_f^{(1)}|^2$ from first phase guess: (i) 0.22 mm, (ii) 1 mm, (iii) 3 mm. The white dashed boxes indicate the target I_f – a 1 mm × 1 mm square. The calculation uses an input Gaussian beam with a $1/e^2$ radius of 1.2 mm.

of the convergence of the algorithm.

A normalised $1\,\text{mm} \times 1\,\text{mm}$ square is used as target throughout the measurements, where the intensity profile is defined as

$$I_f = \begin{cases} 1 & \text{for } |u|, |v| \leq 0.5\,\text{mm}, \\ 0 & \text{elsewhere.} \end{cases} \tag{7.26}$$

The error ϵ between the normalised computed square $|\tilde{U}_f|^2$ at the Fourier plane and the target I_f is simply defined as the standard deviation of the discrepancy between them:

$$\epsilon = \sqrt{\frac{1}{N} \sum_{i,j \in I_f \neq 0} \left[|\tilde{U}_f(u_i, v_j)|^2 - I_f(u_i, v_j) \right]^2}, \tag{7.27}$$

where N is the number of pixels in the sum.

Size of the signal region

First we look at the error ϵ as a function of the radius of the signal region r_{SR}. Measurements are carried out for different values of r_{SR} that are larger than the size of the square, while other parameters are kept constant: (size of $|\tilde{U}_f^{(1)}|^2$/ size of I_f) ≈ 1, mixing parameter $m = 0.5$, and $n = 400$ iterations. As shown by the red curve in Fig. 7.10(a), ϵ is insensitive to r_{SR}, which indicates that the convergence of the MRAF algorithm is largely unaffected by the size of the signal region as long as the whole target intensity pattern sits inside the region.

Size of the intensity pattern after first Fourier transform

We remind ourselves that the size of the intensity pattern $|\tilde{U}_f^{(1)}|^2$ can be simply controlled through multiplying $\phi_{\text{analytical}}(x, y)$ by a prefactor before being used as the first phase input $\phi^{(0)}(x, y)$ into the MRAF algorithm. Keeping the mixing parameter $m = 0.5$, $n = 400$ iterations, and $r_{\text{SR}} = 1.5\,\text{mm}$, we explore the effect on ϵ by changing the size[8] of $|\tilde{U}_f^{(1)}|^2$. Plotted as the black curve in Fig. 7.10(a), one sees that while ϵ stays roughly constant at ~ 0.1 for

---

[8] Here, the size of the square refers to the length of a side of the square.
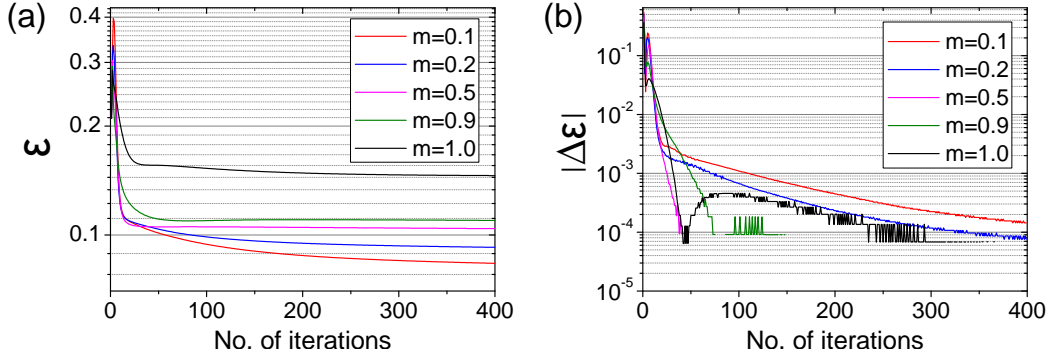
Figure 7.11: Error analysis on varying the mixing parameter of the MRAF algorithm and the number of iterations.

the size of $|\tilde{U}_f^{(1)}|^2$ larger than or equal to that of I_f, the discrepancy between the final intensity pattern and the target I_f increases as the size of $|\tilde{U}_f^{(1)}|^2$ becomes smaller than I_f. This is caused by the introduction of optical vortices, where an example is shown in Fig. 7.10(b)(i). Here, the size of the square after one Fourier transform is about one-fifth (0.22 mm) of the target size. After $n = 400$ iterations, the resulting intensity pattern $|\tilde{U}_f^{(j)}|^2$, $j = 400$ is somewhat erroneous with 32 optical vortices. For measurements with the size of $|\tilde{U}_f^{(1)}|^2$ larger than or equal to I_f, as illustrated in Fig. 7.10(b)(ii) and (iii), optical vortices are not observed after the same number of iterations. Hence we conclude that one should choose the prefactor for the first phase guess such that (size of $|\tilde{U}_f^{(1)}|^2$/ size of I_f) $\gtrsim 1$. In particular, this ratio is chosen to be ~ 1.1 for the rest of this chapter.

Number of iterations n

By choosing $r_{\mathrm{SR}} = 1.5\,\mathrm{mm}$ and (size of $|\tilde{U}_f^{(1)}|^2$/ size of I_f) ~ 1.1, we monitor the error at each iteration of the MRAF algorithm for different mixing parameters m. While $m = 0.1, 0.2, \cdots, 1.0$ are tested, only 5 values of m are shown in Fig. 7.11 for simplicity. As shown in Fig. 7.11(a), one sees a rapid initial drop in error ϵ up to $j \sim 30$, which is followed by a more gentle decrease. The change in error per iteration, $|\Delta\epsilon|$, is plotted in Fig. 7.11(b). Here, the error minimisation stagnates for $m = 0.5$ and $m = 0.9$ as $|\Delta\epsilon| = 0$, while $|\Delta\epsilon|$ of $m = 0.1, 0.2, 1.0$ do not stagnate. In practice, from measuring the light intensity at the Fourier plane with a CCD camera, we see no significant improvement in image quality once $|\Delta\epsilon|$ drops to $\sim 10^{-3} - 10^{-4}$. The number of iterations is therefore fixed to $n = 400$ for the measurements presented in the rest of this chapter.

Mixing parameter m

We learn from Fig. 7.11(a) that the error ϵ tends to be lower for a lower mixing parameter m. This trend, however, does not follow when one measures the light intensity pattern at the Fourier plane with a camera. In addition, the effect of m on the image quality is observed to vary for different target intensity patterns I_f. Consequently, the mixing parameter m is chosen empirically from examining the error between the measured intensity pattern and the target, which will be discussed shortly.

7.4.4   Input beam size dependent image quality

While the speckles can be eliminated through ensuring a less erratically varying phase at the Fourier plane, this is unfortunately not the only property of a coherent light source that distorts the final image. The *edge ringing* effect, which arises when the light field passes through an aperture with sharp edges [235], would cause fringing to the intensity pattern. In mathematical context, it is precisely the boundaries of the SLM panel, characterised by the amplitude transmittance $t_A(x, y)$ in Eq. 7.10, that causes the ringing effect.

We explore the effects on the intensity patterns by using different beam sizes incident on the SLM. Explicitly, we test beams with $1/e^2$ radii of $4.9\,\text{mm}$ (overfilling the SLM), $2.1\,\text{mm}$, and $1.2\,\text{mm}$, where the intensities of the beams at the edge of the SLM are $\sim 50\%$, $\sim 5\%$, and $\sim 0\%$ of the peak intensity respectively. In this measurement, we vary the mixing parameter m while fixing $r_{\text{SR}} = 1.5\,\text{mm}$, which follows from the analysis in Section 7.4.3. The results for a $1\,\text{mm} \times 1\,\text{mm}$ square and a $r = 0.5\,\text{mm}, \sigma = 100\,\mu\text{m}$ ring are shown in Fig. 7.12 and Fig. 7.13 respectively.

We hereby define the *flatness* of the square, and the *smoothness* of the ring, by using a slightly modified expression of the error ϵ from Eq. 7.27, which now reads

$$\epsilon = \sqrt{\frac{1}{N_{\text{ROI}}} \sum_{u', v' \in \text{ROI}} [I_M(u', v') - I_f(u', v')]^2}, \qquad (7.28)$$
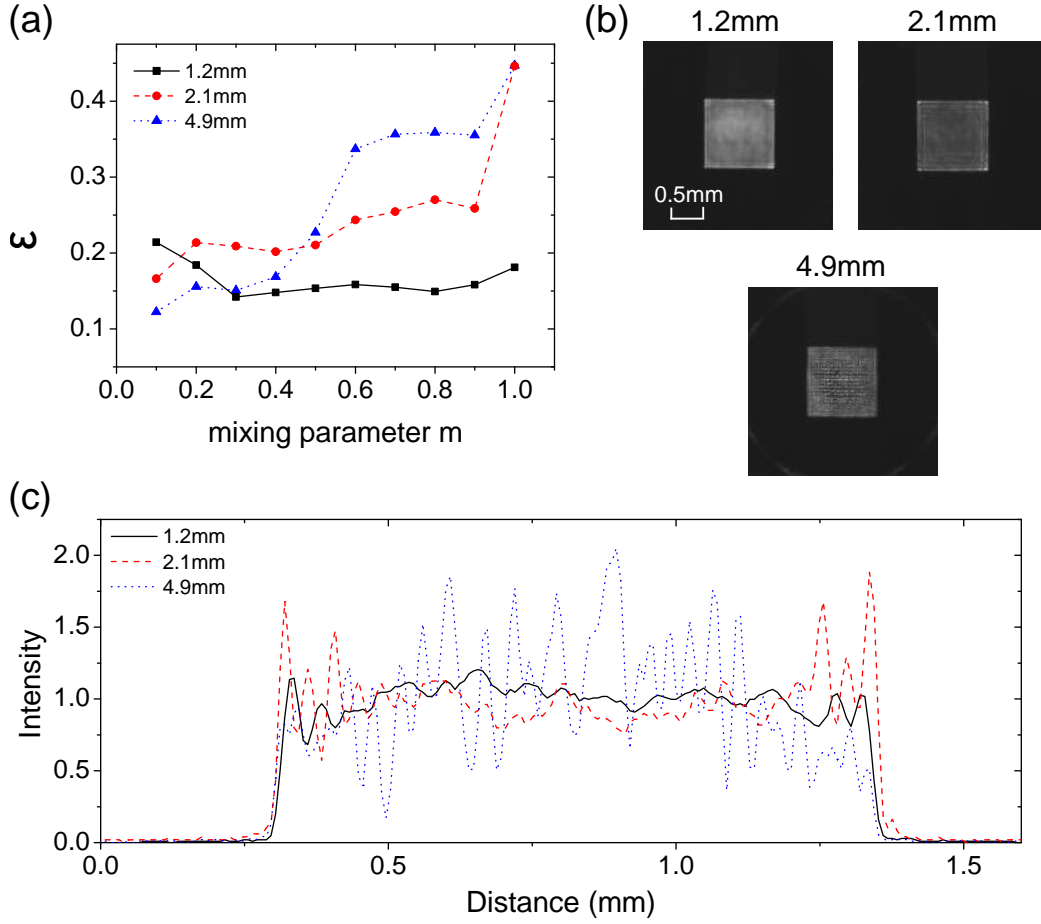
Figure 7.12: Effect of different input beam size on the square intensity pattern. (a) Error as a function of mixing parameter m with different beam sizes. (b) Measured images of the squares at $m = 0.8$. (c) Crosscuts across the middle of the normalised intensity profiles of the squares.

where both the measured intensity I_M and the target intensity I_f are normalised to the mean of the intensity counts in the region of interest (ROI). ROI for the square is the square itself, while it is along the circle with a ring radius r for the ring.

Shown in Fig. 7.12(a), by overfilling the SLM with a beam radius of 4.9 mm, we see that error of the square is low at $\sim 15\%$ for $m = 0.1 - 0.4$, while it dramatically increases for $m \geq 0.5$. The regular fringes caused by the edge ringing effect, as shown in Fig. 7.12(b), leads to an abrupt variation of the intensity. It can be clearly seen from the crosscut shown in Fig. 7.12(c) that the uniform intensity suffers from heavy distortion. For a smaller beam with radius 2.1 mm, while ϵ for $m \leq 0.4$ is $\sim 5\%$ higher than the previous case, it
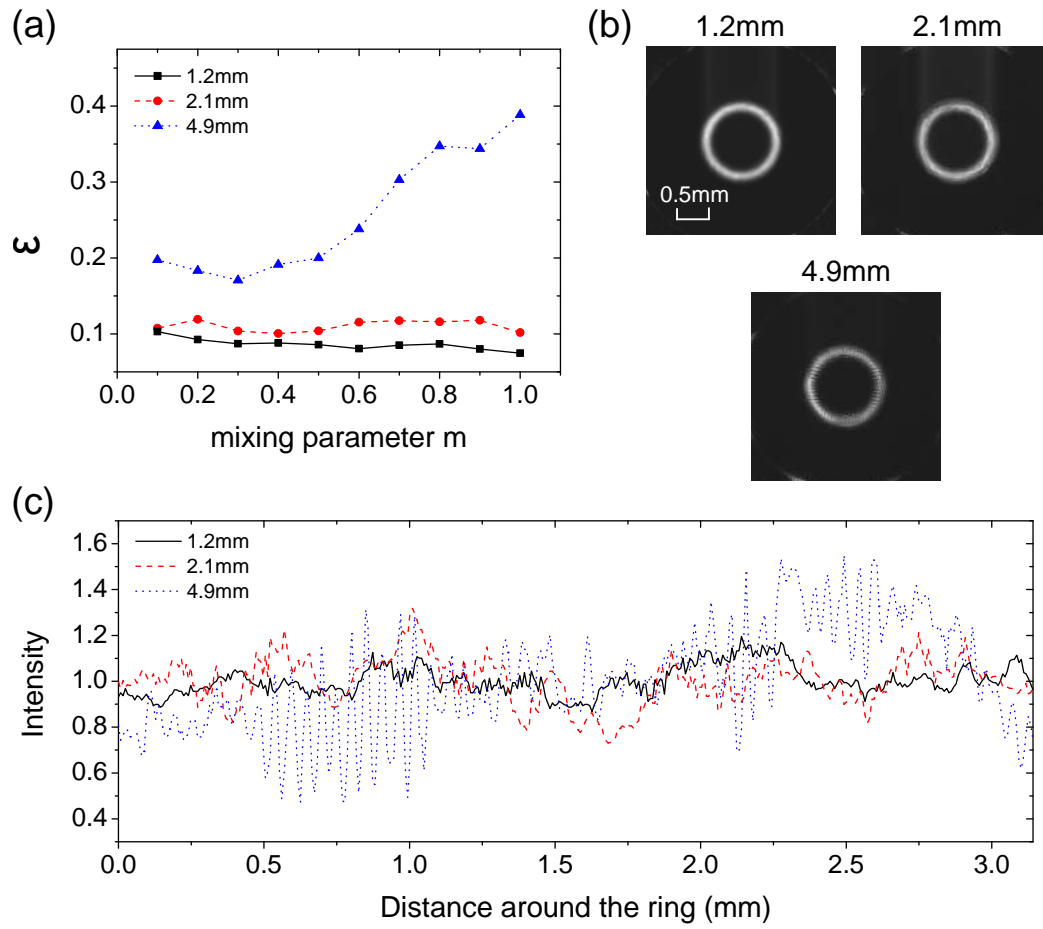
Figure 7.13: Effect of different input beam size on the ring intensity pattern. (a) Error as a function of mixing parameter m with different beam sizes. (b) Measured images of the rings at $m = 0.6$. (c) Normalised intensities around the rings.

stays below 25% apart from the case where $m = 1$ (Gerchberg-Saxton). In contrast, for the 1.2 mm beam (where the hard edges of the SLM panel have no effects on the reflected, modulated beam), the error ϵ stays low at $\lesssim 15\%$ over a broad range of mixing parameters, $0.3 \leq m \leq 0.9$. The elimination of the fringing effect by reducing the input beam size is best illustrated by the crosscuts of the intensity profiles shown in Fig. 7.12(c). In addition, one can readily see the advantage of acquiring a smaller beam that underfills the SLM from Fig. 7.12(a): a good hologram with lower error can be achieved with a higher proportion of light in the signal region, hence a higher light usage efficiency.

The results of the ring, shown in Fig. 7.13, reveal a similar trend. While one can see from Fig. 7.13(b) that the speckles in the manner of Fig. 7.8(c) are absent, heavy fringing distorts the ring that uses the 4.9 mm Gaussian beam. Fig. 7.13(a) shows that ϵ for all values of m in this case are at least twice of that of the two smaller beams. The smoothness of the ring for the 1.2 mm beam, on the other hand, is below 10% for all m with $\epsilon \sim 8 - 9\%$ for $m \geq 0.6$. The small fluctuation of the intensity around this ring casts a distinct contrast from the rings that use larger beam sizes, as plotted in Fig. 7.13(c).

Throughout the rest of this chapter, we underfill the SLM with the 1.2 mm beam due to the vast improvement in image quality and the enhancement in the light usage efficiency. However, the reader should be aware of an obvious downside of employing a smaller beam – the maximum input beam power is severely restricted. With a damage threshold of $10 \, \text{W cm}^{-2}$ (see Table 7.1), the power incident on the SLM is limited to 450 mW for an $r = 1.2$ mm beam. This could mean insufficient trap depth for some holograms. Atom trapping and the trap depths of the holograms will be discussed in Chapter 8.

7.4.5 Beam position and size matching

The application of geometrical beam shaping with a small beam means that the description of the wavefront is vital. Displacing the beam, or simulating an incorrect input beam size, would lead to a skewed, inaccurate measured
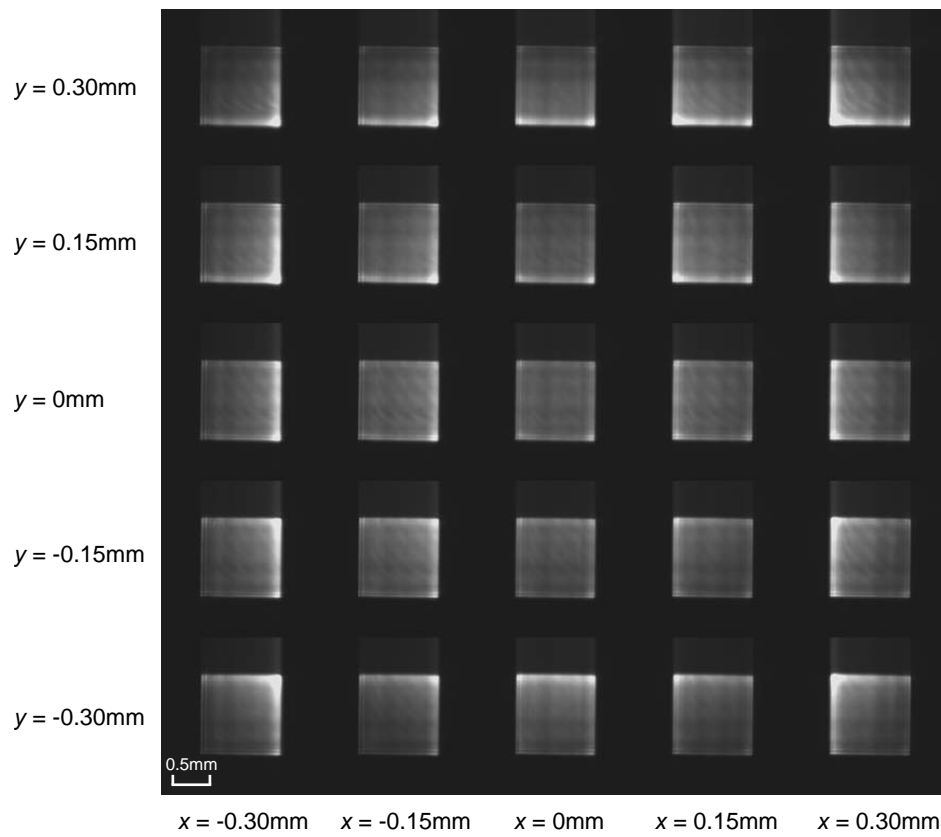
Figure 7.14: Change of intensity distribution of a 1 mm×1 mm square by displacing the simulated input beam position. A 1.2 mm Gaussian beam is used here.
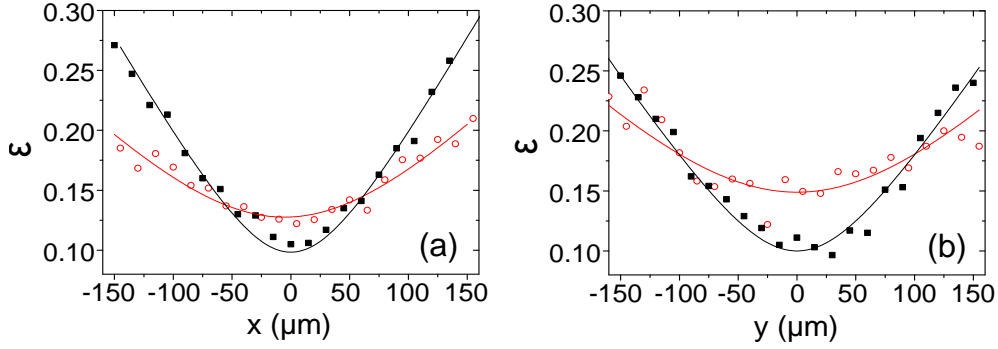
Figure 7.15: Error ϵ of the square at (a) $(x, y) = (x', 0)$ and (b) $(x, y) = (0, y')$ displacements from the simulated beam position. The measurement is repeated for two input Gaussian beam $1/e^2$ radii: $2.1\,\mathrm{mm}$ (red circles) and $1.2\,\mathrm{mm}$ (black squares). The curves are added as a guide of eye.

image at the Fourier plane. In tackling this, we have developed an accurate positioning and radius-matching procedure based on the minimisation of the error ϵ. The $1\,\mathrm{mm} \times 1\,\mathrm{mm}$ square is again employed for the optimisation, while the ROI (see Eq. 7.28) for the error evaluation is a crosscut across the middle of the square.

Beam position:

In positioning the beam accurately, rather than physically steering the beam, we opt to adjust the simulated centre of $I_r(x, y)$ in both the first phase calculation and MRAF algorithms. As a result of the small input beam, a slight mismatch between the physical and simulated beam centres would lead to distortion of the measured image. Indeed, as shown in Fig. 7.14, a deliberate offset to the simulated I_r adds skewness to the otherwise even intensity distribution to the final, measured image. The bigger the offset from $(x, y) = (0, 0)$, the higher discrepancy between the measured and target images and hence an increase in ϵ. The results of these measurements are shown in Fig. 7.15. By finding the minimum point to both x and y-directions, in principle the positions of the physical and simulated I_r can be matched as precisely as $15\,\mu\mathrm{m}$, which is the pixel size of the SLM. In addition, the measurement is repeated for an $r = 2.1\,\mathrm{mm}$ beam and the results are shown in red in Fig. 7.15. Although at the matching point ϵ is higher than that of a $r = 1.2\,\mathrm{mm}$ Gaussian beam, which has been discussed in the previous section, we see a gentler rise in ϵ than $r = 1.2\,\mathrm{mm}$ when the offset increases. This shows that knowing the precise beam position is less critical for larger
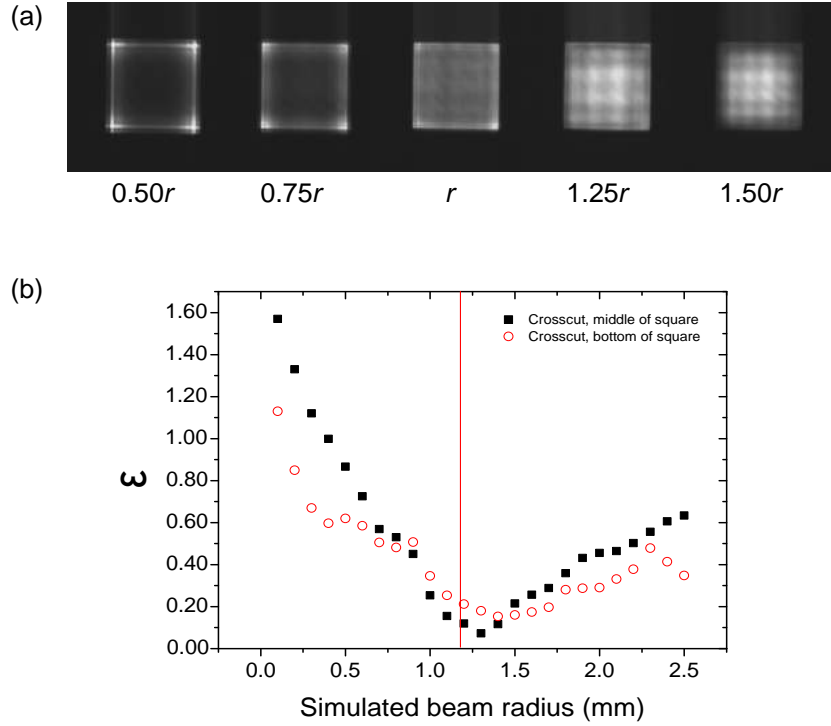
Figure 7.16: Incoming beam with measured Gaussian $1/e^2$ radius $r = 1.2\,\text{mm}$. (a) The effect of the measured intensity pattern if the simulated and measured beam sizes are not matched correctly. (b) Error ϵ of the $1\,\text{mm}\times1\,\text{mm}$ square against simulated beam radius. It is measured with a crosscut through the middle (black square) and the bottom (red circle) of the square. The red line denotes the measured Gaussian beam radius r.

beams as the spatial variation of the intensity, or wavefront, is less rapid.

Beam size:

The matching of beam size is performed in a similar fashion as finding the beam position: we change the simulated Gaussian beam radius and measure the corresponding error. The resulting intensity profiles of the squares are shown in Fig. 7.16(a). If the input beam is small, the calculation of the first phase guess and the MRAF algorithm will generate a phase $\phi^{(n)}$ that creates a large diffraction angle. In contrast, a relatively large beam compared to the target would mean that light is concentrated at the centre as the diffraction angle is small. Fig. 7.16(a) shows that if the simulated beam size is too small compared to the real input beam, the diffraction angle is too large such that too much light is being diverted to the edges of the shape. Similarly, the diffraction is insufficient if the simulated beam size is too large, causing a low intensity at the edges. In both cases, the measured intensity I_M deviates
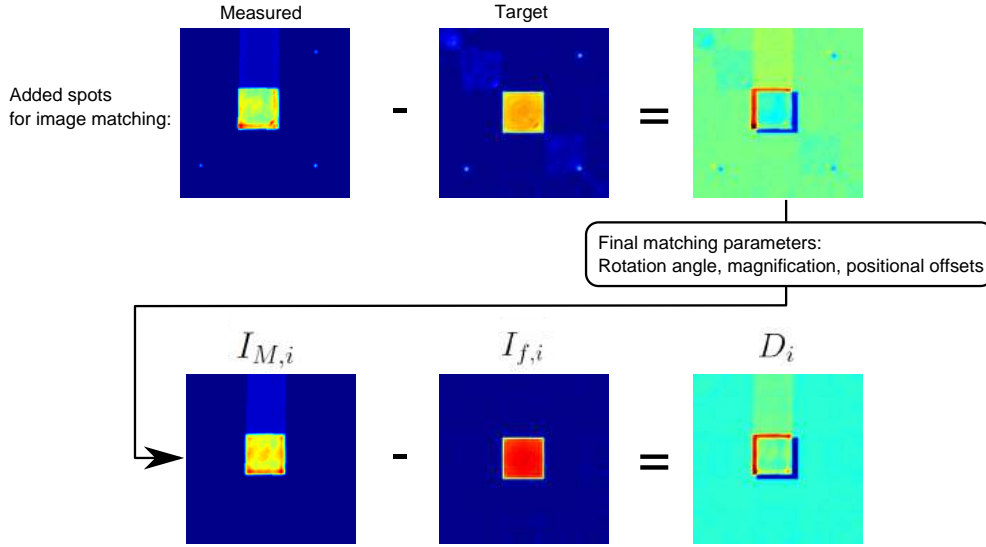
Figure 7.17: The spots matching procedure. The additional spots are required for accurate image matching. Here the measured and target images are deliberately offset as an illustration of the mismatched case - one finds that the spots are not overlapping each other after subtraction of the target from the measured image, as shown in top right. The final matching parameters are subsequently used for accurate image subtraction where no reference spots are added.

from the flat square I_f and hence ϵ increases, as shown in Fig. 7.16(b). Note that the minimum error of the crosscut through the middle of the square is measured at $r = 1.3\,\text{mm}$, which is $100\,\mu\text{m}$ larger measured beam radius. However, as there appears greater leeway at the bottom of both error curves, the simulated radius is kept to be the measured value of $r = 1.2\,\text{mm}$.

The optimised simulated beam position and beam size are then applied to the generation of various kinoforms. Unlike the square where an analysis of the error to a flat-top rectangular intensity profile is trivial, such analysis for more complicated shapes requires direct comparison between the measured and target images. This process will be discussed in the following section.

7.5   Accurate image subtraction

To form a valid comparison between the images, the dimensions and the positions of the normalised[9] measured intensity I_M and the calculated intensity

---

[9]The intensity patterns are normalised to their respective average peak intensities here.
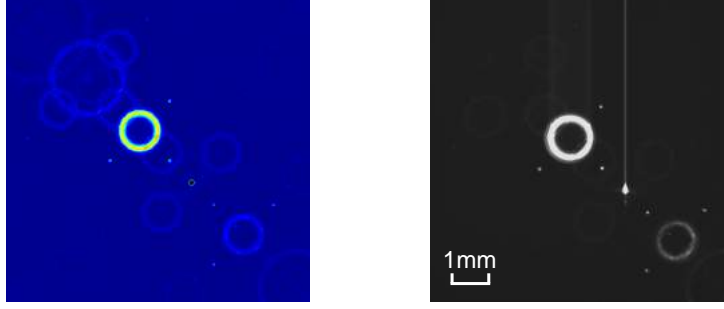
Figure 7.18: Ghost images distort the target intensity profile after 3 additional diffraction limited spots are added. Left: Calculated image. Right: Measured intensity.

$I_f = |\tilde{U}_f^{(n)}|^2$ are required to be matched perfectly. To achieve this, we have devised a procedure described as follows.

1. **Image binning:** In practice, the pixel size of I_M, defined by the pixel size of the CCD camera, is often different from the calculated pixel size defined by Eq. 7.13, hence it is necessary to bin the raw image from the CCD camera such that the new pixel size equals to $a_{u,v}$ (here we assume the camera pixel size $> a_{u,v}$. In the opposite scenario, binning will be applied to I_f instead).

2. **Spots matching:** Matching I_M and I_f manually for general shapes can be tricky, especially for shapes without hard edges (such as a ring). We thus devised a tool to minimise the error associated with the matching process. That is, to introduce 3 additional spots separated by a predefined distance in I_f with 3 additional linear grating phases to the original kinoform. As discussed, these diffraction limited spots are the smallest objects that can be created on the Fourier plane. Matching these 3 reference points rather than using the target images as a reference, we are able overlap both images accurately via image rotation, magnification, and positional offsets. A snapshot of this stage is illustrated in the top panel of Fig. 7.17. The holograms with reference spots, however, are disrupted by many ghost images as shown in Fig. 7.18 and thus cannot replace the original target as I_f. Nevertheless, as the hardware is kept intact throughout the process, the matching parameters obtained from spot matching procedure can simply be applied to the spotless I_M, generated by the original kinoform.

3. **Subtraction:** I_M and I_f can now be directly compared, where the

I_f	Dimensions	m	ϵ	$\epsilon^{(10\%)}$	$\Gamma\,(\%)$
Square	$1\,\mathrm{mm} \times 1\,\mathrm{mm}$	0.8	0.14	0.14	52
Ring	$r = 0.5\,\mathrm{mm}, \sigma = 100\,\mu\mathrm{m}$	0.6	0.08	0.08	39
Kagome	Lattice site $\sigma = 80\,\mu\mathrm{m}$	0.5	0.20	0.09	33
4 Gaussians	$\sigma = 100\,\mu\mathrm{m}$	0.3	0.12	0.07	20
Ring with traps	Traps with $\sigma = 70\,\mu\mathrm{m}$	0.6	0.10	0.04	39
SLM	Feature width $\sim 2\,\mathrm{mm}$	0.6	0.17	0.17	39
Star	$300\,\mu\mathrm{m}$ each side	0.8	0.13	0.13	52
MERRY X'MAS!	$\sigma = 40\,\mu\mathrm{m}$	0.6	0.24	0.11	39
Snowflake	$\sigma = 40\,\mu\mathrm{m}$	0.5	0.27	0.11	33

Table 7.2: The dimensions, mixing parameter m, error ϵ, error of the top 10% intensity of the target intensity $\epsilon^{(10\%)}$, light usage efficiency Γ, as a percentage of the light incident on the SLM, of the holograms presented in Fig. 7.19.

error ϵ of the image (with background omitted) is computed using Eq. 7.28. Furthermore, as shown in the bottom panel of Fig. 7.17, we define the discrepancy D as

$$D = I_M - I_f, \tag{7.29}$$

which will be used for the discussion of further image quality enhancement via active feedback in Section 7.7.

The subtraction gives us a reliable calculation of the error ϵ of all shapes. In addition, following the same treatment in [236], we also calculate the error $\epsilon^{(10\%)}$ for the pixels within the top 10% of the target intensity counts. This is due to the fact that atoms in optical traps equilibrate to about one-tenth of the trap depth [138], as discussed in Section 3.3.5. As the trap depth is directly proportional to the light intensity, only the brightest 10% of the intensity pattern has notable effect to the trapped atoms.

7.6 Example holograms

Using a $r = 1.2\,\mathrm{mm}$ Gaussian input beam with optimised simulated beam positions and sizes, we are able to generate smooth, high quality images. In Section 7.4.4, we have presented the results for a $1\,\mathrm{mm} \times 1\,\mathrm{mm}$ square and an $r = 0.5\,\mathrm{mm}, \sigma = 100\,\mu\mathrm{m}$ ring, where the lowest measured errors are $\epsilon = 0.14$
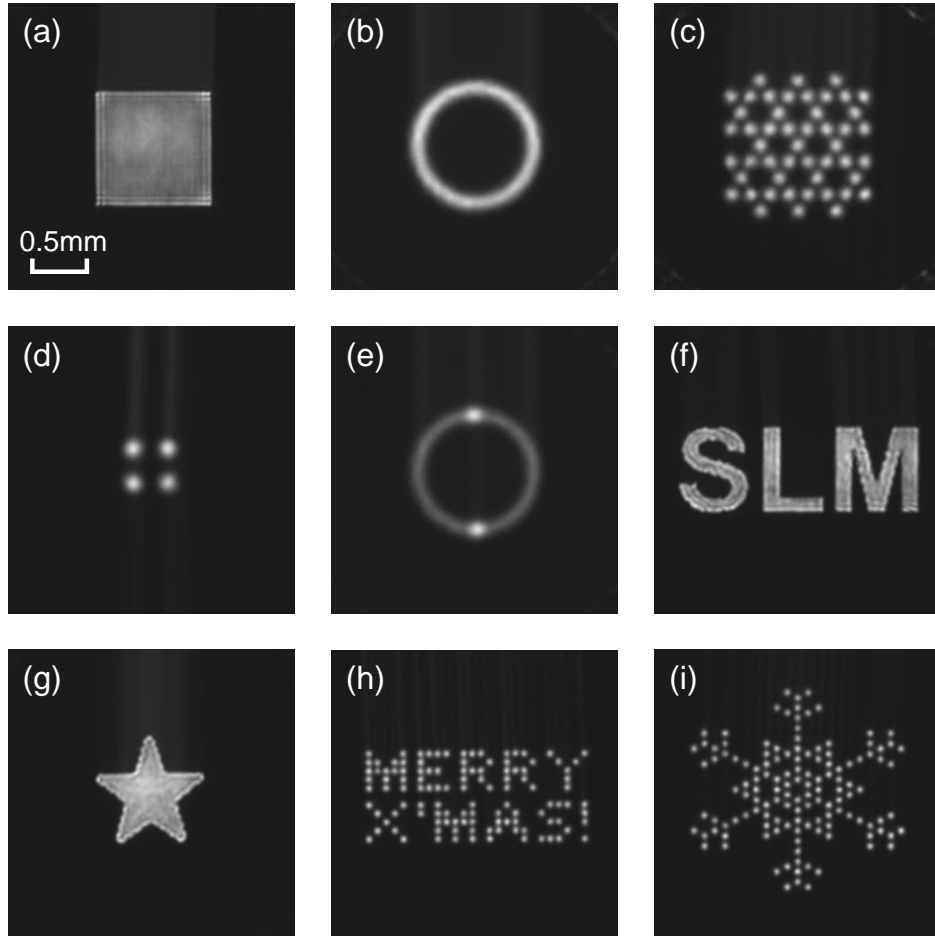
Figure 7.19: Example holograms generated by the SLM. The intensity profiles are: (a) a square, (b) a ring, (c) a Kagome lattice, (d) 4 Gaussians, (e) a ring with two Gaussian traps, (f) letters 'SLM', (g) a star, (h) a festive message to the undergraduate physics students in the form of lattice spelling the words 'MERRY X'MAS!', and (i) a snowflake lattice. The dimensions and parameters used in the algorithm are detailed in Table 7.2.
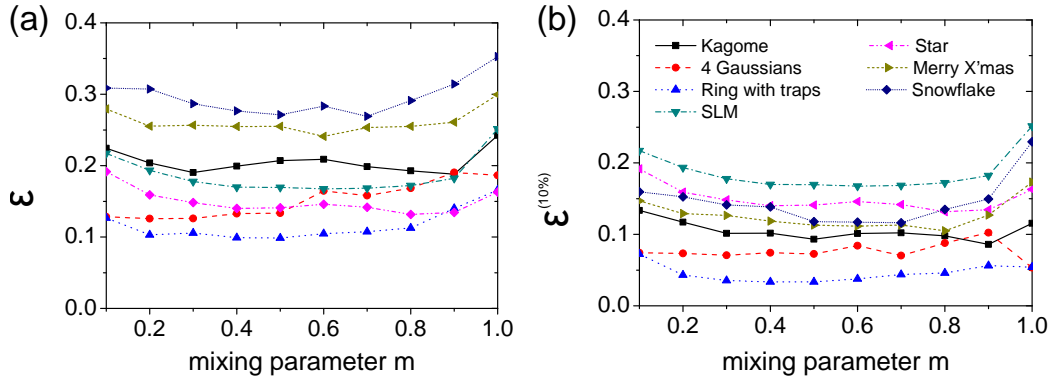
Figure 7.20: Error analysis on different intensity patterns from Fig. 7.19 (excluding the square and the ring where the results are presented in Fig. 7.12 and Fig. 7.13 respectively) with different mixing parameter m. (a) The error ϵ of the hologram. (b) The error $\epsilon^{(10\%)}$ of the pixels within the top 10% of the target intensity counts.

and $\epsilon = 0.08$ respectively. These results are typically comparable to some of the best holograms produced to date [204, 221, 236]. Further examples presented in Fig. 7.19 also show encouraging results. The variations of errors ϵ and $\epsilon^{(10\%)}$ of these patterns as a function of mixing parameter m, shown in Fig. 7.20(a) and (b) respectively, are in similar trends as the square and the ring. With low error values lying within a broad range of mixing parameters (between $m = 0.3$ and $m = 0.8$), one need not commit a harsh trade off of light usage efficiency for the hologram quality [236]. Such efficiency, Γ, calculated through multiplying the mixing parameter m with the proportion of light (65% of the light incident on the SLM), is presented in the last column of Table 7.2. From the same table, one can also see that the errors $\epsilon^{(10\%)}$ of some of the chosen images (the ring, 4 Gaussians, and the ring with traps) are close to the requirement of intensity fluctuation ($\lesssim 0.05$) for which to realise atomtronic experiments with BECs. On the other hand, shapes of uniform intensity, or of higher complexity such as the snowflake lattice, are in general more erroneous. Further improvement in the quality of the hologram can be achieved by means of a feedback that corrects the distortion of the final image by the optical elements [188, 203, 221, 237]. In the next section, we discuss the attempt of the technique reported in ref. [236].

7.7 Feedback

Up to this point, the numerically determined solution to the phase retrieval problem has been based heavily on the assumption that the Fourier plane and the SLM plane are related by a perfect FFT. In practice, however, an arbitrary and non-uniform phase shift is likely to be added to the light field from sources including the nonlinear response of the SLM, aberrations and pupil effects of the lenses, and imperfect curvature of optical elements. This reduces the accuracy of the final image and the only way to compensate for the unwanted phase is via means of feedback. Various feedback and correction methods have been developed [188, 203, 221, 237]. For example, one can retrieve the phase of the total aberration, which can be described by a set of 2D orthogonal functions known as the Zernike polynomials[10] [238], via the Shack-Hartmann algorithm [237]. This aberration phase can then be removed by further kinoform manipulation. By using atoms in situ, aberration correction of the Fourier plane inside a vacuum chamber has been achieved [203]. Here, we implement the straightforward technique reported in [236] where a corrected target intensity is calculated.

7.7.1 Modified MRAF with active correction

The additional feedback loop works as a supplementary loop after the main MRAF algorithm. After n-iterations from the MRAF algorithm, the error ϵ between I_M and I_f is calculated. If ϵ is within the acceptable range, preferably $< 10\%$, which is the intensity fluctuation in state-of-the-art SLM generated holograms [204, 221, 236], no feedback is required and the final kinoform is executed, as shown in the flow-chart in Fig. 7.21. Otherwise, we undergo the feedback loop, shown in red in the figure, via an active correction to the target.

Given the expression for discrepancy D in Eq. 7.29, we now have an accurate description of regions where the intensity is too high (low) as the corresponding elements in D will appear to be positive (negative). In actively compensating for the error in intensity, we calculate the corrected target

---

[10]Each polynomial corresponds to a specific classical aberration such as astigmatism and coma.
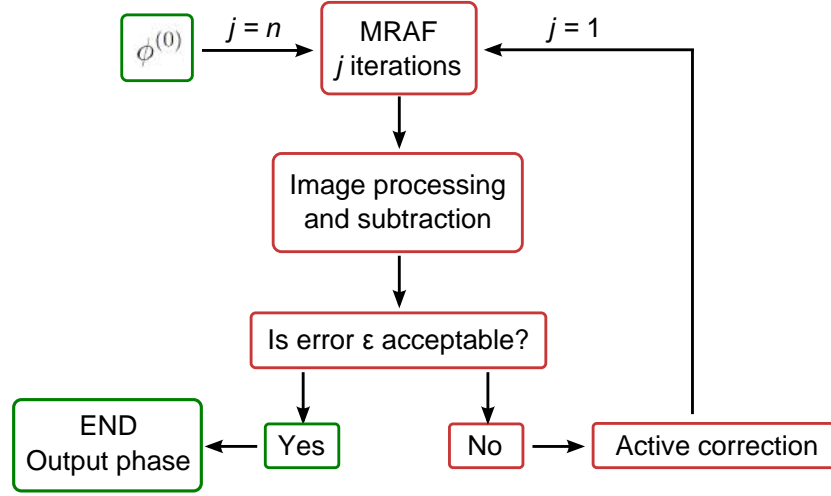
Figure 7.21: Feedback loop, in red, is added after n iterations of the MRAF algorithm. Details of image processing and subtraction are discussed in Section 7.5, where active correction is described in Section 7.7.1.

$I_{f,i+1}$ such that

$$I_{f,i+1} = I_{f,i} - \alpha D_i, \tag{7.30}$$

where i denotes the number of feedback iteration and α is a real parameter that takes value $0 < \alpha \leq 1$. This is the gain parameter [236] which is determined empirically every feedback loop to maximise the performance of the correction. In other words, α is chosen such that the decrease in the ϵ is maximised. The new target $I_{f,i+1}$ replaces $I_{f,i}$ as the new target of the MRAF algorithm where a new phase is generated after 1 MRAF iteration. The feedback loop is then repeated with a new discrepancy D_{i+1}, and a newly determined α. As outlined in red in the flow-chart Fig. 7.21, the feedback loop terminates when ϵ stagnates, or an acceptable ϵ is reached.

7.7.2   Results

To date, we have performed the feedback algorithm with two intensity targets, namely the ring and the square. While for the ring we have been unable to obtain a significant improvement in the smoothness, encouraging results for the square have been shown. Starting with the measured intensity profile of a $600\,\mu\text{m}\times600\,\mu\text{m}$ square after the normal MRAF algorithm shown in Fig. 7.22(a), the ϵ of the crosscut drops from 0.10 to 0.06 after one feedback
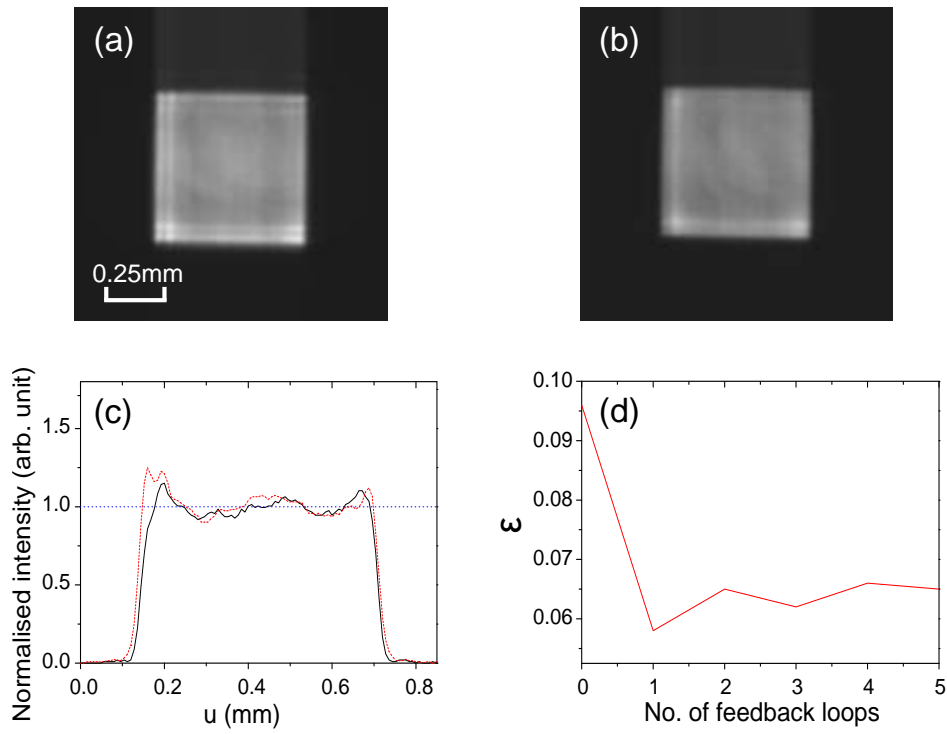
Figure 7.22: (a) Before feedback. (b) After one feedback loop with $\alpha = 0.2$. (c) Comparison of cross-sectional intensity profiles (through the centre of the square) between (a) (red, dashed) and (b) (black, solid). (d) A typical evolution of ϵ of the crosscut after several feedback loops. Here α has been kept the same.

loop with $\alpha = 0.2$. The corrected image, shown in Fig. 7.22(b), shows that the intensity at the edges and at the corner is brought down resulting in a more uniform distribution across the square surface. In order to inspect the effect of the feedback loop closely, we look at the cross-sectional cut through the centre of the square which is shown in the intensity plot Fig. 7.22(c). There is evidence that the abrupt intensity peaks on the edges are reduced, while the intensity remains largely unchanged away from the edges as the corresponding elements in D are very close to zero.

However, despite successfully obtaining a better image after one iteration, we have not seen further improvement after additional feedback loops. While all choices of $\alpha = 0.05, 0.10, \cdots, 1.00$ are tested for each feedback loop, the error ϵ stagnates as shown in the typical feedback run in Fig. 7.22(d). Nevertheless, with the use of a feedback loop, the error of the square is now brought in line with the best reported values of 0.07 [204] and 0.06 [221].

7.8   Summary

The SLM is a maturing technology that offers great potential in beam shaping. In experiments with ultracold atoms, this reconfigurable DOE opens the door to new playgrounds for exciting physics using trapped atoms in arbitrary shaped potentials.

In this chapter, we have explored the working principle of the SLM. By imprinting phase information to the incoming coherent Gaussian beam via the 512×512 pixel array, the desired intensity pattern forms at the Fourier plane $2f$ from the SLM plane. The calculation of the kinoform for a particular target pattern is far from trivial, where an exact analytical solution often does not exist. The error minimising Mixed-Region Amplitude Freedom (MRAF) algorithm is thus employed to solve the phase retrieval problem numerically. While the iterative algorithm offers excellent amplitude convergence, the unconstrained phase at the Fourier plane leads to a randomised phase distribution. As a consequence, the intensity pattern is speckle-disrupted due to the destructive interferences in the Fourier plane.

We have demonstrated that utilising the freedom of the initial phase input to the algorithm has greatly enhanced the image quality. Through an analytical first phase guess, where the separable approximation of the target intensity pattern is calculated, the speckle at the Fourier plane is greatly suppressed. The smoothness of the test patterns is further enhanced by acquiring a smaller input beam, where the edge ringing effect is eliminated. This yields excellent results, which include an $r = 0.5\,\mathrm{mm}$, $\sigma = 100\,\mu\mathrm{m}$ ring of $\epsilon = 0.08$. A feedback system has also been developed for active correction in minimising the discrepancy between the measured and the target intensity patterns, from which the error ϵ of the crosscut of the $600\,\mu\mathrm{m} \times 600\,\mu\mathrm{m}$ square is reduced from 0.10 to 0.06. The results are promising and the intensity patterns should suffice for future applications.

Chapter 8

Atom trapping in arbitrary potentials

With the promising results on the generation of arbitrary intensity patterns with the SLM, we are at a position where we can proceed to putting atoms into such potentials. A 2D light sheet, which is tightly confined in one direction, is implemented to provide axial confinement along the SLM beam at the Fourier plane. In this chapter, we will present the optical setup and the precise alignment of both beams, followed by a discussion of the transfer of atoms into the arbitrary potentials. We will switch back to the conventional coordinate system used in Chapter 2 – 6.

8.1   Introduction

The ultimate goal of developing the ring trap is to realise rotational sensing with Sagnac interferometry using bright solitary waves, in a configuration proposed by Helm *et al.* [52] (summarised in Section 2.5.2). After the realisation of ring potentials, next on the list is to develop an understanding of loading ultracold atoms into the toroidal trap.

To estimate the ring size for the interferometer, we ensure that when the bright solitary wave is loaded, it remains soliton-like over the whole splitting and recombination process. In Chapter 2, it is discussed that sharp transmission responses from a narrow barrier require a sufficiently high velocity

in the high energy regime, where the velocity also needs to satisfy Eq. 2.30 for the system to be definitely out of the classical transmission regime. Assuming a barrier height of $0.5\,\mu\mathrm{K} \times k_\mathrm{B}$, using Fig. 2.3(a) we pick a soliton velocity of $v \sim 2\,\mathrm{mm\,s^{-1}}$ for the system to meet the requirements. In our experiment, soliton-like behaviour has been observed for $\sim 600\,\mathrm{ms}$ (Fig. 5.7). Adding the assumption of negligible initial propagation distance before soliton splitting, the largest distance between the two potential barriers, or the half circumference of the ring, is hence $\sim 1.2\,\mathrm{mm}$. This yields a target ring radius of $r \sim 400\,\mu\mathrm{m}$. The reader should be advised that this relatively *small* ring can only provide a proof of scientific concept. Using Eq. 2.38, the range of rotational frequencies detectable with this ring is $0 < \Omega \lesssim 0.5\,\mathrm{mrad\,s^{-1}}$. Thus in this system, the Earth rotation rate of $\Omega_\mathrm{E} \sim 7 \times 10^{-5}\,\mathrm{rad\,s^{-1}}$ [61] translates to a phase shift of $\delta_\mathrm{S} \sim 0.09\,\mathrm{rads}$, which is small and difficult to be differentiated from zero phase shift [52]. The sensitivity of the interferometer can be improved by the use of a larger ring, as shown in Eq. 2.38. This can be achieved by extending the lifetime of the solitary wave, a future goal of this research.

In understanding the transfer of atoms from the crossed dipole trap into the ring trap, we wish to first 'fill the ring with atoms', hence it is desirable to create a smaller ring potential than the one described above. Opting for a ring with size comparable to the dipole trap, we choose a ring with a radius in the order of $r \sim 50\,\mu\mathrm{m}$. However, throughout Chapter 7 the $f = 150\,\mathrm{mm}$ Fourier lens was used. With a calculated Fourier plane pixel size of $20.78\,\mu\mathrm{m}$ (Eq. 7.13), the diameter of this $r = 50\,\mu\mathrm{m}$ ring on the Fourier plane calculated with the algorithms is only 5 pixels across. A shorter focal length, such as $f = 30\,\mathrm{mm}$, is hence a more suitable choice of Fourier lens, where here the pixel size is one-fifth of the case with the $f = 150\,\mathrm{mm}$ lens. Unfortunately, as a result of spatial restrictions in the apparatus, a one-lens system with short focal length is extremely difficult to implement. Hence, alternatively, we use an additional pair of telescope lenses after the $f = 150\,\mathrm{mm}$ Fourier lens to form a projected and rescaled Fourier plane inside the science cell. The choice of the lenses will be discussed in Section 8.3.1.

The algorithms used for generating the arbitrary shapes in Chapter 7 rely on
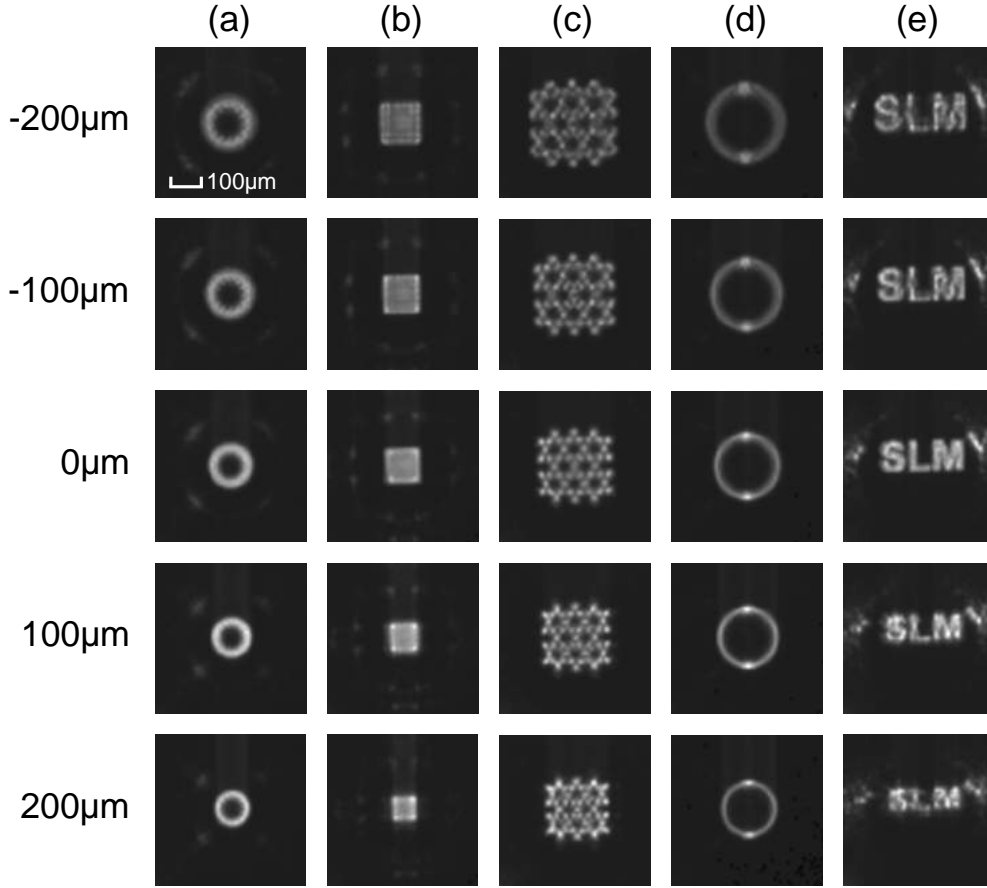
Figure 8.1: The propagation of the first order diffracted light field of the SLM about the Fourier plane, which is marked at $0\,\mu$m. Positive distance denotes images further away from the Fourier lens. The Fourier lens used here is $f = 30\,$mm. (a) Ring with $r = 50\,\mu$m and $\sigma = 20\,\mu$m. (b) $100\,\mu$m $\times$ $100\,\mu$m square. (c) Kagome lattice with lattice site $\sigma = 8\,\mu$m and minimum spacing $s = 30\,\mu$m. (d) $r = 90\,\mu$m and $\sigma = 20\,\mu$m ring with 2 Gaussian spots of widths $\sigma = 14\,\mu$m. (e) Letters 'SLM'.

placing amplitude constraints on both the Fourier plane and the SLM plane. Thus there is no control over the light at any other positions along the propagation path. The evolution of the shape of the first order diffracted beam after the Fourier lens is non-trivial and varies with the kinoform. As shown in different examples in Fig. 8.1, the light converges as it propagates after the Fourier lens. The intensity patterns on either side of the Fourier plane show strong resemblance to the target image, albeit deformed. Consequently, an optical light sheet (LS), which is tightly focussed in one direction, is required to provide the longitudinal confinement along the SLM beam at the Fourier plane.
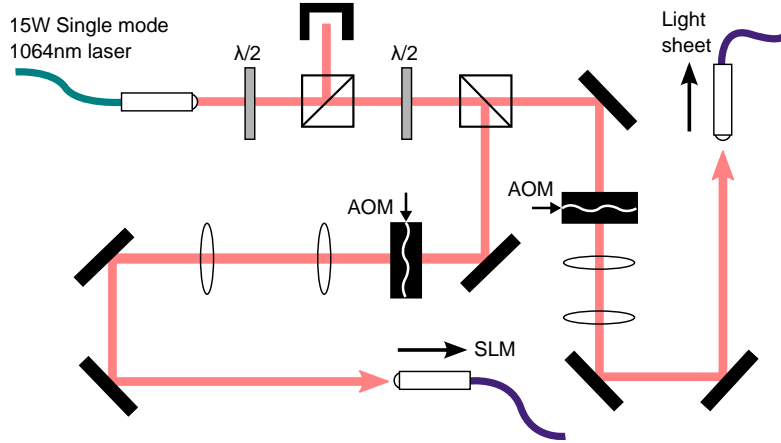
Figure 8.2: Optical setup for light source for both the light sheet and the SLM.

8.2   Light sheet potential

8.2.1   Optical setup

Both the SLM and LS beams are derived from the single mode $\lambda = 1064\,\mathrm{nm}$ 15 W fibre laser originally employed for the old crossed dipole trap. Shown in Fig. 8.2, the beam is split into two separate paths which are coupled to their respective optical fibres after a pair of telescope lenses. The power of the SLM and LS beams are individually controlled by an AOM operating in a servo loop.

The LS beam is delivered to the science cell with the optical setup illustrated in Fig. 8.3(a). On the same level as the dipole beams, the LS beam is first collimated to a radius of $500\,\mu\mathrm{m}$ by a fibre collimator (Thorlabs F230APC-1064). The vertical beam radius is subsequently expanded to $2.75\,\mathrm{mm}$ via two successive cylindrical lenses, namely $f = -13.7\,\mathrm{mm}$ (Thorlabs LK1816L1-C) and $f = 75.6\,\mathrm{mm}$ (Thorlabs LJ1054L1-C). After two steering mirrors, the beam is aligned at $20°$ relative to the probe beam, which is focussed by a $f = 80\,\mathrm{mm}$ cylindrical lens in a 2-axes translation lens mount (Thorlabs SCP05) secured directly on the bottom coil mount, as shown in Fig. 8.3(b). The incident angle is chosen such that the waist can be brought close to the prism surface (minimum displacement from the prism is $1.5\,\mathrm{mm}$), while not obstructing the probe beam path nor clipping the prism. For the purpose of alignment, the first cylindrical lens is mounted on a single axis translation
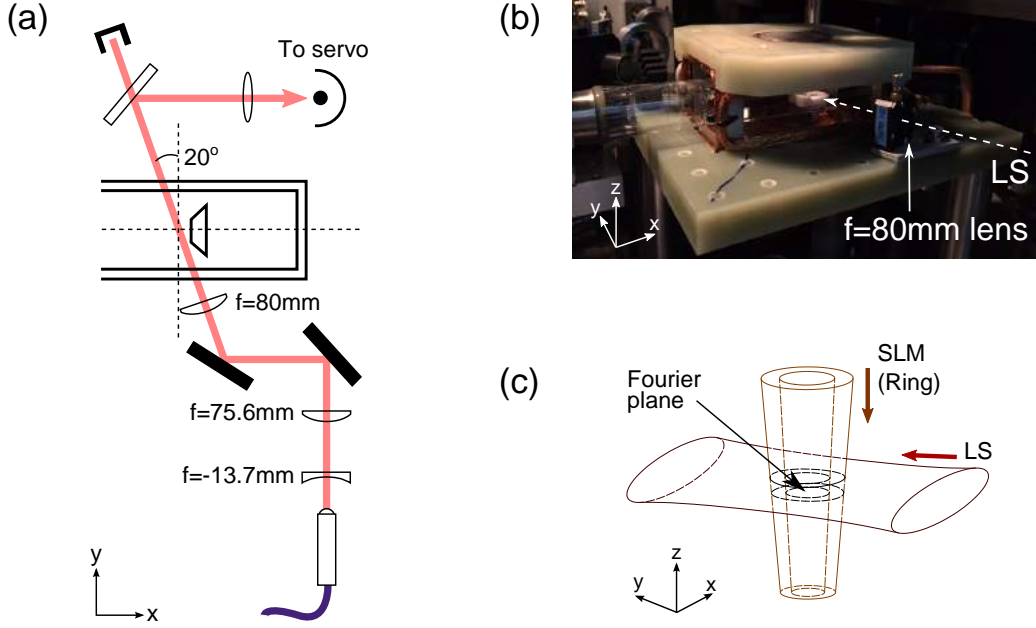
Figure 8.3: Optical setup of the light sheet (LS). (a) Schematic diagram of the optical layout. (b) Photo of the LS setup. The $f = 80\,\text{mm}$ cylindrical lens is mounted close to the science cell. (c) Illustration of the formation of a ring trap, where the LS beam intersects the SLM beam at the Fourier plane.

stage with 13 mm travel (Thorlabs MT1/M). From theoretical calculations, every 1 mm decrease in the distance between the first two lenses displaces the final focus of the LS by 1.23 mm further away from the $f = 80\,\text{mm}$ lens, whilst the waist changes by $\sim 0.5\,\mu\text{m}$. Final beam waists in this system are measured as $14\,\mu\text{m}$ and $520\,\mu\text{m}$ using the home built Gaussian beam profiler. The tightly focussed waist appears to be larger than originally anticipated ($10\,\mu\text{m}$), and we attribute the discrepancy to the fact that the beam is collimated to a smaller-than-anticipated beam size. This increases the ellipticity of the trap geometry of the horizontal plane. At the maximum power of 179 mW, the trap frequencies (in the order of: along the beam propagation; perpendicular to the propagation; vertical) of a pure trap are calculated to be $2\pi \times (4.1, 9.2, 310)\,\text{Hz}$. This corresponds to a trap depth of $710\,\text{nK} \times k_\text{B}$ (or $2.4\,\mu\text{K} \times k_\text{B}$ with levitation).

8.2.2   Installation and alignment

The initial alignment of the LS follows the technique similar to ref. [188]. After ensuring the LS is at the correct height on both sides of the science
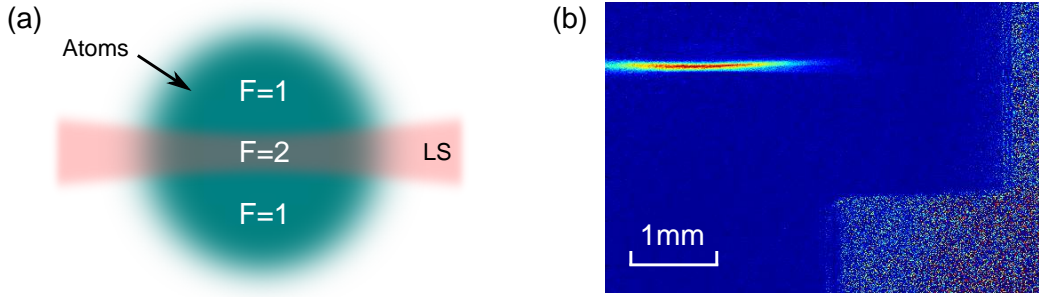
Figure 8.4: Initial light sheet alignment using the repump light. (a) Only the fraction of the atomic cloud sliced by the LS ends up in the $F = 2$ state, which is detectable through absorption imaging. (b) An absorption image of (a).

cell, the repump light is coupled into the LS fibre. As a consequence, only atoms in the path of the LS are pumped to the $F = 2$ state, which is detectable through absorption imaging, as illustrated in Fig. 8.4(a). Fig. 8.4(b) shows an absorption image where only the atoms in the thermal cloud (after 12 ms expansion from the quadrupole trap) sliced by the repump LS can be imaged. This technique, however, only helps us to locate the LS at approximately the correct vertical position. With an imaging path 20° from the LS, OD is summed along the beam and hence the position of the waist could not be located from horizontal imaging. Moreover, the 780 nm repump beam has a focus displaced by 650(50) μm from that of the 1064 nm beam. Further precise alignment therefore requires us to switch back to the original LS light.

Precise alignment requires atoms to be loaded into the LS from the crossed dipole trap at the end of the evaporation sequence described in Chapter 6 where atoms are cooled to near degeneracy in the hybrid trap. The $\lambda = 1064$ nm LS is ramped on to 144 mW whilst both dipole beams are ramped off simultaneously in 250 ms. The transfer into a pure LS trap is completed by a subsequent 250 ms ramp off of the quadrupole trap. The cold atomic sample transferred is used for optimisation of both beam *tilt* and *position*.

Tilt:

The orientation of the LS is important due to the 2D pancake geometry. It is vital for the LS to be horizontally level, as the pitch and the roll of the LS would further reduce the low trap depth. The definition of the pitch, roll, and
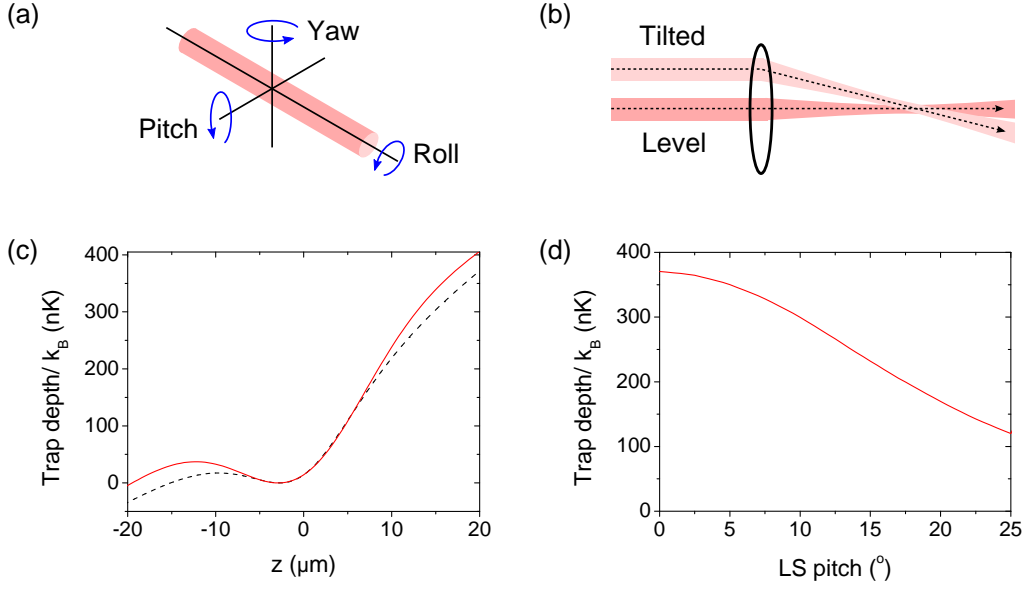
Figure 8.5: Effect of the LS pitch on the trap depth. (a) Illustration of the pitch, yaw, and roll of the beam. (b) Illustration of the beam with a pitch $\neq 0°$ (tilted). (c) Vertical trap potentials of the level LS (red solid) and the tilted LS with a pitch angle of $20°$ (black dashed). The power at the LS trap is $144\,\mathrm{mW}$. (d) Decrease of the trap depth of LS at $144\,\mathrm{mW}$ due the LS pitch angle.
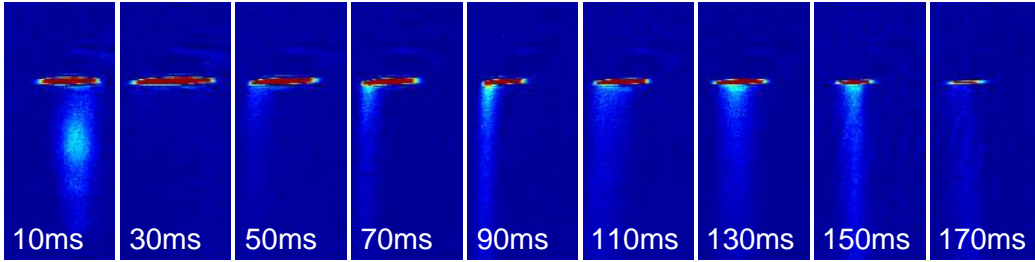
Figure 8.6: Atom loss from tilted LS. These are absorption images from horizontal imaging at different time instances after the transfer of atoms into the LS.

yaw of the beam is illustrated in Fig. 8.5(a). While the horizontal imaging is used for adjusting the roll of the LS, due to the orientation of the beams, the pitch cannot be corrected in the same way. A non-zero pitch of the LS beam results in a tilted beam, as illustrated in Fig. 8.5(b), which weakens the overall trap due to the interplay with gravity. As shown in Fig. 8.5(c), while a level LS beam alone has a trap depth of $365\,\mathrm{nK} \times k_\mathrm{B}$ at $144\,\mathrm{mW}$, it greatly decreases to $174\,\mathrm{nK} \times k_\mathrm{B}$ at $20°$ pitch angle. The decrease in the trap depth becomes more significant at higher pitch angle, as plotted in Fig. 8.5(d).

A lower-than-expected trap depth increases the difficulty in retaining atoms, which leads to an inevitable atom loss. This is shown in the horizontal ab-
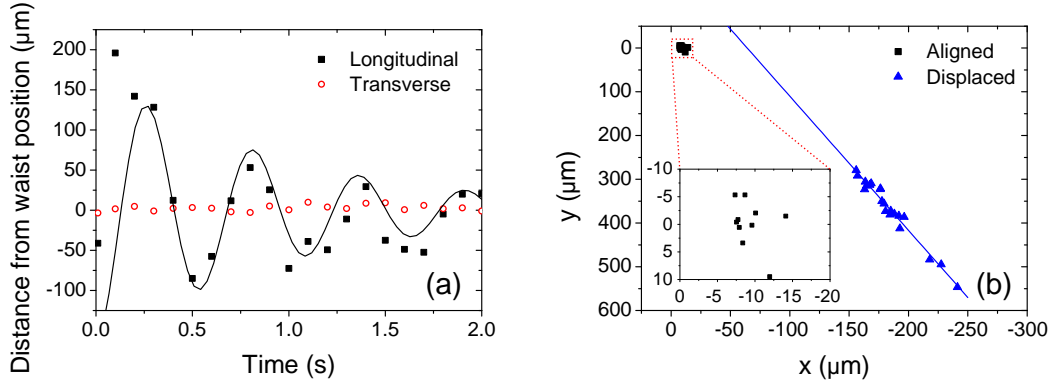
Figure 8.7: Alignment of the LS position. (a) Oscillatory motion of the centre of mass of the atoms along the LS (longitudinal) after they are transferred from the crossed dipole trap into the displaced LS trap. No transverse oscillation is observed. (b) Comparison of the oscillatory motion of the atoms in an aligned LS (black squares) with a displaced LS (blue triangles). $(x, y) = (0, 0)$ denotes the position of the crossed dipole trap. The blue line is a linear fit to the data points of the oscillation of the centre of mass of the atomic cloud in the displaced LS. Inset: Close up of the positions of the atom clouds after loading into an aligned LS. Measurements are taken every $100\,\mathrm{ms}$ after LS loading.

sorption images in Fig. 8.6. At $10\,\mathrm{ms}$ after atoms are loaded into the LS, one sees only a fraction of the atoms are transferred into the LS while the rest are dropped and lost from the trap. The atoms then undergo harmonic oscillation along the LS as the waist is not overlapping the crossed dipole trap. We observe severe atom loss from $50\,\mathrm{ms}$ onwards as the atomic cloud approaches the lower end of the tilted LS trap. One can thus correct the pitch of the LS by minimising the loss, which can be achieved through the use of the steering mirrors shown in Fig. 8.3(a).

Position:

The alignment procedure involves translating the centre of the oscillatory motion to the position of the dipole trap using vertical imaging. Fig. 8.7(a) shows a typical example of such oscillations along the LS propagation direction where the LS waist is at $(x, y) = (-175, 350)\,\mu\mathrm{m}$ relative to the crossed dipole trap centre.[1] As the beam intersects the WG (x-direction) at $70°$, the oscillatory motion of the atoms has both x and y components. The data in Fig. 8.7(a) is obtained through rotating the coordinate system by $70°$. The oscillation amplitude decreases as the waist is brought closer to the crossed

---

[1]For reference, the prism is located at $(x, y) = (2.96, 0)\,\mathrm{mm}$.
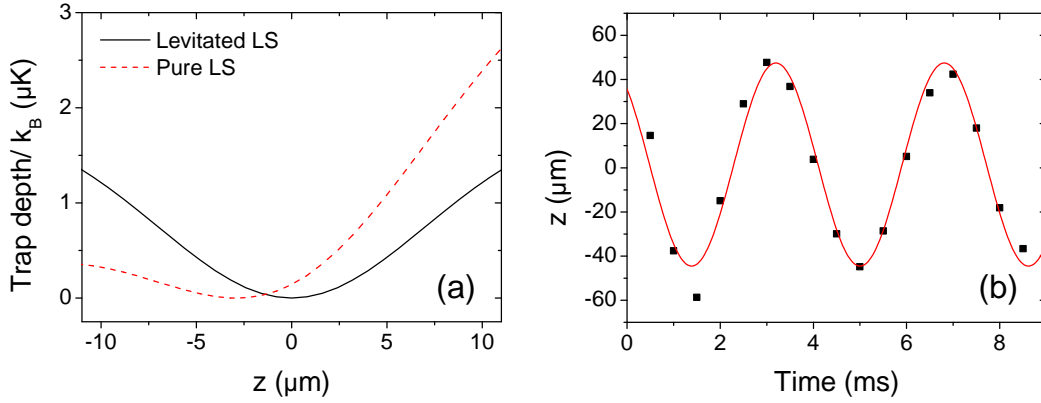
Figure 8.8: Measuring the vertical trap frequency of the LS. (a) Vertical trap potentials of a levitated LS (black solid) and a pure LS with gravity (red dashed). At a power of $144\,\mathrm{mW}$, the trap frequencies are $2\pi \times 305\,\mathrm{Hz}$ and $2\pi \times 267\,\mathrm{Hz}$ respectively. (b) Induced vertical oscillation of the atomic cloud.

dipole trap by steering the last mirror and adjusting the translation stage of the first cylindrical lens. Once both traps overlap, the atoms appear to be almost stationary upon transfer, shown by the data points in the red box in Fig. 8.7(b).

Once the tilt and the position of the LS are optimised, atom loss from the trap in the manner shown in Fig. 8.6 and the oscillation in the trap are both eliminated. This leads to an enhanced lifetime in the trap, where atoms can be held in the LS for well over $10\,\mathrm{s}$. With the vertical waist of the LS ($14\,\mu\mathrm{m}$) being much smaller than that of the dipole trap ($70\,\mu\mathrm{m}$ for the MB), atom loss during the transfer is inevitable. The optimised loading efficiency of ultracold atoms from the hybrid trap into the aligned, pure LS is $\sim 50\%$. Typically, loading is carried out towards the end of the BEC evaporation sequence, where $N = 5 \times 10^5$ atoms of $T \sim 100\,\mathrm{nK}$ are successfully transferred into the pure LS trap.

8.2.3 Characterisation of the light sheet

In order to measure the vertical trap frequency ω_z, our approach is to induce oscillatory motion to the centre of mass of the atoms in the trap. Here, while the $250\,\mathrm{ms}$ simultaneous ramp off of the dipole beams and ramp on to $144\,\mathrm{mW}$ of the LS is identical to what has been used earlier on, it is followed by a switch off of the quadrupole trap rather than the original $250\,\mathrm{ms}$ ramping
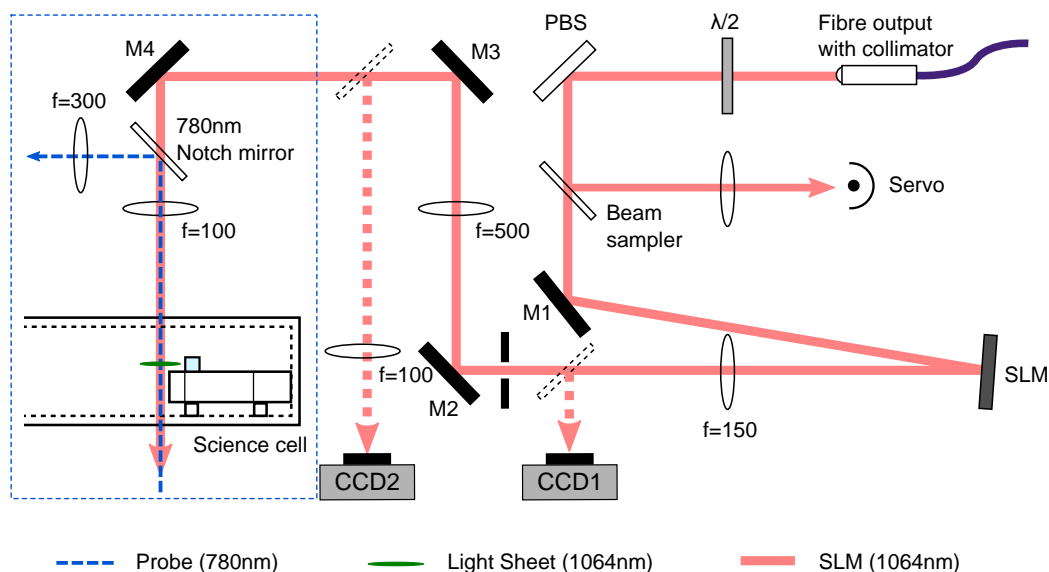
Figure 8.9: Incorporating the SLM setup into the main experiment. The blue dashed box indicates optics on the vertical plane viewed from the side, where the rest are mounted on a horizontal breadboard. The SLM beam (red solid), which shares the same optical path with the vertical imaging probe beam (blue dashed) before entering the science cell, intersects the light sheet (green oval), which enters the science cell (into the page) from the side at 70°. The rectangles with dashed border lines mark the positions of the mirrors that divert the beam to the CCD cameras. CCD1 monitors the intensity pattern with dimensions as calculated in the algorithm, while CCD2 monitors the intensity pattern 5 times smaller. M1 – 4 are mirrors for beam steering.

off. Due to gravity, the unlevitated LS trap has a trap centre $\sim 3\,\mu$m below the equivalent of the levitated LS trap, as shown in Fig. 8.8(a). As a result, the atoms experience a 'kick' from the abrupt switching and subsequently undergo oscillation about the vertical trap centre of the LS. The results are shown in Fig. 8.8(b), where the trap frequency of the pure LS trap at $144\,$mW is measured to be $\omega_z = 2\pi \times 270(4)\,$Hz. Through modelling the sagging trap under gravity, such a measured frequency translates to a vertical waist of $w_z = 13.9(1)\,\mu$m, which is in excellent agreement with the waist size measured using the Gaussian beam profiler.

8.3 Incorporating the SLM into the experiment

8.3.1 Optical setup

The optical setup for arbitrary trap formation is illustrated in Fig. 8.9. Here, the optics outside the blue dashed box are mounted on the same horizontal plane 133 mm above the black breadboard shown in Fig. 6.6. The height is chosen such that the components for the SLM beam do not obstruct that of the vertical imaging system. Collimated to a $1/e^2$ radius of 1.2 mm via the Thorlabs F220APC-1064 fibre collimator, the beam polarisation is ensured to be aligned to the SLM polarisation axis by a PBS (Thorlabs PBSW-1064). The $\lambda/2$ waveplate provides manual control on the power incident on the SLM. The reflected beam then passes through the beam sampler (Thorlabs BSF10-C) where a small amount of light is reflected for power servoing. The beam is incident on the SLM panel at $\sim 10°$ from the normal, where the maximum power at this point is restricted to 230 mW[2]. Similar to the previous optical setup in Fig. 7.3, the Fourier lens of $f = 150$ mm (Thorlabs AC508-150-C) is placed one focal length from the SLM. This lens, together with the optics further in the beam path, are aligned centred to the first order diffracted beam, rather than the unmodulated zeroth order, in order to minimise aberrations due to the curvature of the lenses. In addition, only the first order diffracted beam is allowed through the aperture placed at the Fourier plane 150 mm from the lens. This is to avoid the possibility of extra traps in the science cell caused by the zeroth order spot and other higher diffraction orders.

After the aperture, $\sim 65\%$ of the beam power originally incident on the SLM remains (see Section 7.2.2), from which the power is distributed between the signal and noise region based on the choice of mixing parameter m in the MRAF algorithm. As shown in Fig. 8.9, the SLM beam then shares the same beam path with the counter propagating 780 nm probe beam for vertical absorption imaging after passing through the notch mirror, where the probe beam is reflected towards the imaging camera. Thus the first imaging lens,

---

[2]This can be further increased to a limit of 450 mW if needed.

an achromatic doublet (Thorlabs AC508-100-B) with $f = 100\,\text{mm}$, serves as the second telescope lens of the SLM beam. A $f = 500\,\text{mm}$ lens (Thorlabs AC508-500-C) is chosen for the first telescope lens to yield a magnification of $f_2/f_1 = 0.2$ (with f_1 and f_2 represent the focal lengths of the first and second telescope lens respectively). This lens is placed at $\sim 650\,\text{mm}$ from the Fourier lens and plays an important role in SLM beam alignment which will be discussed in Section 8.3.2. The theoretical pixel size at the new Fourier plane is therefore $4.2\,\mu\text{m}$. From this point onwards, unless otherwise stated, we refer this rescaled plane as the Fourier plane.

8.3.2 SLM beam alignment

We use the following procedure to achieve precise alignment of the SLM beam such that the Fourier plane is brought to the aligned LS position.

Longitudinal:
Consider the simple telescope described in Section 8.3.1. With the position of the second lens fixed, translating the position of the first lens by Δz changes the image distance after the second lens by $\Delta z'$. Using the thin lens equation, and providing that $|\Delta z|$ is small, such shift in our system is given by

$$\Delta z' = -\left(\frac{f_2}{f_1}\right)^2 \Delta z = -\left(\frac{100}{500}\right)^2 \Delta z = -0.04\Delta z. \tag{8.1}$$

In other words, reducing the separation of the telescope lenses by $25\,\text{mm}$ moves the Fourier plane (or the focus of the Gaussian beam) towards the $f = 100\,\text{mm}$ lens by $1\,\text{mm}$. This method of displacing the Fourier plane is illustrated in Fig. 8.10(a). Through calculating the Gaussian beam propagation, moving the $f = 500\,\text{mm}$ lens by $\pm 40\,\text{mm}$ results an approximately linear change of the Gaussian waist by $\sim 5\%$. The change is small, thus by measuring the beam size at a fixed point while varying the lens position sees the Gaussian propagation recovered, as shown in Fig. 8.10(b). The alignment into the science cell is similar to that of the narrow potential well described in Section 5.2.2, where the position of the Fourier plane is identified via atom trapping at the waist of the Gaussian beam (the kinoform used here is a diffraction grating). Atoms are transferred to the SLM beam at the end
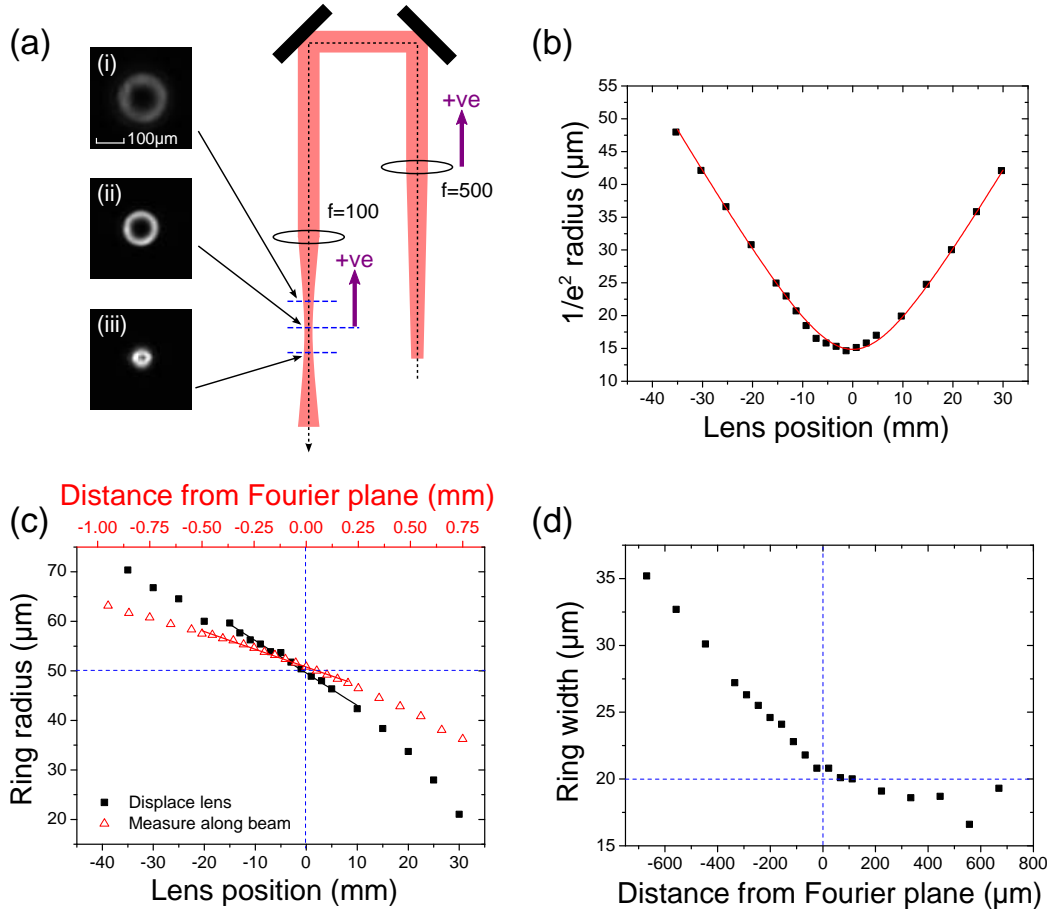
Figure 8.10: Longitudinal alignment of the SLM beam. (a) Mechanism to translate the location of the Fourier plane. Pushing the $f = 500\,\mathrm{mm}$ lens forward reduces the distance between the Fourier plane and the $f = 100\,\mathrm{mm}$ lens. The red shaded path illustrates the propagation of a normal Gaussian beam. With a target intensity pattern of an $r = 50\,\mu\mathrm{m}$, $\sigma = 20\,\mu\mathrm{m}$ ring, the images on left are the intensity patterns at (i) $-1.35\,\mathrm{mm}$, (ii) $0\,\mathrm{mm}$, (iii) $1.60\,\mathrm{mm}$ from the Fourier plane. (b) Measured $1/e^2$ radius of a Gaussian beam (red in (a)) at a fixed point after the $f = 100\,\mathrm{mm}$ lens with different positions of the $f = 500\,\mathrm{mm}$ lens. (c) Measured radius of the ring with ring dimensions defined in (a). Black square: fixing the measurement position, changing the $f = 500\,\mathrm{mm}$ lens position. Red triangle: changing the measurement position, fixing the lens position. The straight curves are linear fit to the data, see text. (d) Measured $1/e^2$ ring width, with ring dimensions defined in (a).

of the BEC cooling sequence described in Section 6.6. The SLM beam is ramped on to 129 mW and the MB, WG, and quadrupole trap are ramped off simultaneously in 250 ms. This is followed by a 75 ms hold of atoms in the SLM trap before imaging.

The calibration of the first telescope lens position versus the Fourier plane position is achieved by making use of the convergence of the ring pattern. Using CCD2 in Fig. 8.9, the radius of an $r = 50\,\mu$m, $\sigma = 20\,\mu$m ring is measured. As shown in Fig. 8.10(c), it varies linearly at $\pm \sim 200\,\mu$m about the position of the Fourier plane. Fixing the measurement position and varying the $f = 500$ mm lens position gives a change of radius at a rate of $-0.65(2)\,\mu$m per $+1$ mm lens displacement. In reverse, by fixing the lens position but tracing the ring size along the beam one measures a rate of $-0.0146(2)\,\mu$m per $+1\,\mu$m along the beam. From the two gradients, we obtain that a 1 mm displacement of the Fourier plane requires a $22.5(7)$ mm translation of the $f = 500$ mm position, which is in good agreement with the theoretically calculated value. We attribute the slight discrepancy to the thickness of the achromatic doublets. We note that the change in the ring width, however, does not vary linearly, as shown in Fig. 8.10(d). This measurement is used for the calculation of the trap depth of the ring at different points along the SLM propagation, which will be discussed in Section 8.4.

Transverse:

In order to maintain the quality of the desired intensity pattern, one needs to align the SLM beam such that it passes through the centre of the last lens with an incident angle at, or close to, 90°. Adjusting the alignment only through steering the last mirror (M4) changes the incident angle on the lens, as well as the incident position relative to the centre of the lens. This translates the position of the Fourier plane as it changes the propagation direction of the SLM beam after the lens, which reduces the incident angle of the SLM beam on the LS. This can be easily examined by monitoring the change of the shape at a fixed 2D plane with respect to mirror steering. Shown in Fig. 8.11 with the example of $r = 50\,\mu$m, $\sigma = 20\,\mu$m ring, the x translation of the SLM beam is coupled to the shrinking of radius and width along the direction of displacement.
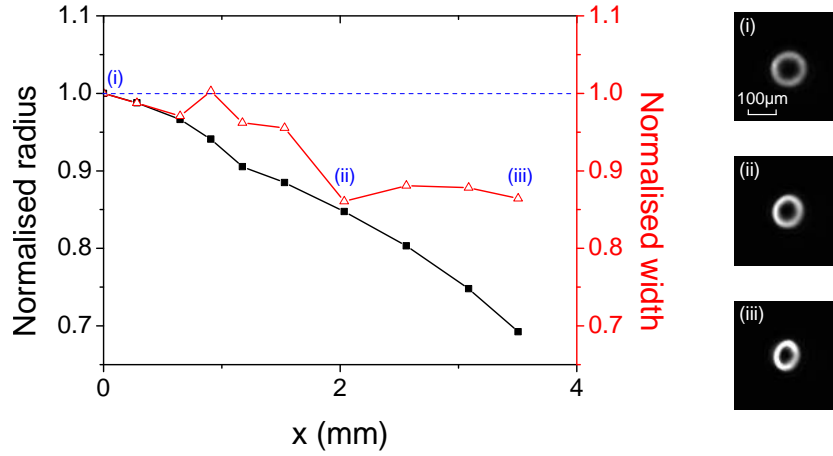
Figure 8.11: Transverse alignment of the SLM beam by steering the last mirror before the $f = 100\,\text{mm}$ lens. The changes in ring radii (black squares) and widths (red triangles) with respect to the transverse displacement of the ring on the Fourier plane are plotted. $x = 0\,\text{mm}$ denotes the position of the intensity pattern on the Fourier plane from which the laser beam is incident perpendicularly at the centre of the lens. Measured images at $x =$ (i) $0\,\text{mm}$, (ii) $2.03\,\text{mm}$, and (iii) $3.50\,\text{mm}$ are shown in the right hand column.

For the alignment of the horizontal position of the SLM beam, we make use of the vertical imaging probe for two main reasons. Firstly, the vertical beam path is centred at the $f = 100\,\text{mm}$ imaging lens. Secondly, using an aperture, one can create a small beam (diameter $\sim 2\,\text{mm}$) with the position of the atoms in the crossed dipole trap at the centre of the beam. Once the centre of the SLM beam path overlaps with that of the apertured probe beam through steering M3 and M4, the SLM beam is at close proximity to the crossed dipole trap. The experimental sequence for the transverse alignment is similar to the longitudinal alignment, except for that the LS is also ramped on to $144\,\text{mW}$ during the $250\,\text{ms}$ ramp to provide confinement along the z-direction. Using the location of the atoms, this method of alignment has brought the SLM beam within $\sim 100\,\mu\text{m}$ from the dipole trap. Although the beam steering is inevitable here for further fine adjustment, Fig. 8.11 shows that the effect to the intensity pattern should be minimal (a displacement of $\sim 300\mu\text{m}$ sees the both the ring radius and width changes by 5%).

In order to check if both beams are correctly aligned, where the LS beam is intersecting the SLM beam at the Fourier plane, we assess the shape of the thermal cloud in the SLM+LS potential. This is achieved by first switching
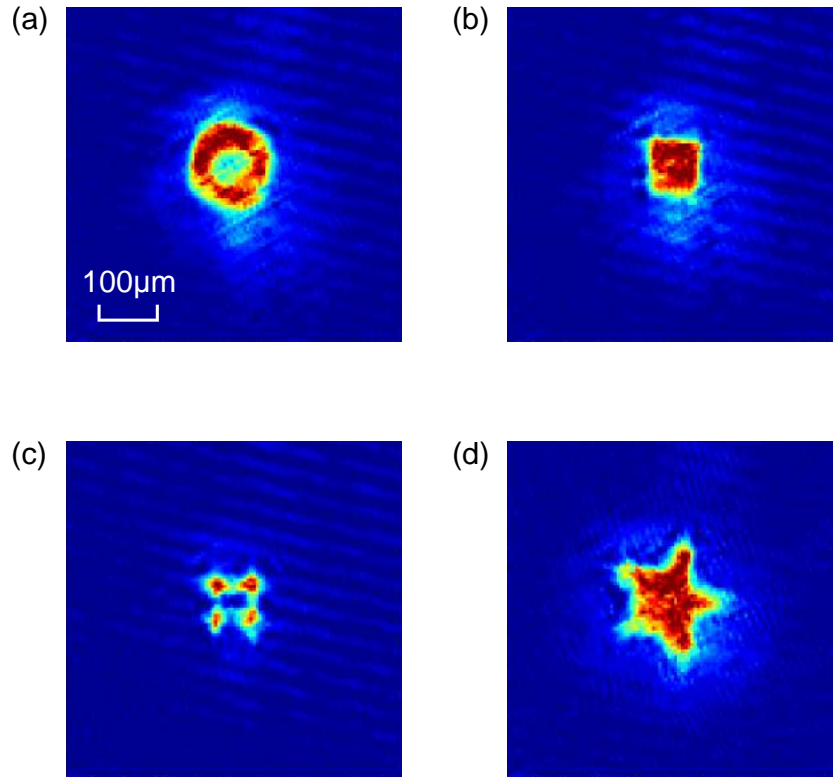
Figure 8.12: Absorption images of atoms in arbitrary trap shapes. (a) A ring with $r = 50\,\mu$m and $\sigma = 20\,\mu$m. (b) A $80\,\mu$m$\times 80\,\mu$m square. (c) A 4-site lattice with spacing of $60\,\mu$m. (d) A star with all sides the same at $60\,\mu$m. The large thermal cloud with low OD in the background is the fraction of atoms that is *not* captured by the SLM+LS trap and thus falls due to gravity.

the phase pattern on the SLM from the grating to the kinoforms generated by the MRAF algorithm. At the end of the BEC evaporation trajectory in the hybrid trap (see Section 6.6), the atoms are held in this trap for 1 s whilst the LS is ramped on to 144 mW. It is followed by ramping both WG and MB off and ramping the SLM beam on to 92 mW in 100 ms. The quadrupole gradient is kept at just below exact levitation at 27.3 G cm^{-1} throughout this process. Fig. 8.12 shows the absorption images of thermal atoms in 4 different shapes after a 50 ms hold in the trap. The dimensions of the images agree with the target values, which confirms that the positions of both beams are optimised.

8.4 Atom trapping in the arbitrary optical potentials

In this section, we present the data of the current status of the experimental progress. By making use of the MB, LS, and SLM beams, trapping of ultra-cold atoms in ring traps in our experiment is realised. Unfortunately, after the transfer into the SLM+LS trap, we encounter relatively high atom loss from the trap which reduces the overall lifetime of the ring trap. We begin by laying out the loading procedure, followed by a qualitative insight of the atom loss mechanism. In addition, we will also present the analysis of the smoothness of the ring trap.

8.4.1 Loading atoms into the ring trap

The loading procedure takes $\sim$ 2 s which is summarised in Fig. 8.13. At the end of the final power ramp of the dipole beams in the evaporation, the atoms are held in the crossed dipole trap whilst the SLM is ramped on in 1 s. It is followed by a 500 ms ramp off of the WG, whilst the dithering amplitude of the MB is increased to 220 μm. The MB power is ramped up simultaneously to 1.7 W in order to ensure that the strong confinement along the vertical direction is maintained. Recalling the robust nature of the SLM beam propagation, the intensity pattern remains approximately unchanged over the vertical radius of the MB (70 μm). Hence, in the case where the target pattern is a ring, the resulting atom cloud resembles the shape of a
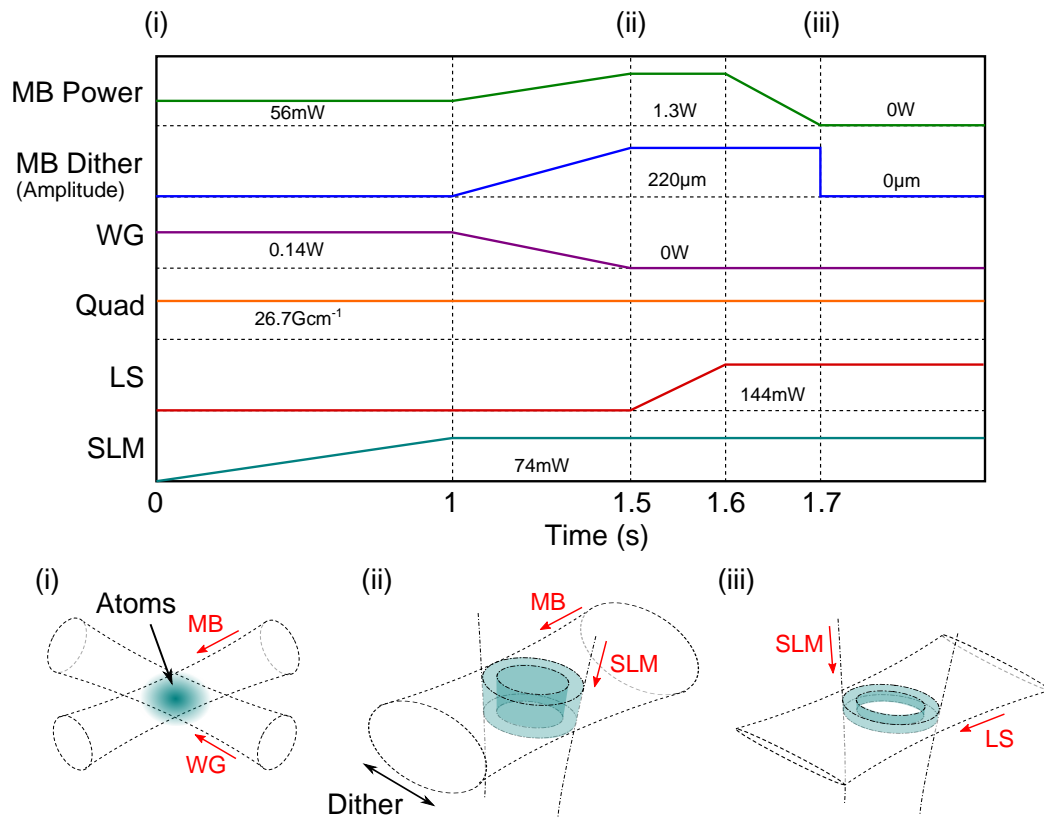
Figure 8.13: Loading procedure of the ring trap. The experimental loading sequence shows the operations of the beams and the quadrupole trap after the end of the evaporative cooling routine. Different stages of the transfer process are illustrated: Ultracold atoms in (i) crossed dipole trap, (ii) dithered MB and SLM potential, and (iii) final potential with SLM and LS.
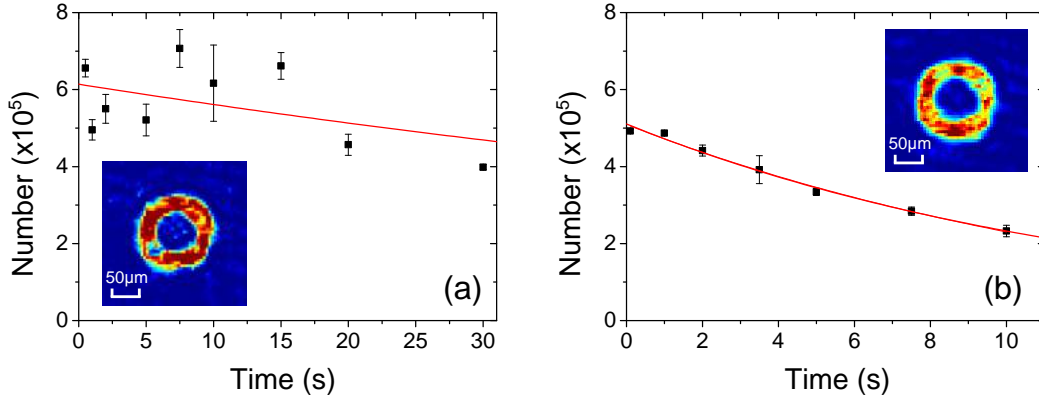
Figure 8.14: Lifetime measurements of (a) the dithered MB and SLM trap and (b) the SLM+LS trap. In the measurements, atoms are held at (a) configuration ii, and (b) configuration iii, of Fig. 8.13 for various durations before release. The atom number is measured after 37 ms TOF. Insets are absorption images of the atom-filled rings of $r = 50\,\mu\text{m}, \sigma = 20\,\mu\text{m}$.

hollow cylinder, as shown in Fig. 8.13(ii). The transfer into the SLM+LS trap is achieved by ramping the LS on to 144 mW in 100 ms, and subsequently ramping the MB off in 100 ms. This can be thought of taking a slice of the hollow cylindrical atomic cloud at the position of the Fourier plane, as shown in Fig. 8.13(iii).

8.4.2 Atom loss from the arbitrarily shaped traps

Through measuring atom loss from the trap, the lifetime of the SLM+LS ring is found to be 12.7(6) s, as shown in Fig. 8.14(b). This is compared to the results of the equivalent measurement with the dithered MB+SLM trap as presented in Fig. 8.14(a). Although in this case a reliable lifetime cannot be deduced due to a large error, it is apparent that the lifetime of the SLM+LS trap is inferior to the dithered MB+SLM trap. Perhaps more puzzling, while atoms stay trapped in the pure LS *alone*, the addition of the SLM beam at a certain power range, which varies for different intensity patterns, significantly enhances the atom loss. This is observed in both pure and levitated SLM+LS traps. In the following, we present two possible causes of the loss that have been investigated to the date that this thesis is written.

Dipole force along the SLM beam
From Section 8.1 it is shown that the propagation of the SLM beam, where
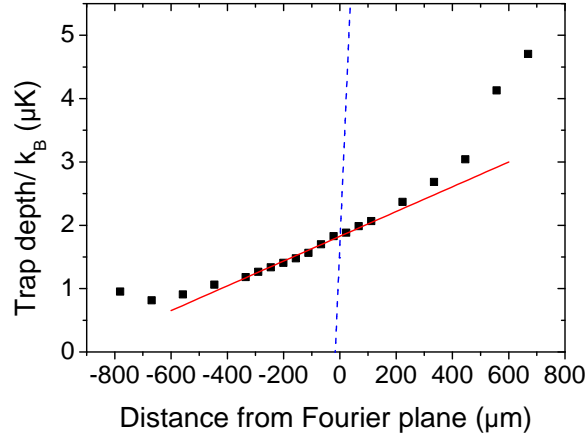
Figure 8.15: Trap depth of the ring along the SLM beam propagation. The red solid line is a linear fit to the experimental data from $-330\,\mu$m to $110\,\mu$m. This is compared to the gravity, indicated by the blue dashed line.

the target intensity pattern is a ring, resembles a converging hollow cone. Hence the peak intensity increases as the beam propagates further away from the Fourier plane, and so as the trap depth U_0. One suspicion is that the dipole force on the atoms along the SLM beam is strong enough to drag atoms out of the SLM+LS trap. To investigate this, we first assume that the intensity pattern of the SLM beam about the Fourier plane is a perfect Gaussian ring. Using the measured radius and ring width presented in Fig. 8.10(c) and (d), we calculate the potential depth U_0 at a given power P along the beam. The derivation of the trap depth of a ring trap is presented in Appendix B. As shown in Fig. 8.15, U_0 varies approximately linearly within $\pm 200\,\mu$m about the position of the Fourier plane. The gradient (red solid line), proportional to the dipole force acting on the atoms, is calculated to be $2\,\mu$K mm^{-1}. By comparing it to the potential gradient of gravity $mg/k_{\mathrm{B}} \sim 100\,\mu$K mm^{-1} (where m is the atomic mass of ^{87}Rb and $g = 9.81\,\mathrm{m\,s}^{-2}$ is the gravitational acceleration), the possibility that the atoms are pulled out of the SLM+LS potential by the SLM beam dipole force is ruled out.

Heating effect from the transfer

Another possible explanation to the atom loss is that the temperature of atoms increases during the transfer process. As such, atoms could become too hot to remain in the trap. Indeed, in the example of transferring atoms into a tighter harmonic trap, atoms are likely to be heated if the process is non-adiabatic, which reduces the PSD [239]. In the case where the form of

trap geometry changes during the transfer, the density of states is altered which can also cause the temperature to increase, even if the loading is adiabatic. Such an effect in the transfer of a Bose gas from a harmonic potential into a ring trap has been evaluated analytically and numerically for both thermal and degenerate cases [85]. In brief, let us consider the thermodynamics of the system. In adiabatic loading, entropy is preserved and hence remains constant throughout the process. The entropy S for a thermal system $T \gg T_c$ is given by [83, 85]

$$\frac{S}{k_B N} = (\alpha + 1) - \ln \zeta(\alpha) - \ln \text{PSD} + \ln \zeta \left(\frac{3}{2} \right), \tag{8.2}$$

where the trap geometry dependent parameter α is as defined in Section 2.2.1. Assuming all atoms are transferred from the harmonic trap (h) to the ring trap (r), one can readily see that

$$\frac{\text{PSD}_r}{\text{PSD}_h} = \frac{\zeta(\alpha_h)}{\zeta(\alpha_r)} \exp(\alpha_r - \alpha_h) = 0.54. \tag{8.3}$$

In other words, at the end of the loading process, the PSD is approximately half of the initial value in the harmonic trap. This is likely to cause an increase in the temperature of the atoms. For our system, the $r = 50\,\mu\text{m}$, $\sigma = 20\,\mu\text{m}$ ring trap is formed from $72\,\text{mW}$ in SLM and $144\,\text{mW}$ in LS beams, resulting a levitated trap of $\sim 3\,\mu\text{K} \times k_B$ with trap frequencies $\omega_{r,z} \sim 2\pi \times (180, 300)\,\text{Hz}$. With a loading time $\sim 1\,\text{s} \gg \min(2\pi/\omega_{r,z}) \approx 6\,\text{ms}$, the transfer process can be regarded as adiabatic [84]. The temperature of the atoms prior to and after the transfer is measured after $37\,\text{ms}$ TOF,[3] where an increase from $\sim 100\,\text{nK}$ to $\sim 250\,\text{nK}$ is observed. As a result, one requires a trap depth of $\sim 2.5\,\mu\text{K} \times k_B$, rather than $\sim 1.0\,\mu\text{K} \times k_B$ (atoms equilibrate to $\sim 10\%$ of the trap depth), for the loaded atoms to remain trapped.

In conclusion, to avoid atom loss from the heating effect, it is important to either reserve enough overhead in the SLM beam power (hence a deeper trap), or transfer atoms that are cooled to, or close to, degeneracy. A ring BEC can be achieved by either carrying out evaporation in the final trap, or through transferring a degenerate gas. In particular, providing that the condensate

---

[3]This assumes a harmonic trap, thus such a comparison can only form a qualitative argument.
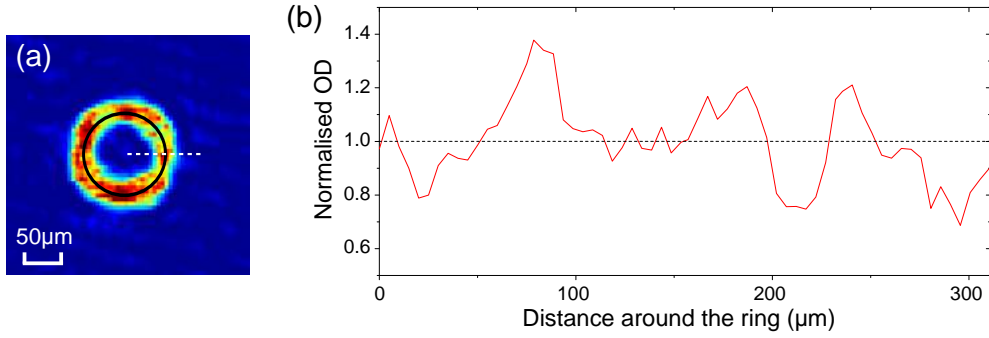
Figure 8.16: Smoothness of the SLM+LS ring trap. (a) Absorption image of the ring. The OD along the the ring, marked with the black circle, is measured. The measurement, begins at the white dashed line, is taken clockwise around the ring. (b) Normalised OD along the ring. Normalisation is obtained through dividing the experimental data points by their mean value.

fraction in the partially condensed system *in the harmonic trap* is above some threshold, it does not transform back into a thermal system and the condensate fraction is well preserved during such adiabatic loading [84, 85].

8.4.3 Smoothness of the ring trap

We recall that the target smoothness of any trap features is required to be no larger than $\sim 5\%$ [190]. Propagation of a bright soliton through a potential with small fluctuations can lead to unexpected behaviour. We have already seen in Chapter 5 that the additional small potential ripples to the deep potential well causes an enhancement to the quantum reflection. In a weak random nonlinear potential, the rather 'rocky' propagation path can cause either or both of the soliton mass and velocity to decay [240].

In Chapter 7, we have measured the standard deviation for different intensity patterns at the original Fourier plane (after the $f = 150\,\text{mm}$ lens), where the values are presented in Table 7.2. However, due to the extra glass surfaces of the lens, mirrors, and the science cell along the beam path, images can be distorted by aberrations. As a consequence, the quality of the intensity patterns is likely to worsen at the projected Fourier plane inside the science cell. By redefining the term 'smoothness' as the standard deviation of the OD compared with the target values, we measure the smoothness of the ring in the science cell using the trapped atoms. Using the atom-filled SLM+LS ring shown in Fig. 8.16(a), we measure the OD fluctuation along the ring.

The standard deviation of the normalised OD, as shown in Fig. 8.16(b), is measured to be 15.5%. Much work for improving the smoothness is hence required before one can use the ring trap for interferometry experiments.

8.5   Comments and limitations

In the hope of utilising this current setup for future interferometry experiments with solitons, we outline some of the challenges that need to be addressed.

- The trap geometry of the light sheet is not symmetric/circular along the horizontal directions. As a result, the trap frequency is non-zero along the ring which deviates from the system considered in Section 2.5.2. For a propagating bright soliton, the periodicity of the trap potential along the ring can also induce effects such as radiative soliton decay [240]. This can be solved by correcting the ring intensity using the SLM, or by carrying out modification to the combinations of the LS optics.

- The current transfer method cannot be applied for the creation of bright solitary waves. In the hope of loading an attractive condensate into the ring, the crossed dipole trap should overlap the path of the ring, but not the centre of the ring. This can be achieved by either realigning the SLM beam, or by shifting the ring pattern through an application of a different grating on the SLM.

- The optical depth of the absorption images of atoms in arbitrary trap shapes is typically in the order of $\sim 3 - 4$, which sits at the limit of such a traditional imaging method in providing proper measurements of the column density of the cloud [241]. With the low probe intensity to saturation intensity ratio, these clouds appear to be optically thick and little probe light can penetrate through. This leads to poor signal-to-noise ratio, as well as a loss of the information of the density profile. The smoothness measurement described in Section 8.4.3 could therefore contain artifact from the imaging system. Alternative imaging techniques, such as strong saturation absorption imaging [241], is thus required for obtaining images that truly reflect the density pro-

files at high density, which should result in a better measurement of the quality of the arbitrary traps.

- Although the feedback loop described in Section 7.7 has proved to reduce the discrepancy between the measured and target intensity patterns, the resulting improvement ($\sim 4\%$) is somewhat minute. While the feedback loop is yet to be tested with the use of atoms to date, other powerful aberration correction tools, such as the Shack-Hartmann algorithm [188, 203, 237], should also be considered. This method relies on truncating the SLM panel into areas of linear phases (gratings). The fraction of the beam incident on one of these areas are diffracted by a known angle and is subsequently focussed to a spot at the Fourier plane after one, or a series of, lenses (see Section 7.2.4). Any phase aberration the beam picks up along its path would cause a displacement from the target spot position. This can be used to retrieve the aberration related phase information. In our experiment, this technique requires the use of atoms trapped at the focus. Using a smaller beam which underfills the SLM panel leads to an inability to retrieve the phase aberrations in regions with low intensity and thus insufficient trap depths.

8.6   Summary

In this chapter, we have demonstrated the trapping of atoms in arbitrary optical potentials. Such potentials are formed by a combination of the SLM beam and a 2D light sheet which provides the necessary confinement along the direction of the SLM beam propagation. A dithered MB is also employed during the loading process. In the current state of the experiment, $\sim 5 \times 10^5$ ultracold atoms are successfully loaded into a ring trap with dimensions $r = 50\,\mu$m, $\sigma = 20\,\mu$m, which has a lifetime of $12.7(6)$ s. An increase in the cloud temperature is observed after the transfer, where we attribute the change in trapping geometry to be the cause. The quality of the ring suffers from the aberrations at the glass surfaces along the beam path, which sees the measured smoothness of the ring plunge down to 15.5%. Aberration correction is hence one of the major challenges that requires addressing in the future. Nevertheless, the understanding of the transfer mechanics and atom trapping in ring potentials brings us closer to the ultimate goal of

realising a rotational interferometer using bright solitary waves.

Chapter 9

Conclusion and outlook

9.1 Summary

In this thesis we have demonstrated two important steps towards bright solitary wave interferometry for rotational sensing, namely:

- The splitting of bright solitary waves (Part I);

- Atom trapping in a ring potential (Part II).

In Chapter 2, we reviewed the theoretical studies on how bright solitary waves can be utilised to construct matter-wave interferometers. We discussed that the splitting and recombination of solitons at narrow potentials depend strongly, but not exclusively, on the kinetic energy and the relative phase of the solitons respectively. Loading the soliton into a ring trap, and utilising the phase dependence of the outcome of soliton recombination at barriers, form the main components of a solitary wave Sagnac interferometer.

Using the first generation of our experimental apparatus, as summarised in Chapter 3, we showed in Chapter 4 the creation of ^{85}Rb BECs through direct evaporative cooling in the crossed dipole trap. We demonstrated the creation of bright solitary waves by transferring the BEC into an optical waveguide, and subsequently tuning the atoms to a small and negative scattering length via the $155\,\mathrm{G}$ Feshbach resonance. The soliton's particle-like behaviour was shown from its classical reflection from a wide repulsive barrier.

We reported the realisation of soliton splitting in Chapter 5, where quantum reflection of up to 25% of atoms from a narrow potential well was observed. Such a potential well was created by a tightly focussed light sheet with a waist of $1.9(2)\,\mu$m. The measured reflection fraction was, however, larger than the theoretical prediction for a Gaussian beam. By modelling the system, we found that the presence of multiple diffraction intensity maxima of the light sheet, rather than a single Gaussian maxima, could cause an enhancement in the reflection.

In Chapter 6 we presented the upgrade of the experimental apparatus. The second generation consisted of additional magnetic coils which provided control of the magnetic curvature. A new dipole trap formed from a waveguide and a moving beam allowed us to displace the trap centre to close to the Dove prism, enabling the future experiment of probing atom-surface interaction with solitons – one of the long term goals of the project. Using the new equipment, we also demonstrated the creation of ^{87}Rb BECs in both the static and the time averaged optical dipole traps.

A ring trap is at the heart of the proposed scheme of the bright solitary wave interferometer. This was generated by the SLM through imprinting phase information to the laser beam, as discussed in Chapter 7. This reconfigurable diffractive optical element allowed us to create not only a ring trap, but traps of any arbitrary shapes. The kinoforms for smooth and speckle-free holograms were achieved through an analytical first phase guess and the Mixed-Region Amplitude Freedom (MRAF) algorithm, combined with the use of a smaller beam that underfilled the SLM panel. We reported high quality intensity patterns, which included an $r = 0.5\,\text{mm}, \sigma = 100\,\mu$m ring with an error of 0.08. Finally, in Chapter 8, we presented the implementation of this SLM optical setup, along with a horizontal light sheet, into the main experimental setup. With the light sheet intersecting the SLM beam at the Fourier plane, which were both aligned to the position of the dipole trap, we demonstrated the successful transfer and the trapping of ultracold atoms in the ring potential.

9.2   Outlook

The ability to split solitary waves and trap atoms in ring potentials is a stepping stone to the realisation of the bright soliton Sagnac interferometer. The soliton interactions with the attractive potential has also taught us ways to proceed to probing the surface potential using solitons – one of the long term goals of the experiment. In the final part of this thesis, we look at the future work required to achieve these ultimate goals of the project.

The smoothness of the ring, as highlighted in Section 8.4.3, requires improvement as one must ensure a smooth propagation path for solitons to avoid unexpected scattering events. While this can be achieved by means of feedback (discussed in Chapter 7) with atoms, the foremost task prior to such an operation is to improve the vertical imaging system. As suggested in Section 8.5, the poor signal-to-noise ratio and a loss of spatial and optical depth information when imaging the trapped atoms *in situ* can mask the exact density profile of the atoms, and hence the intensity profile, of the ring potential. To overcome such limitation of the low intensity absorption imaging, alternatives such as the high intensity absorption imaging [241] should be considered. Moreover, the goal of this project requires the ability to trace the splitting and subsequent recombination of the *same* soliton at potential barriers. As the current imaging technique is destructive, it is not suitable for studying the dynamics and the evolution of the same atomic sample at multiple time instances. Hence, to address this, a non-destructive imaging technique, such as Faraday imaging [242], dispersive light scattering [243], or partial-transfer absorption imaging [244], will be required in the future.

Along with the upgrade to the imaging system, the next stage is to revisit the creation of bright solitary waves from ^{85}Rb BECs using the second generation of the experimental apparatus. Moreover, a key difference between the interferometry scheme proposed in [52] (also see Chapter 2) and our experiment described in Chapter 5 is that soliton splitting and recombination are facilitated by a narrow potential *barrier*, as opposed to a potential *well*. Thus to proceed, a blue detuned laser beam with an optical setup similar to that for the potential well will need to be developed and installed. By aligning this blue detuned light sheet to intersect the waveguide, we can carry out in-

teresting soliton splitting experiments similar to the measurement described in Chapter 5. The removal of axial confinement using the curvature coil, together with the freely adjustable launch velocity that strongly depends on the acceleration of the moving beam [175], give great scope to experimentally explore the energy regimes described in Chapter 2. In particular, decoupling of the soliton velocity from the trap geometry means that very slow, spatially well separated solitons are achievable. This offers interesting physics, such as the creation of mesoscopically entangled Bell states via quantum superpositions of the solitary waves [116].

To realise the solitary wave interferometer for rotational sensing, it will first require a displacement of the ring with methods discussed in Chapter 8, such that the crossed dipole trap intersects along the path of the ring. With the ring intensity corrected using the SLM, the smooth toroidal potential will then be intersected by the blue detuned light sheet described above. This creates the two potential barriers that are half a ring circumference apart, as illustrated in Fig. 2.5(b). By inspecting the population transfer after the recombination of split solitons at the barrier, one can deduce the phase relation between the solitons, and subsequently the Earth's rotation rate. This solitary wave interferometer will be capable of producing measurements with precision surpassing the standard quantum limit [127].

In addition, the current setup has all the components required for exploring atom-surface interactions with bright solitons. The 3.25 mm scanning range of the moving beam (Section 6.4.1) allows us to translate the dipole trap close to the Dove prism, which sits 2.96 mm from the default position of the trap. The prism is designed such that an additional blue detuned laser beam can be used to produce an evanescent wave potential at the surface of the prism [68, 69]. Combining with the surface potential as discussed in Section 2.4, the potential at the prism surface can be tuned from attractive to repulsive depending on the laser power. By releasing the bright soliton into the waveguide towards the surface, this allows us to probe the short-range atom-surface potential. Theoretical studies [48] have shown that such a system could serve as an excellent surface probe with superior precision over other systems where ultracold gases or repulsive BECs are used.

Appendix A

Coil data

Calculation of the magnetic field and curvature
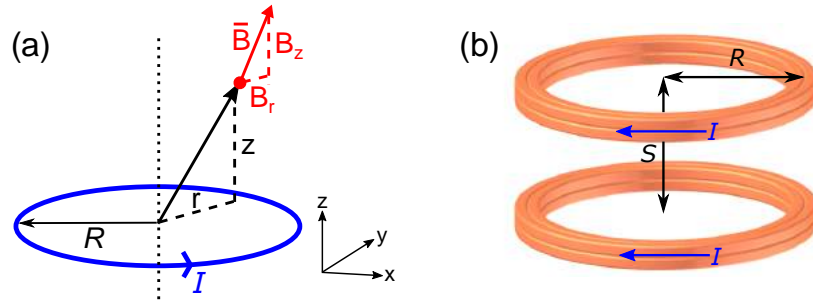
Figure A.1: The magnetic field of a current loop at any point in space. In the schematic diagram, a circular coil with current I and radius R has a magnetic field $\bar{B}$ at point (r, z). (b) A coil pair with a coil separation S. Each coil has n turns and a radius R.

A circular coil with a radius R and a current I generates a magnetic field $\bar{B}$ at point (r, z) in space, as illustrated in Fig. A.1(a). Using the Biot Savart law, one obtains the axial (B_z) and radial (B_r) components of such magnetic field:

$$B_z = \frac{\mu_0 I}{2\pi} \frac{1}{((R+r)^2 + z^2)^{1/2}} \left[K(k) + \frac{R^2 - r^2 - z^2}{(R-r)^2 + z^2} E(k) \right] \qquad \text{(A.1)}$$

and

$$B_r = \frac{\mu_0 I}{2\pi} \frac{z}{r\left((R+r)^2 + z^2\right)^{1/2}} \left[-K(k) + \frac{R^2 + r^2 + z^2}{(R-r)^2 + z^2} E(k)\right]. \qquad \text{(A.2)}$$

Here, $K(k)$ and $E(k)$ are the complete elliptic integral, of the first kind and second kind respectively, where $k = \sqrt{4Rr/[(R+r)^2 + z^2]}$ [245]. Let us now consider a pair of n-turn coils, where one coil is placed at $z = S/2$ and its counterpart at $z = -S/2$ such that the coils are separated by the distance S, as shown in Fig. A.1(b). The resulting magnetic field is simply the sum of $\bar{B}$ produced by each coil. In particular, the total axial magnetic field $B_{z,\text{tot}}$ along the coil axis (hence $r = 0$) is

$$B_{z,\text{tot}}|_{r=0} = \frac{\mu_0 n I R^2}{2} \left[\frac{1}{\left((z+S/2)^2 + R^2\right)^{3/2}} \pm \frac{1}{\left((z-S/2)^2 + R^2\right)^{3/2}}\right], \qquad \text{(A.3)}$$

where $+ (-)$ represents the coil configuration where the current I in the coils are flowing in the same (opposite) direction. Similarly, with the current in both coils flowing in the same direction, the magnetic field $B_{z,\text{tot}}$ on the $z = 0$ plane is

$$B_{z,\text{tot}}|_{z=0} = \frac{\mu_0 n I}{\pi\left((R+r)^2 + (S/2)^2\right)^{1/2}} \left[K(k) + \frac{R^2 - r^2 - (S/2)^2}{(R-r)^2 + (S/2)^2} E(k)\right], \qquad \text{(A.4)}$$

while $B_{z,\text{tot}}|_{z=0} = 0$ if the current in the coils are flowing in opposite direction. The radial curvature of the axial magnetic field on the $z = 0$ plane by readily calculating the second derivatives $\partial^2 B_{z,\text{tot}}/\partial r^2$ of Eq. A.4. Evaluating at $r = 0$ (or $k = 0$), and hence $K(k) = E(k) = \pi/2$, the expression for the radial field curvature is greatly simplified to

$$\left.\frac{\partial^2 B_{z,\text{tot}}}{\partial r^2}\right|_{r=0,z=0} = \frac{\mu_0 n I R^2}{\left(R^2 + (S/2)^2\right)^{7/2}} \left[2R^2 - 5\left(\frac{S}{2}\right)^2\right]. \qquad \text{(A.5)}$$
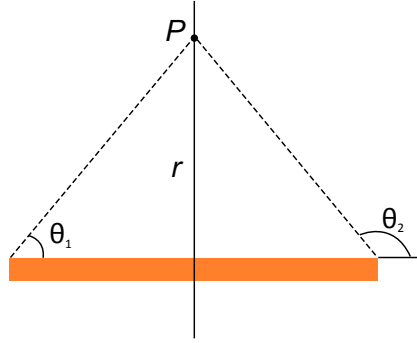
Figure A.2: Magnetic field at point P from a finite wire.

In order to calculate the expected field for a pair of rectangular coils, one can readily derive the equation by evaluating the magnetic fields from 4 separate finite wires. The magnetic field at a distance r from a finite wire is given by

$$B = \frac{\mu_0 I}{4\pi r}(\cos\theta_1 - \cos\theta_2), \tag{A.6}$$

where θ_1 and θ_2 are the angles which parameterise the length of the finite wire as shown in Fig. A.2. Now consider a rectangular coil with dimensions $2a$ and $2b$, the *total* magnetic field at point P along the axial axis x contributed by one side of length $2a$ is

$$B_a = \frac{\mu_0 I}{2\pi} \frac{a}{\left[(x^2 + b^2)(x^2 + a^2 + b^2)\right]^{1/2}}, \tag{A.7}$$

and similarly for one side of length $2b$ is

$$B_b = \frac{\mu_0 I}{2\pi} \frac{b}{\left[(x^2 + a^2)(x^2 + a^2 + b^2)\right]^{1/2}}. \tag{A.8}$$

We can now extract the field component along the x-direction by multiplying the above equations by $b/(x^2 + b^2)^{1/2}$ and $a/(x^2 + a^2)^{1/2}$ for side $2a$ and $2b$ respectively. By symmetry, the fields along the axial axis contributed by the other two sides are the same as their counterparts. Finally, by placing one coil at $x = S/2$ and one at $x = -S/2$, the axial magnetic field at the centre of the n-turn rectangular coil pair (of dimensions $2a \times 2b$) is

$$B = \frac{\mu_0 n I a b}{\pi} \left[\frac{1}{\left((x + S/2)^2 + b^2\right) \left((x + S/2)^2 + a^2 + b^2\right)^{1/2}} \right.$$
$$+ \frac{1}{\left((x + S/2)^2 + a^2\right) \left((x + S/2)^2 + a^2 + b^2\right)^{1/2}}$$
$$+ \frac{1}{\left((x - S/2)^2 + b^2\right) \left((x - S/2)^2 + a^2 + b^2\right)^{1/2}}$$
$$\left. + \frac{1}{\left((x - S/2)^2 + a^2\right) \left((x - S/2)^2 + a^2 + b^2\right)^{1/2}} \right]. \tag{A.9}$$
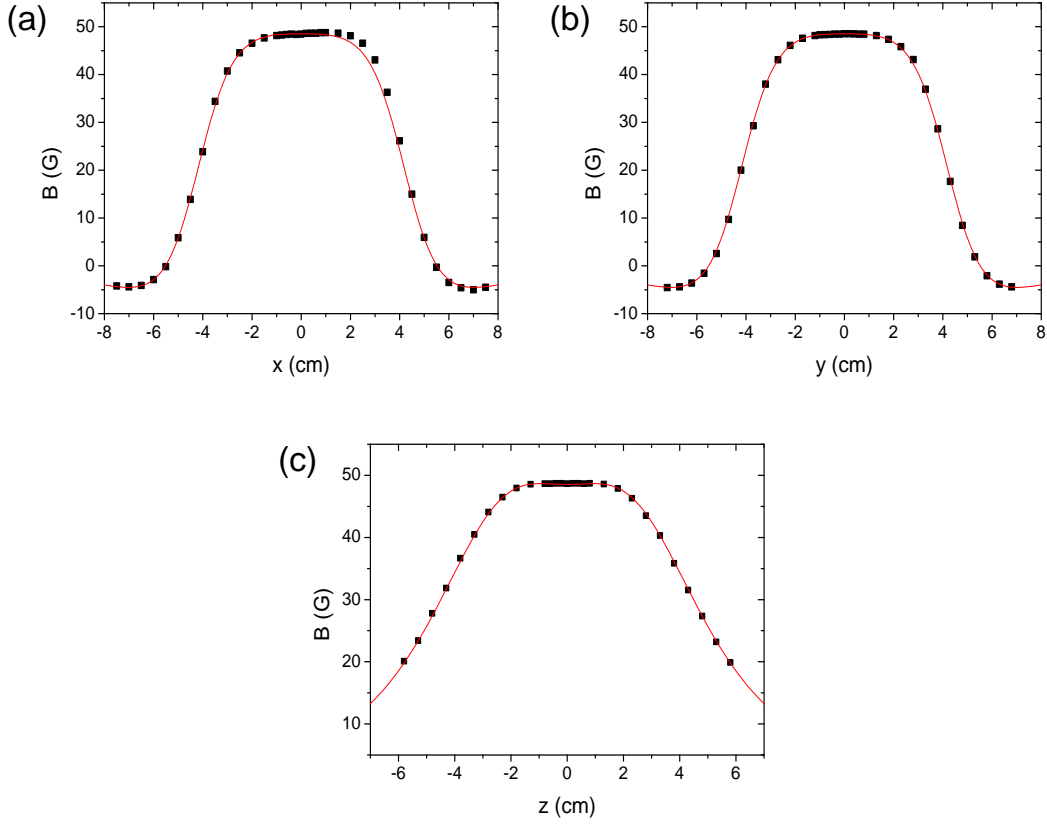
Bias coils

Figure A.3: Calibration of the bias coils using a current of $60\,\mathrm{A}$. (a) and (b) show the field along the radial directions, and (c) shows the field along the axial direction. The bias coils have 2×2 turns using $3.5\,\mathrm{mm} \times 3.5\,\mathrm{mm}$ copper wire. The fit uses Eq. A.3 and Eq. A.4 with the real parameters presented in Table A.1.

	Theoretical	Real
Inner Diameter [mm]	79	79
Outer Diameter [mm]	93	94
Inner Separation [mm]	38	39
Outer Separation [mm]	52	52
Equivalent coil radius [mm]	43.0	42.9
Equivalent coil separation [mm]	45.0	45.4
Resistance per coil [mΩ]	2.9	4.4
Field [$\mathrm{G\,A^{-1}}$]	0.807	0.813

Table A.1: Comparison of the expected and measured parameters of the bias coils.
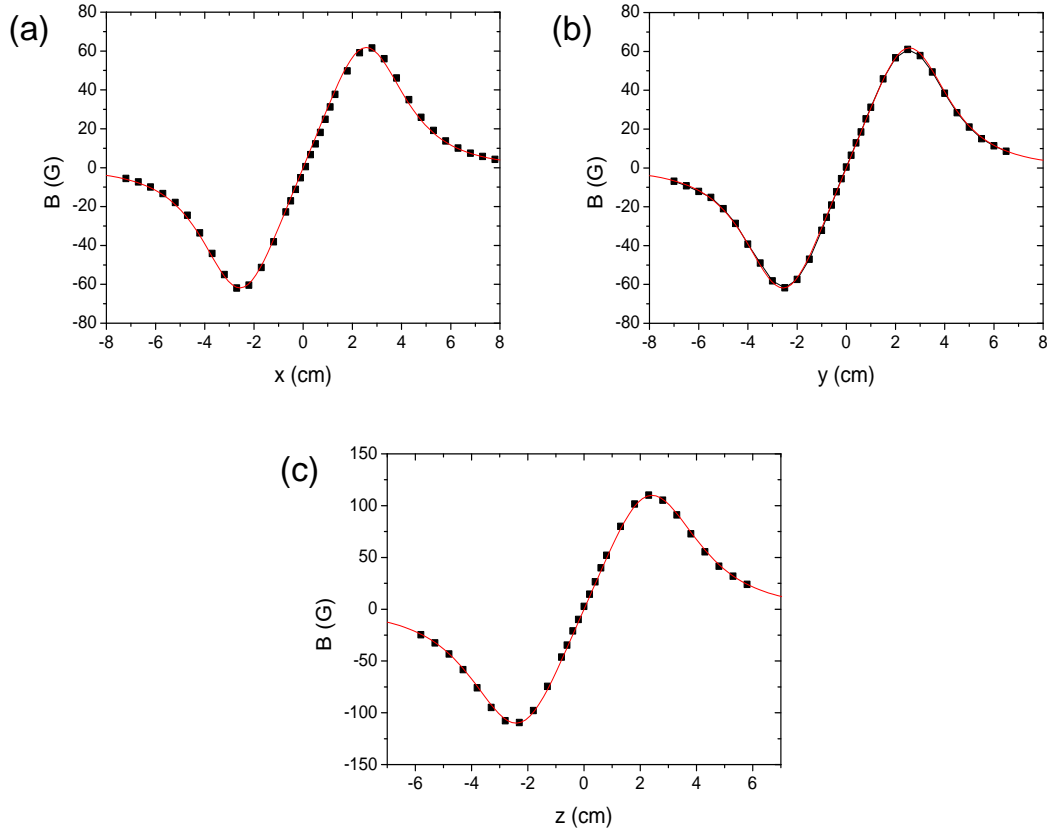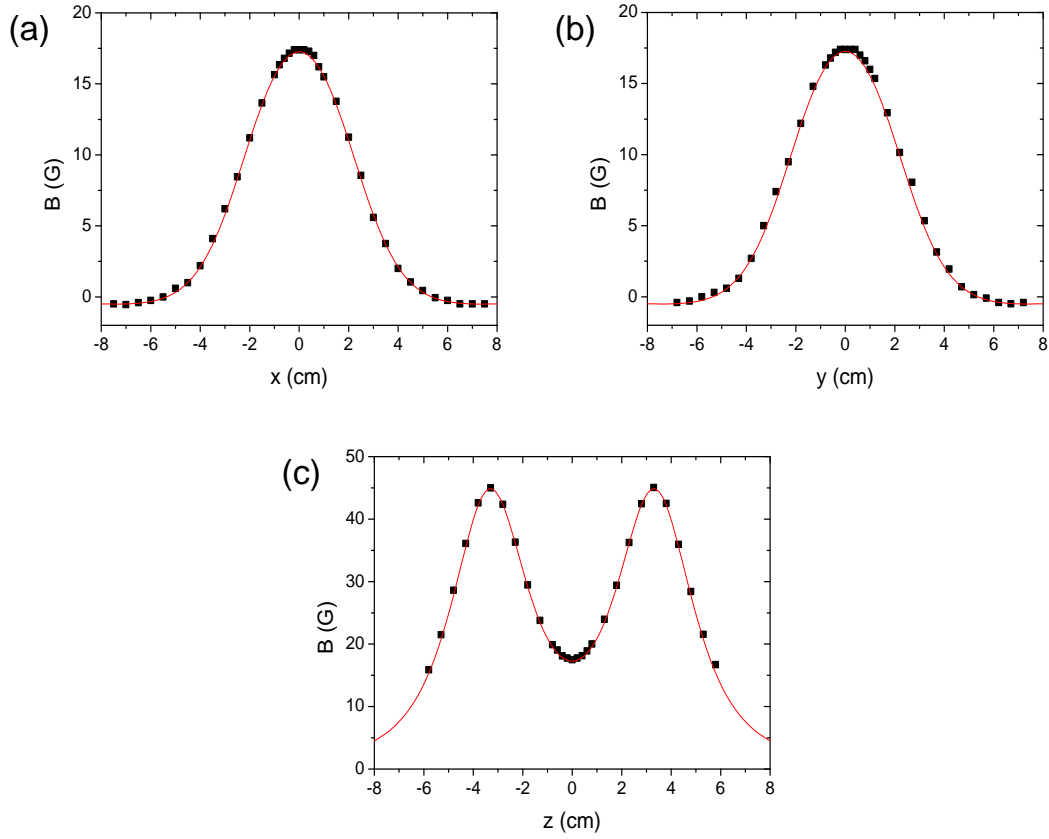
Quadrupole coils

Figure A.4: Calibration of the quadrupole coils using a current of 60 A. (a) and (b) show the field along the radial directions, and (c) shows the field along the axial direction. The quandrupole coils have 3×3 turns using $3.5\,\text{mm} \times 3.5\,\text{mm}$ copper wire. The fit uses Eq. A.3 with the real parameters presented in Table A.1. Note the quadrupole coils are in anti-Helmholtz configuration.

	Theoretical	Real
Inner Diameter [mm]	43	43
Outer Diameter [mm]	64	64
Inner Separation [mm]	36	36
Outer Separation [mm]	56	55
Equivalent coil radius [mm]	26.0	26.9
Equivalent coil separation [mm]	47.0	45.4
Resistance per coil [mΩ]	3.8	5.9
Field Gradient[G A^{-1}cm^{-1}]	0.995	1.022

Table A.2: Comparison of the expected and measured parameters of the quadrupole coils.

Curvature coils

Figure A.5: Calibration of the curvature coils using a current of 5 A. (a) and (b) show the field along the radial directions, and (c) shows the field along the axial direction. The curvature coils have 33 turns using copper wire with 1 mm diameter. The fit uses Eq. A.3 and Eq. A.4 with the real parameters presented in Table A.3.

	Theoretical	Real
Inner Diameter [mm]	43	43
Outer Diameter [mm]	55	56
Inner Separation [mm]	60	61
Outer Separation [mm]	76	76
Equivalent coil radius [mm]	24.2	24.0
Equivalent coil separation [mm]	66.0	66.7
Resistance per coil [mΩ]	107.3	140.3
Field [G A^{-1}]	3.558	3.502
Radial field curvature [G A^{-1} cm^{-2}]	-0.54	-0.53

Table A.3: Comparison of the expected and measured parameters of the curvature coils.
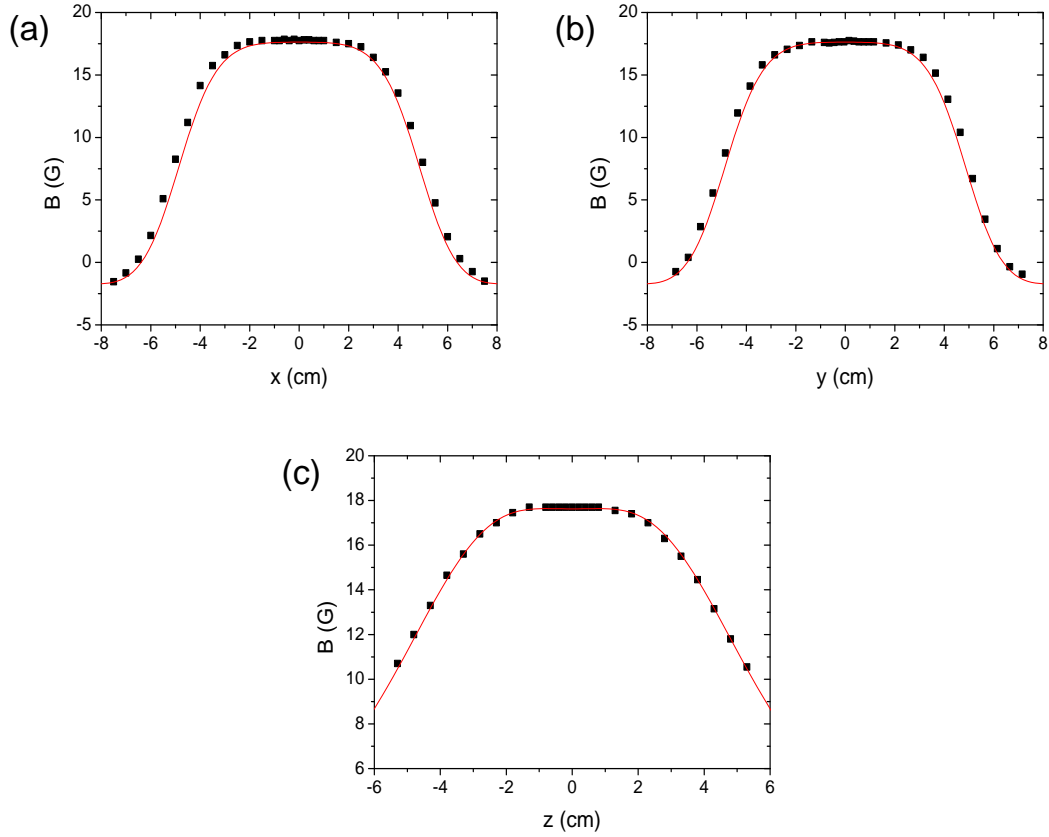
Cancellation coils

Figure A.6: Calibration of the cancellation coils using a current of 5 A. (a) and (b) show the field along the radial directions, and (c) shows the field along the axial direction. The cancellation coils have 20 turns using copper wire with 0.80 mm diameter. The fit uses Eq. A.3 and Eq. A.4 with the real parameters presented in Table A.4.

	Theoretical	Real
Inner Diameter [mm]	100	101
Outer Diameter [mm]	106	N/A
Inner Separation [mm]	48	48
Outer Separation [mm]	57	57
Equivalent coil radius [mm]	51.4	50.1
Equivalent coil separation [mm]	51.4	51.6
Resistance per coil [mΩ]	215.9	140.3
Field [G A^{-1}]	3.500	3.615

Table A.4: Comparison of the expected and measured parameters of the cancellation coils.

Up-Down shim coils
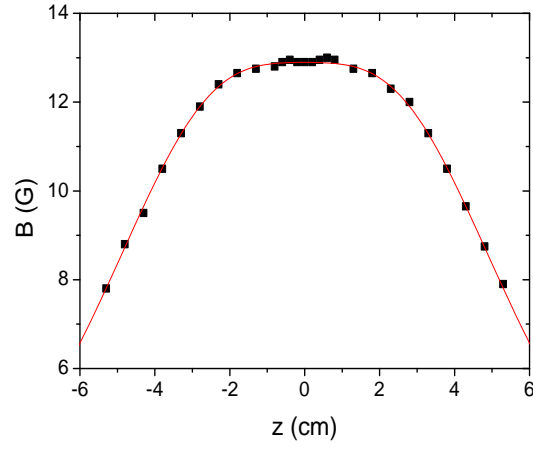
Figure A.7: Calibration of the Up-Down shim coils using a current of 5 A. Here shows the field along the axial direction. The Up-Down shim coils have 15 turns using copper wire with 0.80 mm diameter. The fit uses Eq. A.3 and Eq. A.4 with the real parameters presented in Table A.5.

	Theoretical	Real
Inner Diameter [mm]	106	N/A
Outer Diameter [mm]	110	110
Inner Separation [mm]	48	48
Outer Separation [mm]	57	57
Equivalent coil radius [mm]	53.9	53.3
Equivalent coil separation [mm]	51.4	51.6
Resistance per coil [mΩ]	169.8	218.2
Field [G A^{-1}]	2.579	2.639

Table A.5: Comparison of the expected and measured parameters of the Up-Down shim coils.

North-South shim coils

Figure A.8: Calibration of the North-South shim coils using a current of 5 A. Here shows the field along the axial direction. The North-South shim coils have 25 turns using copper wire with 0.80 mm diameter. The fit uses Equation A.9 with the real parameters presented in Table A.6.

	Theoretical	Real
Inner length (horizontal) [mm]	58	58
Inner length (vertical) [mm]	44	43
Outer length (horizontal) [mm]	68	68
Outer length (vertical) [mm]	54	53
Inner Separation [mm]	118	118
Outer Separation [mm]	128	130
Equivalent coil dimensions (H×V) [mm]	62×48	62×46
Equivalent coil separation [mm]	123	124
Resistance per coil [mΩ]	183.8	239.6
Field [G A^{-1}]	0.898	0.834

Table A.6: Comparison of the expected and measured parameters of the North-South shim coils.
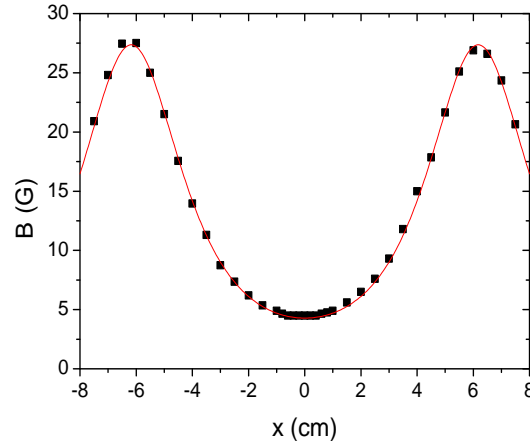
East-West shim coils
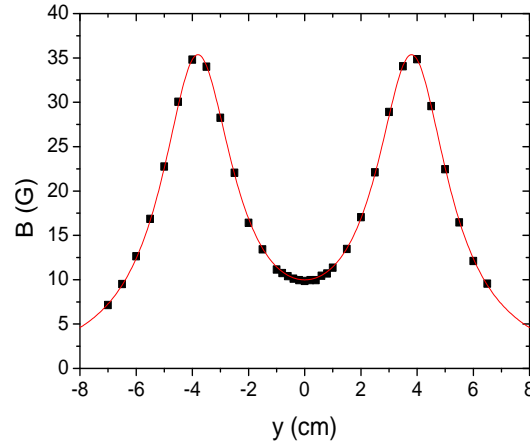
Figure A.9: Calibration of the East-West shim coils using a current of 5 A. Here shows the field along the axial direction. The East-West shim coils have 25 turns using copper wire with 0.80 mm diameter. The fit uses Equation A.9 with the real parameters presented in Table A.7.

	Theoretical	Real
Inner length (horizontal) [mm]	118	119
Inner length (vertical) [mm]	26	26
Outer length (horizontal) [mm]	128	128
Outer length (vertical) [mm]	36	36
Inner Separation [mm]	70	70
Outer Separation [mm]	82	130
Equivalent coil dimensions (H×V) [mm]	123×31	100×31
Equivalent coil separation [mm]	76	76
Resistance per coil [mΩ]	257.4	273.2
Field [G A^{-1}]	2.024	1.997

Table A.7: Comparison of the expected and measured parameters of the East-West shim coils.

Appendix B

Calculation of trap depth of a ring

To compute the trap depth of the ring potential at the Fourier plane of the SLM beam, we first consider extending the Gaussian beam profile I in one-dimension

$$I = I_0 \exp\left(-\frac{2x^2}{w^2}\right) \tag{B.1}$$

into a ring form with radius R and $1/e^2$ width w (I_0 is the peak intensity of the ring). The total laser power P of the ring is related to the ring intensity via

$$
\begin{aligned}
P &= \int_0^\infty \int_0^{2\pi} I_0 \exp\left(-\frac{2(r-R)^2}{w^2}\right) r \, \mathrm{d}r \mathrm{d}\theta \\
&= 2\pi I_0 \int_0^\infty \exp\left(-\frac{2(r-R)^2}{w^2}\right) r \, \mathrm{d}r.
\end{aligned}
\tag{B.2}
$$

Using substitution of $u = r - R$, we obtain

$$
\begin{aligned}
P &= 2\pi I_0 \int_{-R}^\infty (u+R) \exp\left(-\frac{2u^2}{w^2}\right) \mathrm{d}u \\
&= 2\pi I_0 \left[\int_{-R}^\infty -\frac{w^2}{4} \frac{\mathrm{d}}{\mathrm{d}u} \exp\left(-\frac{2u^2}{w^2}\right) \mathrm{d}u + R \int_{-R}^\infty \exp\left(-\frac{2u^2}{w^2}\right) \mathrm{d}u \right].
\end{aligned}
\tag{B.3}
$$

From mathematics textbook:

$$\int_0^\infty \exp\left(-\frac{x^2}{a^2}\right) \mathrm{d}x = \frac{\sqrt{\pi}a}{2} \tag{B.4}$$

and

$$\int_a^0 \exp\left(-\frac{x^2}{b^2}\right) \mathrm{d}x = -\frac{1}{2}\sqrt{\pi}b\operatorname{erf}\left(\frac{a}{b}\right), \tag{B.5}$$

We get

$$
\begin{aligned}
P &= 2\pi I_0 \left[-\frac{w^2}{4}\left[\exp\left(-\frac{2u^2}{w^2}\right)\right]_{-R}^\infty \right. \\
&\quad \left. + R\left[\int_{-R}^0 \exp\left(-\frac{2u^2}{w^2}\right) \mathrm{d}u + \int_0^\infty \exp\left(-\frac{2u^2}{w^2}\right) \mathrm{d}u\right]\right] \\
&= 2\pi I_0 \left[\frac{w^2}{4}\exp\left(-\frac{2R^2}{w^2}\right) + R\left[-\frac{\sqrt{\pi}}{2}\frac{w}{\sqrt{2}}\operatorname{erf}\left(-\frac{\sqrt{2}R}{w}\right) + \frac{\sqrt{\pi}}{2}\frac{w}{\sqrt{2}}\right]\right] \\
&= \pi I_0 \left[\frac{w^2}{2}\exp\left(-\frac{2R^2}{w^2}\right) + \sqrt{\frac{\pi}{2}}Rw\left(1 + \operatorname{erf}\left(\frac{\sqrt{2}R}{w}\right)\right)\right].
\end{aligned}
\tag{B.6}
$$

Using Eq. 3.5, the trap depth of the ring is hence

$$U_0 = \frac{\alpha P}{\pi\left[\frac{w^2}{2}\exp\left(-\frac{2R^2}{w^2}\right) + \sqrt{\frac{\pi}{2}}Rw\left(1 + \operatorname{erf}\left(\frac{\sqrt{2}R}{w}\right)\right)\right]}, \tag{B.7}$$

where α is the polarisability. In cases where $R \gg w$, $\operatorname{erf}\left(\frac{\sqrt{2}R}{w}\right) \to 1$ and thus

$$U_0 = \frac{\alpha P}{\pi\left[\frac{w^2}{2}\exp\left(-\frac{2R^2}{w^2}\right) + \sqrt{2\pi}Rw\right]}. \tag{B.8}$$

Bibliography

[1] S. N. Bose, *Plancks gesetz und lichtquantenhypothese*, Z. Phys. **26**, 178 (1924). 1

[2] A. Einstein, *Quantentheorie des einatomigen idealen gases*, Sitzungsber. K. Preuss. Akad. Wiss. , 261 (1924). 1

[3] A. Einstein, *Quantentheorie des einatomigen idealen gases*, Sitzungsber. K. Preuss. Akad. Wiss. , 3 (1925). 1

[4] D. R. Tilley and J. Tilley, *Superfluidity and Superconductivity*, 3rd ed. (Institute of Physics Publishing, 1990). 1

[5] A. Griffin, D. W. Snoke, and S. Stringari, *Bose-Einstein Condensation* (Cambridge University Press, 1995).

[6] J. F. Annett, *Superconductivity, Superfluids and Condensates (Oxford Master Series in Physics)* (Oxford University Press, 2004). 1, 10, 11

[7] M. H. Anderson, J. R. Ensher, M. R. Matthews, C. E. Wieman, and E. A. Cornell, *Observation of Bose-Einstein condensation in a dilute atomic vapor*, Science **269**, 198 (1995). 1

[8] K. B. Davis *et al.*, *Bose-Einstein condensation in a gas of sodium atoms*, Phys. Rev. Lett. **75**, 3969 (1995). 1

[9] C. C. Bradley, C. A. Sackett, J. J. Tollett, and R. G. Hulet, *Evidence of Bose-Einstein condensation in an atomic gas with attractive interactions*, Phys. Rev. Lett. **75**, 1687 (1995). 1, 3

[10] G. Roati *et al.*, ^{39}K *Bose-Einstein condensate with tunable interactions*, Phys. Rev. Lett. **99**, 010403 (2007). 2

[11] G. Modugno *et al.*, *Bose-Einstein condensation of potassium atoms by sympathetic cooling*, Science **294**, 1320 (2001). 2

[12] S. L. Cornish, N. R. Claussen, J. L. Roberts, E. A. Cornell, and C. E. Wieman, *Stable* ^{85}Rb *Bose-Einstein condensates with widely tunable interactions*, Phys. Rev. Lett. **85**, 1795 (2000). 2, 3, 45, 47

[13] A. L. Marchant, S. Händel, S. A. Hopkins, T. P. Wiles, and S. L. Cornish, *Bose-Einstein condensation of* ^{85}Rb *by direct evaporation in an optical dipole trap*, Phys. Rev. A **85**, 053647 (2012). 2, 7, 45, 50, 53, 54, 55

[14] T. Weber, J. Herbig, M. Mark, H.-C. Nägerl, and R. Grimm, *Bose-Einstein condensation of cesium*, Science **299**, 232 (2003). 2

[15] S. Kraft, F. Vogt, O. Appel, F. Riehle, and U. Sterr, *Bose-Einstein condensation of alkaline Earth atoms:* ^{40}Ca, Phys. Rev. Lett. **103**, 130401 (2009). 2

[16] S. Stellmer, M. K. Tey, B. Huang, R. Grimm, and F. Schreck, *Bose-Einstein condensation of strontium*, Phys. Rev. Lett. **103**, 200401 (2009). 2

[17] Y. N. M. de Escobar *et al.*, *Bose-Einstein condensation of* ^{84}Sr, Phys. Rev. Lett. **103**, 200402 (2009).

[18] S. Stellmer, M. K. Tey, R. Grimm, and F. Schreck, *Bose-Einstein condensation of* ^{86}Sr, Phys. Rev. A **82**, 041602 (2010). 2

[19] T. Fukuhara, S. Sugawa, and Y. Takahashi, *Bose-Einstein condensation of an ytterbium isotope*, Phys. Rev. A **76**, 051604 (2007). 2

[20] K. Aikawa *et al.*, *Bose-Einstein condensation of erbium*, Phys. Rev. Lett. **108**, 210401 (2012). 2

[21] A. Griesmaier, J. Werner, S. Hensler, J. Stuhler, and T. Pfau, *Bose-Einstein condensation of chromium*, Phys. Rev. Lett. **94**, 160401 (2005). 2

[22] Q. Beaufils *et al.*, *All-optical production of chromium Bose-Einstein condensates*, Phys. Rev. A **77**, 061601 (2008). 2

[23] M. R. Andrews *et al.*, *Observation of interference between two Bose condensates*, Science **275**, 637 (1997). 2

[24] Z. Hadzibabic, S. Stock, B. Battelier, V. Bretin, and J. Dalibard, *Interference of an array of independent Bose-Einstein condensates*, Phys. Rev. Lett. **93**, 180403 (2004). 2

[25] P. Kevrekidis, D. Frantzeskakis, and R. Carretero-González, *Emergent Nonlinear Phenomena in Bose-Einstein Condensates* (Springer, 2008). 2, 3, 14, 15, 75

[26] N. J. Zabusky and M. D. Kruskal, *Interaction of "solitons" in a collisionless plasma and the recurrence of initial states*, Phys. Rev. Lett. **15**, 240 (1965). 2

[27] P. G. Drazin and R. S. Johnson, *Solitons: an Introduction* (Cambridge University Press, 1992). 2

[28] J. S. Russell, *Report on waves*, Fourteenth meeting of the British Association for the Advancement of Science , 311 (1844). 2, 3

[29] L. F. Mollenauer, R. H. Stolen, and J. P. Gordon, *Experimental observation of picosecond pulse narrowing and solitons in optical fibers*, Phys. Rev. Lett. **45**, 1095 (1980). 3

[30] A. Hasegawa and Y. Kodama, *Guiding-center soliton in optical fibers*, Opt. Lett. **15**, 1443 (1990).

[31] Y. S. Kivshar and G. Agrawal, *Optical solitons: from fibers to photonic crystals* (Elsevier Science, 2003).

[32] D. Y. Tang, H. Zhang, L. M. Zhao, and X. Wu, *Observation of high-order polarization-locked vector solitons in a fiber laser*, Phys. Rev. Lett. **101**, 153904 (2008).

[33] Y. V. Kartashov, B. A. Malomed, and L. Torner, *Solitons in nonlinear lattices*, Rev. Mod. Phys. **83**, 247 (2011). 3

[34] K. Stasiewicz *et al.*, *Slow magnetosonic solitons detected by the Cluster spacecraft*, Phys. Rev. Lett. **90**, 085002 (2003). 3

[35] Y. Togawa *et al.*, *Interlayer magnetoresistance due to chiral soliton lattice formation in hexagonal chiral magnet* $CrNb_3S_6$, Phys. Rev. Lett. **111**, 197204 (2013). 3

[36] T. Heimburg and A. D. Jackson, *On soliton propagation in biomembranes and nerves*, Proc. Natl. Acad. Sci. USA **102**, 9790 (2005). 3

[37] C. Chin, R. Grimm, P. Julienne, and E. Tiesinga, *Feshbach resonances in ultracold gases*, Rev. Mod. Phys. **82**, 1225 (2010). 3, 45, 46

[38] J. M. Gerton, D. Strekalov, I. Prodan, and R. G. Hulet, *Direct observation of growth and collapse of a Bose-Einstein condensate with attractive interactions*, Nature **408**, 692 (2000). 3, 18

[39] J. L. Roberts *et al.*, *Controlled collapse of a Bose-Einstein condensate*, Phys. Rev. Lett. **86**, 4211 (2001). 18, 47

[40] E. A. Donley *et al.*, *Dynamics of collapsing and exploding Bose-Einstein condensates*, Nature **412**, 295 (2001). 3, 18, 47, 54

[41] L. Khaykovich *et al.*, *Formation of a matter-wave bright soliton*, Science **296**, 1290 (2002). 3, 18, 46

[42] K. E. Strecker, G. B. Partridge, A. G. Truscott, and R. G. Hulet, *Formation and propagation of matter-wave soliton trains*, Nature **417**, 150 (2002). 3, 4, 18, 25

[43] S. L. Cornish, S. T. Thompson, and C. E. Wieman, *Formation of bright matter-wave solitons during the collapse of attractive Bose-Einstein condensates*, Phys. Rev. Lett. **96**, 170401 (2006). 3, 4, 18, 47

[44] A. L. Marchant *et al.*, *Controlled formation and reflection of a bright solitary matter-wave*, Nat. Commun. **4**, 1865 (2013). 3, 7, 18, 45, 46, 55, 56, 58, 60

[45] A. D. Martin, C. S. Adams, and S. A. Gardiner, *Bright solitary-matter-wave collisions in a harmonic trap: Regimes of solitonlike behavior*, Phys. Rev. A **77**, 013620 (2008). 4, 9, 10

[46] N. G. Parker, A. M. Martin, S. L. Cornish, and C. S. Adams, *Collisions of bright solitary matter waves*, J. Phys. B: At. Mol. Opt. Phys. **41**, 045303 (2008). 4, 9, 10, 24

[47] J. H. V. Nguyen, P. Dyke, D. Luo, B. A. Malomed, and R. G. Hulet, *Collisions of matter-wave solitons*, Nat. Phys. **10**, 918 (2014). 4, 18, 24

[48] S. Cornish *et al.*, *Quantum reflection of bright matter-wave solitons*, Physica D: Nonlinear Phenomena **238**, 1299 (2009). 4, 5, 6, 18, 25, 32, 81, 84, 181

[49] A. D. Martin and J. Ruostekoski, *Quantum dynamics of atomic bright solitons under splitting and recollision, and implications for interferometry*, New J. Phys. **14**, 043040 (2012). 5, 10

[50] C. Weiss and Y. Castin, *Creation and detection of a mesoscopic gas in a nonlocal quantum superposition*, Phys. Rev. Lett. **102**, 010403 (2009). 10, 23

[51] J. L. Helm, S. J. Rooney, C. Weiss, and S. A. Gardiner, *Splitting bright matter-wave solitons on narrow potential barriers: Quantum to classical transition and applications to interferometry*, Phys. Rev. A **89**, 033610 (2014). 5, 6, 10, 18, 19, 21, 24, 26, 70

[52] J. L. Helm, S. L. Cornish, and S. A. Gardiner, *Sagnac Interferometry Using Bright Matter-Wave Solitons*, Phys. Rev. Lett. **114**, 134101 (2015). 4, 5, 6, 10, 19, 25, 28, 84, 153, 154, 180

[53] N. F. Ramsey, *A molecular beam resonance method with separated oscillating fields*, Phys. Rev. **78**, 695 (1950). 4

[54] R. Colella, A. W. Overhauser, and S. A. Werner, *Observation of gravitationally induced quantum interference*, Phys. Rev. Lett. **34**, 1472 (1975). 4

[55] M. Kasevich and S. Chu, *Atomic interferometry using stimulated Raman transitions*, Phys. Rev. Lett. **67**, 181 (1991). 4

[56] F. Riehle, T. Kisters, A. Witte, J. Helmcke, and C. J. Bordé, *Optical Ramsey spectroscopy in a rotating frame: Sagnac effect in a matter-wave interferometer*, Phys. Rev. Lett. **67**, 177 (1991). 4, 28

[57] R. Geiger *et al.*, *Detecting inertial effects with airborne matter-wave interferometry*, Nat. Commun. **2**, 474 (2011). 5

[58] M. J. Snadden, J. M. McGuirk, P. Bouyer, K. G. Haritos, and M. A. Kasevich, *Measurement of the Earth's Gravity Gradient with an Atom Interferometer-Based Gravity Gradiometer*, Phys. Rev. Lett. **81**, 971 (1998). 5

[59] J. M. McGuirk, G. T. Foster, J. B. Fixler, M. J. Snadden, and M. A. Kasevich, *Sensitive absolute-gravity gradiometry using atom interferometry*, Phys. Rev. A **65**, 033608 (2002). 5

[60] J. B. Fixler, G. T. Foster, J. M. McGuirk, and M. A. Kasevich, *Atom interferometer measurement of the Newtonian constant of gravity*, Science **315**, 74 (2007). 5

[61] T. L. Gustavson, *Prevision rotation sensing using atom interferometry*, PhD thesis, Stanford University, (2000). 5, 27, 28, 154

[62] D. S. Durfee, Y. K. Shaham, and M. A. Kasevich, *Long-term stability of an area-reversible atom-interferometer Sagnac gyroscope*, Phys. Rev. Lett. **97**, 240801 (2006).

[63] S. Wu, E. Su, and M. Prentiss, *Demonstration of an area-enclosing guided-atom interferometer for rotation sensing*, Phys. Rev. Lett. **99**, 173201 (2007). 5

[64] T. P. Billam, S. L. Cornish, and S. A. Gardiner, *Realizing bright-matter-wave-soliton collisions with controlled relative phase*, Phys. Rev. A **83**, 041602 (2011). 5, 9, 25

[65] J. Cuevas, P. G. Kevrekidis, B. A. Malomed, P. Dyke, and R. G. Hulet, *Interactions of solitons with a Gaussian barrier: splitting and recombination in quasi-one-dimensional and three-dimensional settings*, New J. Phys. **15**, 063006 (2013). 5, 9, 19, 25

[66] G. D. McDonald *et al.*, *Bright solitonic matter-wave interferometer*, Phys. Rev. Lett. **113**, 013002 (2014). 5

[67] S. Händel, *Experiments on ultracold quantum gases of ^{85}Rb and ^{87}Rb*, PhD thesis, Durham University, (2011). 6, 30, 32, 33, 41, 90, 92, 94

[68] A. L. Marchant, *Formation of bright solitary matter-waves*, PhD thesis, Durham University, (2012). 6, 18, 33, 41, 43, 55, 72, 108, 181

[69] T. P. Wiles, *Dynamics of bright solitary matter-waves*, PhD thesis, Durham University, (2013). 7, 30, 31, 41, 55, 60, 61, 67, 90, 94, 181

[70] A. L. Marchant *et al.*, *Quantum reflection of bright solitary matter-waves from a narrow attractive potential*, (2015), arXiv:1507.04639. 8

[71] C. Weiss and Y. Castin, *Elastic scattering of a quantum matter-wave bright soliton on a barrier*, New J. Phys. **45**, 455306 (2012). 9

[72] J. Holmer, J. Marzuola, and M. Zworski, *Fast soliton scattering by delta impurities*, Commun. Math. Phys. **274**, 187 (2007). 9, 18, 19, 20, 25

[73] J. Holmer, J. Marzuola, and M. Zworski, *Soliton splitting by external delta potentials*, J. Nonlinear Sci. **17**, 349 (2007). 9, 18, 25

[74] C. Lee and J. Brand, *Enhanced quantum reflection of matter-wave solitons*, Europhys. Lett. **73**, 321 (2006). 9, 21, 61, 72

[75] T. Ernst and J. Brand, *Resonant trapping in the transport of a matter-wave soliton through a quantum well*, Phys. Rev. A **81**, 033614 (2010). 9, 18, 21, 61, 70

[76] B. Gertjerenken, T. P. Billam, L. Khaykovich, and C. Weiss, *Scattering bright solitons: Quantum versus mean-field behavior*, Phys. Rev. A **86**, 033608 (2012). 9, 10, 19, 21, 22, 23

[77] J. L. Helm, T. P. Billam, and S. A. Gardiner, *Bright matter-wave soliton collisions at narrow barriers*, Phys. Rev. A **85**, 053621 (2012). 10, 18, 19, 20, 21, 25, 26, 70

[78] J. Polo and V. Ahufinger, *Soliton-based matter-wave interferometer*, Phys. Rev. A **88**, 053628 (2013). 10, 26

[79] B. Gertjerenken and C. Weiss, *Nonlocal quantum superpositions of bright matter-wave solitons and dimers*, J. Phys. B: At. Mol. Opt. Phys. **45**, 165301 (2012). 10

[80] A. I. Streltsov, O. E. Alon, and L. S. Cederbaum, *Scattering of an attractive Bose-Einstein condensate from a barrier: Formation of quantum superposition states*, Phys. Rev. A **80**, 043616 (2009). 10, 23, 25

[81] M. Ueda, *Fundamentals and New Frontiers of Bose-Einstein Condensation* (World Scientific, 2010). 10, 11

[82] C. Pethick and H. Smith, *Bose-Einstein condensation in dilute gases*, 2nd ed. (Cambridge University Press, 2008). 11, 12

[83] I. Gotlibovych, *Degenerate Bose gases in a uniform potential*, PhD thesis, University of Cambridge, (2014). 11, 173

[84] A. S. Bradley, *Scale-invariant thermodynamics of a toroidally trapped Bose gas*, Phys. Rev. A **79**, 033624 (2009). 11, 173, 174

[85] D. Baillie, P. B. Blakie, and A. S. Bradley, *Geometric scale invariance as a route to macroscopic degeneracy: Loading a toroidal trap with a Bose or Fermi gas*, Phys. Rev. A **82**, 013626 (2010). 11, 173, 174

[86] C. J. Foot, *Atomic Physics (Oxford Master Series in Physics)* (Oxford University Press, 2004). 11, 12, 34

[87] H. J. Metcalf and P. van der Straten, *Laser Cooling and Trapping* (Springer, 1999). 11, 34, 35

[88] F. Dalfovo, S. Giorgini, L. P. Pitaevskii, and S. Stringari, *Theory of Bose-Einstein condensation in trapped gases*, Rev. Mod. Phys. **71**, 463 (1999). 12, 18, 55

[89] L. P. Pitaevskii and S. Stringari, *Bose Einstein Condensation* (Clarendon Press Oxford, 2003). 12

[90] E. A. Cornell and C. E. Wieman, *Nobel Lecture: Bose-Einstein condensation in a dilute gas, the first 70 years and some recent experiments*, Rev. Mod. Phys. **74**, 875 (2002). 13

[91] W. Ketterle, *Nobel lecture: When atoms behave as waves: Bose-Einstein condensation and the atom laser*, Rev. Mod. Phys. **74**, 1131 (2002). 13

[92] D. M. Stamper-Kurn *et al.*, *Optical confinement of a Bose-Einstein condensate*, Phys. Rev. Lett. **80**, 2027 (1998). 13

[93] J. Weiner, V. S. Bagnato, S. Zilio, and P. S. Julienne, *Experiments and theory in cold and ultracold collisions*, Rev. Mod. Phys. **71**, 1 (1999).

[94] R. Grimm, M. Weidemller, and Y. B. Ovchinnikov, *Optical dipole traps for neutral atoms*, Adv. At. Mol. Opt. Phy. **42**, 95 (2000). 37, 69, 70, 97

[95] M. D. Barrett, J. A. Sauer, and M. S. Chapman, *All-optical formation of an atomic Bose-Einstein condensate*, Phys. Rev. Lett. **87**, 010404 (2001). 13

[96] L. D. Carr and Y. Castin, *Dynamics of a matter-wave bright soliton in an expulsive potential*, Phys. Rev. A **66**, 063602 (2002). 15, 18

[97] T. P. Billam, S. A. Wrathmall, and S. A. Gardiner, *Variational determination of approximate bright matter-wave soliton solutions in anisotropic traps*, Phys. Rev. A **85**, 013627 (2012). 15, 16

[98] N. Parker, *Numerical studies of vortices and dark solitons in atomic Bose-Einstein condensates*, PhD thesis, Durham University, (2004). 15

[99] V. E. Zakharov and A. B. Shabar, *Exact theory of two-dimensional self-focusing and one-dimensional self-modulation of waves in nonlinear media*, J. Exp. Theor. Phys. **34**, 62 (1971). 15

[100] L. D. Carr, C. W. Clark, and W. P. Reinhardt, *Stationary solutions of the one-dimensional nonlinear Schrödinger equation. I. Case of repulsive nonlinearity*, Phys. Rev. A **62**, 063610 (2000). 15

[101] S. Burger *et al.*, *Dark solitons in Bose-Einstein condensates*, Phys. Rev. Lett. **83**, 5198 (1999). 15

[102] J. Denschlag *et al.*, *Generating solitons by phase engineering of a Bose-Einstein condensate*, Science **287**, 97 (2000). 15

[103] Z. Dutton, M. Budde, C. Slowe, and L. V. Hau, *Observation of quantum shock waves created with ultra-compressed slow light pulses in a Bose-Einstein condensate*, Science **293**, 663 (2001). 15

[104] N. S. Ginsberg, J. Brand, and L. V. Hau, *Observation of hybrid soliton vortex-ring structures in Bose-Einstein condensates*, Phys. Rev. Lett. **94**, 040403 (2005). 15

[105] B. P. Anderson *et al.*, *Watching dark solitons decay into vortex rings in a Bose-Einstein condensate*, Phys. Rev. Lett. **86**, 2926 (2001). 15

[106] J. P. Gordon, *Interaction forces among solitons in optical fibres*, Opt. Lett. **8**, 596 (1983). 16, 24

[107] V. M. Pérez-García, H. Michinel, J. I. Cirac, M. Lewenstein, and P. Zoller, *Dynamics of Bose-Einstein condensates: Variational solutions of the Gross-Pitaevskii equations*, Phys. Rev. A **56**, 1424 (1997). 16

[108] L. Salasnich, A. Parola, and L. Reatto, *Effective wave equations for the dynamics of cigar-shaped and disk-shaped Bose condensates*, Phys. Rev. A **65**, 043614 (2002). 16

[109] J. L. Helm, *Soliton dynamics in the Gross Pitaevskii equation: splitting, collisions and interferometry*, PhD thesis, Durham University, (2014). 16, 19, 25

[110] M. Ueda and A. J. Leggett, *Macroscopic quantum tunneling of a Bose-Einstein condensate with attractive interaction*, Phys. Rev. Lett. **80**, 1576 (1998). 18

[111] H. B. G. Casimir and D. Polder, *The influence of retardation on the London-van der Waals forces*, Phys. Rev. **73**, 360 (1948). 18

[112] S. Y. Buhmann, *Dispersion Forces I: Macroscopic Quantum Electrodynamics and Ground-State Casimir, Casimir-Polder and van der Waals Forces* (Springer, 2013). 18

[113] R. Côté, B. Segev, and M. G. Raizen, *Retardation effects on quantum reflection from an evanescent-wave atomic mirror*, Phys. Rev. A **58**, 3999 (1998). 18

[114] C. H. Wang, T. M. Hong, R. K. Lee, and D. W. Wang, *Particle-wave duality in quantum tunneling of a bright soliton*, Opt. Express **20**, 22675 (2012). 18

[115] U. Al Khawaja and H. T. C. Stoof, *Formation of matter-wave molecules*, New J. Phys. **13**, 085003 (2011). 19

[116] B. Gertjerenken *et al.*, *Generating mesoscopic Bell states via collisions of distinguishable quantum bright solitons*, Phys. Rev. Lett. **111**, 100406 (2013). 23, 181

[117] L. D. Carr and J. Brand, *Spontaneous soliton formation and modulational instability in Bose-Einstein condensates*, Phys. Rev. Lett. **92**, 040401 (2004). 24

[118] L. Khaykovich and B. A. Malomed, *Deviation from one dimensionality in stationary properties and collisional dynamics of matter-wave solitons*, Phys. Rev. A **74**, 023607 (2006). 24

[119] T. Fogarty, A. Kiely, S. Campbell, and T. Busch, *Effect of interparticle interaction in a free-oscillation atomic interferometer*, Phys. Rev. A **87**, 043630 (2013). 25

[120] L. Zehnder, *Ein neuer interferenzrefracktor*, Zeitschrift für Instrumentenkunde **11**, 275 (1891). 25

[121] G. Sagnac, *L'éther lumineux démontreé par l'effet du vent relatif d'éther dans un interféromètre en rotation uniforme*, C. R. Acad. Sci. **157**, 708 (1913). 27

[122] G. Sagnac, *Sur la preuve de la réalité de l'éther lumineux par l'expérience de l'interférographe tournant*, C. R. Acad. Sci. **157**, 1410 (1913). 27

[123] R. Anderson, H. R. Bilger, and G. E. Stedman, *'Sagnac' effect: A century of Earth-rotated interferometers*, Am. J. Phys. **62**, 975 (1994). 27

[124] S. A. Werner, J. L. Staudenmann, and R. Colella, *Effect of Earth's rotation on the quantum mechanical phase of the neutron*, Phys. Rev. Lett. **42**, 1103 (1979). 28

[125] F. Hasselbach and M. Nicklaus, *Sagnac experiment with electrons: Observation of the rotational phase shift of electron waves in vacuum*, Phys. Rev. A **48**, 143 (1993). 28

[126] T. P. Billam, A. L. Marchant, S. L. Cornish, S. A. Gardiner, and N. G. Parker, *Bright solitary matter waves: formation, stability and interactions. In progress in optical science and photonics, vol. 1, spontaneous symmetry breaking, self-trapping and josephson oscillations. (ed. Malomed, B. A.)* (Springer, Berlin, Heidelberg, 2013). 28

[127] J. J. Cooper, D. W. Hallwood, and J. A. Dunningham, *Entanglement-enhanced atomic gyroscope*, Phys. Rev. A **81**, 043624 (2010). 29, 181

[128] S. Boixo *et al.*, *Quantum metrology: dynamics versus entanglement*, Phys. Rev. Lett. **101**, 040403 (2008). 29

[129] A. L. Marchant, S. Händel, T. P. Wiles, S. A. Hopkins, and S. L. Cornish, *Guided transport of ultracold gases of rubidium up to a room-temperature dielectric surface*, New J. Phys. **13**, 125003 (2011). 32, 72

[130] D. J. McCarron, S. A. King, and S. L. Cornish, *Modulation transfer spectroscopy in atomic rubidium*, Meas. Sci. Technol. **19**, 105601 (2008). 32

[131] G. C. Bjorklund, *Frequency-modulation spectroscopy: a new method for measuring weak absorptions and dispersions*, Opt. Lett. **5**, 15 (1980). 32

[132] P. D. Lett *et al.*, *Observation of atoms laser cooled below the Doppler limit*, Phys. Rev. Lett. **61**, 169 (1988). 34

[133] E. Majorana, *Oriented atoms in a variable magnetic field*, Nuovo Cimento **9**, 43 (1932). 36

[134] Y.-J. Lin, A. R. Perry, R. L. Compton, I. B. Spielman, and J. V. Porto, *Rapid production of ^{87}Rb Bose-Einstein condensates in a combined magnetic and optical potential*, Phys. Rev. A **79**, 063631 (2009). 36, 39, 101

[135] M. S. Safronova, B. Arora, and C. W. Clark, *Frequency-dependent polarizabilities of alkali-metal atoms from ultraviolet through infrared spectral regions*, Phys. Rev. A **73**, 022505 (2006). 38

[136] C.-L. Hung, X. Zhang, N. Gemelke, and C. Chin, *Accelerating evaporative cooling of atoms into Bose-Einstein condensation in optical traps*, Phys. Rev. A **78**, 011604 (2008). 40

[137] W. Ketterle and N. J. van Druten, *Bose-Einstein condensation of a finite number of particles trapped in one or three dimensions*, Phys. Rev. A **54**, 656 (1996). 41

[138] K. M. O'Hara, M. E. Gehm, S. R. Granade, and J. E. Thomas, *Scaling laws for evaporative cooling in time-dependent optical traps*, Phys. Rev. A **64**, 051403 (2001). 41, 68, 145

[139] J. L. Roberts, *Bose-Einstein condensates with tunable atom-atom interactions: the first experiments with ^{85}Rb BECs*, PhD thesis, University of Colorado, (2001). 41, 42, 43, 49, 50

[140] S. B. Papp *et al.*, *Bragg spectroscopy of a strongly interacting ^{85}Rb Bose-Einstein condensate*, Phys. Rev. Lett. **101**, 135301 (2008). 45

[141] P. A. Altin *et al.*, *Measurement of inelastic losses in a sample of ultracold ^{85}Rb*, Phys. Rev. A **81**, 012713 (2010). 45, 50

[142] M. Bartenstein *et al.*, *Collective excitations of a degenerate gas at the BEC-BCS crossover*, Phys. Rev. Lett. **92**, 203201 (2004). 46

[143] T. Bourdel *et al.*, *Experimental study of the BEC-BCS crossover region in lithium 6*, Phys. Rev. Lett. **93**, 050401 (2004). 46

[144] J. Herbig *et al.*, *Preparation of a pure molecular quantum gas*, Science **301**, 1510 (2003). 46

[145] C. A. Regal, C. Ticknor, J. L. Bohn, and D. S. Jin, *Creation of ultracold molecules from a Fermi gas of atoms*, Nature **424**, 47 (2003). 46

[146] A. J. Moerdijk, B. J. Verhaar, and A. Axelsson, *Resonances in ultracold collisions of ^{6}Li, ^{7}Li, and ^{23}Na*, Phys. Rev. A **51**, 4852 (1995). 47

[147] J. L. Roberts, N. R. Claussen, S. L. Cornish, and C. E. Wieman, *Magnetic field dependence of ultracold inelastic collisions near a Feshbach resonance*, Phys. Rev. Lett. **85**, 728 (2000). 47, 52

[148] T. Volz, S. Dürr, S. Ernst, A. Marte, and G. Rempe, *Characterization of elastic scattering near a Feshbach resonance in* ^{87}Rb, Phys. Rev. A **68**, 010702 (2003). 47

[149] N. R. Claussen *et al.*, *Very-high-precision bound-state spectroscopy near a* ^{85}Rb *Feshbach resonance*, Phys. Rev. A **67**, 060701 (2003). 47

[150] P. A. Altin *et al.*, *Collapse and three-body loss in a* ^{85}*Rb Bose-Einstein condensate*, Phys. Rev. A **84**, 2 (2011). 47, 50, 85

[151] S. B. Papp, J. M. Pino, and C. E. Wieman, *Tunable miscibility in a dual-species Bose-Einstein condensate*, Phys. Rev. Lett. **101**, 040402 (2008). 47

[152] J. P. Burke, *Theoretical investigation of cold alkali atom collisions*, PhD thesis, University of Colorado, (1999). 48, 49

[153] J. P. Burke, J. L. Bohn, B. D. Esry, and C. H. Greene, *Prospects for mixed-isotope Bose-Einstein condensates in rubidium*, Phys. Rev. Lett. **80**, 2097 (1998). 47, 49

[154] W. Ketterle, D. S. Durfee, and D. M. Stamper-Kurn, *Making, probing and understanding Bose-Einstein condensates. Proceedings of the International School of Physics 'Enrico Fermi', Course CXL, edited by M. Inguscio, S. Stringari and C.E. Wieman* (IOS Press, Amsterdam, 1999). 48

[155] T. Guénault, *Statistical Physics* (Chapman & Hall, 1995). 48

[156] C. Chin, *Cooling, collisions and coherence of cold cesium atoms in a trap*, PhD thesis, Stanford University, (2001). 48

[157] T. Weber, J. Herbig, M. Mark, H.-C. Nägerl, and R. Grimm, *Three-Body Recombination at Large Scattering Lengths in an Ultracold Atomic Gas*, Phys. Rev. Lett. **91**, 123201 (2003). 49, 52

[158] P. O. Fedichev, M. W. Reynolds, and G. V. Shlyapnikov, *Three-body recombination of ultracold atoms to a weakly bound s level*, Phys. Rev. Lett. **77**, 2921 (1996). 49

[159] B. D. Esry, C. H. Greene, and J. P. Burke, *Recombination of three atoms in the ultracold limit*, Phys. Rev. Lett. **83**, 1751 (1999). 85

[160] P. F. Bedaque, E. Braaten, and H.-W. Hammer, *Three-body recombination in Bose gases with large scattering length*, Phys. Rev. Lett. **85**, 908 (2000). 49

[161] E. A. Burt *et al.*, *Coherence, Correlations, and Collisions: What One Learns about Bose-Einstein Condensates from Their Decay*, Phys. Rev. Lett. **79**, 337 (1997). 50, 85

[162] A. J. Moerdijk, H. M. J. M. Boesten, and B. J. Verhaar, *Decay of trapped ultracold alkali atoms by recombination*, Phys. Rev. A **53**, 916 (1996). 50

[163] F. H. Mies, C. J. Williams, P. S. Julienne, and M. Krauss, *Estimating bounds on collisional relaxation rates of spin-polarized ^{87}Rb atoms at ultracold temperatures*, J. Res. Natl. Inst. Stand. Technol. **101**, 521 (1996). 50

[164] P. A. Ruprecht, M. J. Holland, K. Burnett, and M. Edwards, *Time-dependent solution of the nonlinear Schrödinger equation for Bose-condensed trapped neutral atoms*, Phys. Rev. A **51**, 4704 (1995). 53

[165] L. D. Landau and E. M. Lifshitz, *Course of theoretical physics, Vol. 3* (Butterworth-Heinemann, 2000). 62

[166] E. Hecht, *Optics*, 4th ed. (Pearson Education, 2002). 62

[167] W. Alt, *An objective lens for efficient fluorescence detection of single atoms*, Optik **113**, 142 (2002). 64

[168] M. Weber, J. Volz, K. Saucke, C. Kurtsiefer, and H. Weinfurter, *Analysis of a single-atom dipole trap*, Phys. Rev. A **73**, 043406 (2006).

[169] J. F. Sherson *et al.*, *Single-atom-resolved fluorescence imaging of an atomic Mott insulator*, Nature **467**, 68 (2010). 64

[170] M. Born and E. Wolf, *Principles of optics*, 7th ed. (Cambridge University Press, 2003). 79

[171] G. Brooker, *Modern Classical Optics*, 2nd ed. (Oxford University Press, 2006).

[172] S. G. Lipson, H. Lipson, and D. S. Tannhauser, *Optical Physics*, 3rd ed. (Cambridge University Press, 1995). 79

[173] C. M. Fabre *et al.*, *Realization of a distributed Bragg reflector for propagating guided matter waves*, Phys. Rev. Lett. **107**, 230401 (2011). 79

[174] A. Yariv, *Introduction to optical electronics* (Holt, Rinehart and Winston, 1976). 96

[175] A. Rakonjac, *A versatile collider for ultracold atoms*, PhD thesis, University of Otago, (2012). 96, 181

[176] *Isomet application note: Acousto-optic modulation*, `http://www.isomet.com/App-Manual_pdf/AO%20Modulation.pdf`, Accessed: 3 September 2015. 96

[177] T. A. Savard, K. M. O'Hara, and J. E. Thomas, *Laser-noise-induced heating in far-off resonance optical traps*, Phys. Rev. A **56**, R1095 (1997). 97

[178] S. K. Schnelle, E. D. van Ooijen, M. J. Davis, N. R. Heckenberg, and H. Rubinsztein-Dunlop, *Versatile two-dimensional potentials for ultracold atoms*, Opt. Express **16**, 1405 (2008). 98

[179] V. I. Balakshy, V. B. Voloshinov, V. A. Karasev, V. Y. Molchanov, and V. Semenkov, *Compensation of thermal effects in acousto-optic deflector*, Proc. SPIE **2713**, 164 (1996). 99

[180] P. F. Griffin, *Laser cooling and loading of Rb into a large period, quasi-electrostatic, optical lattice*, PhD thesis, Durham University, (2005). 99

[181] T. Lauber, J. Küber, O. Wille, and G. Birkl, *Optimized Bose-Einstein-condensate production in a dipole trap based on a 1070-nm multifrequency laser: Influence of enhanced two-body loss on the evaporation process*, Phys. Rev. A **84**, 043641 (2011). 102, 103

[182] W. Hung *et al.*, *Storage time of cold Rb atoms in an optical dipole trap formed by a multimode fiber laser*, J. Opt. Soc. Am. B **32**, B32 (2015). 102

[183] M. Inguscio and L. Fallani, *Atomic physics: precise measurements and ultracold matter* (Oxford University Press, 2013). 110

[184] A. Marte *et al.*, *Feshbach resonances in rubidium 87: Precision measurement and analysis*, Phys. Rev. Lett. **89**, 283202 (2002). 110

[185] G. D. Bruce, J. Mayoh, G. Smirne, L. Torralbo-Campo, and D. Cassettari, *A smooth, holographically generated ring trap for the investigation of superfluidity in ultracold atoms*, Phys. Scr. **2011**, 014008 (2011). 112, 113

[186] C. Ryu *et al.*, *Observation of persistent flow of a Bose-Einstein condensate in a toroidal trap*, Phys. Rev. Lett. **99**, 260401 (2007). 112

[187] A. Ramanathan *et al.*, *Superflow in a toroidal bose-einstein condensate: An atom circuit with a tunable weak link*, Phys. Rev. Lett. **106**, 130401 (2011).

[188] S. Moulder, *Persistent Currents in Bose-Einstein Condensates*, PhD thesis, University of Cambridge, (2013). 112, 147, 148, 157, 176

[189] C. Ryu, P. W. Blackburn, A. A. Blinova, and M. G. Boshier, *Experimental realization of Josephson junctions for an atom SQUID*, Phys. Rev. Lett. **111**, 205301 (2013). 112, 113

[190] K. C. Wright, R. B. Blakestad, C. J. Lobb, W. D. Phillips, and G. K. Campbell, *Driving phase slips in a superfluid atom circuit with a rotating weak link*, Phys. Rev. Lett. **110**, 025302 (2013). 112, 174

[191] J. A. Sauer, M. D. Barrett, and M. S. Chapman, *A storage ring for neutral atoms*, Phys. Rev. Lett. **87**, 270401 (2001). 112

[192] A. S. Arnold, C. S. Garvie, and E. Riis, *A large magnetic storage ring for Bose-Einstein condensates*, Phys. Rev. A **73**, 041606(R) (2005). 112

[193] B. E. Sherlock, M. Gildemeister, E. Owen, E. Nugent, and C. J. Foot, *Time-averaged adiabatic ring potential for ultracold atoms*, Phys. Rev. A **83**, 043408 (2011). 112

[194] A. Turpin *et al.*, *Blue-detuned optical ring trap for Bose-Einstein condensates based on conical refraction*, Opt. Express **23**, 1638 (2015). 112

[195] K. Henderson, C. Ryu, C. MacCormick, and M. G. Boshier, *Experimental demonstration of painting arbitrary and dynamic potentials for Bose-Einstein condensates*, New J. Phys. **11**, 043030 (2009). 113

[196] C. Ryu and M. G. Boshier, *Integrated coherent matter wave circuits*, New J. Phys. **17**, 092002 (2015). 113

[197] D. R. Scherer, C. N. Weiler, T. W. Neely, and B. P. Anderson, *Vortex formation by merging of multiple trapped bose-einstein condensates*, Phys. Rev. Lett. **98**, 110402 (2007). 113

[198] L. Corman *et al.*, *Quench-induced supercurrents in an annular two-dimensional Bose gas*, Phys. Rev. Lett. **113**, 135302 (2014). 113

[199] S. Bergamini *et al.*, *Holographic generation of micro-trap arrays for single atoms*, J. Opt. Soc. Am. B **21**, 1889 (2004). 113

[200] X. He, P. Xu, J. Wang, and M. Zhan, *Rotating single atoms in a ring lattice generated by a spatial light modulator*, Opt. Express **17**, 21007 (2009).

[201] L. Brandt *et al.*, *Spatial light modulators for the manipulation of individual atoms*, Appl. Phys. B **102**, 443 (2011).

[202] F. Nogrette *et al.*, *Single-atom trapping in holographic 2D arrays of microtraps with arbitrary geometries*, Phys. Rev. X **4**, 021034 (2014).

[203] R. M. W. van Bijnen *et al.*, *Patterned Rydberg excitation and ionisation with a spatial light modulator*, New J. Phys. **17**, 023045 (2015). 113, 147, 148, 176

[204] A. L. Gaunt and Z. Hadzibabic, *Robust digital holography for ultracold atom trapping*, Sci. Rep. **2**, 721 (2012). 113, 128, 147, 148, 151

[205] A. L. Gaunt, T. F. Schmidutz, I. Gotlibovych, R. P. Smith, and Z. Hadzibabic, *Bose-einstein condensation of atoms in a uniform potential*, Phys. Rev. Lett. **110**, 200406 (2013). 113

[206] D. Rhodes *et al.*, *Atom guiding along high order Laguerre-Gaussian light beams formed by spatial light modulation*, J. Mod. Opt. **53**, 547 (2006). 113

[207] D. C. O'Shea, T. J. Suleski, A. D. Kathman, and D. W. Prather, *Diffractive Optics: Design, Fabrication, and Test* (SPIE Press, 2004). 114

[208] F. Wyrowski, *Diffractive optical elements: iterative calculation of quantized, blazed phase structures*, J. Opt. Soc. Am. A **7**, 961 (1990). 114, 121

[209] S. Reichelt and N. Leister, *Computational hologram synthesis and representation on spatial light modulators for real-time 3D holographic imaging*, JPCS **415**, 012038 (2013). 117

[210] J. Goodman, *Introduction to Fourier Optics*, 3rd ed. (Roberts and Company Publishers, 2005). 117, 118, 122, 127, 128

[211] H. Stark, *Applications of Optical Fourier Transforms*, 1st ed. (Academic Press, 1982). 117, 118

[212] T. Harte, G. D. Bruce, J. Keeling, and D. Cassettari, *A conjugate gradient minimisation approach to generating holographic traps for ultracold atoms*, Opt. Express **22**, 26548 (2014). 123

[213] L. Legeard, P. Réfrégier, and P. Ambs, *Multicriteria optimality for iterative encoding of computer-generated holograms*, Appl. Opt. **36**, 7444 (1997). 123

[214] M. A. Seldowitz, J. P. Allebach, and D. W. Sweeney, *Synthesis of digital holograms by direct binary search*, Appl. Opt. **26**, 2788 (1987). 123

[215] R. W. Gerchberg and W. O. Saxton, *A practical algorithm for the determination of phase from image and diffraction plane pictures*, Optik **35**, 237 (1972). 123, 124

[216] Z. Zalevsky, D. Mendlovic, and R. G. Dorsch, *Gerchberg-Saxton algorithm applied in the fractional Fourier or the Fresnel domain*, Opt. Lett. **21**, 842 (1996).

[217] J. R. Fienup, *Phase retrieval algorithms: a comparison*, Appl. Opt. **21**, 2758 (1982). 123

[218] R. Irwan and R. G. Lane, *Phase retrieval with prior information*, J. Opt. Soc. Am. A **15**, 2302 (1998). 124

[219] H. H. Bauschke, P. L. Combettes, and D. R. Luke, *Phase retrieval, error reduction algorithm, and Fienup variants: a view from convex optimization*, J. Opt. Soc. Am. A **19**, 1334 (2002). 124

[220] M. Pasienski and B. Demarco, *A high-accuracy algorithm for designing arbitrary holographic atom traps*, Opt. Express **16**, 2176 (2008). 125, 128

[221] R. M. W. van Bijnen, *Quantum engineering with ultracold atoms*, PhD thesis, Technische Universiteit Eindhoven, (2013). 126, 129, 130, 132, 147, 148, 151

[222] S. Lowenthal and D. Joyeux, *Speckle removal by a slowly moving diffuser associated with a motionless diffuser*, J. Opt. Soc. Am. **61**, 847 (1971). 127

[223] S. Kubota and J. W. Goodman, *Very efficient speckle contrast reduction realized by moving diffuser device*, Appl. Opt. **49**, 4385 (2010).

[224] C. Remmersmann, S. Stürwald, B. Kemper, P. Langehanenberg, and G. von Bally, *Phase noise optimization in temporal phase-shifting digital holography with partial coherence light sources and its application in quantitative cell imaging*, Appl. Opt. **48**, 1463 (2009).

[225] P. Langehanenberg, G. V. Bally, and B. Kemper, *Application of partially coherent light in live cell imaging with digital holographic microscopy*, J. Mod. Opt. **57**, 709 (2010). 127

[226] L. Golan and S. Shoham, *Speckle elimination using shift-averaging in high-rate holographic projection*, Opt. Express **17**, 1330 (2009). 127

[227] T. Nomura, M. Okamura, E. Nitanai, and T. Numata, *Image quality improvement of digital holography by superposition of reconstructed images obtained by multiple wavelengths*, Appl. Opt. **47**, D38 (2008).

[228] C. Quan, X. Kang, and C. J. Tay, *Speckle noise reduction in digital holography by multiple holograms*, Opt. Eng. **46**, 115801 (2007).

[229] L. Rong, W. Xian, F. Pan, S. Liu, and R. Li, *Speckle noise reduction in digital holography by use of multiple polarization holograms*, Chin. Opt. Lett. **8**, 653 (2010).

[230] W. Xian *et al.*, *Improvement of speckle noise suppression in digital holography by rotating linear polarization state*, Chin. Opt. Lett. **9**, 9 (2011). 127

[231] G. D. Bruce, *Alternative techniques for the production and manipulation of ultracold atoms*, PhD thesis, University of St. Andrews, (2012). 128

[232] H. Aagedal, M. Schmid, T. Beth, S. Teiwes, and F. Wyrowski, *Theory of speckles in diffractive optics and its application to beam shaping*, J. Mod. Opt. **43**, 1409 (1996). 128

[233] H. Aagedal *et al.*, *Analytical beam shaping with application to laser-diode arrays*, J. Opt. Soc. Am. A **14**, 1549 (1997). 129, 130

[234] O. Bryngdahl, *Optical map transformations*, Opt. Commun. **10**, 164 (1974). 131

[235] P. S. Considine, *Effects of coherence on imaging systems*, J. Opt. Soc. Am. **56**, 1001 (1966). 136

[236] G. D. Bruce *et al.*, *Feedback-enhanced algorithm for aberration correction of holographic atom traps*, J. Phys. B: At. Mol. Opt. Phys. **48**, 115303 (2015). 145, 147, 148, 149

[237] R. Bowman, A. Wright, and M. Padgett, *An SLM-based ShackHartmann wavefront sensor for aberration correction in optical tweezers*, J. Opt. **12**, 124004 (2010). 147, 148, 176

[238] J. Ruoff and M. Totzeck, *Orientation Zernike polynomials: a useful way to describe the polarization effects of optical imaging systems*, J Micro Nanolithogr MEMS MOEMS **8**, 031404 (2009). 148

[239] M. Inguscio, S. Stringari, and C. E. Wieman, *Bose-Einstein Condensation in Atomic Gases: Proceedings of the International School of Physics "Enrico Fermi", Varenna on Lake Como, Villa Monastero, 7-17 July 1998* (Società Italiana di Fisica Bologna - Italy, 1999). 172

[240] F. K. Abdullaev and J. Garnier, *Propagation of matter-wave solitons in periodic and random nonlinear potentials*, Phys. Rev. A **72**, 061605 (2005). 174, 175

[241] G. Reinaudi, T. Lahaye, Z. Wang, and D. Guéry-Odelin, *Strong saturation absorption imaging of dense clouds of ultracold atoms*, Opt. Lett. **32**, 3143 (2007). 175, 180

[242] M. Gajdacz *et al.*, *Non-destructive Faraday imaging of dynamically controlled ultracold atoms*, Rev. Sci. Instrum. **84**, 083105 (2013). 180

[243] M. R. Andrews *et al.*, *Direct, nondestructive observation of a Bose condensate*, Science **273**, 84 (1996). 180

[244] A. Ramanathan *et al.*, *Partial-transfer absorption imaging: A versatile technique for optimal imaging of ultracold gases*, Rev. Sci. Instrum. **83**, 083119 (2012). 180

[245] M. W. Garrett, *An elliptic integral computer package for magnetic fields, forces, and mutual inductances of axisymmetric systems, and a versatile line tracing routine* (Oak Ridge National Laboratory operated by Union Carbide Corporation for the U.S. Atomic Energy Commission, 1965). 183